The effect of fibre arrangement on the dissolution dynamics of silk fibres in the ionic liquid 1-ethyl-3-methylimidazolium acetate

Xin Zhang

Department of Physics and Astronomy

University of Leeds

Submitted in accordance with the requirements for the degree of

Doctor of Philosophy

January 2023

The candidate confirms that the work submitted is her own, except where work which has formed part of jointly-authored publications has been included. The contribution of the candidate and the other authors to this work has been explicitly indicated below. The candidate confirms that appropriate credit has been given within the thesis where reference has been made to the work of others.

This thesis is dedicated to my dear mum Jinchuan, dad Dianxue.
Thank you both for your unconditional love and support.

Believe you can and you're halfway there.
Theodore Roosevelt

Acknowledgements

I would like, first and foremost, to express my sincere gratitude and biggest thanks to my supervisors Prof. Michael Ries and Dr. Peter Hine for their invaluable guidance, support and encouragement. All the cool ideas and fun discussions we had, either in office, lab, Bragg's cafe or over Teams during the pandemic have certainly made my PhD journey more enjoyable. I will forever be grateful.

Secondly, I would like to acknowledge Dr. James Hawkins, Dr. Yunhao Liang for providing training with the equipment, discussions on the analysis, to make the beginning of this project less of a struggle. Also, my appreciation go to each and individual of you, Maer, Alex, Fatimah, Nora, Amjad, Ashley, Samiah, James, Ieuan, from our Biopolymer Dream Team, for all your contributions to make this research team more family-like. I will miss you all!

A huge thanks to our experimental officer, Dr. Dan Baker, for all the help you gave me with the lab equipment, LaTex codes and inspired discussions on the project. Many thanks to all the other researchers from Soft Matter Physics group, for being so friendly and kind, I enjoyed our 10 mins talk sessions and cake mornings. Thanks to Dr. Mannan Ali for providing the training on X-ray. Also thanks to all staff members from the physics mechanical workshop for providing the mould, frames and other kits.

My special thanks go to my friends, Shuang, Zhenming, Yunhao, James, Joy, Terence, Chaochao, Kangyi, Dahuang, Josie, my xiongdi

and many more, for the great support and cooking delicious meals for me. My great appreciation go to my parents and family, for their unconditional love and support, without them I wouldn't be who I am and where I am today, I love you all. I wouldn't miss the chance for thanking my cats, Milly and Tofu, for warming my seats and keeping me company. Couldn't have done it without the best people and cats around me.

Last but certainly not the least, I would like to thank my boyfriend, James, and his family, for their enormous help in many ways, from tiny to massive matters. Thanks for always believing in me, encouraging and supporting me in studies and in life. Love you!

Author's Publication

Time–Temperature Superposition of the Dissolution of Silk Fibers in the Ionic Liquid 1-Ethyl-3-methylimidazolium Acetate

Xin Zhang, Michael E. Ries, Peter J. Hine
Biomacromolecules, 2021, 22, 3, 1091–1101
https://doi.org/10.1021/acs.biomac.0c01467

Under Review

Dissolution dynamics of woven all-silk composites fabricated in the ionic liquid 1-ethyl-3-methylimidazolium acetate (under review)

Xin Zhang, Michael E. Ries, Peter J. Hine
Composites Science and Technology.

Abstract

Natural fibres are a highly topical class of reinforcement materials as alternatives for synthetic fibres to manufacture composites for a broad range of applications. Silks, as one group of biopolymers, are structural proteins and offer new prospects due to their compatibility, superior mechanical properties and good processibility. All-silk composites (ASCs) were fabricated via a partial dissolution method, utilising *Bombyx mori* silk fibres as raw material, ionic liquid 1-ethyl-3-methylimidazolium acetate [C2mim][OAc] as the solvent, and methanol as the coagulant. The aim of this thesis is to understand the dissolution dynamics of silk fibres in [C2mim][OAc], through investigating the dependence of time, temperature, fibre arrangement, and addition of reducing agent on the dissolution behaviour. Single, array and woven ASCs were separately fabricated and studied. Cross-sectional images on single ASCs obtained from optical microscopy and Scanning Electron Microscope (SEM) revealed that the raw silk thread contains hundreds individual multifilaments, and so the dissolution starts on the surface of each individual filament, forming a close-packed thread core and gradually creating a coagulated layer of matrix surrounding its core. Radial integration of the intensity distribution curves collected from Wide-angle X-ray azimuthal scans enabled the quantitative measurement of the average crystalline orientation (P_2) within the partially dissolved ASCs. P_2 values were further found to be directly related to the fraction of preferred oriented crystalline and the randomly oriented crystalline, following this, a simple linear mixing rule was employed for the first time, to calculate the coagulated volume fraction of matrix (V_m) from the P_2 values. Measured P_2 and

V_m data derived from three fibre arrangements, consistently displayed equivalences between time and temperature, which were confirmed through the successful employment of a shifting method in log space, leading to the construction of their master curves at a chosen reference temperature. The required shift factors were plotted versus the inverse temperatures, linear relationships were found, implying the dissolution showed Arrhenius-like behaviour, and enabled the calculation of the dissolution activation energy (E_a). Tensile properties of the ASCs were measured, and all three parameters (tensile strength, Young's modulus, and elongation at break) were also found to obey time-temperature superposition (TTS) principle, allowing the employment of the same shifting method, and again, the determination of E_a.

The measured average E_a for dissolving silk fibres with different arrangements were compared, it was intriguing to see that the required E_a for dissolving single silk threads (128 ± 6 kJ/mol) and array silk threads (123 ± 10 kJ/mol) were approximately the same, however, a noticeable lower E_a was seen for the woven silk fabric (92 ± 2 kJ/mol). Meanwhile, the dissolution speeds were found to follow the order (from high to low): single > array > woven silk. Furthermore, the addition of a reducing agent (RA), sodium sulfite, as part of the solvent to prepare single ASCs, was found to have no effect on the dissolution rate, conversely the resulting silk fibroin film was seen to have improved tensile properties. Likewise, the woven ASCs prepared from the mixture of IL and RA were found to have enhanced peel strength, suggesting a better interfacial bonding between fibre and matrix.

Contents

List of Figures

Chapter 1

Introduction

1.1 Motivation and Aims

1.1.1 Sustainable Development Requirement on Fibre Reinforced Composites

Composite materials have a wide range of applications in industries including aerospace, automotive, manufacturing and many more on a grand scale worldwide [10]. In global industry, a large demand on composite materials lie in carbon fibre reinforced polymer matrix composites (CFRPs) and glass fibre-reinforced polymeric composites (GFRPs) [11, 12]. Among these, CFRPs have been reported to have an annual demand increased from 40 kilo tonnes (kt) in 2010 to over 160 kt in 2020, with an estimate to surpass 190 kt by 2050 [13–16]. The higher demand of CFRP directly contribute to one of the major environmental challenges associated with waste generation, i.e. 30 - 40 % of waste carbon fibres are generated during the production of CFRP and the waste from CFRP end-of-life products [15, 17, 18]. Recently, the National Composite Centre has reported that UK produces 110,000 tonnes of composites per year and more than 95 % of the raw materials and resins are derived from oil [19]. The difficulty in the separation of the elements during the recycling process and the degraded performance after recycling, leads to only 15 % of the composites being reused and recycled at the end of their life [19]. Though progress on technologies aiming to recycle waste

composite material has begun, including the utilisation of pyrolysis and solvolysis techniques to separate the fibres and resin for reuse. However, it has been pointed out that the recycling process is still energy costly and has a significant impact on the environment [20, 21]. Moreover, there are concerns about potential environmental pollution regarding man-made fibre composite materials, as it has been reported that the constituent components used in resin based composites are found to have environmental pollution potential during the degradation process [22].

Human activities significantly contribute to the increase in the emission of carbon dioxide and other greenhouse gases, resulting in climate change and global warming [23–26]. The depletion of fossil energy resources, primarily oil, has become a rising global challenge [27]. In September 2015, all member states from the United Nation proposed 17 sustainable development goals (SDGs) and 169 targets with the great ambition to guide the global sustainable development and achieve the full implementation of this agenda by 2030 [28]. The increase in awareness of the sustainable development has stimulated the idea of replacing non-renewable petroleum based materials in the production of fibre reinforced composites [29].

1.1.2 Potentials on All-Natural Fibre Composites

Natural fibres are gradually making their way to become the alternative for synthetic fibres for the use as the composite reinforcement, to incorporate with polymer matrices in the production of composites materials, due to their low cost, lightness of weight, reduced energy consumption and biodegradability [30, 31]. In the automotive industry, it has been reported that various panels, trim parts and brake shoes produced using natural fibres have reduced the weight by over 10 % and reduced the overall cost by 5 % [32, 33]. However, the surface incompatibility between natural fibres and most of the polymer matrices can result in poor interfacial adhesion between fibre and matrix phase, and thus negatively impact the physical and mechanical performance of the resulting composites [30, 34, 35].

Though it can be compensated by applying different chemical treatments to modify the natural fibres, however, the amount of organic solvents introduced during the process may become environmentally unsustainable [36].

To overcome the incompatibility between natural fibres and polymer matrices, another potential route is to prepare self-reinforced polymer composites (SRPMs), also regarded as all-polymer composites, where both the reinforcement and matrix are the same polymer [37]. The advantages of SRPMs also extend to their pure chemical functionality, and potentially easier recyclable process because of the homogeneity compared to composites made from different constituents [37]. In 1975, Capiati and Porter [38] first developed all polyethylene (all-PE) composites by partially melting the crystals within the fibres and provide a gradual change in the morphology between fibre and matrix, leading to a competitive interfacial shear strength comparing to glass fibre reinforced with polyester and epoxy resins. Following the success of all-PE composites, research on single-polymer composites began around the world, leading to the development of all-polypropylene (all-PP) composites [39–42].

Following the concept of self-reinforced composites and sustainable design of composite materials, all-natural fibre composite was first introduced by Nishino et. al [43], leading to the fabrication of all-cellulose composites (ACCs). Subsequently, extensive studies have been carried out utilising various sources of cellulose to fabricate ACCs, including ramie [44], cotton [45–47], hemp [48, 49], flax [50], microcrystalline cellulose [51–54] and regenerated cellulose fibres such as Lyocell and Bocell [3, 55–57]. The high interests on ACCs is mainly due to the good interfacial bonding and high strength of cellulosic materials [58].

Although there has been substantial quantities of research dedicated to plant-based all-polymer composites, comparatively few studies are seen for another group of natural fibres, animal-based fibres (chicken feather, silk, wool, etc.). It is acknowledged that biomaterials having evolved for millions of years, their properties often exceed man-made materials and have a wide range of applications in

medical fields and beyond [59, 60]. For example, the specific hierarchical architecture of protein within silk fibres facilitates their superior mechanical properties, such as a comparable specific strength to steel and nearly as elastic as rubber [61–63]. The favourable biocompatibility and outstanding mechanical properties of silk fibroin also made them popular for bioengineering applications including tissue engineering, drug delivery, and biodegradable medical devices [64–69]. It appears remarkable that, given the outstanding physical and mechanical properties of silk proteins, more research investment is yet to be made with regards to the employment of silk fibres to produce all-silk composites (ASCs). As such, this is currently an evolving field with significant potential for future technological applications. This thesis therefore focuses on utilising *Bombyx mori* (*B. mori*) silk fibres and partial dissolution method to fabricate ASCs, and investigates the dissolution behaviour of different arrangements of silk fibres in the chosen solvent. In order to effectively implement applications in the context of ASCs, the fundamental dissolution dynamics during the fabrication process including the influences of time and temperature on the dissolution; the microstructure, average crystalline orientation and mechanical behaviour of the resulting ASCs will be investigated. The findings in this thesis hopefully open up insights into silk-based composite materials.

1.2 Thesis Structure

Following the introduction above, the next chapter of this thesis, Chapter 2, will give a more detailed review on the current challenges and limitations of some commonly-available fibre-reinforced composites and how natural fibre reinforced composites (NFRC) can overcome these issues. It will continue to introduce the dissolution methods to produce ASCs before further explaining the context of *B. mori* silk fibres, interaction between different ionic liquids with silk fibres, coagulation process and the underlying theory behind the dissolution as a means to design the experiments and analysis the findings.

In Chapter 3, the experimental techniques utilised to carry out the characterisation on the fabricated all silk composites will be described. Chapter 4 will

provide the fabrication methods for preparing single ASCs and the silk fibroin (SF) films with a detailed investigation into the dissolution behaviour of single *B. mori* silk threads and the resulting single ASCs. Chapter 5 will then explore how the addition of reducing agent sodium sulfite as part of solvent influences the dissolution of single silk threads. The effects will be investigated through analysing the changes in the dissolution rate, activation energy and the mechanical properties of the resultant single ASCs and SF films. Chapters 6 and 7 will continue to analyse the dissolution behaviour on two other different arrangements of silk fibres, with Chapter 6 exploring the array silk threads and Chapter 7 explicating the woven silk fabrics. The dissolution rates and activation energies derived from three arrangements of silk fibres will be compared and included in Chapter 7, along with the effects of the introduced reducing agent on the tensile properties and interfacial adhesion on the fabricated woven ASCs. Finally, Chapter 8 will draw together the main findings of this thesis and provide the potential future work. The thesis structure is summarised in Figure 1.1, as shown below.

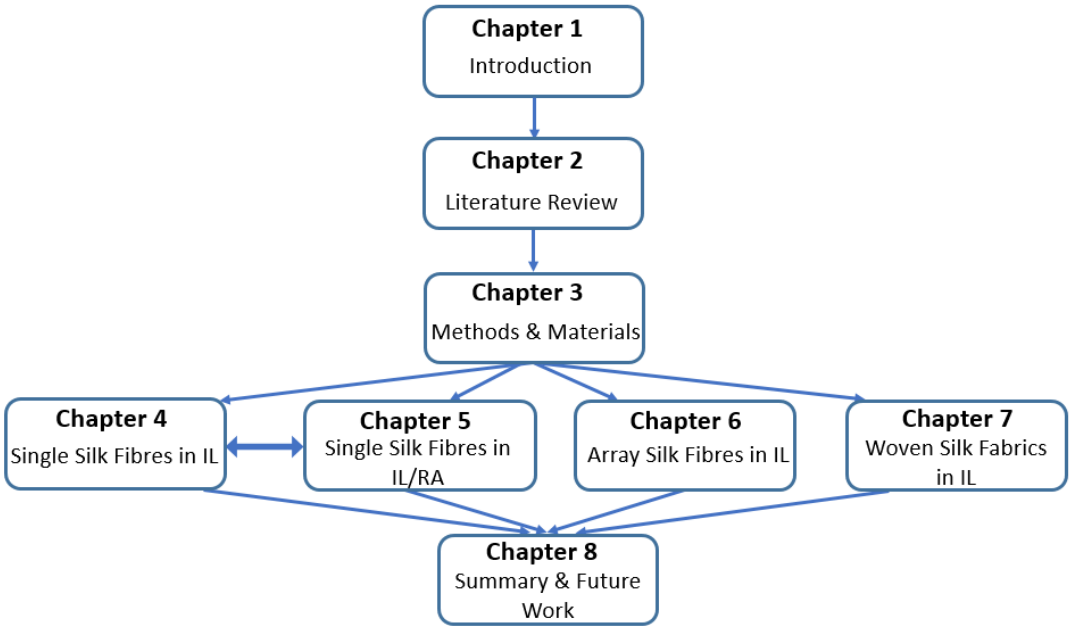

Figure 1.1: Schematic representation of thesis structure.

Chapter 2

Literature Review

2.1 Composites

Composites are a combination of components, usually at least two constituents with distinctly different physical or chemical properties, named reinforcement phase and matrix phase [1]. Many materials are recognised as composite materials. For example, cob mud bricks are made of mud clay and straw, wood is composed of fibrous cellulose with a matrix of lignin, concrete consists of loose stones with a matrix of cement and modern composites use fibres and particles embedded with ceramic, metal or polymer binders [70]. There are four primary types of composites, polymer matrix composites (PMCs), metal matrix composites (MMCs), ceramic matrix composites (CMCs) and carbon matrix composites (CAMCs), whilst PMCs are the most extensively used type of composites [71]. Figure 2.1 shows the configurations for composites with most common reinforcement forms, including long fibres (continuous fibres), short fibres (discontinuous fibres), monofilaments and particles [1].

To design a composite for a specific type of application, it is vital to consider the properties displayed by the potential reinforcement/matrix materials [1]. The primary characteristics to drive the use of composites are weight reduction for their relative stiffness, strength and toughness. Liu et al. [72] reported that tensile strength of carbon fibre reinforced composites are much higher than steel while having a significantly lower density. Generally, properties of composites can

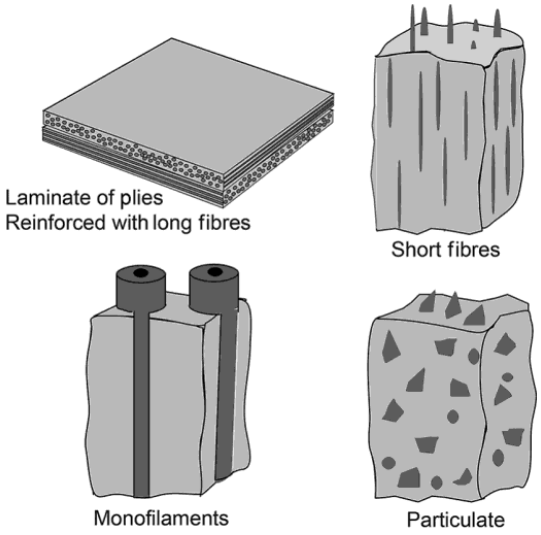

Figure 2.1: Different types of reinforcement forms. Reproduced from ref [1], Cambridge University Press, ©2012.

be tailored through choosing the different reinforcement and matrix phase and embedding various extra functionality, leading them to a myriad of applications.

2.1.1 Fibre-Reinforced Composites (FRCs)

Fibre-reinforced composites are composed of fibres of high stiffness and strength embedded in or bonded to a matrix. Both fibres and matrix maintain their characteristics, and provide a combination of properties that cannot be reached as an individual [73]. In principle, fibres carry the load, while the surrounding matrix acts as a load transfer medium and keeps the fibres in the desired location and orientation and protects them from environmental damages. Glass, carbon and aramid (Kevlar and Twaron) fibres are widely used as reinforcement to produce PMCs, MMCs and CAMCs, and found to provide durable and reliable components in automotive, aerospace and armour applications [71]. Das [74] has estimated that the use of GFRP as structural components could result in a 20-35 % reduction in vehicle weight, and more impressively, the use of CFRP could yield a 40-65 % reduction in weight.

The most common matrices to produce FRCs are polymeric to produce PMCs, because of their low density and can be processed at low temperatures [75]. Matrix within PMCs also recognised as resin, and further classified as thermoset, thermoplastic and elastomeric composites. Thermoset materials undergo a curing process where the polymer chains are crosslinked, leading to a rigid product and cannot be reshaped afterwards. Thermoplastics can be repeatedly softened and reshaped by the application of heat, and thus more recyclable compared to thermosets. Examples for thermosetting polymer matrices are epoxy, polyester, vinyl ester, polyurethane, bismaleimides and other thermoset polyimides. On the other hand, polyethylene (PE), polypropylene (PP), polyphenylene sulfide, polysulfone, polyvinyl chloride, polystyrene PLA and other thermoplastic polyimides are commonly used as thermoplastic polymer matrices. The most well-known elastomeric material is rubber, thus the elastomeric composites also named as rubber composites [71, 75, 76].

However, as covered in section 1.1.1, the sustainability concepts and new environmental regulations are driving natural fibres to become the replacement for synthetic fibres for the production of eco-friendly FRCs [28, 29, 77].

2.1.2 Natural Fibre-Reinforced Composites (NFRCs)

Based on its origin, fibres are categorised into plant, animal or mineral to produce NFRCs. The primary structural component of plant fibres is cellulose, whereas animal fibres are generally composed of protein. Mineral-based fibres are found from asbestos group of minerals, and were widely used as composites in building materials in the past before the adverse properties associated with health issues were recognised [75, 78]. As covered in section 1.1.2, due in a large part to the low cost, lightweightness and potentially biodegradability, the application of natural fibre reinforced polymer composites is rapidly rising in the automotive and aerospace sectors [30, 31, 79–81].

In the automobile market, Draxlmaier Group and Faurecia supply interior parts of automobiles using NFRCs, including headliners, side and back walls,

seat backs, and rear deck trays to GM, Audi and Volvo [82]. Typical examples of NFRCs for the application in automobiles are flax/PP, hemp/PE, kenaf/PP, bamboo/PBS, and utilisation of other natural fibres such as sisal, jute, wood, cotton, coconut, in combination with various polymer matrices [83–85]. Whilst in the aerospace market, Airbus and Boeing have tried to reinforce natural fibres to prepare light weight composites to improve the fuel efficiency [80, 86].

However, glass fibres are predominant as reinforcement fibres in the market for the composite industry, because of some concerns regarding the use of natural fibres [30]. Firstly, there is large variation in the physical properties of natural fibres, depending on the harvesting season/region, maturity of the plant and where the fibres are harvested from, etc [87]. In addition, moisture absorption is also one of the challenges exhibited by natural fibres, absorbing moisture from the surrounding environment may cause dimensional changes or create adverse internal stress [73]. As covered in section 1.1.2, one of the other major drawbacks of natural fibres is the low compatibility with polymeric matrices, which may cause non-uniform dispersion of fibres. Other drawbacks such as limited thermal stability, low resistance to rotting and microbe may affect the overall mechanical performance of NFRCs [88]. Moreover, PP and PE are the two most commonly adopted thermoplastic matrices for NFCs. The difficulty in recycling thermosets matrices is one of the concerns, thus leading to the development of self-reinforced polymer composites.

2.1.3 All-Polymer Composites

All-polymer composites represent one emerging family of composite materials, also recognised as self-reinforced polymer composites (SRPMs), with the same polymer serving as both the reinforcement and matrix phases [37, 89, 90]. The history for the development and driving force on all-polymer composites have been briefly introduced in section 1.1.2.

The majority of SRPMs are formed from semicrystalline polymers, commonly contain highly aligned reinforcement fibres, with matrix from the same polymer

but different crystalline structure. The design of SRPMs (reinforcement/matrix) generally follows the combinations - semicrystalline/amorphous and semicrystalline/semicrystalline [90]. Similar to the FRCs, all-polymer composites can be classified into synthetic fibre-based and natural fibre-based. The most reported all-polymer composites are found to produce from synthetic fibres such as polyolefin-based (PE, PP), polyester-based (PLA, PET, PMMA), polyamide-based (Nylon) and natural fibres such as protein, cellulose and starch-based [37]. The techniques involved to design and fabricate all-polymer composites include thermal processing (overheating) [91], hot compaction [39, 41, 92, 93], cool drawing [94], partial dissolution [51], etc [95–97].

The first all-polymer composite was first produced 30 years ago. Hence, the study of all-polymer composites is still a new and developing field, the fundamental problems and processing techniques are far from mature, and only few products are commercially available, such as Pure®, Armordo®and Curv®that are based on all-polypropylene composites. On the other hand, all-polymer composites are particularly important in biomaterials applications, since any additives composed of different chemicals could affect biocompatibility and biodegradability [37, 98]. As mentioned, extensive studies have focused on cellulose-based composites. There are two main dissolution methods to prepare all-natural fibre composites and will be introduced in following section.

2.2 Dissolution Methods

Following the success of all polymer composites like all polyethylene (PE) [99] and all polypropylene (PP) [40] composites, all cellulose composites have been firstly proposed as a self-reinforced natural fibre composite through two methods: a conventional impregnation method [43, 55, 100] and a surface selective dissolution method [3]. Closely followed by the instruction on preparing all-cellulose composites, all silk composites has been investigated preparing through the impregnation method.

2.2.1 Impregnation Method (Two-step method)

Similar to all cellulose composites prepared by Gindl et al. [100], Yuan et al. [2] has investigated an approach to produce all silk composites, where silk fibres are impregnated into a silk fibroin matrix. Basically, the degummed silk fibres were dissolved in LiBr aqueous solution, followed by the process of dialyzation and centrifugation, to form a 15 wt. % silk fibroin solution. Therefore, a solution with dissolved silk fibroin was served as regenerated silk fibroin (RSF) solution. On the other hand, the both end fixed silk fibres were aligned parallel to each other and treated with LiBr aqueous solution. After repeatedly rinsing with deionised water, the fibres were impregnated into a matrix, which functioned as reinforcement, as illustrated in Figure 2.2 [2].

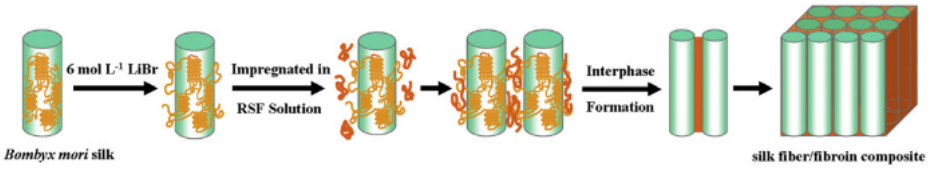

Figure 2.2: A two-step method to prepare all silk composites, using silk fibres as reinforcement and silk fibroin solution as the matrix. Reproduced from ref [2], *Elsevier Ltd*, ©2010.

All silk composites manufactured through such a two-step method possessed relatively good interfacial strength and high mechanical and thermal properties, which indicates the effectively molecular diffusion across the interface between the fibre and the matrix occurred.

2.2.2 Parital Dissolution Method (One-step method)

Soykeabkaew et al. [3] have invented a relatively similar approach to prepare all cellulose composites. In this method, both the fibres and the matrix are cellulose, and the surface layer of cellulose fibre is partially dissolved to form the matrix phase. Meanwhile, the remaining inner cellulose fibre cell cores maintain their original highly oriented crystallite structure, which served as the reinforcement

phase in the composite. Generally, the dissolved cellulose fibres are regarded as the matrix phase, which provide a condition for all the cellulose fibres to "weld" together in certain areas and form a perfect interface, as shown in Figure 2.3 [3].

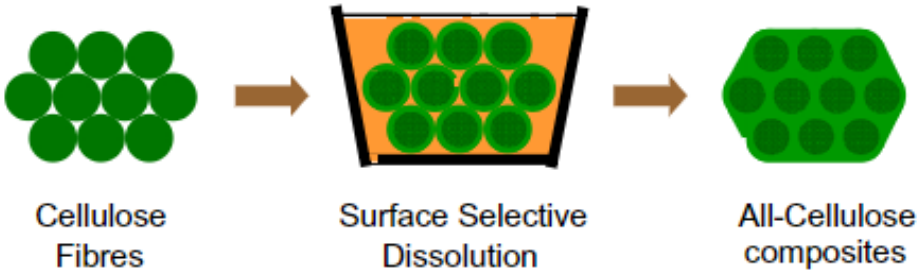

Figure 2.3: Partially dissolved surface of cellulose fibres to prepare all cellulose composites. Reproduced from ref [3], *Elsevier Ltd*, ©2009.

2.3 Silk

Animal fibres such as silk, wool, chicken feathers, horse hair, etc. are the second most important source of natural fibres and can act as the reinforcement phase in NFRCs [101]. Natural silk fibres spun from silkworms and spiders have attracted a large amount of interest because of their remarkable biological, structural and mechanical properties [102]. Due to the difference in the amino acid composition, silk fibres produced from silkworms and spiders have different structural properties, and it is acknowledged that some spider silks are stronger than silkworm silks [62]. However, due to the cannibalistic nature of spiders, it is extremely challenging to make a high yield of industrial production of spider silks [102–104]. On the other hand, silkworm silks have been developed through domestication and artificial selection of the moths for more than 4000 years, with enormous amount of applications in textile and biomedical fields [105–109]. For these reasons, silkworm silk is considered as the natural fibre source in this thesis.

2.3.1 *Bombyx mori* Silk Hierarchical and Crystalline Structures

The mulberry silkworm, also named *B. mori*, exhibits high strength and high elongation properties, owing to the high level of protein production and strong regulatory control. A single *B. mori* silk thread, approximately 10–25 μm in diameter, contains two fibrous core proteins named fibroin, and a protective, glue like coating named sericin that surrounds the fibroin threads to hold them together, as illustrated in Figure 2.4 [4]. Fibroin is a hydrophobic protein and contains filaments that are assembled from microfibrils of ca. 10 nm width [110]. Whilst sericin is generally a water soluble, amorphous protein polymer and thus it is relatively straightforward to remove by a chemical process known as degumming. The degummed silk provides a high lustre and silk feeling [111].

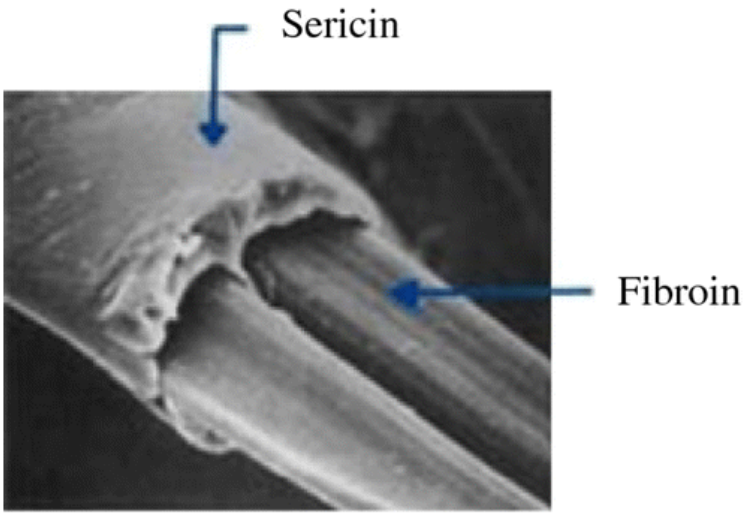

Figure 2.4: Cross-section image of silk thread. Reproduced from ref [4], *Taylor & Francis*, ©2012.

On the molecular level, the silk fibroin (SF) cores consist of two protein chains, a light (L-chain) and a heavy chain (H-chain) with molecular weight of approximately 26 kDa, 350 kDa, respectively [112–115]. The L-chain and H-chain are

covalently linked through a disulfide bond at the C-terminus, between two cysteines (Cys-c20 of H-fibroin and Cys-172 of L-fibroin), forming a H-L complex and holding the fibroin together [69, 116, 117], see Figure 2.5. Another 25 kDa polypeptide (P25) is also reported by researchers, and suggest that *B. mori* silk fibroin composes of H-chain, L-chain, and P25, at a molar ratio of 6:6:1 [118]. P25 is a glycoprotein, which is associated with H-L complex through hydrophobic interactions [119].

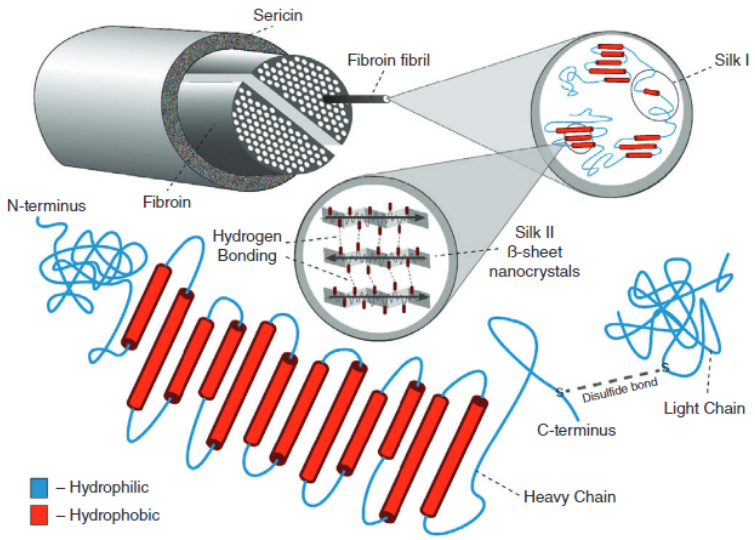

Figure 2.5: Schematic representation of the *B. mori* silk structure. Reproduced from ref [5], *National Center for Biotechnology Information (NCBI)*, ©2018 Wiley Periodicals, Inc.

In the H-chain, the molecules themselves have a segment copolymer-like arrangement, which consists of 12 hydrophobic crystalline blocks and separated from each other by 11 short hydrophilic amorphous regions. Within the 12 hydrophobic blocks, glycine (G)-X repeats are the predominate sequences that take up 94 % of the sequence, where X represents alaine (A) at 65 %, serine (S) at 23 % and tyrosine (Y) at 9 % [120]. These highly repetitive GAGAGS amino acid sequences form the stable antiparallel β-sheet crystallites [121–123]. In contrast, the amino acid sequence of L-chain is non-repetitive and more hydrophilic and relatively elastic, which provides the high extensibility of silk fibres [103, 120].

The crystalline structure of *B. mori* silk fibres implies that the β-sheets are highly structured, with all the glycines packed on one face of the β-sheet, and all the alanines as side-chains on the other face, forming a upside-down alignment. Consequently, β-sheets compose of short vertical spacings ($\sim$3.6 Å) for glycine-glycine packing, and longer spacings ($\sim$5 Å) for alanine-alanine packing [116].

It is known that silk fibroin contains three conformations, random coil, α-helix (silk I) and antiparallel β-pleated sheet (silk II), as illustrated in Figure 2.5 [5, 124]. In fact, some researchers found there is actually a small amount of unstable silk III obtained in the fibroin secondary structure that exists in the air/water interphase [125, 126].

The water soluble silk I structure is unstable to mechanical or shear stress, thus it easily converts to antiparallel β-sheet (silk II structure) when exposed to methanol or potassium chloride [127]. The work by Ishida et al. [124] investigated the solvent induced conformational transition of *B. mori* silk fibroin by using solid state ^{13}C NMR. It is worth mentioning that the conformational transition of regenerated silk fibroin, from the random coil or silk I to silk II form is able to be achieved after treating with certain polar solvents such as alcohols and acetone. And the extent of change is related to the ease of the hydration/dehydration process by these solvents. Theoretically, the disruption of the hydration layer of fibroin due to methanol or ethanol facilitates the aggregation of fibroin molecules, enabling it to rearrange into more regular and stable structures through hydrogen bonding. Therefore, by altering the types of organic solvents, the conformational character of silk fibroin is able to be controlled through silk II content [124], which will be discussed in details in section 2.5. Silk II corresponds to the antiparallel β-sheet crystal structure obtained once silk has been spun. In the laboratory, this polymorph results from the exposure of silk I to mechanical/physical and chemical treatments, such as stirring, heating, exposure to methanol or water annealing procedures. The formation of the β-sheet structure is possible due to the rearrangement of the repetitive regions that form the H-chain of SF, and the

intra and intermolecular interactions by hydrogen bonding, van Der Waals forces and hydrophobic interactions [103].

Silk II is the most stable state due to strong hydrogen bonding between adjacent peptide blocks, resulting in increased mechanical properties including rigidity and tensile strength [112, 128, 129]. Therefore, the highly crystalline secondary structure of silk establishes a strong potential for crystal formation and this largely accounts for the remarkable mechanical characteristics. While the amorphous molecular chains consist of β-turn, helix and random coil structures that bridge different β-sheet nanocrystals and exhibit elasticity through large deformations [130].

2.3.2 *Bombyx mori* Silk Fibre Composites

As mentioned earlier, the favourable biocompatibility, biodegradation and excellent mechanical performance of *B. mori* silk fibres made them popular for uses in biomedical applications [64–69]. Recently, studies on *B. mori* silk fibres/polymeric matrices composites have been found in engineering field, beyond their traditional uses in textile and biomedical applications. Several groups of researchers have individually studied the crashworthiness characteristics [131–133], the effect of an external trigger configuration on the crashworthiness [134, 135] and the impact performance [136, 137] of silk/epoxy composites.

Additionally, a few studies have reported that regenerated silk matrix composite materials reinforced by silk fibres have higher tensile strength and are more predictable in failure than any other plant fibres and even glass fibre textiles [2, 138–141]. As mentioned in section 2.2.1, Yuan et al.[2] have employed the two-step method for producing all silk composite, degummed silk fibres were completely immersed in silk fibroin solution. They compared the mechanical properties of regenerated SF matrix with silk/fibroin composite with various silk fibre mass ratio. More recently, Marine et al. [142] optimised the two-step preparation by varying the organisation (straight fibre method, relaxed fibre method and

dipping method) of single fibre in the matrix system to produce all-polymer composites. They used either partially degummed silk fibres or completely degummed silk fibres to prepare multifibre reinforced composite. The mechanical properties of regenerated silk composite prepared through these two different methods are shown in Table 2.1, where composite-X means composite with X percentage of silk fibres in the composites.

	Breaking stress(MPa)	Breaking elongation(%)	Tensile modulus(GPa)	References
RSF matrix	60±8	2.1±0.2	3.7±0.4	[2]
Composite-10	83±7	11±1	3.1±0.2	[2]
Composite-20	142±7	24±2	3.0±0.2	[2]
Composite-25	151±5	27±1	2.8±0.1	[2]
Mono composite(Straight)	18±11	0.8±0.4	3.0±1.8	[142]
Mono composite(Relaxed)	10±4	0.6±0.3	2.1±0.3	[142]
Mono composite(Dipping)	384±36	16±2	12.9±1.1	[142]
Multi composite (Bmd)	74±37	7±4	3.3±0.9	[142]
Multi composite (Bmpd)	89±66	13±7	3.0±1.3	[142]

Table 2.1: Comparison of the overall mechanical properties of silk fibre/fibroin composites with RSF matrix.

Table 2.1 shows that the brittle RSF matrix was toughened by silk fibre in the parallel direction, especially the breaking stress of composite-25 was twice as strong as that of the pure RSF matrix. Therefore, it indicated that the overall mechanical properties of RSF matrix were gradually enhanced with the incorporation of silk fibres, and the mechanical properties of composite was improved by increasing amount of silk fibres obtained in the reinforcement. In addition, compared to the straight and relaxed method, the dipping method shows relatively better mechanical properties, which indicates that the dipping method results in the encapsulation of fibre into fibroin matrix to provide a good interfacial strength within the regenerated composite. Besides, the multi-reinforced composite with the partially degummed fibres had slightly higher breaking strength than those

with completely degummed fibres, but the elongation of the former composite was nearly twice the elongation of the latter composite.

Consequently, from the reported observations on the mechanical properties of silk-based composites, it is suggested that there are various parameters that can affect the composite mechanical properties, i.e. diameter/length/orientation of fibre, bonding between fibre-matrix, and fibre volume fraction, etc [2, 85, 142]. Other studies on the mechanical performance on natural fibre reinforced composites have found to have similar suggestions. Laranjeira et al. [143] studied jute/polyester composites and suggested that with higher fibre content and when tensile test conducted along the fibre axis direction, composites were found to have greater tensile and impact behaviour. Additionally, the crack in the matrix and fibre interfacial bonding shows a deleterious effect on the overall composite mechanical properties. Hence, to obtain a high-performance silk-based composite, it requires the knowledge of the dependence of these variables on the mechanical behaviour of the composite.

2.4 Ionic Liquids as Solvents for Silk

To dissolve the degummed silk fibres, breaking the large amount of intra- and inter-molecular hydrogen bonds between amino acids along the entire polypeptide chain is required and disruption of stacks of β-sheets are particularly important. The hydrogen bonding and the hydrophobic nature of these crystalline regions make it difficult to dissolve in some common organic solvents [144]. Besides, many organic solvents can cause depolymerisation of SF and thus alter the molecular weight [145, 146].

Ionic liquid (IL), also known as 'molten salt', with anions and cations, represents a unique class of solvents that possess remarkable versatility and tunability [147]. The extremely low melting points, low or zero vapour pressure, high thermal stability and easily altered structure, makes ionic liquid popular solvents to dissolve some high crystallinity natural materials, i.e. lignocellulosic materials [148] and protein based natural materials [147].

Imidazolium based ionic liquid was firstly investigated to be used as a 'green solvent' to dissolve cellulose by Swatloski et al. in 2002 [149], with different solubility of cellulose in a wide range of salts, ranging from 5 to 25 wt.%. The research has shown that ILs can be used as non-derivatizing solvents for cellulose. Compared to volatile organic solvent, ionic liquid in a way, can be easily separated from the desired products and is potentially recyclable. Expectedly, the research on dissolution of silk by using ILs was then studied by Phillips et al. [150] in 2004. Their studies suggested that both the cation and anion play a role on the dissolution of SF in ILs, with the anion has a larger effect as anions are stronger hydrogen bond acceptors than cations. The anions associated with the hydrogen atoms of the OH groups, whereas the cations associated with the oxygen atoms [149]. The more the cation and anion are able to participate in hydrogen bonding, the greater the solubility of the SF. Since Phillips, there is a growing interest on utilising ionic liquids to dissolve SF [151–158], researchers have found that there are three main types of ionic liquids that can break hydrogen bonds between β-sheets structures of SF, including 3-methyl imidazolium-based ionic liquids, protic ionic liquids and choline salts [154–156], with 3-methyl imidazolium-based ionic liquids being the most extensively studied ILs to dissolve SF [157]. It has been suggested that the solvent capacity of SF in 1-alkyl-3-methylimidazolium ILs correlates to the length of the alkyl substituent when the ILs compose of the same halogens. It is considered that the shorter the length of the alkyl substituent, the stronger the hydrophilicity of the ionic liquid, therefore the silk solubility is able to be controlled by the selection of ionic liquids [150]. The mechanism for the dissolution of silk fibres using one of the ionic liquid, 1-ethyl-3-methylimidazolium acetate ([C2mim][OAc]), is shown in Figure 2.6.

A summary of the solubility data for silk fibroin in ionic liquids are shown in Table 2.2, and it implies that the presence of the chloride ion plays the most important role in the dissolution of silk fibroin and the solubility of silk increases in the order $Dmbim^+Cl^- > Bmim^+Cl^- > Emim^+Cl^-$ [147].

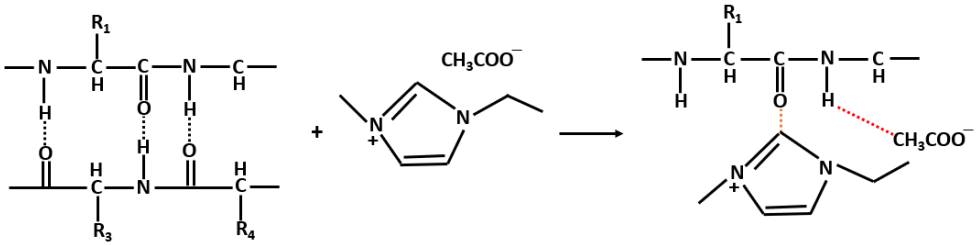

Figure 2.6: Reaction scheme for the dissolution of silk fibres using the ionic liquid 1-ethyl-3-methylimidazolium acetate ([C2mim][OAc]).

	anion				
cation	Cl^-	Br^-	I^-	$BF4^-$	$AlCl4^-$
$Bmim^+$	13.2 %	0.7 %	0.2 %	0.0 %	c
$Dmbim^+$	8.3 %	c	c	c	c
$Emim^+$	23.3 %	c	c	0.0%	0.0 %

Table 2.2: Solubility by weight for silk fibroin in ionic liquids (c: System not tested). Reproduced from ref [147], *Frontiers*, ©2007.

Phillips et al. [150] have further examined the solubility of the silk fibroin in $Bmim^+Cl^-$ with wide angle X-ray scattering (WAXS) by examining the crystal structure. The WAXS result shows that a broad amorphous peak appeared in silk solution but no β-sheet structure, which indicates that $Bmim^+Cl^-$ is capable to disrupt the hydrogen bonds in the crystalline domains. In addition, the absence of peaks associated with $Bmim^+Cl^-$ crystallinity suggests that there are strong interactions between the $Bmim^+Cl^-$ and silk fibroin.

Stanton et al. [6] reported that the selection of ionic liquids has a great impact on the structure, morphology and properties on silk cellulose blended films. A 10 wt.% silk and cellulose blended solution (silk:cellulose, 1:9) was prepared by individually dissolving the blended materials in various imidazolium based ionic liquids, followed by immersing in water for the regeneration of the blended films. The FT-IR result shows the peaks for Amide I and Amide II from the regenerated films for each ILs are shifted to a higher wavenumber when compared to the pure

silk sample. It implies that the disruption on the inter- and intra- hydrogen bonds by the ionic liquid occurs in the system, which result in the change of overall shape of the β-sheets. The crystal fraction of β-sheet was calculated in the Amide I regions of the ionic liquid, indicating the crystallinity of the silk material as a function of the ionic liquid, the results are shown in Table 2.3 [6]. Theoretically, the more the ionic liquids interact with the polymers, the greater the interruption of the hydrogen bonding network, the more changes occurs in the β-sheets. It was observed that the films with the chloride anion were the lowest in crystallinity and EMIMAc was slightly more crystalline. Meanwhile, the BmimBr and Bmim-$MeSO_3$ are composed of the highest amount of crystallinity which indicates that the larger anions had an increase in percent crystallinity of β-sheets in silk.

Ionic Liquid	β-sheet crystal fraction
AmimCl	31.0%
EmimCl	37.1%
EMIMAc	39.2%
BmimCl	37.5%
BmimBr	58.6%
Bmim-$MeSO_3$	58.9%

Table 2.3: Calculated β-sheet crystal fraction within the silk-cellulose film, coagulated from various types of ionic liquids. Reproduced from ref [6], *Elsevier Ltd*, ©2018.

It can also be suggested that the topographical and morphological properties of regenerated silk cellulose blended films varies from the different ionic liquids through the evidence from the scanning electron microscopy (SEM) results [6]. Figure 2.7 [6] demonstrates the morphology of 10 % silk-cellulose films coagulated from different ILs, as listed in Table 2.3. It suggests that the blended film coagulated from the ILs that compose of the same anion (Cl^-) exhibit a more uniform morphology, whereas obvious differences in morphology for the films coagulated from similar cations (EmimAc, EmimCl) can be observed. It also implies that the films coagulated from ILs that contain bromine or the methane sulfonate groups, display fibrous-like morphology. The ILs with the chloride anion group

appears to be more uniform unlike those of the bromine or the methane sulfonate groups, which appears more fibrous-like. They also suggest that the reason for the observed porous surface of the film coagulated from EmimAc, could be the removal of acetate anion group during the coagulation process when immersing the solution in water.

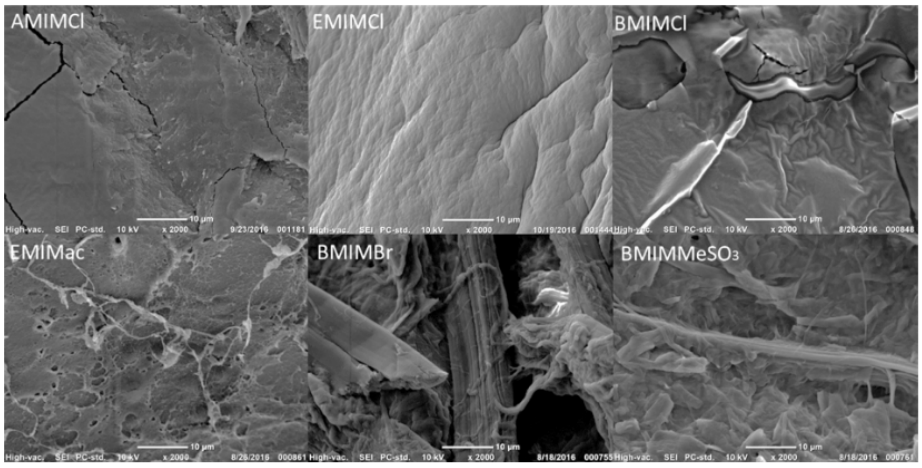

Figure 2.7: SEM images of the morphology of the 10 % silk-cellulose films coagulated from six different ionic liquids. Reproduced from ref [6], *Elsevier Ltd*, ©2018.

2.5 Coagulation

It is acknowledged that to form the desired product in a favourable structural form after dissolution, the key process is to remove solvent from the polymer solution. It is relatively straightforward if the solvent is volatile, this can be achieved simply by evaporation of the solvent. Whereas for non-volatile solvents, the removal of solvent from the polymer solution is then accomplished by diffusional interchange with a anti-solvent bath. This process is recognised as 'coagulation', where the fibres lose their solubility and precipitate from the solution, followed by solidification and reform into the desired product [159].

The unique structure of silk makes it versatile in processing, which can be

further coagulated from the silk fibroin solution and exhibit a range of structural forms, such as sponges, films, hydrogels and nanoscale electrospun non-woven mats [6, 127, 147, 150, 160, 161]. The generation of various structural forms not only depends on the choice of ionic liquids but also on the coagulation solvent bath.

It is worth mentioning that the coagulation of natural fibres is usually accompanied with a conformational transition, such as the crystalline structure of cellulose changes from a cellulose I to either a cellulose II, amorphous or intermediate structure [162]; the structure of silk fibroin changes from a random coil to well oriented β-sheet structure [163]. The coagulation process of SF not only affects the secondary structure of SF but also its molecular weight and physicochemical and morphological properties [164, 165].

As previously mentioned in section 2.3.1, the conformational character of RSF film is highly dependent on the rinse treatment [166]. Phillips et al. [150] found that acetonitrile yields a convoluted film with little crystallinity, methanol yields a transparent film with a high degree of crystallinity, which agrees with methanol treatment of silk inducing the β-sheet structure. In contrast, the RSF treated with water result in the dissolution of the silk film. However, Mantz R.A. et al.[147] further investigated that neutral water dissolves the silk fibroin whereas acidic water yields a fibrous matte structure when used as regeneration bath. They also found that the complete removal of the ionic liquid depends on the rinse time in the regenerating solvent.

On the other hand, Chen et al. [167] were interested in the formation of β-turn structure, they reported that the kinetics of β-turn formation varies not only in the RSF or solution, but also depends on the concentration of ethanol used to induce the conformation transition. The presence of sufficient water provides good chain mobility to allow alcohol to be effective at removing the water shell around the hydrophobic fibroin. In theory, the formation of β-turn only requires the slight adjustment of four amino residues within a loose hairpin loop, while much larger adjustments are required to form extensive β-sheets. Therefore, the greater

concentration of ethanol, the lower water content present, the more possibility for forming the β-turn rather than β-sheet structure. It can be concluded that the difference in free water content and the rate of hydrophobic dehydration decides the chain motility which results in different conformation content in regenerated silk fibroin.

In addition, Zhou et al. [168] showed that the conformation transition rate is crucial to the behaviour of the silk and consequently to the mechanical properties of the RSF fibres. If the transition rate is too slow, either the cross-section of the fibres is irregular, or the fibre cannot be formed at all. On the other hand, when methanol is the coagulation bath, if the rate of coagulation is too fast, the resulting fibre is very brittle. Therefore, the moderate coagulation rate during conformation transition, allows the protein chains free to move and adjust their position relative to each other enabling the silk fibroin chains to refold easily to form β-sheet and β-turn. Ling et al. [169] reported similar observations, they used time-resolved FTIR to investigate the kinetics of the conformation transition in silk fibroin solution, and suggested that the moderate coagulation rate allows a greater efficiency for the alignment of molecular segments, which leads to the resulting coagulated silk fibres with a larger breaking strain.

Interestingly, Goujon et al. [156] reported that protic ionic liquids (pILs) can be used as the coagulant for silk fibroin. They suggest that the unique hydrogen bonds in pILs make them limited in dissolving silk fibres, whereas it is ideal to use as coagulant. The choice of pILs has a great impact on the structure and morphology of the resulting coagulated silk foams. In particular, they demonstrated that silk foam coagulated from the pIL - triethylammonium mesylate (TeaMs) contains 45 % of α-helix structure, which in return increases the tensile strength of the resulting silk fibres.

2.6 Dissolution Kinetic Factors and Activation Energy

As introduced in section 2.3.1, the strong hydrogen bonding between the repetitive polypeptides, van Der Waals forces and hydrophobic interactions create the stable molecular structure of silk fibroin. For the effective dissolution of SF, it is therefore crucial to consider the interactions between the chosen solvent and the stable structure of SF. As covered in section 2.4, since 2004, the implementation of different types of ILs as solvent for preparing silk-based materials has shown large interest across academia research and industrial applications. From literature, it is evident that various factors affect the solubility of SF when using ILs as the solvent, such as the selection of IL (as previously described in section 2.4) [150, 170–172], physical properties of IL (its melting point) [151, 173], dissolution time, temperature [174, 175] and the implementation of ultrasound treatment [176–179], etc. However, limited studies are so far found focusing on the dissolution kinetics and mechanisms.

Zhang et al. [180] explored the changes on the silk fibre structure when adding the chosen solvent ($CaCl_2$-Formic acid), they claimed that dissolution of silk fibroin starts with the fibre swelling, followed by the solvent precipitate and infiltration into the fibre, and finally it disintegrates macrofibres into microfibres, then eventually nanofibrils. Freddi et al. [181] proposed that the dissolution of SF is thermodynamically favoured, increasing the dissolution temperature promotes the swelling of silk fibres, and in return, accelerates the solvent diffusion towards the target reactive sites. They also suggested that the solvent penetration and diffusion rates are the limiting factors for lowering the overall kinetics for the dissolution process. The mechanism of dissolution can therefore be suggested as - the solvent molecules diffuse and penetrate into silk fibres to break intermolecular hydrogen bonds, whilst forming new hydrogen bonds with the SF chains.

For a thermodynamic process, from the initial state to the final state, if the change in the free energy is negative then the process will happen spontaneously, conversely a positive value of the free energy change the process will require energy

to occur [182]. If the process occurs under the condition of isobaric (constant pressure) and isothermal (constant temperature), the spontaneity can therefore be measured through the change in the Gibbs free energy, as defined in Equation 2.1:

$$\Delta G = \Delta H - T\Delta S \tag{2.1}$$

where ΔH is change in enthalpy, ΔS is change in entropy. The change in enthalpy can be further defined as:

$$\Delta H = \Delta E + P\Delta V \tag{2.2}$$

where ΔE is the change of internal energy, P is the pressure, V is the volume, and PΔV is the related work been done by the system at a constant pressure.

Considering the breakage of bonds within the reactant molecules, energy in the form of heat must be provided to the reactants, to allow them being 'activated'. The 'activated' reactants often need to pass through a transition state before generating the products. It is known that the amount of energy needed to raise the reactants to this transition state is defined as the activation energy, E_a. Once the reactants have given sufficient amount of energy to climb over this peak, the energy is then released and new bonds are formed, yielding the products. As introduced, if the reaction is isobaric, the energy difference between reactants (initial state) and products (final state) is now referred as the enthalpy of reaction (ΔH_R). If ΔH_R is positive (negative), the reaction is then regarded as endothermic (exothermic), as shown in Figure 2.8 [183].

Most chemical reactions have an energetic barrier, also variously referred as potential barrier, an activation barrier, or an activation energy (as introduced). It is known that a transition between two atomic or molecular states can be separated by an energy barrier. Even in exothermic reactions (Figure 2.8b), when the products are thermodynamically favoured over reactants, there can still be a significant energy barrier to overcome in order to initiate the reaction. The occurrence of a chemical reaction usually associates with the collision theory, the

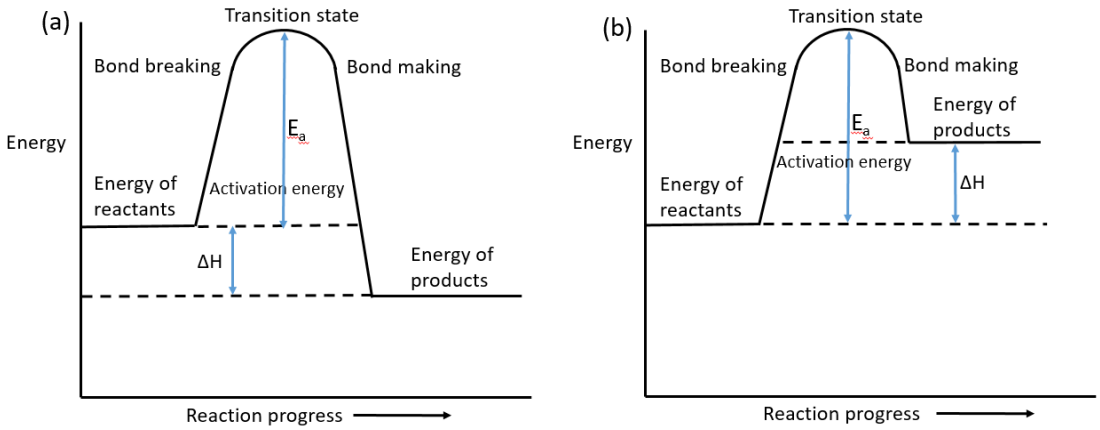

Figure 2.8: Schematic draw of a reaction energy pathway for (a) exothermic reaction, (b) endothermic reaction; the difference in energy between reactants and transistion state is defined as the activation energy, E_a.

reaction happens when the reactants collide with enough energy to penetrate the molecular van der Waals forces. Temperature plays a key role on the reaction rate, and temperature dependence chemical reactions are often quantitatively described through collision theory model. According to the collision theory, the rate of the reaction largely depends on the number of energetic collisions between reactants, however, usually the reactants may need to collide in a particular orientation and energy may need to be present in a specific form, which lead to the consideration of three factors that decide the occurrence of a successful reactive collision, encounter rate/collision rate, energy requirement and steric requirement. After taking all these three terms into account, the reaction rate is expressed in Equation 2.3:

$$rate = P\sigma_C \left(\frac{8k_BT}{\pi\mu}\right)^{\frac{1}{2}} exp\left(-\frac{E_a}{RT}\right) n_A n_B \tag{2.3}$$

where P is steric factor, σ_C is the collision cross section, Pσ_C describes the reaction cross section, k_B is the Boltzmann's constant, T is the absolute temperature, μ is the mass of the molecule, $\left(\frac{8k_BT}{\pi\mu}\right)^{\frac{1}{2}}$ describes the Maxwell-Boltzmann distribution of velocities, E_a is activation energy, R is gas constant, n_A and n_B are the

concentrations of the two reactants. Subsequently, the temperature-dependent parameter correlating the rate to the concentrations is defined as the rate constant, and typically given by the symbol k or k(T), as expressed in Equation 2.4. It is important noting that the rate constant is only a constant at a fixed temperature.

$$k(T) = P\sigma_C \left(\frac{8k_B T}{\pi\mu}\right)^{\frac{1}{2}} \exp\left(-\frac{E_a}{RT}\right) \tag{2.4}$$

Furthermore, for the uncatalysed reaction, the rate constant follows the proportionality

$$k_{uncat}(T) \propto \exp\left(-\frac{E_a}{RT}\right) \tag{2.5}$$

The simple collision theory (Equation 2.4) is next able to rationalise the form of the Arrhenius equation, from which the temperature dependence of the rate constant can be further defined, as given in Equation 2.6,

$$k(T) = A \exp\left(-\frac{E_a}{RT}\right) \tag{2.6}$$

where A is the pre-exponential factor. It is experimentally recognised that the effect of temperature on the reaction rate, in many chemical reactions, follows the Arrhenius equation (Equation 2.6). If this equation is expressed in log form, then:

$$\ln k = \ln A - \frac{E_a}{RT} \tag{2.7}$$

Both the pre-exponential factor and activation energy can thus be calculated from the plot of ln k against 1/T. A straight line is consequently obtained from the Arrhenius plot, with an intercept of ln A and a slope of -E_a/R. It is worth noting that for a small range of temperatures, Arrhenius equation works well for most practical conditions, because the temperature dependence of pre-exponential is

relatively weak and negligible compared to the temperature dependence of activation energy on temperature [184].

It has shown that the rate of reaction depends on the reactant concentrations (Equation 2.3) and temperature (Equation 2.6), however there are still many other factors that affect the rate of reaction, such as the type of solvent, solvent viscosity and polarity, etc.

In polymer dissolution, there are two transport processes, solvent diffusion and chain disentanglement. When the uncrosslinked/amorphous polymer is in contact with a thermodynamically compatible solvent, the solvent will diffuse into the polymer, and lead to its plasticisation. Consequently, a gel-like swollen layer is formed surrounding the polymer, generating a interface between polymer and solvent [185]. An initial study by Ueberreiter and Asmussen [7, 186], explored the dispersion of carbon black particles in the polymer, and they demonstrated the formation of a swollen surface layer at the beginning of the dissolution process. They summarised the stage of polymer dissolution and the formation of this layer that exists in between pure polymer and pure solvent, as shown in Figure 2.9. They claimed that the dissolution mechanism follows: the solvent molecules first penetrate and fill the free volume within the glassy state polymer (the start of diffusion), next a solid swollen layer is built (polymer still in glassy state), then a gel layer is formed (polymer swollen in a rubber-like state), and a liquid layer is formed (all solid surrounded in a streaming liquid).

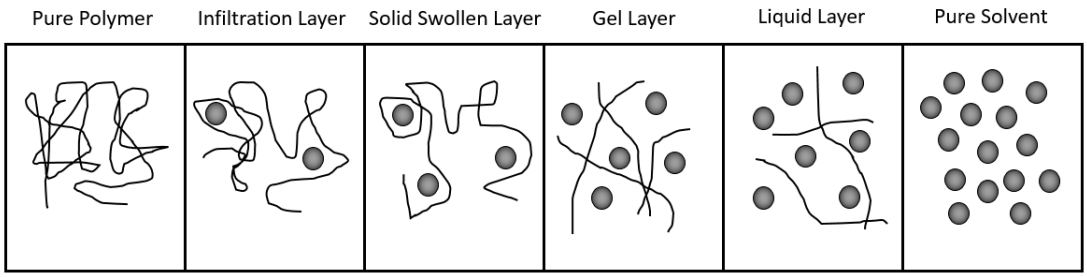

Figure 2.9: Schematic draw of polymer diffusion. Reproduced from ref [7], *John Wiley & Sons*, ©1962.

Additionally, the disentanglement of polymer chains also plays a key role in the polymer dissolution [187]. There are several factors that affect the chain disentanglement, i.e. polymer molecular weight [186], polymer structure/composition [188–191], the type of solvents [175, 192–195] and external parameters (agitation, stirring, temperature, radiation, etc) [7, 175, 196].

From recent research on the dissolution of silk fibroin in ionic liquids, Susanin et al. [175] reported that the type of ILs, dissolution time and temperature significantly change the molar mass of the resulting silk fibroin and alter the corresponding dissolution rate. They also suggested the use of BMIMAc at 60 °C for $<$ 120 min or at 90 °C for $<$ 30 min are the optimal conditions for dissolution of SF, in order to generate intact H-chain of SF. The discussed various parameters directly govern the dissolution rate. In short, it is demonstrated that the underlying principles of the dissolution kinetics have a large degree of complexity, the interplay of various parameters need to be considered.

2.7 Reducing Agents

A reducing agent, also known as reductant, loses electrons and is oxidised during a chemical reaction. A reducing agent is recognised as the electron donor, and in one of its lower possible oxidation states.

Most protein-based natural fibres, such as wool and silk, contain cysteine amino acid groups, which are capable of forming disulfide bonds between thiol groups. It is well-known that wool fibre contains highly cross-linked disulfide bonds, which makes it difficult to be hydrolysed by chemicals [197]. There are two common ways to achieve the hydrolysis of wool fibres: (i) applying strong acid or alkali to degrade proteins [198]; and (ii) using oxidising or reducing agents to assist the breakage of disulfide bonds [199–201]. Thiol-disulfide exchange reactions can significantly change the structure of the proteins and therefore lead to the versatility of applications [202, 203]. It is established that thiols can be oxidised to disulfides, whilst disulfides can be reduced to thiols [204].

Studies have shown the key for conducting the dissolution of wool fibres is to break disulfide bonds, in order to destroy the spatial arrangements inside wool macromolecules [205]. Thiols such as 2-mercaptoethanol (β-ME), dithiothreitol (DTT) and dithioerythritol (DTE), have demonstrated their capability for the efficient reduction of disulfide bonds in proteins [206–208]. There are other types of reducing agents that have been reported capable of extracting keratin from feathers, wool and hair, such as sodium sulfide (Na_2S) [209, 210], sodium disulfite ($Na_2S_2O_5$) [211, 212], sodium sulfite (Na_2SO_3) [213–216] and sodium bisulfite (NaHSO3) [217, 218], etc.

As covered in section 2.3.1, silk fibroin consists of two major polypeptides, H-chain and L-chain that are linked through a disulfide bond between two cysteine residues. Lucas et al. [219] first established the occurrence of cysteine residues within silk fibroin. Since Lucas, protein chemists started research on cysteine-containing peptides from silk fibroin. Robson et al. [220] by 1970 and Earland et al. [221] by 1973, have individually identified the formation of intra-chain disulfide bonds in two different sequences that containing cysteine residues. Interestingly, the disulfide bond linkage between H-chain and L-chain, was only first identified by Shimura et al. [222] in 1982. They found the separation of two chains only happen after the addition of 2-mercaptoethanol (β-ME), which is commonly recognised as the reducing agent for the cleavage of disulfide bonds [207]. Furthermore, in 1989, Yamaguchi et al. [223] identified that L-chain contains three Cys residues, of which two of them form the intramolecular disulfide linkage, leaving the third one at a relatively hydrophilic region to form disulfide linkage with the H-chain. Through genomic sequencing and peptide analysis, in 1999, Tanaka et al. [8] further established that there are three Cys residues at the C-terminal site of H-chain. In combination of the study by Yamaguchi et al., Tanaka et al. [8] proposed the positions for the intra- and intermolecular disulfide bonds within the H-L complex of silk fibroin, as shown in Figure 2.10.

Similarly, a few studies have shown the breakage of disulfide linkage within

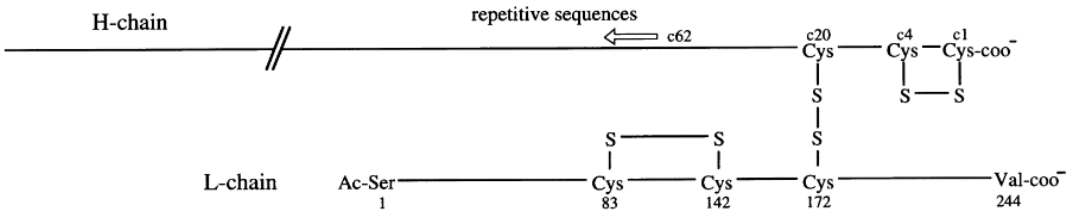

Figure 2.10: Inter- and intramolecular disulfide bonds in the light (L-) and heavy (H-) chains of *B. mori* silk fibroin. Reproduced from ref [8], *Elsevier Ltd*, ©1999.

the silk proteins can be achieved through adding reducing agents. Through SDS-PAGE electrophoresis, Grip et al. [224] have demonstrated that the addition of reduced glutathione/Tris-HCl (GSH) can promote the reduction of disulfide bond between C-terminal domain in spider silk. More recently, Jiang et al. [225] reported that the breakage of disulfide bond between H-chain and L-chain of silk fibroin has been achieved by dialysis separation technique with the addition of reducing agent, DTT. They found the breakage of disulfide bond can reduce the degree of entanglement of the molecular segment, and as a result, the viscosity of silk fibroin solution is decreased. The ability of breaking disulfide bond in the H-L complex through the addition of reducing agent, promotes the formation of the high-molecular-weight silk fibroin polypeptide, thus creates the potential for its wide applications in biomedical and green chemistry field.

2.8 Summary

This Chapter has introduced the background of various types of composites, including their typical composition, features and applications. The history, development and benefits of all-polymer composites have been introduced, and the potentially 'green' dissolution method to prepare all-silk composites has been demonstrated.

Some key features and properties of *B. mori* silk fibres have been introduced, including its composition, microstructural properties, hierarchical and crystalline structures. Recent studies relating to the properties of all-silk composites (only found fabricated using two-step dissolution method), have been covered. Ionic liquid, as the potential 'green' solvent, its properties and recent studies on silk fibroin/IL have been introduced. Moreover, the meaning of coagulation, the conformational change in silk fibroin during coagulation and the effects of various coagulation conditions on the properties of the resulting RSF have been covered. Finally, mechanism and kinetics of polymer dissolution, factors affecting dissolution rate, the correlation between collision theory and Arrhenius equation, benefits of adding reducing agent have been briefly introduced. These will provide a fundamental understanding of the background physics surrounding all-silk composites and its dissolution dynamics, giving an aid in designing the experiments and studying the findings.

Chapter 3

Experimental Methods and Materials

3.1 Introduction

This chapter aims to give a brief introduction of the different characterisation techniques conducted throughout the project.

3.2 Materials

Degummed *B. mori* silk threads were purchased online from Airedale Yarns and used as the source of silk fibres. They were stored in a cool dry place before use. One silk thread consists of a few hundred individual silk filaments, each with a density of 1.361 $g\ cm^{-3}$ at 25 $°C$ [226]. To prepare woven silk composites, a plain weave process was then applied to weave the silk thread to silk fabric. Experiments carried on single silk threads will be discussed in Chapters 4 and 5, while the studies on the array silk threads will be explored in Chapter 6, woven silk fabrics in Chapter 7. The ionic liquid 1-ethyl-3-methylimidazolium acetate [C2mim][OAc] was chosen as the solvent, because it has been widely studied by other members of our group [191, 227–230]. It was purchased from Sigma-Aldrich,

with a purification of 97 %. Methanol was used as the coagulant as it has been reported to yield a high degree of crystallinity in the dissolved and coagulated silk phase [231].

3.3 Structure and Morphology Characterisation

The unprocessed raw silk threads/fabrics and all silk composites were encapsulated in an epoxy resin block in order to allow the surface and cross-sectional morphology to be imaged using an optical microscope. The epoxy resin was prepared by mixing the resin and the hardener (EpoxiCure 2, BUEHLER) in a weight ratio of 5:1. To obtain cross-sectional images, silk threads and fabrics were embedded in epoxy resin and allowed to harden at room temperature for 3 days. The silk threads and fabrics were then solidified perpendicular to the resin surface, then ground and polished down the resin to a thickness between 20 to 30 mm, to reveal a clear polished surface for high resolution images to be taken. The machine used to grind and polish the samples is Struers Rotopol 11. A representation schematic image of the embedded single silk threads is shown in Figure 3.1a, while an example of the resultant resin with single ASCs and woven silk fabrics embedded inside are shown in Figure 3.1b and c, respectively.

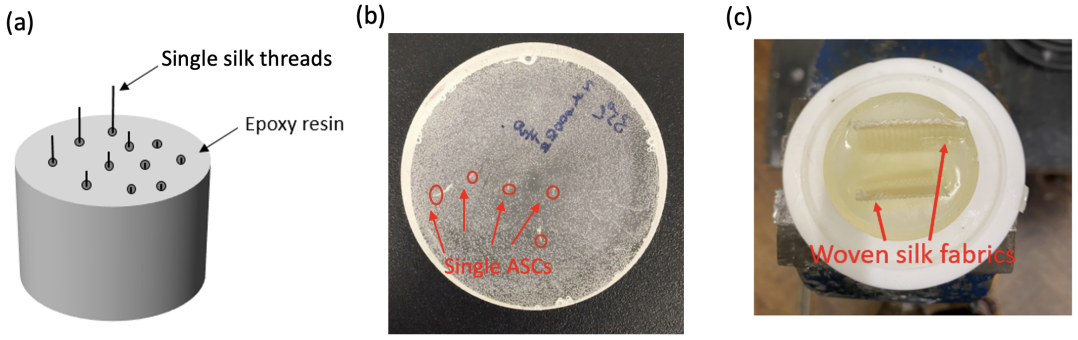

Figure 3.1: (a) Schematic representation of single silk threads embedded in epoxy resin block; (b) single ASCs, and (c) raw woven silk fabrics embedded in epoxy resin block, ready for taking the cross-sectional microscope images.

3.3.1 Optical Microscopy

Low magnification microscope cross-sectional images of raw silk threads/fabrics and all silk composites were acquired in reflection or transmission, using an optical microscope (BH2-UMA, Olympus Corporation, Japan) equipped with a CCD (charge-coupled device) camera. For better comparison, images for individual composites were captured under magnification 100x, 200x, and 500x. The morphological parameters derived from the optical microscope images were observed and measured using the image processing software Image J.

3.3.2 Scanning Electron Microscope (SEM)

The surface of the epoxy resin blocks were glued onto conductive tape and sputter coated with Quorum Technologies SC 7620. Then the coated epoxy resins were transferred into the Zeiss EVO MA15 Scanning Electron Microscope for observation at an accelerating voltage of 10 kV. Similar to using optical microscope, the images taken from SEM were analysed and measured using Image J software. The observed images will be showed and discussed in the section 4.3.1 below.

3.4 Wide-Angle X-Ray Diffraction (WAXD)

Wide-Angle X-ray Diffraction is the most well-known family of techniques to investigate the crystalline structure of polymers. WAXD is high sensitivity to small changes, therefore it can be utilised to identify structural similarities and characterise molecular structural alignments [232]. More often, WAXD is employed on thick or powered samples because of its penetration depth and thus its ability to

reveal internal structural properties of the materials [233]. In-depth understanding of the fibre molecular structural properties is often crucial to development of a successful composite material.

In this project, the apparatus used is a 'DRONEK 4-AXES, Huber Diffractionstechnik GmbH Co. KG, Germany'. It is used to study the 2θ diffraction curves, crystal orientation and 2D diffraction patterns of resultant samples. The X-ray beam was operated in transmission mode and irradiated perpendicular to the fibre axis of the composites. An empty metal frame was scanned and air scatter was subtracted off from the 2θ and azimuthal (α) experimental data, respectively.

3.4.1 XRD 2D Diffraction Pattern

Ultra-speed X-ray Occlusal films were purchased from Carestream in a size of 5.7 x 7.6 cm, and stored in a safe environment away from heat, chemicals and radiation prior to the usage. In order to capture the image produced by the interaction of X-ray and samples of silk fibres, the apparatus was set up as indicated in Figure 3.2. The silk threads/fabrics were glued on a metal tube where the X-ray beam emitted from, and fully covered the X-ray beam emission hole of which the diameter of approximately 200 μm. X-ray sensitive film was clipped on a holder with a sample to the film distance of 52 mm and left for exposure of X-ray for 2.5 hours.

Subsequently, in order to examine the diffraction patterns on the film, the procedure of developing the X-ray film was carried out in a dark room with safe lights operated. Two tanks of solution are required, developer solution (RG Universal RTU X-Ray Developer, Champion) and fixer solution (GBX Fixer, Carestream). According to the manufacture manual, pure developer solution is needed while the fixer solution was diluted with water at a ratio of 4:1 (water : fixer solution). There are few steps involved to develop the film. Firstly,

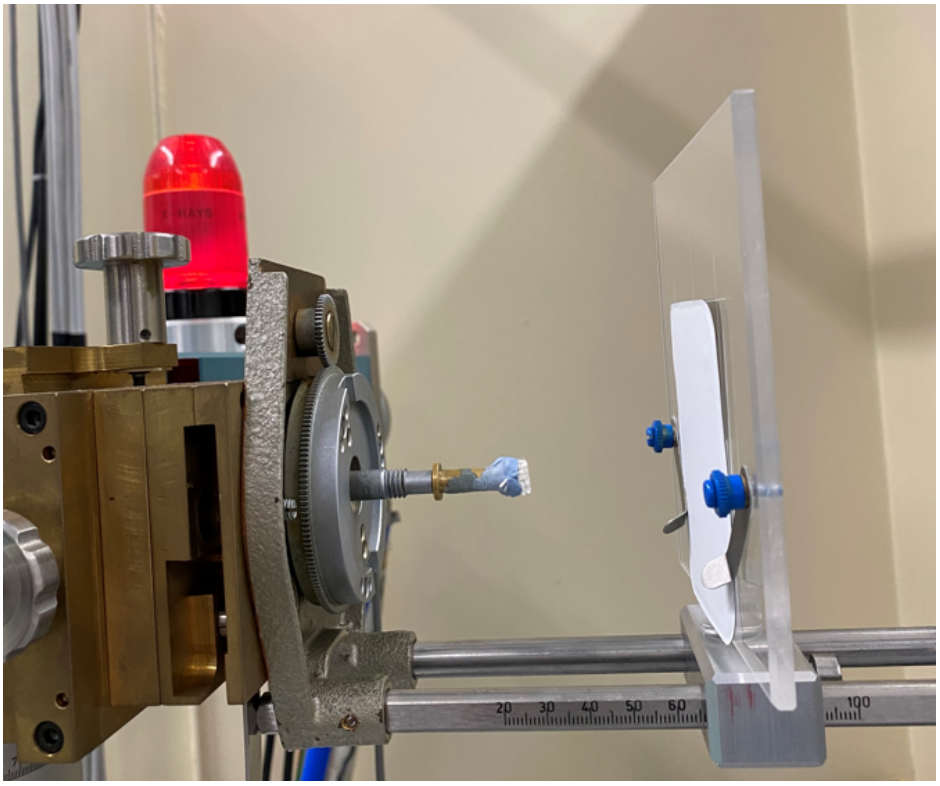

Figure 3.2: Apparatus set up for collecting XRD 2D diffraction patterns in a X-ray sensitive film.

disassemble the film package in the dark, then fully immersing the X-ray film in the developer solution for 5 mins. After 5 mins, lift the lower corner of film straight up out of the developer solution for several seconds to make sure most of the solution drains off the film. Next, transferred the film into the prepared fixer solution and submerse for another 5 mins. Great care was taken during handling the film in order to avoid finger print marks or scratches. Upon the fixation process was complete, lift the film up and allow the excess solution to drain off. Followed by washing the film thoroughly under a running water tap for several seconds then submerse into a water tank, and agitate the film vigorously. After 10 mins, the film was hung in a drying rack in a dust-free area at room temperature. Once the film is completely dried, it is then ready for examination.

3.4.2 WAXD 2θ Scan

WAXD 2θ (equatorial) scan was utilised to collect diffraction curves for all silk composites (ASCs) and coagulated silk film (CSF) samples and characterise their degree of crystallinity and crystal structure. The experiments were performed at room temperature, using Cu Kα radiation (λ = 1.54 Å) at the voltage and current of 40 kV and 30 mA, respectively. WAXD data was collected from 2θ = 5 - 40° at a 2θ step of 0.2°, and 40 seconds counting time for each step (scanning rate at 0.3 °/min). Figure 3.3 a and b demonstrate schematically the paths of 2θ and α scans, respectively.

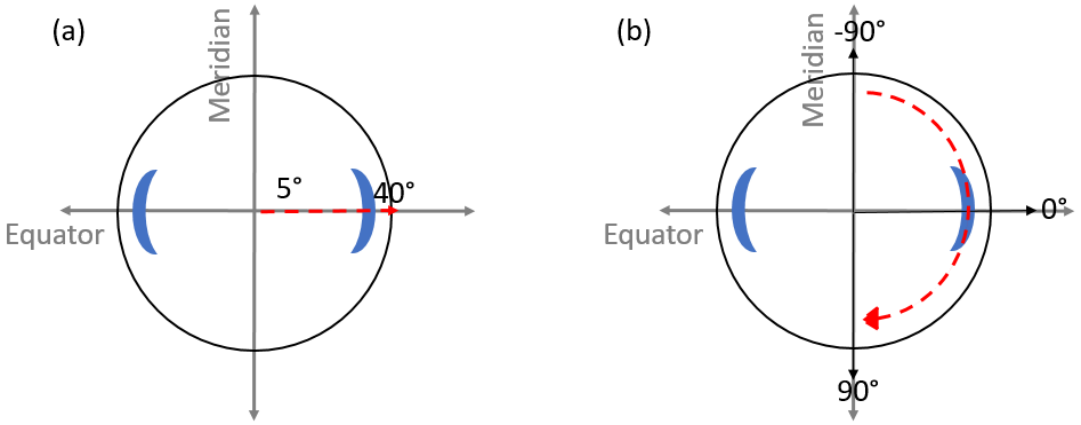

Figure 3.3: A schematic diagram to show the WAXD (a) 2θ and (b) α scans, red dotted lines indicate the respective paths.

3.4.3 WAXD azimuthal (α) Scan

As discussed above, WAXD can be used to characterise the molecular orientation and detect any molecular alignment changes. Polymers, due to their long chain

structure, are highly susceptible to orientation [234]. Theoretically, compared to processed fibres, the raw fibre has the highest orientation factor value because all the molecules are preferentially oriented without being disrupted by the dissolution process. In other words, the changes of fibre molecular orientation are proportionally equal to the amount of matrix being generated. An azimuthal (meridional) scan was applied to detect the fibre secondary structure molecular alignment, by measuring the diffraction intensity along the α angle on a fixed 2θ angle, as shown in Figure 3.3b.

Consequently, an angle was chosen where the maximum crystalline intensity from the 2θ scan was found (20.6° for raw silk fibre) and 2θ was then kept fixed. The intensity distribution was then collected by rotating the samples between azimuthal angles, from - 90° to 90° (0° = vertical), at a scanning rate of 2 °/min, as shown in Figure 3.4

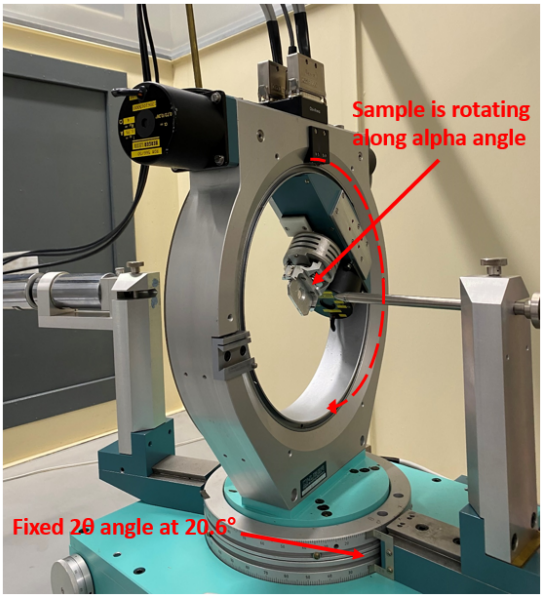

Figure 3.4: Apparatus set up for conducting WAXD azimuthal (α) scans, with the sample being held in a metal frame at a fixed 2θ angle (20.6°), whilst rotating along α angles between -90° to 90°.

Accordingly, the average orientation can be determined from the intensity distribution of the corresponding diffraction on the Debye ring by using the 2^{nd} Legendre Polynomial function, as given in Equation 3.1. The P_2 value is most often used to describe the orientation degree of objects of interest (a crystallographic plane) relative to a chosen direction (a fibre axis) [235][236].

$$P_2 = \frac{1}{2}(3 < \cos^2 \alpha > -1) \tag{3.1}$$

where $\langle \cos^2 \alpha \rangle$ is the average cosine squared value of the azimuthal angle α, in a two dimensional azimuthal scan. It can be determined from the distribution of intensity of the meridional reflections, and calculated using Equation 3.2.

$$\langle \cos^2 \alpha \rangle = \frac{\int_{-\pi/2}^{\pi/2} I(\alpha) \cos^2 \alpha \mathrm{d}\alpha}{\int_{-\pi/2}^{\pi/2} I(\alpha) \mathrm{d}\alpha} \tag{3.2}$$

where I (α) is the scattered intensity at α along the diffraction profile. The measured I (α) value was taken from the obtained WAXD scatter curve, and directly put into a built Excel spreadsheet, to calculate $\langle \cos^2 \alpha \rangle$ and P_2 by using the Equations 3.1, 3.2 shown above, respectively. The integrals in Equation 3.2 were carried out for a fixed value of 2θ.

The diffraction curves obtained from WAXD azimuthal scans were input into OriginPro 2019 program, in order to calculate the value of full width at half height (FWHH), which will be discussed in section 4.3.2. The errors associated with the specimen conditions, including specimen displacement and thickness variations, were considered the main systematic errors. Metal frame with ASC sample was placed carefully in the same position for each measurement to reduce systematic errors. The random errors caused by the fluctuations in the X-ray photons and environmental conditions were reduced by repeated measurements. The obtained P_2 and FWHH values were averaged over at least 3 measurements. Standard error of the mean was calculated using $\sigma/\sqrt{n}$ (σ is standard deviation, n is number of measurements) to make error bars, which is consistent when providing error bars for other measured parameters. Additionally, 'n = x' will be presented in

the caption for each corresponding figure and table, where x represents the exact number of measurements.

3.5 Mechanical Properties Tests

The mechanical properties of single, array and woven all silk composites and the CSF (the matrix phase) were examined through using the Instron 5565 universal test machine equipped with a 10 kN calibrated load cell at room temperature. Tensile tests were carried out for single, array and woven ASCs whilst three-point bending tests were applied to CSF samples. Subsequently, ultimate tensile strength, elongation at break and Young's modulus for each sample was determined. All the load-extension data were converted into stress-strain curves, and the results obtained from mechanical tests were averaged over at least 3 measurements. To reduce systematic errors, the same micrometer was used to measure the thickness/width/cross-sectional area of the specimen, and the same equipment setup was applied to obtain the mechanical properties from the corresponding types of testing. The testing was carried under controlled lab environment (humidity, temperature, etc.) to reduce associated random errors. And 'n = x' will be presented in the captions for the corresponding figures and tables, where x represents for the number of measurements.

3.5.1 Tensile Tests

Apparatus set up to carry out tensile tests is indicated in Figure 3.5. Prior to tensile testing, the cross-sectional area of each single ASC sample was measured from the density, the weight and the length of the sample. For each of the woven ASC sample, a micrometer was used for measuring the thickness, whilst the width was kept at 5 mm in order to measure the cross-sectional area. To minimise the slippage between the sample and the grips, two small pieces of silicon carbide papers were used to grip the two ends of the sample. The gauge length was set to 20 mm, and the cross-head speed in the direction parallel to the fibre array was

2 mm/min. The tensile Young's Modulus E_c (in the initial linear strain range of 0.0050-0.0100) was measured from the stress-strain curves.

Figure 3.5: A piece of woven silk fabrics was gripped at two ends with small pieces of grinding paper, ready to conduct tensile testings.

The tensile stress at break (σ) was measured by using Equation 3.3, which is defined as ultimate tensile strength in this project.

$$\sigma = \frac{F}{A} \tag{3.3}$$

where
F : force (N), A : area (m^2)
A = w·t, when specimen is strip shaped woven composite
w : width (5 mm), t: thickness
A = $\frac{m}{\rho \cdot l}$, when specimen is single composite
m : mass, ρ: density, l: length

The Young's modulus of each sample was calculated by using Equation 3.4.

$$\mathrm{E} = \frac{F/A}{\Delta L/L} \tag{3.4}$$

where
E : Young's Modulus, (Pa)
F/A : Stress, (Pa)
L : Original length, (m)
ΔL : Change in length, (m)
$\Delta L/L$: Elongation at break

3.5.2 Three-Point Bending Tests

Three-point bending flexural tests were performed on the CSF (as it was too brittle to be gripped for a tensile test) using the same machine equipped in a compression mode with a 10 kN calibrated load cell. The apparatus set up is illustrated in Figure 3.6. The test was performed with a cross-head speed at 2

mm/min and a bending span of 20 mm. The thickness and width of the sample were measured using micrometer prior to the testing.

Figure 3.6: Apparatus set up for carrying out three-point bending tests in this project.

The flexural modulus at the maximum stress was determined from the stress-strain curves, and was calculated at the outer surface of the test specimen at mid-span. The flexural stress and the flexural strain can be calculated by using Equations 3.5 and 3.6, subsequently. The flexural modulus of the sample can be calculated using Equation 3.7.

$$\sigma = \frac{3PL}{2bh^2} \tag{3.5}$$

where

σ : stress at the outer surface at mid-span, (MPa)

P : applied force, (N)

L : support span, (mm)
b : width of matrix, (mm)
h : thickness of matrix (mm)

$$\epsilon_f = \frac{6Dh}{L^2} \tag{3.6}$$

where
ϵ_f : maximum strain at the outer surface, (mm/mm)
D : mid-span deflection, (mm)
L : support span, (mm)
h : thickness of matrix (mm)

$$E_f = \frac{mL^3}{4bh^3} \tag{3.7}$$

where
E_f : Young's modulus of sample, (MPa)
L : support span, (mm)
b : width of matrix, (mm)
h : thickness of matrix (mm)
m : slope of the force deflection curve

3.5.3 Peel Tests

To determine the peel strength between fibre and matrix phase within the two layers woven all silk composites fabricated in Chapter 7, peel tests were performed. The two layers woven ASCs were cut into strip shape, at a size of 50 mm x 20 mm (length x width).

To start the test, the foil was firstly removed. Again, to minimise the slippage,

two small silicon carbide papers were used to grip the edges of the specimen, with one layer sticks up and the other sticks down, and the bonded area sticks out horizontally, as shown in Figure 3.7. The test was conducted at a crosshead speed of 40 mm/min.

Figure 3.7: Apparatus set up for carrying out peel tests for determine peel strength of two layers woven all silk composites in this project.

The peel strength is the measure of the average force acting on the width of the bonding surface, when the specimen is peeled at a constant velocity. The applied load was recorded for each specimen. The peel strength is then determined using the average load divided by the width of the specimen, as expressed in Equation 3.8, with the unit of N/mm [237].

$$Peelstrength = \frac{F}{W} \tag{3.8}$$

Chapter 4

The Properties of Single All-Silk Composites Fabricated in the Ionic Liquid 1-Ethyl-3-Methylimidazolium Acetate

4.1 Introduction

Among animal fibres, silk fibres have attracted a large amount of interest, due to a combination of biodegradability, biocompatibility and remarkable mechanical properties [238][239][138][240]. The structure and properties of silk fibres, and other researchers' studies on the interaction between different ILs with silk fibres have been introduced, recalling section 2.4.

This chapter aims to conduct a fundamental study of the dissolution dynamics of single silk threads in the ionic liquid 1-ethyl-3-methylimidazolium acetate ([C2mim][OAc]). First, the detailed dissolution process for fabricating single all silk composites (ASCs), and the fabrication process of making coagulated silk film will be presented. Next, the microstructure of raw and partially dissolved single all silk composites, the orientation of nanocrystallites, the volume frac-

tion of matrix within single ASCs, as well as their mechanical properties will be presented and analysed. The time-temperature superposition relationship of the dissolution, the corresponding activation energies, and the applicable of the rule of mixtures (ROM) theory for the effectiveness of the modulus and strength will be assessed, and notable findings will be discussed.

4.2 Materials and Methods

4.2.1 Materials

Materials were initially introduced in section 3.2, and the sample properties were tested using the standardised protocols as outlined in sections 3.3, 3.4, 3.5. The specifics of each experiment will be introduced as they are encountered in the chapter.

4.2.2 Fabrication of Single All Silk Composites (ASCs)

Single silk threads were placed in the longitudinal direction and then fixed at both ends in an 8 cm x 8 cm poly(tetrafluoroethylene) (Teflon) frame. A Teflon dish was filled with excess [C2mim][OAc] and placed in a vacuum oven (Shellab 17L Digital Vacuum Oven SQ-15VAC-16, Sheldon Manufacturing, Inc., USA) for 1 h, to carry out a pre-heating process before the dissolution experiments began. Then, the frame with the single silk threads was completely immersed into the preheated IL bath in the vacuum oven, for the designed lengths of time, at temperatures of 30, 35, 40 or 50 °C (see Figure 4.1a) under vacuum to minimize the water content.

When each procedure was finished, the partially dissolved single silk threads were removed from the IL bath and then soaked in a methanol (MeOH) bath for coagulation, as shown in Figure 4.1b, and the used [C2mim][OAc] was collected to be recycled. The coagulated ASCs were then washed in methanol for two days

changing the medium twice. Finally, a one hour drying process in the vacuum oven at 100 °C was applied (Figure 4.1c).

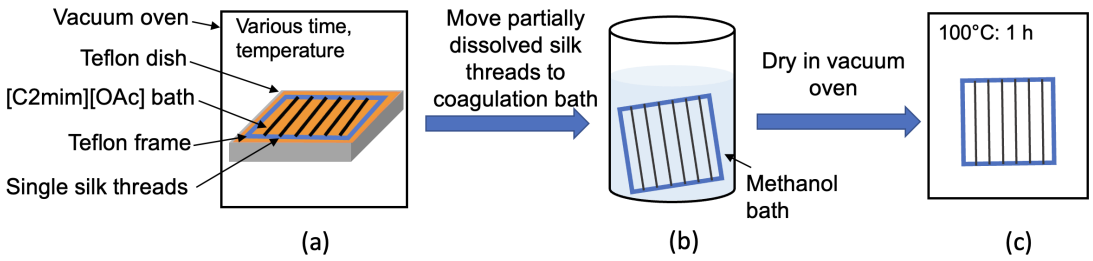

Figure 4.1: A schematic diagram to show the single ASCs fabrication process, starting from (a) dissolution, then (b) coagulation, (c) then finally drying in vacuum oven.

4.2.3 Preparation of Silk Fibroin (SF) Solution and a Coagulated Silk Film (CSF)

The degummed *B. mori* silk thread was first dried in a vacuum oven set at a temperature of 65 °C for 24 hours, after which silk thread was then chopped in short pieces and dissolved in [C2mim][OAc] solution with a magnetic stirrer, for 24 hours at 100 °C, at a speed of 80 rpm, as shown on Figure 4.2a. An amber coloured 10 % (w/v) SF solution was then obtained, which was then cast into a 5 cm x 5 cm polystyrene petri dish placed on a upside down beaker, and put into a larger scale beaker filled with methanol. The beaker was sealed and placed on a hotplate, allowing the methanol to slowly evaporate overnight inside the beaker, at 60 °C, and give controlled coagulation (Figure 4.2b). The cast film was then washed with methanol statically for 2 days, changing the medium twice, and then finally dried in a vacuum oven at 100 °C for one hour.

The resulting film showed a light amber colour with a thickness of 40 µm, and was termed the coagulated silk film (CSF), as showed in Figure 4.3. This film is

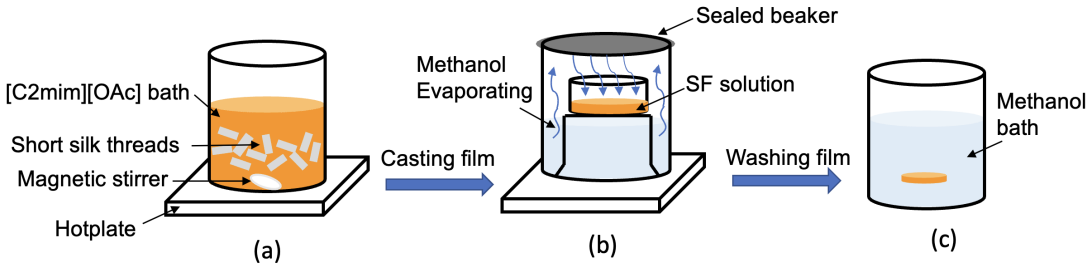

Figure 4.2: A schematic diagram to show the film casting procedure, (a) dissolve short silk threads in [C2mim][OAc] solution, (b) controlled coagulation of the film using evaporated methanol, (c) washing the film in a methanol bath.

considered representative of the matrix phase of the all silk composites including single ASCs as presented in this Chapter and woven ASCs presented in Chapter 7.

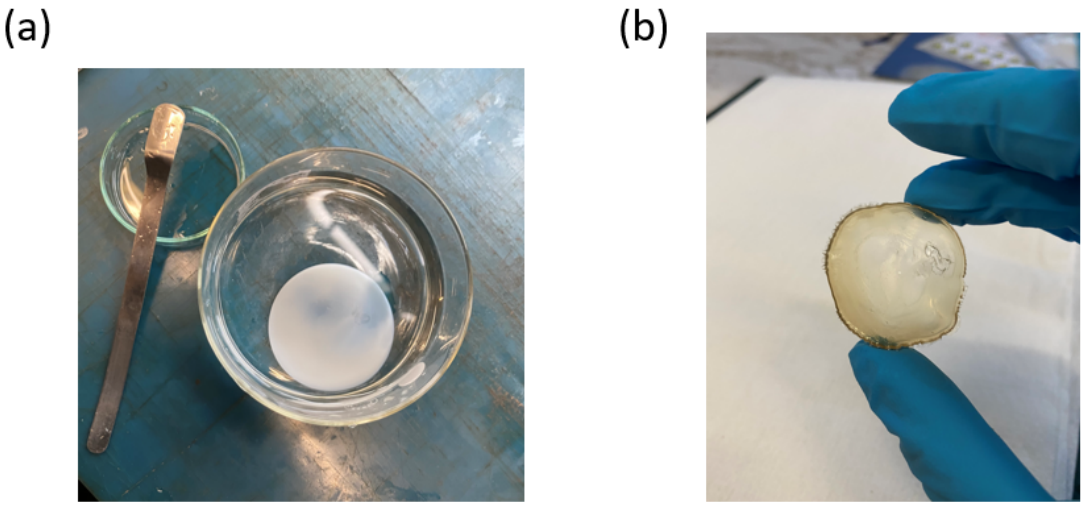

Figure 4.3: Coagulated silk film (a) submerged in the methanol bath, (b) after drying under vacuum oven.

4.3 Results and Discussion

4.3.1 Microstructure of Single ASCs

Cross-sectional optical images of the single ASCs structures processed for different lengths of time, at 30 °C are presented in Figure 4.4. It can be seen that a single unprocessed silk thread contains several hundred filaments, and forms a loose microstructure with significant inner space. It is likely that the unprocessed silk threads can swell in the epoxy resin as they are not bound together with any coagulated silk matrix. As the dissolution progresses, there was a trend that the overall cross-sectional size of the final silk composite was gradually decreased (as the proportion of matrix phase increased). Interestingly, the gaps between each individual filament were decreased (Figure 4.4a-d), and eventually a tightly compacted lenticular shape of a silk composite thread emerged after 2 h (Figure 4.4e). Figure 4.4 e-h indicates that the amount of the inner core filaments continuously reduced with time. The dissolved fibres turning into matrix appear in the outer layer of thread core and surrounding at each of filaments to form a close packing silk composite. This transition in morphology is also shown in the series of samples made at 40 °C, seen in Figure 4.5. While the interfacial bonding of ASCs processed under 60 °C for 1 h is shown in Figure 4.6. Noticeably, the dissolved silk fibres were coagulated and formed as matrix filled up the gap between each single silk filaments.

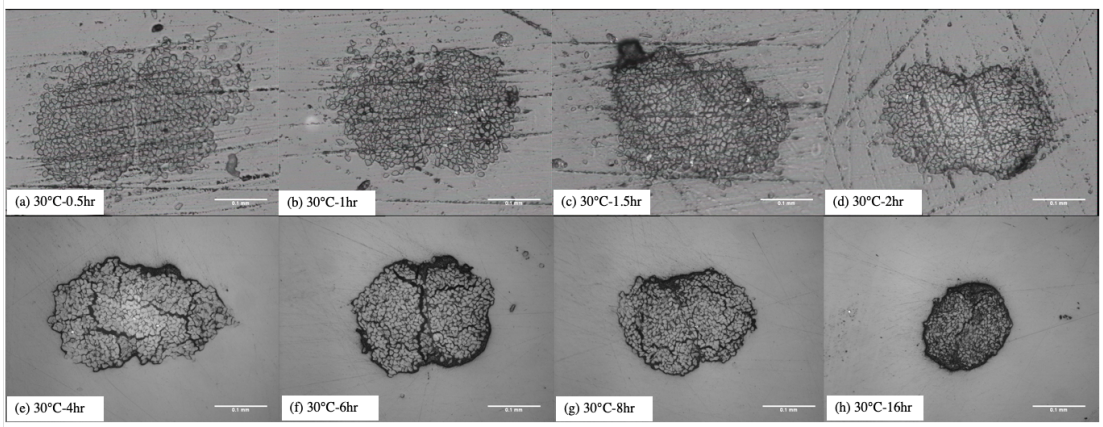

Figure 4.4: Microscopy cross-sectional images of single partially dissolved silk threads, processed under 30 °C, for different lengths of time, and observed at 200x magnification.

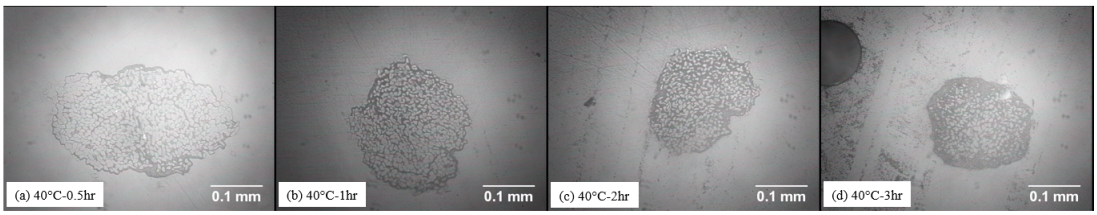

Figure 4.5: Cross-sectional images of single ASCs processed at (a) 40 °C-0.5 h, (b) 40 °C-1 h, (c) 40 °C-2 h, (d) 40 °C-3 h, observed at 200x magnification.

It can be proposed that in the early dissolution stage (up to 2 h at 30 °C) the IL infiltrates in between each filament. In these early dissolution times, the outer layer of each individual filament is dissolved and forms a silk matrix. Eventually, once all of the inner space is filled and a close-packed structure is formed, it becomes more difficult for the IL to penetrate through. As seen in Figure 4.7, the size of silk filaments appears smaller in the outer layer of the thread core compared with that in inner core filaments; a clear halo of silk matrix is observed. It can therefore be proposed that as dissolution proceeds, the IL dissolves the exposed outer layers of the fibres, forming a well-adhered silk thread core and an outer halo of silk matrix.

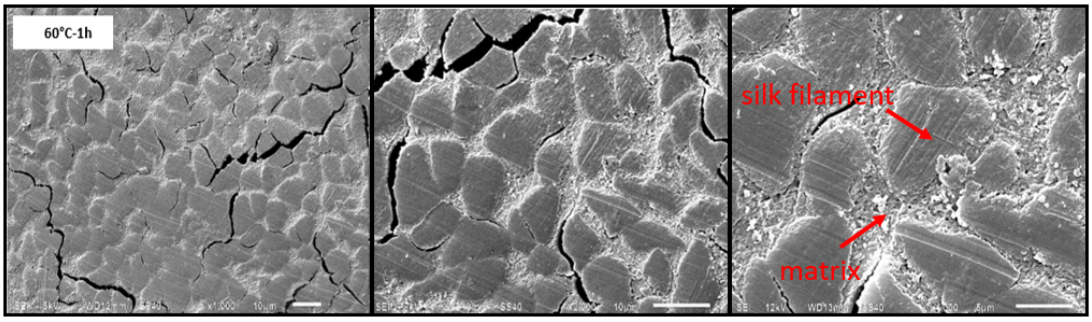

Figure 4.6: The scanning electron micrographs of single partially dissolved silk thread, processed under 60 °C for one hour, observed at 1000x, 2000x, 4000x magnification, from left to right.

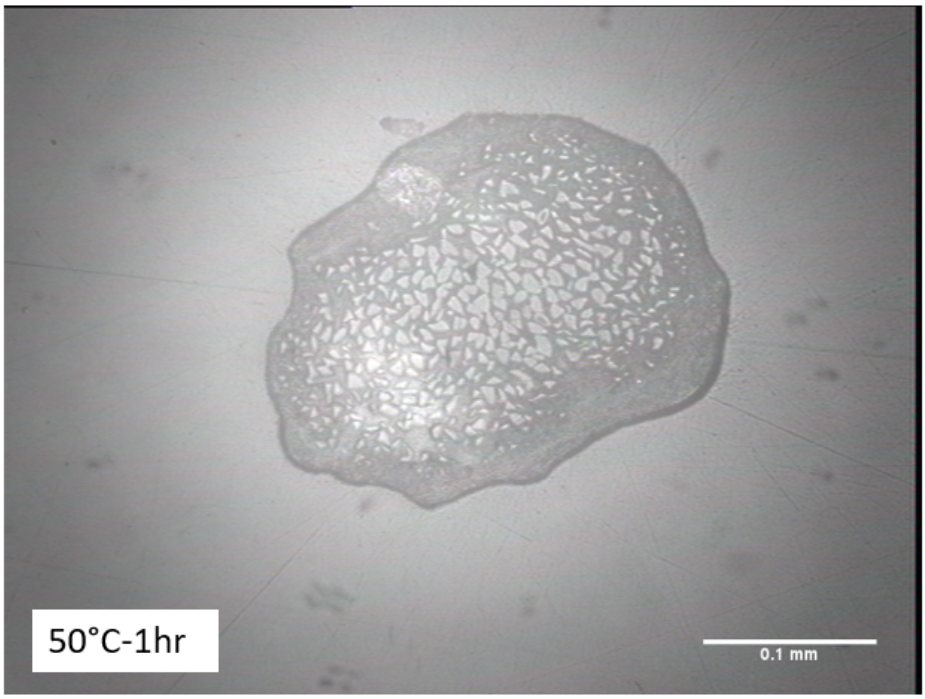

Figure 4.7: Optical microscope image of a single silk thread processed under 50 °C for 1 h, observed under 200x magnification.

4.3.2 Characterisation of the Crystalline Orientation for the Single ASCs and Coagulated Silk Film

Figures 4.8 a and b illustrate the 2D WAXD diffraction patterns of the raw silk thread and CSF. It can be observed that the raw silk thread was characterised by a series of strong diffraction spots, whereas the CSF showed a series of rings. This phenomenon reveals that the dissolution and coagulation process transforms the aligned crystal structure of the raw silk fibres into a randomly oriented crystal structure of the matrix.

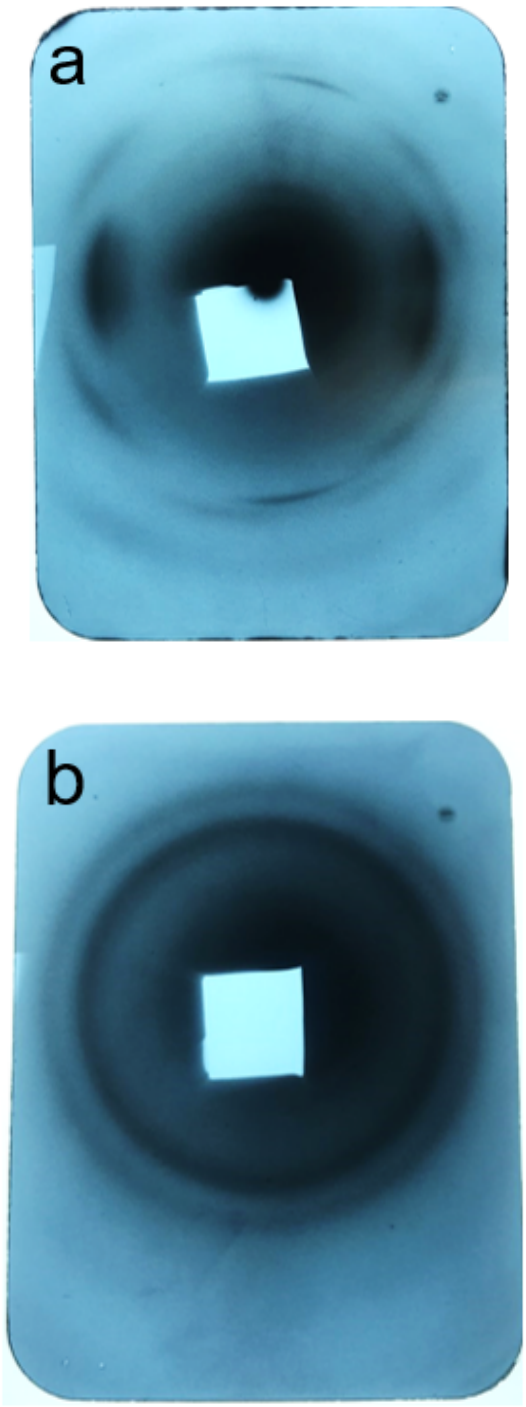

Figure 4.8: WAXD 2D diffraction patterns of (a) raw silk thread, (b) completely dissolved and coagulated silk film (SF film).

Figure 4.9a shows a typical WAXD 2θ diffraction profiles of a raw silk thread, a partially dissolved thread (50 °C for 1 hour) and the coagulated silk film from [C2mim][OAc] solution with 5 wt.% silk fibres. As revealed in Figure 4.8, the dissolution process applied on the raw silk thread changed the resultant crystalline structure, particularly for the CSF (the matrix phase). However, the 2θ scans showed that the position of the three most obvious crystalline diffraction peaks (9.8°, 20.6° and 29°) were all present for the samples at the different dissolution stages. Most importantly, the diffraction curve of the raw silk thread was very similar to the partially dissolved thread curve, with only a small reduction in the intensity of the highest diffraction peak. For this reason it was concluded that the change in the crystalline structure could not be used to follow and measure the dissolution fraction in these silk thread composites, as it was previously used successfully for single cotton composites [228]. In contrast to this, WAXD azimuthal scans for the same three samples, illustrated a much more dramatic change in the intensity distribution (see Figure 4.9b). This is related to a large difference between the highly aligned crystalline orientation of the raw silk threads and the randomly oriented crystals in the coagulated silk film (matrix phase). The three collected azimuthal scans were normalised to give the same total area under the curves.

As mentioned above in section 3.4.3, a WAXD azimuthal scan was carried out by fixing 2θ at the angle with the highest crystalline diffraction peak (20.6°), and then scanning through azimuthal angles from -90° to 90°. At this 2θ position, there was only one crystalline peak in the diffraction curve located at $\theta = 0°$. Our proposal is that the average orientation of each silk thread composite is a sum of the preferred crystalline orientation in the unprocessed silk thread and the randomly oriented coagulated silk film. For the silk thread composite, the normalised peak height was seen to fall which was directly related to the percentage of crystalline regions being dissolved by the IL and being transformed into a randomly oriented crystalline structure after coagulation, increasing the height of this second component. Interestingly, as shown in Figure 4.10, the full width half height (FWHH) of the central silk reflection at $\theta = 0°$, was found to remain

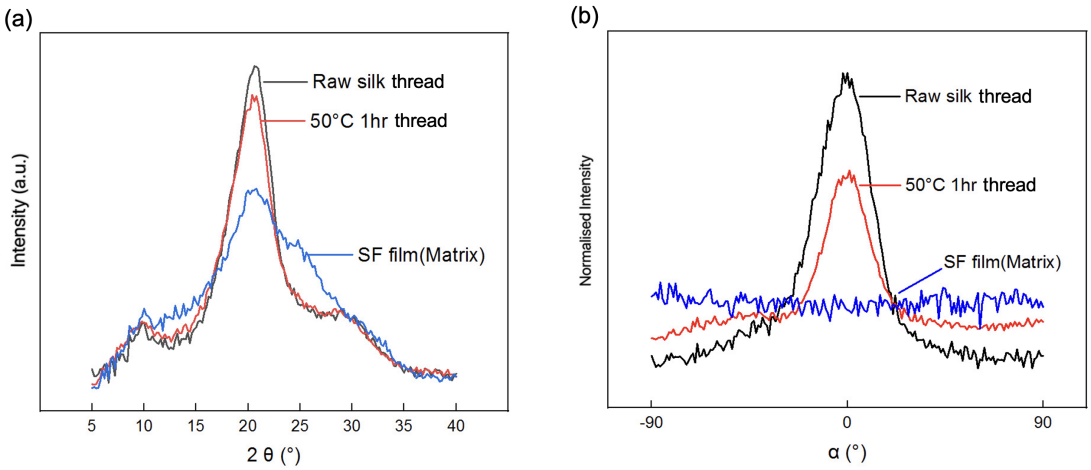

Figure 4.9: Comparison of WAXD diffraction profiles of raw silk thread, partially dissolved silk thread, and coagulated silk fibroin film, at (a) 2θ scan, (b) azimuthal scan.

constant as the dissolution progressed, suggesting strongly that, the undissolved portion of each silk filament is unaffected by the dissolution process.

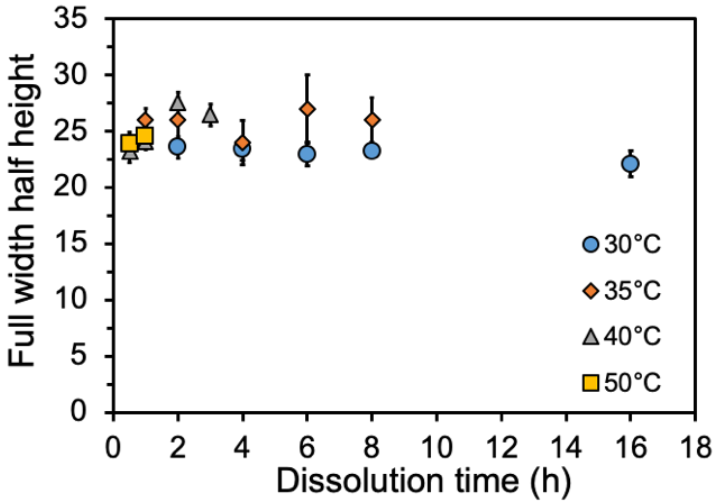

Figure 4.10: Full width half height of WAXD azimuthal scan diffraction curves at different times and temperatures, n = 3.

Figure 4.9b indicates that the raw silk thread shows the highest peak intensity, whereas the CSF shows a constant intensity distribution throughout the whole scanning angle, confirming random crystalline orientation. This can also be seen in Figure 4.8. Compared to the raw silk thread, the normalised peak intensity of the partially dissolved silk thread is lower while its baseline (from the CSF component) is higher, caused by the dissolution process transforming the silk fibres into a randomly oriented coagulated silk fraction whose intensity is therefore independent of α. Our proposal is that the fraction of dissolved silk can therefore be determined by measuring the average orientation of each silk thread composite, along with the values for the raw silk thread and the coagulated film, through following a simple rule of mixtures, which will be explained in detail in section 4.3.3.

It is worth mentioning here the (020) crystallographic plane, whose normal is close to the chain axis direction was examined [241][242]. Because of the scattering vector was kept perpendicular to the thread face, here only the evaluation of the average orientation was obtained. To study the orientation in the whole volume of the silk thread, the out-of-plane rotation need to be taken into consideration.

Accordingly, the average P_2 value of each partially dissolved silk thread composite obtained from processing at various times and temperatures, could be calculated from the distribution curve by numerical integration of the collected data using Equations 3.1 and 3.2, and these results are shown in Figure 4.11. Theoretically, the P_2 value should be equal to 0.25 for a random 2D distribution, and equal to 1 for a perfect alignment. As the randomly oriented component increased in the composite this would result in a fall in the average P_2 value. As expected, composites processed under longer dissolution times or higher dissolution temperatures, were measured to have a lower P_2 value, as shown in Figure 4.11. For ASC processed in [C2mim][OAc] at various times and temperatures, a broadly linear reduction of the average P_2 value was seen. For this reason, similar average P_2 values could be achieved at different reaction temperatures, with a shorter dissolution time needed when the temperature was increased. It can be

assumed that [C2mim][OAc] continuously and effectively dissolves the silk fibres to gradually generate more coagulated silk fraction (randomly oriented crystal structure) in the composite.

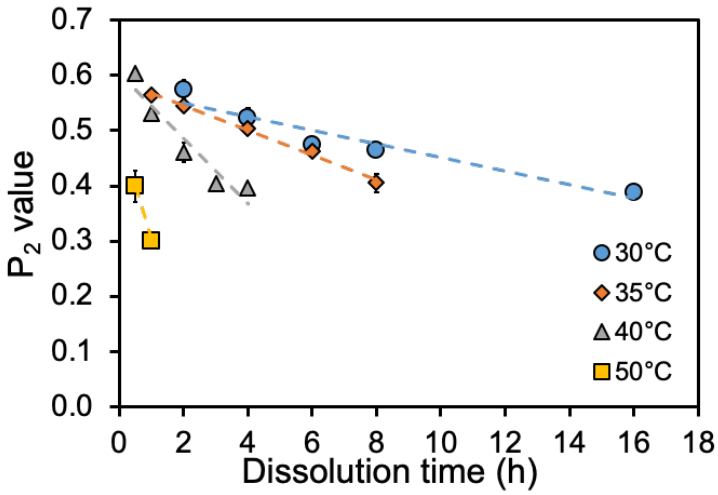

Figure 4.11: Averaged P_2 values calculated from WAXD azimuthal scans for single ASCs being dissolved in [C2mim][OAc] at various times and temperatures, n = 3.

The average P_2 values measured from the silk thread composites (Figure 4.11) showed that the dissolution process occurred more rapidly at higher temperatures. It is proposed that the relationship between dissolution time and temperature could be combined into one curve ("master curve") using the concept of time-temperature superposition, which has been used extensively in polymer rheology measurements [243–245]. A similar approach was recently proposed by this group in the study of the dissolution of flax fibres in [C2mim][OAc] [227]. From this previous work, the idea is to examine the data as a function of the logarithm of the time (ln time) and superimpose the various temperature curves in ln time. A simple multiplicative factor (a_T) could thus relate the temperature and time results, via Equations 4.1 and 4.2.

$$t_R = t_1 a_T \tag{4.1}$$

$$\ln t_R = \ln t_1 + \ln a_T \tag{4.2}$$

where T_1 is the temperature, T_R is reference temperature, t_1,t_R is the time before and after scaling respectively, and ln a_T is the shift factor in ln time. The master curve could thus be constructed by simultaneously shifting different temperature curves horizontally along the logarithm of dissolution time axis, to achieve the best possible overlap with a chosen reference temperature set. Figure 4.12 illustrates schematically the construction of the master curve, which involved a number of steps to generate the best master curve by using the middle temperature (40 °C -grey data points) as the reference T_R data set (in ln time), allowing the line to be extended to give further guidance. Then the other temperature curves were shifted along the X axis (in ln time) towards the reference set to make them overlap, with the horizontal shift called the shift factor (ln a_T). Next, a second polynomial was fitted to the obtained superimposed data sets, and then the individual shift factors were varied to maximise the R^2 value, so as to provide the best fit between this polynomial and the shifted points.

Figure 4.13 shows this final master curve for the variation of the average P_2

value with ln time shifted to 40 °C.

It is more useful to plot the average P_2 value with respect to the linear dissolution time for the silk threads dissolving in [C2mim][OAc], as shown in Figure 4.14. It can be expected that completely dissolving the silk thread could be achieved by a 7 h dissolution time at 40 °C, as its P_2 value approached that of the randomly oriented silk film, i.e. 0.25.

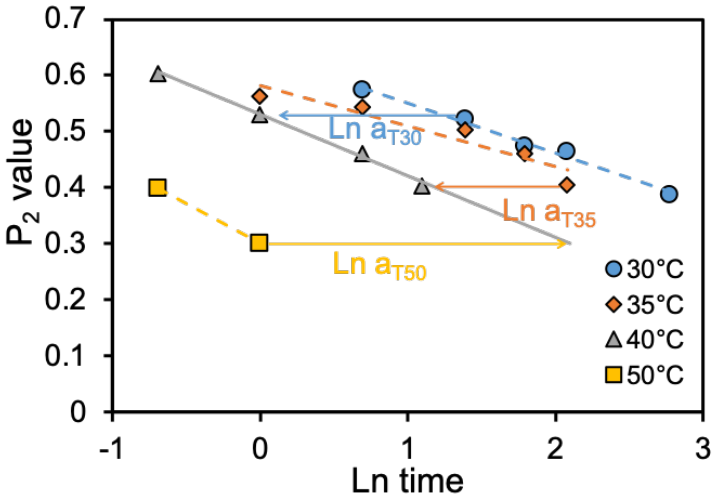

Figure 4.12: A graph to show details of shift method, by using 40 °C as reference temperature.

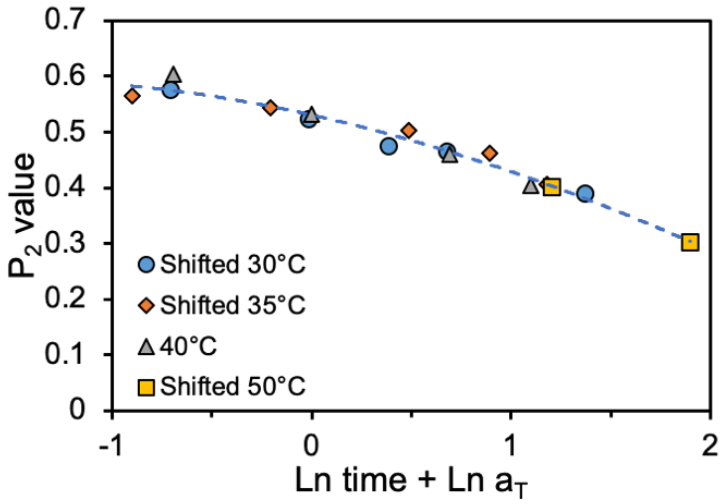

Figure 4.13: Shifted P_2 value of single ASCs, generated as a master curve in ln space.

Now the natural logarithm of the shift factors versus the inverse of temperatures can be plotted, as shown in Figure 4.15. This plot is linear which indicates that the dissolution process follows an Arrhenius like behaviour, i.e. Equations 4.3 and 4.4 [246].

$$a_T = A \exp\left(-\frac{E_a}{RT}\right) \tag{4.3}$$

$$\ln a_T = \ln A - \frac{E_a}{RT} \tag{4.4}$$

where E_a is the Arrhenius activation energy, R is the gas constant and T is the temperature. The dissolution activation energy of the single silk threads in [C2mim][OAc] was therefore calculated at 138 ± 13 kJ/mol.

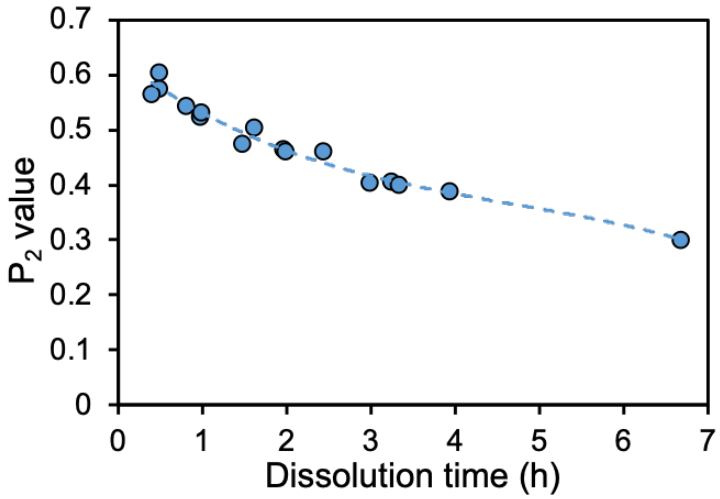

Figure 4.14: Master curve for P_2 value of single ASCs with respect to dissolution time, at a reference temperature 40 °C.

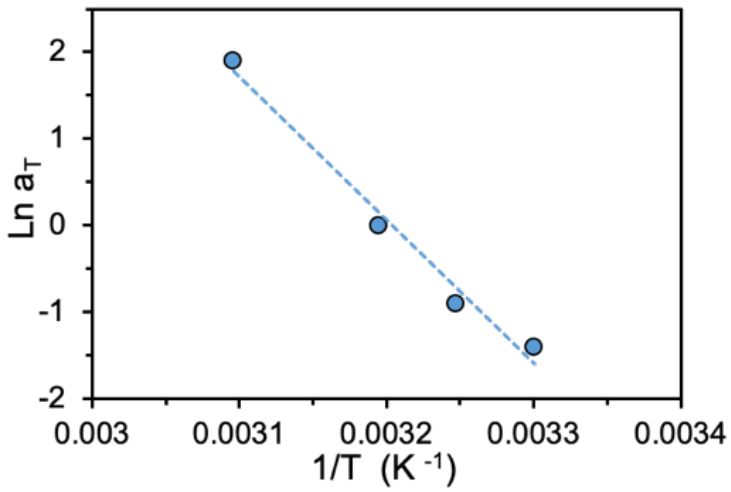

Figure 4.15: P_2 shift factors ($\ln a_T$) as a function of inverse temperature, indicating Arrhenius behaviour.

4.3.3 Measurement of the Volume Fraction of the Coagulated Silk Matrix (V_m) in the Single ASCs

As the dissolution process breaks hydrogen bonds and disulfide bonds in the crystalline regions of the silk fibre, the preferentially oriented crystalline structure is transformed into a randomly oriented coagulated fraction. This was seen from the WAXD azimuthal scans, where the average P_2 value was seen to fall as the dissolution reaction progresses, suggesting the amount of ordered crystalline structure being dissolved increases. The P_2 value of the two individual components, of the composites, fibre and matrix, were measured to be 0.62 (P_2 raw fibre) from the single unprocessed raw silk thread and 0.25 (P_2 matrix) from the coagulated silk film. As illustrated in Figure 4.16, it is next proposed that the coagulated matrix fraction (V_m) of each partially dissolved silk thread composite, can be quantitatively determined from the measured average P_2 value, by assuming a linear mixing rule as expressed in Equations 4.5 and 4.6. It is expected that following V_m TTS analysis can lead to similar value of Ea as calculated from the P_2 method, due to the mathematical relationship between these two parameters.

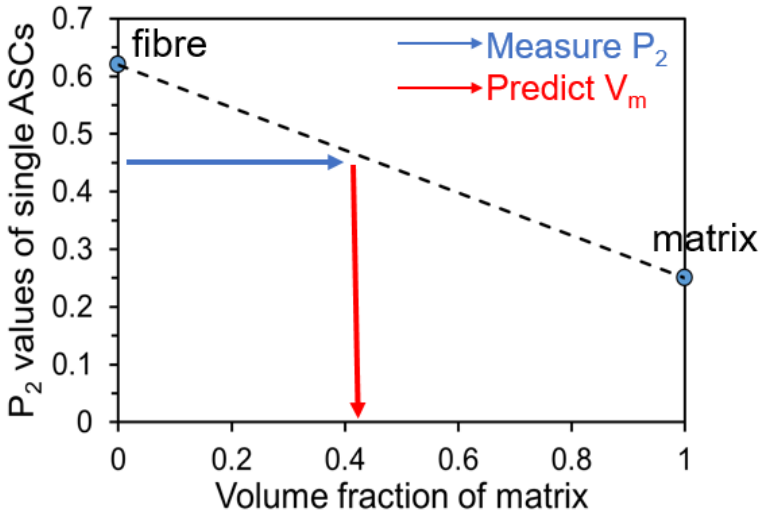

Figure 4.16: A diagram demonstrates how to measure V_m values from the respective P_2 values through a linear mixing rule.

$$P_2 = P_2^{fibre} V_f + P_2^{matrix} V_m \tag{4.5}$$

V_f is the volume fraction of the fibre. Rearranging Equation 4.5 to make V_m, the subject leads to

$$V_m = \frac{P_2^{fibre} - P_2^{composite}}{P_2^{fibre} - P_2^{matrix}} \tag{4.6}$$

Assuming $V_f + V_m = 1$.

Therefore, the value of the dissolved and coagulated matrix fraction, V_m for ASC obtained under various dissolution temperature as a function of dissolution time can be calculated and this is shown in Figure 4.17. As expected, longer dissolution times generated more of the randomly oriented matrix phase and consequently lead to a reduction of the remaining silk fibre fraction and an associated large V_m. These results agreed with the previous cross-sectional optical microscope images (Figure 4.4), showing that the amount of the remaining silk filaments reduced with the dissolution time, and the matrix amount correspondingly increased.

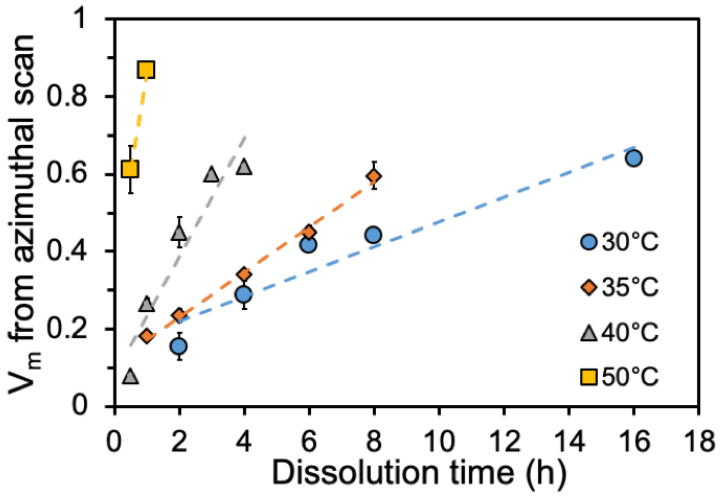

Figure 4.17: Single ASCs volume of matrix measured from difference in P_2 value, n = 3.

As demonstrated above, the silk fibre dissolution process displays time temperature superposition, so the V_m should likewise obey TTS. In Figure 4.18a, a shifted master curve of the V_m values of the obtained ASCs was constructed by using the same shifting method, as introduced above, again using 40 °C as the reference temperature.

After all the data points from different temperatures were shifted, the complete master curve in dissolution time was obtained, and is shown in Figure 4.18b. This curve showed the change in the matrix fraction, V_m, of the silk composites dissolving in [C2mim][OAc] with respect to dissolution time, at a reference temperature 40 °C. In the first two hours, the [C2mim][OAc] dissolved up to 50 % of fibre. However, in the second stage 2 to 4 hours only a further 20 % of silk fibres were dissolved, which indicates that the dissolution rate has slowed down. However, from the shifted master curve, the dissolution process still follows the time-temperature superposition principle.

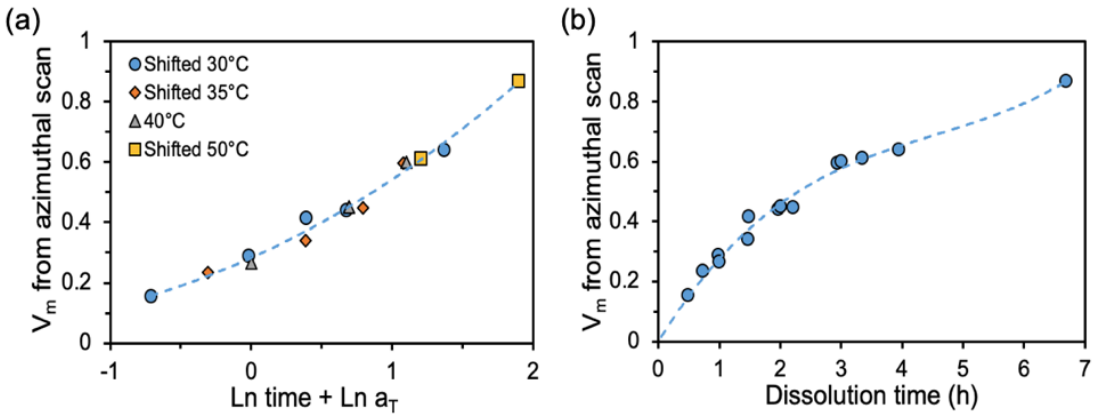

Figure 4.18: Master curves of (a) Shifted V_m value of ASC in ln space, (b) V_m value of single ASCs with respect to dissolution time, at a reference temperature 40 °C.

These shift factors, from the V_m TTS shifting, can now be plotted as a function of inverse temperature as before for the P_2 results. A straight line is again found to

fit the data points, reflecting Arrhenius behaviour, as shown in Figure 4.19. From these V_m measurements, the dissolution of single silk threads in [C2mim][OAc] was calculated to have an activation energy of 139 ± 15 kJ/mol. This is very similar to the value obtained from the P_2 TTS analysis and is a confirmation of the validity of our procedure, and indicates that P_2 and V_m parameters are mathematically related to each other.

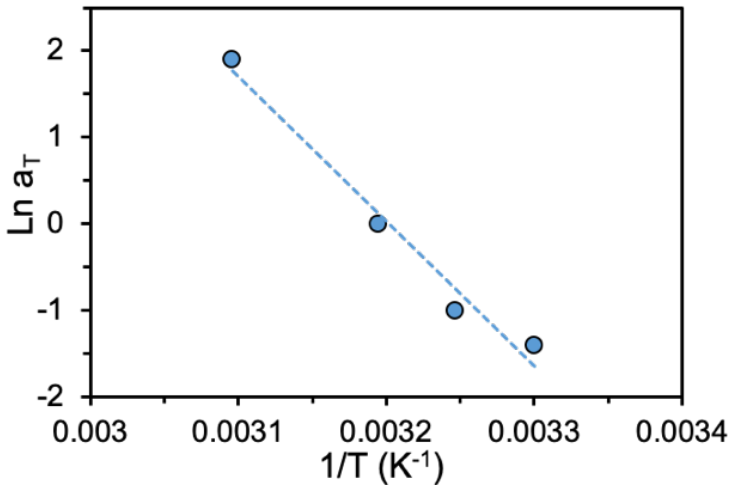

Figure 4.19: V_m shift factors (ln a_T) as a function of inverse temperature, indicating Arrhenius behaviour.

4.3.4 Mechanical Properties of Single ASCs

Figure 4.20 illustrates the stress-strain curve for a single ASC obtained at 30 °C for 4 hours. It is acknowledged that the area underneath the stress-strain curve represents the tensile toughness of the sample, which is defined as the energy one sample can absorb before it breaks. Thus, it is interesting to measure the tensile toughness of this representative sample, which gives a value of 21.9 J m $^{-3}$. Other researchers have measured the tensile toughness of silk-epoxy composites at room temperature (20 °C), and reported values of 8 J m $^{-3}$ and 45 J m $^{-3}$, when incorporating 60 % volume fraction of *B. mori* and *Antheraea pernyi* silks, respectively [247].

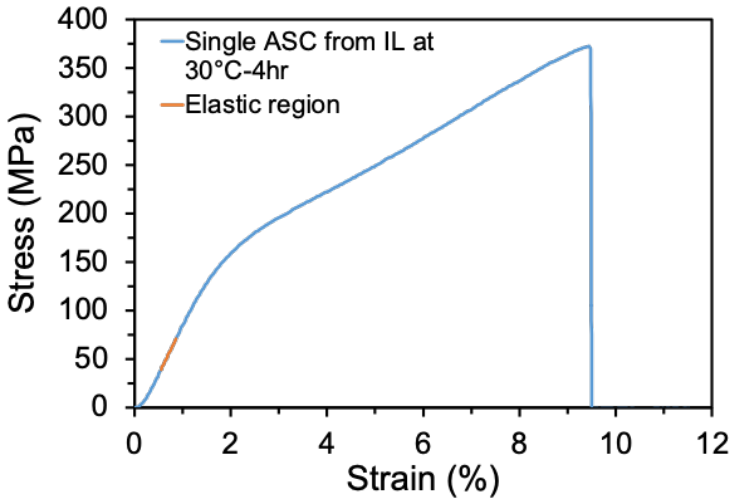

Figure 4.20: Stress-strain curve for single ASC obtained from IL system at 30 °C for 4 hours.

Figure 4.21 shows the results of Young's Modulus measurements carried out on silk ASCs formed at a temperature of 30 °C for times up to 16 hours. It would be expected, from a simple parallel rule of mixtures that the Young's Modulus of

each processed single ASCs would continuously decrease, due to the amount of the reinforcing fibre reducing. However, as shown in Figure 4.21, the measured modulus gradually increases at the early stages of the dissolution, reaching a maximum at around 2 hours and then afterwards decreases.

As mentioned previously when discussing the optical micrographs of the raw and partially dissolved threads in section 4.3.1, the specific thread structure resulted in significant interior space in between each filament. At an early dissolution stage, it is suggested that the created matrix is not sufficient to fill up all the gaps between filaments. The results of this would be that there is not good stress transfer between all the filaments (insufficient matrix) resulting in a lower measured modulus. Similar observations were reported by Soykeabkaew et. al [55] in all cellulose composites. Furthermore, they observed that after 2 h of immersion time, a sufficient amount of the outer layer of fibres was dissolved to create a matrix phase to bond the remaining thread core. This could also explain why the experimental Young's Modulus value of a raw undissolved silk thread was only 6.17 GPa, which was close to the value of those at early stages of the dissolution (0.5, 1 h at 30 °C).

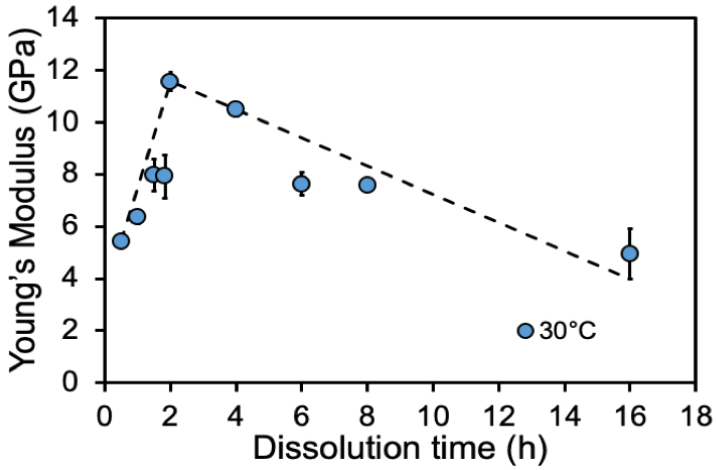

Figure 4.21: Modulus values of single ASCs dissolved for different length of time, at 30 °C, the dashed line is guide for the eye, and not a fit to the data, n = 3.

Consequently, combined with previous silk thread microstructure results as mentioned in section 4.3.1, the dissolution procedure of a single silk thread can be proposed by the schematic diagram, shown in Figure 4.22. In the early stage, [C2mim][OAc] can infiltrate in between each filament of raw silk thread (Figure 4.22a), transforming the dissolved fibres into the matrix to provide a close-packing thread microstructure (Figure 4.22b), which is named the 'preformed stage'. At 2 h (30 °C), all of the internal space is filled and the measured Young's modulus reaches a peak. Following this, more silk fibres are dissolved forming an outer ring on the preformed thread core (Figure 4.22c). As more matrix is generated, the thicker this ring becomes, eventually a completely dissolved film matrix would be formed (Figure 4.22d). It is next proposed that to form a composite from a single silk thread, then the optimum dissolved fraction (∼20 %) would occur at two hours at 30 °C. However, to make a composite with multiple threads, more matrix phase would be required to combine all of the various threads into a homogeneous composite (this is normally around 30-40 % for a typical composite or in this case around 1 hour at 40 °C).

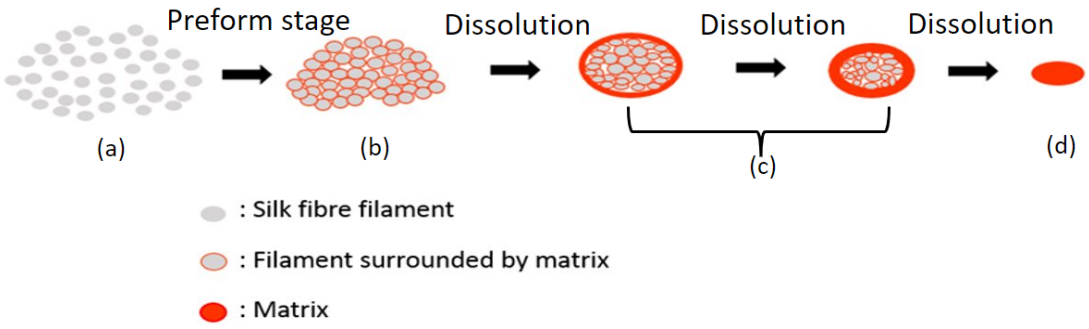

Figure 4.22: Schematic representation of a single silk thread dissolution procedure; dissolution starts from (a) undissolved raw silk thread to (b) ASC with close-packing microstructure, (c) ASCs with different amounts of matrix, and (d) completely dissolved film matrix.

The Young's Modulus value of single ASCs obtained from various dissolution temperatures are summarised in Figure 4.23, after removing the results before

the preformed stage. It demonstrates a trend that the experimentally measured Young's Modulus continuously decreases and does so more rapidly at higher temperatures.

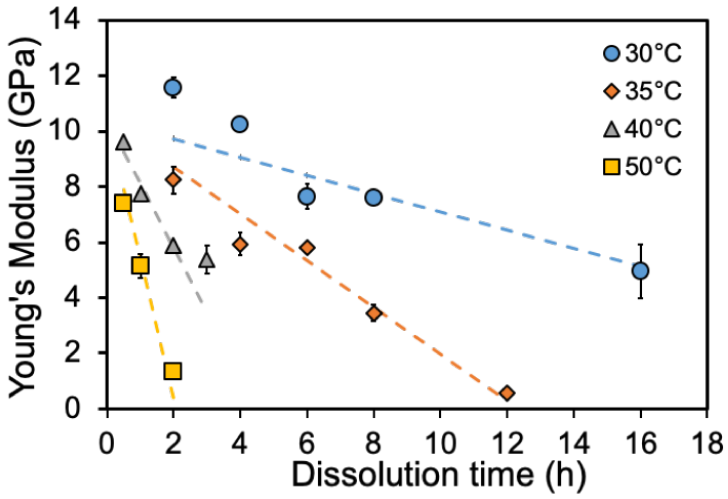

Figure 4.23: The Young's Modulus for each processed single ASCs at various dissolution times and temperatures, n = 3.

Now, it is possible to see if the variation of the modulus measurements also obeys the time-temperature superposition principle. Figure 4.24a shows the results of using the same shifting procedure as described above, again using 40 °C as the reference temperature. These results indicate that the modulus curves at different temperatures were related to one another by certain shift factors (ln a_T). Interestingly, in terms of composite production, the same modulus value could be obtained by either increasing the dissolution temperature or increasing the dissolution time. After all of the individual data points were shifted, the complete TTS curve of single ASCs Young's Modulus values (in dissolution time) is shown in Figure 4.24b, based on a 40 °C reference temperature.

These results mirror the shape of the matrix fraction master curve (Figure 4.18b) as this is the main controlling factor in determining the composite modulus.

Figure 4.18b shows that the matrix fraction initially increases quickly with the dissolution time, leading to the rapidly decreasing modulus shown in Figure 4.24b. As the matrix dissolution rate slows (when all the interior spaces in the silk multi-filaments are filled), then the fall in Young's modulus also slows down as shown in Figure 4.24b.

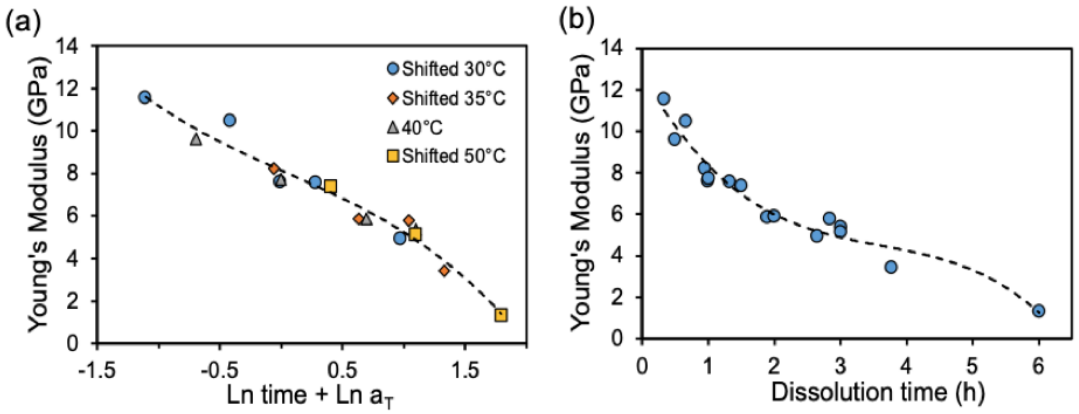

Figure 4.24: Master curves of (a) Shifted Young's Modulus value of ASC in ln space, (b) each processed single ASC as a function of dissolution time, at a reference temperature 40 °C, the intercept of this curve gives single unprocessed silk thread Young's Modulus to be 12.74 GPa.

Figure 4.25 shows that relationship between the shifting factors and inverse temperature is once again Arrhenius, being linear when the ln shift factors are plotted against $1/T$. The dissolution activation energy from Figure 4.25 was measured to be 116 ± 12 kJ/mol. This is similar to the two values obtained from the P_2 and V_m time-temperature shifting.

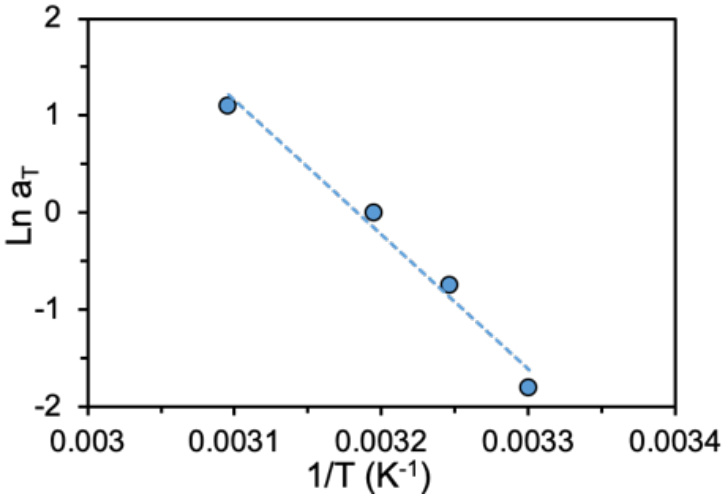

Figure 4.25: Young's Modulus shift factors (ln a_T) as a function of the respective inverse temperatures, indicating Arrhenius behaviour.

Next, the ultimate tensile strength values of each obtained single ASC were also determined from their corresponding stress-strain curves. Figure 4.26 shows the strength values of single ASCs obtained from a range of times at 30 °C. Interestingly, it is once again evident that the existence of the 'preformed stage' during early stage of dissolution. Similar to the observed phenomenon from modulus values at 30 °C, recalling Figure 4.21, due to the loose structure of raw silk thread core, there is not enough matrix being generated from early dissolution hours to provide sufficient stress transfer between all the filaments, which results in a relatively lower strength values. And once the gap between filaments is filled by sufficient amount of matrix, here at 2 hours dissolution under 30 °C, a close-packed thread core would be generated and create a strong bond between fibre and matrix, consequently the resultant composite owes the greatest strength value. Thereafter, the increased dissolution times result in a increased amount of fibres being dissolved and transformed into matrix, thus a broadly reduction of composite strength value is seen between 2 to 16 hours of dissolution time.

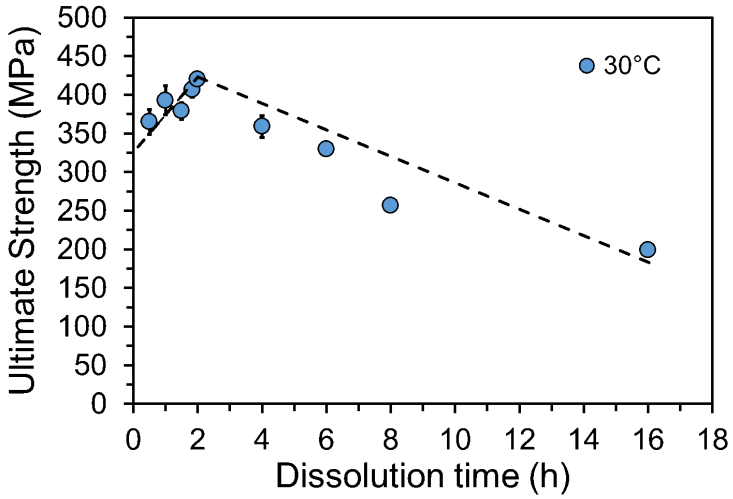

Figure 4.26: Ultimate strength value of single ASCs dissolved for different length of time, at 30 °C, the dashed line is guide for the eye, and not a fit to the data, n = 3.

Figure 4.27a shows the strength value of single ASCs obtained from a range of times and temperatures, it should be noted that the data from 'preformed stage' is removed because it relates to a different dissolution stage - before the close-packed thread core structure is formed. It can be observed that ultimate tensile strength values decrease approximately linearly with longer dissolution time or higher dissolution temperature, which is consistent with the observed changes of Young's modulus values. Thus, same shifting method was applied to shift strength values at various temperature sets towards a chosen reference temperature set (again, 40 °C here), to achieve a best overlap with the greatest R^2 value. The constructed master curve is given in Figure 4.27b. Then a complete TTS curve of ultimate tensile strength for single ASCs at a 40 °C reference temperature with respect to the linear dissolution time, is shown in Figure 4.27c. It can be seen that the ultimate tensile strength decreases rapidly at early dissolution hours, and slow down afterwards. Noticeably, master curves of ultimate tensile strength (Figure 4.27c) and Young's modulus (Figure 4.24b) are almost identical to each other, both showed a significant reduction of the values in the

first 3 hours of dissolution at 40 °C. Figure 4.27d shows the shift factors obtained from shifting each temperature set when plotted versus $1/T$, which indicates a linear relationship, from which an Arrhenius behaviour was once again found, the activation energy was calculated from the gradient of the line, gave a value of 139 ± 19 kJ/mol. This value is similar to the E_a determined in section 4.3.2 by following the orientation changes within each single ASC (138 ± 13 kJ/mol), and close to the E_a obtained earlier in this section through following the changes of Young's modulus values (116 ± 12 kJ/mol). This is an evidence that following the ultimate tensile strength changes can also track the dissolution dynamics of single silk threads in [C2mim][OAc].

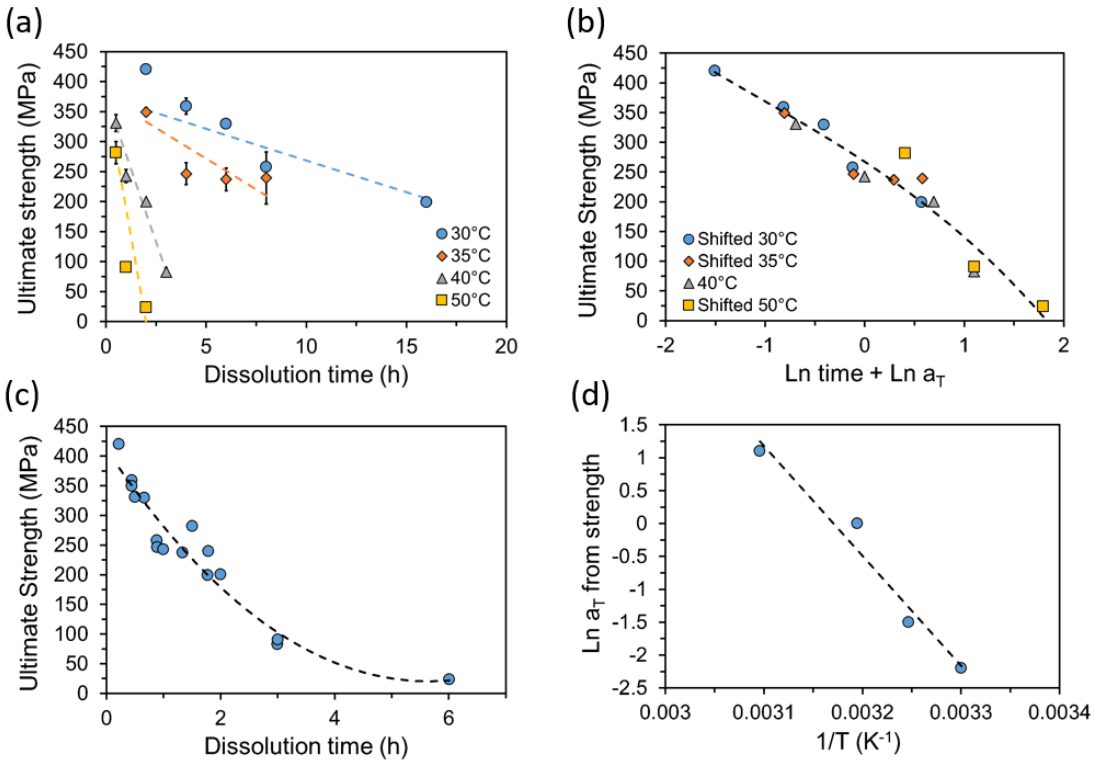

Figure 4.27: (a) Ultimate strength of single ASCs at various times and temperatures, n = 3. (b) Master curve of ultimate strength in ln space, after TTS shifting. (c) Master curve of ultimate strength of single ASCs over linear dissolution time, at a reference temperature of 40 °C. (d) Shifting factors versus $1/T$, and found to follow Arrhenius behaviour.

Furthermore, the corresponding elongation at break values were also determined from the respective stress-strain curves, for single ASCs fabricated from various times and temperatures, the results are shown in Figure 4.28a. It can be seen that the strain values decrease with the increased time and temperature and even more rapidly at higher temperatures which once again implies time-temperature equivalence. Therefore, the introduced shifting method was again applied, data from different temperature sets were firstly plotted in natural logarithmic time, and next simultaneously shifted towards the chosen reference temperature set (40 °C here). After shifting, the constructed master curve is given in Figure 4.28b. The changes of strain over linear dissolution time is expressed as a master curve in Figure 4.28c. Interestingly, as opposite to the changes of modulus and strength, the strain value initially decreases slowly with the dissolution time (between 0-1 hour time at 40 °C), and drops more rapidly thereafter. It is possible that at early dissolution hours, the created matrix plays as a bonding role more crucially, and maintain a good stress transfer between fibre and matrix. However, as the dissolution progresses, the proportion of the matrix rises and directly results in a continuously decreased values of breaking strain for the corresponding single ASC. Subsequently, Figure 4.28d shows the required shift factors plotted against the respective inverse temperatures, and indicates a linear relationship which further yields to a E_a value of 118 ± 10 kJ/mol. Interestingly, this measured E_a value is in agreement with the E_a measured from the changes of modulus values (116 ± 12 kJ/mol), which suggests that following the changes of strain values is another way to determine the required dissolution activation energy.

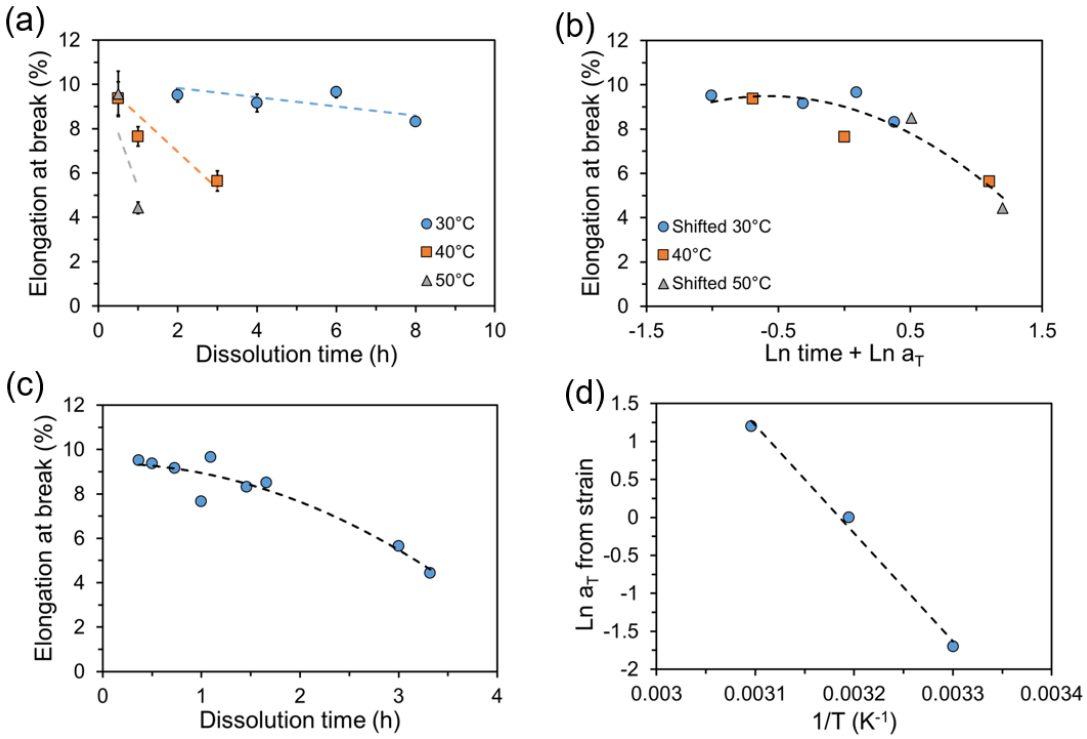

Figure 4.28: (a) Elongation at break values for single ASCs at various times and temperatures, n = 3. (b) Master curve of elongation at break plotted in natural logarithmic time, after TTS shifting. (c) Master curve of elongation at break for single ASCs over linear dissolution time, at a reference temperature of 40 °C. (d) Shifting factors versus $1/T$, and found to have an Arrhenius behaviour.

Table 4.1 summarises the values of ultimate tensile strength with the corresponding elongation at break values for the raw silk thread, coagulated silk fibroin film, as well as each single ASC including the samples from the 'preformed stage'. It can be seen from this table that the single unprocessed raw silk thread owes relatively high strength and strain value, which is in good agreement with reported values (300-740 MPa) from other researchers [62, 127, 248–250]. However, the fully dissolved and coagulated silk fibroin film displays a mediocre mechanical behaviour compared to the raw silk thread, which also agrees with the reported weak strength, strain, and brittleness for the regenerated silk film in dry state (0.5-3 % breaking strain) [251–254]. As introduced in the literature review section (2.5), the large content of β-sheet is formed during the coagulation process in methanol bath attributes to the less extensible characteristics of the film. This once again reflects the changes in Figure 4.28c, the continuous growth of brittle matrix during the dissolution process directly contributes to the decreased breaking strain values for the single ASCs fabricated at longer dissolution times under 40 °C.

	Ultimate tensile strength (MPa)	Elongation at break (%)
Raw single thread	471 ± 15	9.9 ± 0.7
30 °C - 0.5hr	365 ± 16	12 ± 0.3
30 °C - 1hr	393 ± 19	11 ± 0.6
30 °C - 1.5hr	379 ± 11	10 ± 0.4
30 °C - 1.83hr	407 ± 10	11 ± 0.2
30 °C - 2hr	420 ± 3	9.5 ± 0.3
30 °C - 4hr	359 ± 14	9.2 ± 0.4
30 °C - 6hr	330 ± 7	9.7 ± 0.3
30 °C - 8hr	257 ± 7	8.3 ± 0.2
30 °C - 16hr	199 ± 7	6.2 ± 0.2
35 °C - 2hr	349 ± 7	6.7 ± 0.6
35 °C - 4hr	246 ± 18	6.5 ± 0.2
35 °C - 6hr	237 ± 19	8.0 ± 0.3
35 °C - 8hr	239 ± 44	7.4 ± 0.6
40 °C - 0.5hr	331 ± 14	9.3 ± 0.8
40 °C - 1hr	243 ± 11	7.7 ± 0.4
40 °C - 2hr	200 ± 4	9.9 ± 0.4
40 °C - 3hr	83 ± 7	5.6 ± 0.5
50 °C - 0.5hr	282 ± 19	9.6 ± 1.0
50 °C - 1hr	91 ± 5	4.4 ± 0.3
50 °C - 2hr	24	2.5
CSF (Matrix)	10 ± 2	0.59 ± 0.01

Table 4.1: The ultimate tensile strength and elongation at break values for single ASCs fabricated from various times and temperatures under the ionic liquid [C2mim][OAc], n = 3.

A comparison of the four measured dissolution activation energies for dissolving single silk threads in [C2mim][OAc] can be found in Figure 4.29. It can be seen that E_a values derived from four different methods all present very similar values, with an average value of 128 ± 6 kJ/mol. This suggests a good validation of our measurement methods.

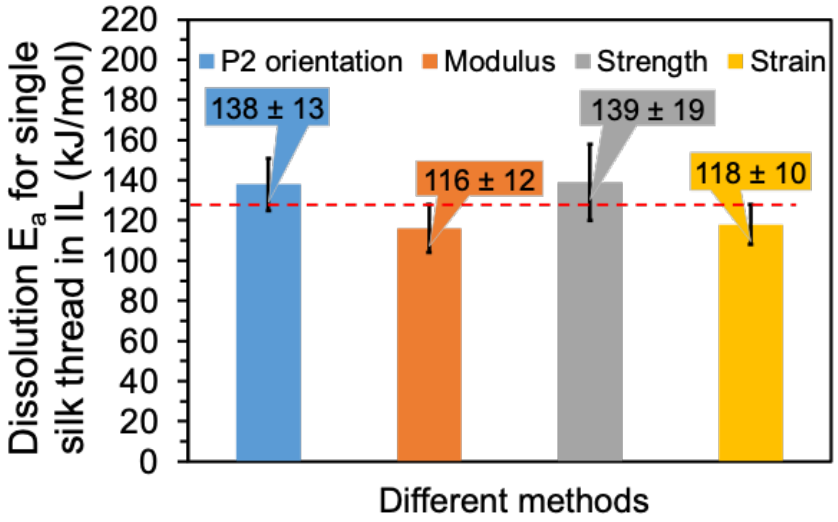

Figure 4.29: A graph to summarise the dissolution activation energy measured through four different methods as introduced in this chapter, horizontal dashed line indicates the average value, which goes through all measurements within their error bars.

4.3.5 Rule of Mixtures Theory Applied on the Mechanical Parameters with the Corresponding V_m

The mechanical behaviour of the resulting composites, such as tensile properties, can be predicted utilising micromechanical models, including Halpin Tsai and rule of mixture (ROM) models [255]. Modelling can reveal the structure-property relationship within the composites, with little time and cost, comparing to obtaining results from a range of experiments [256]. ROM models are more often utilised because it is relatively simple and yields acceptable prediction values [257, 258].

After acquiring the Young's Modulus values of each processed single ASCs, it is of interest to see how these correlate with the matrix fraction V_m obtained from the WAXD azimuthal scan, in particular to assess the applicability of the well-known ROM in our fibre composites and to quantify the effect of reinforced

fibre volume on the resulted mechanical behaviour.

Therefore, the Young's Modulus master curve values of each ASCs (in Figure 4.24b) was plotted as a function of the corresponding V_m master curve values from the azimuthal scan (in Figure 4.18b) and is shown in Figure 4.30. Based on the parallel and series rules of mixture models [259], Voigt (parallel and upper bound) [260, 261] and Reuss (series and lower bound) [262] predictions were used to estimate the effective modulus in the composite. Plotting the ROM model boundary curves requires the two limiting moduli values, i.e. the ordered silk fibres from the raw single silk thread and the coagulated silk matrix from the prepared film. Extrapolation of the modulus TTS curve (Figure 4.24b) gives the preformed well-aligned silk thread modulus value as 12.7 ± 1.3 GPa ($V_m = 0$). The three-point bending experiment measured on the coagulated silk film gave a value of 1.6 ± 0.3 GPa ($V_m = 1$). Refer to section 4.2.3 for details on film fabrication, and section 3.5.2 for three-point bending test.

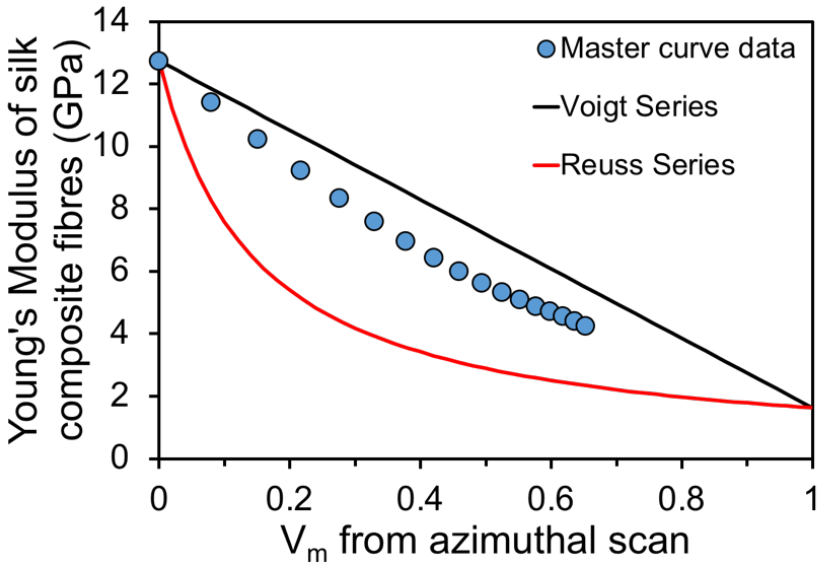

Figure 4.30: Rule of mixture curve for single ASCs, Young's Modulus plotted as a function of corresponding V_m, with Voigt and Reuss boundary lines to indicate the rule of mixture theory.

The Voigt model assumes that the strain of the fibre is equal to the strain of matrix (parallel model), while the Reuss series proposes that the stress of fibre was equal to the stress of matrix [263]. It could be observed that all the master curves data points, as expected, lie between the two boundary curves. The results are much closer to the Voigt rule of mixtures, up to a matrix fraction (V_m) of ~70 %, which is a normal location for most fibre reinforced composite materials. It is important to noted that both ROM models were made based on the assumptions that fibres and matrix act as perfectly linear elastic materials, homogeneous fibre distribution within matrix, fibres perfectly aligned and spaced, perfect bonding between fibre-matrix and matrix is void free [255, 264]. It is therefore expected that discrepancies between experimental results and theory may occur due to a number of reasons such as imperfections in the fibre-matrix interface, fibre misalignment, and defects in both matrix and fibres [265–269].

In order to further understand the deviations between theory and experimentally measured Young's modulus values, the master curve of elongation at break for single ASCs (ϵ_c) (Figure 4.28c) is plotted with respect to the master curve of V_m (Figure 4.18b). Figure 4.31 shows how the ϵ_c varies in accordance with the V_m. It can be noticed that as the V_m rises, the ϵ_c is seen to decline. However, initially, when V_m is ≤ 0.25, a slow reduction of strain values is seen, with the ϵ_c values stay steadily ≥ 9 %, and still close to the strain value of single raw silk thread, 9.5 % (obtained through extrapolating backward to the point V_m is 0). After this stage, a much quicker reduction rate is seen, with ϵ_c decreases from 9 % to 4.5 %, when V_m ranges from 0.25 to 0.6. It is evident that the ϵ_c varies with the V_m values, which suggests that the single silk composites are not strictly following the iso-strain condition [263]. This may contribute to the reasons of the existence of discrepancies between experimental and theory results, in Figure 4.30.

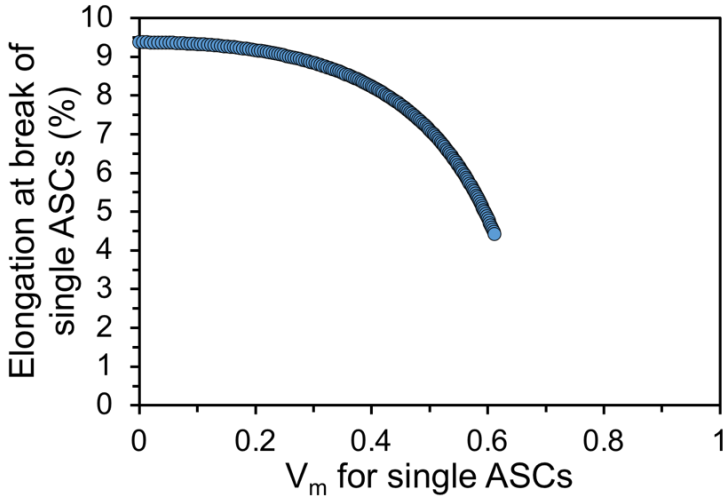

Figure 4.31: Master curve of elongation at break of single ASCs plotted against the master curve of V_m.

At the same time, it is worth mentioning that in our fabricated composites system, the failure strain of the fibre (ϵ_f) is higher than the failure strain of the matrix (ϵ_m), see Table 4.1. Based on composites theory [9], as illustrated in Figure 4.32, in the case of $\epsilon_f > \epsilon_m$ (Figures 4.32 a and c), for the strain up to ϵ_m, the composite stress is expressed by the simple rule of mixtures, as expressed in Equation 4.7:

$$\sigma_{composite} = \sigma_{fibre} V_f + \sigma_{matrix} V_m \tag{4.7}$$

For the strain above ϵ_m, matrix then starts to undergo microcracking, however, it does not lead to composite failure. Instead, the composite will extend with increase in the applied stress. As the matrix cracking continues, the additional load is now transferred into the fibres. If the strain does not reach the ϵ_f during this stage, the stress of the composite will rise due to the further extension, subsequently the load is now carried completely by the fibres. Therefore, the final failure of the composites will occur when the strain reaches ϵ_f, and at this

point, the composite failure stress ($\sigma_{composite}$) is given by $\sigma_{fu}V_f$, σ_{fu} is fibre stress.

On the other hand, if the fibres break before the matrix has progressively transferred all the load to them, then the strength of the composites can thus be calculated using Equation 4.8:

$$\sigma_{composite} = \sigma_{fmu}V_f + \sigma_{mu}V_m \tag{4.8}$$

where σ_{fmu} is the fibre stress at the onset of matrix cracking. The composite failure stress is therefore depends on the volume fraction of fibre. The volume fraction of fibre above which the fibres can sustain a fully transferred load is obtained using Equation 4.9:

$$\sigma_{fu}V_f = \sigma_{fmu}V_f + \sigma_{mu}V_m \tag{4.9}$$

which leads to a determination of the onset volume fraction of fibre (f'), as given in Equation 4.10:

$$f' = \frac{\sigma_{mu}}{\sigma_{fu} - \sigma_{fmu} + \sigma_{mu}} \tag{4.10}$$

This theory is of particular importance when designing the composites with preferable properties, because the properties change as a function of volume fraction of fibre/matrix.

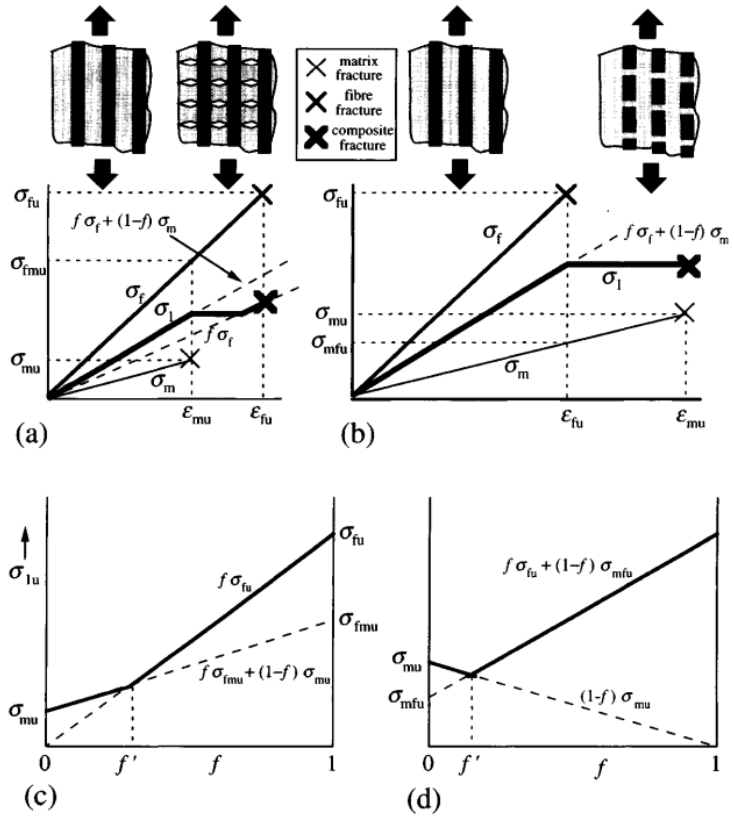

Figure 4.32: Schematic plots of axial tensile failure for long-fibre composites. (a) and (c) refer to a composite system where the fibre has a higher failure strain than the matrix, and show the respectively stress-strain curves, as well as the dependence of composite failure stress on V_f; (b) and (d) show the same plots for the composite system where the matrix has the higher failure strain. Reproduced (adapted) from ref [9], Cambridge University Press, ©2012.

It is thus of final interest to evaluate the dependence of the composite failure strength on the volume fraction of fibre. Consequently, the master curve of the ultimate strength of single ASCs (Figure 4.27c) is plotted as a function of the master curve of fibre volume fraction, V_f (1 - V_m), as demonstrated in Figure 4.33. The ultimate strength of raw silk thread was obtained from extrapolating the strength data sets at 30 °C (Figure 4.27a) backward to the point at which the dissolution time is 0, gave a value of 471 ± 15 MPa, and the strength of

coagulated silk film was determined from the three-point bending experiment, gave an average value of 10 ± 2 MPa (recalling Table 4.1). As seen in Figure 4.33, for higher fibre volume fractions ($0.3<V_f<1$), there is a gradual decrease in the composite ultimate tensile strength from the raw silk thread strength value (471 MPa) to ∼ 100 MPa at V_f=0.3. Additionally, at the range of $0<V_f<0.3$, a further decline of the composite strength value with the decrease of fibre volume fraction can be seen, and eventually when the V_f reaches 0, the composite strength is equal to the matrix strength (∼ 10 MPa).

Such phenomenon agrees with the established theory of the dependence of composite failure stress on V_f (Figure 4.32c) [9], and indicates that there are two possible failure regimes: for high fibre volume fraction, the load is carried by the fibres just prior to the matrix cracking, thus the composite ultimate strength is essentially the fibre strength ($\sigma_{composite} = \sigma_{fu}V_f$); for low fibre volume fraction, matrix failure results in composite failure, the composite reaches its ultimate strength when the matrix fails at its cracking strength (as given in Equation 4.8). It can be therefore concluded that the fibre strength is dominant in determining the axial strength of the composite, and the composite strength increases with fibre volume fraction. It has been reported that mechanical properties of composites improve with certain increases in V_f [270][271]. There is strong evidence that the proper selection of a sufficient amount of fibre volume fraction plays a key role for strengthening the composites.

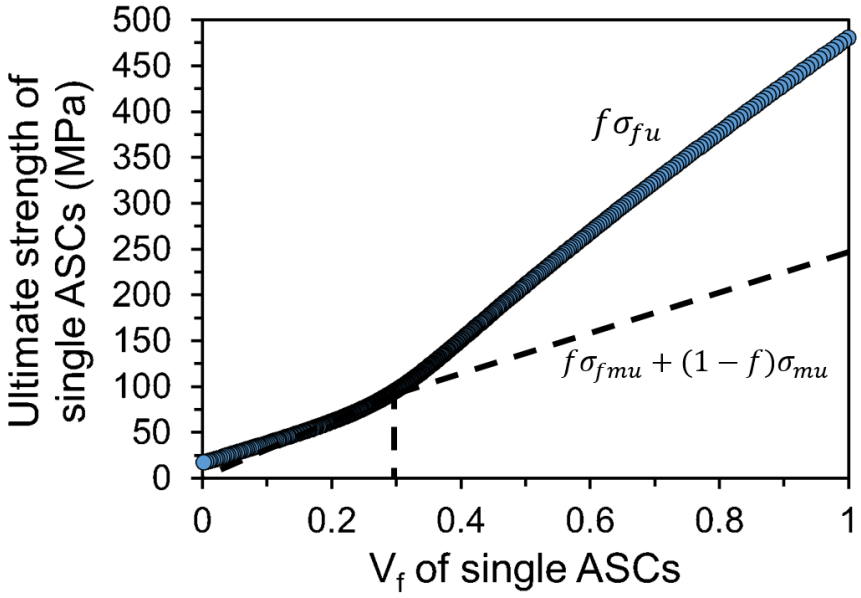

Figure 4.33: Rule of mixture curve for single ASCs ultimate strength as a function of the corresponding V_f.

4.4 Summary

This chapter has studied the dissolution dynamics of single silk threads in the ionic liquid 1-ethyl-3-methylimidazolium acetate ([C2mim][OAc]), as well as the structure and properties of the resulting composites. Partial dissolution method has been utilised to prepare single all silk composites. [C2mim][OAc] was chosen as the solvent and methanol as the coagulant. The dissolution process was carried out under various times and temperatures allowing a range of the partially dissolved silk thread composites to be fabricated. A number of experimental techniques were performed to conduct the analysis including: Optical microscope, scanning electron microscope, wide-angle X-ray diffraction and mechanical testing.

By using the optical microscope, it was found that one single ASC is composed of original undissolved silk filaments surrounded by a coagulated silk matrix phase. The tensile Young's Modulus of each silk composite filament was measured, and it was found that under 30 °C, the modulus value initially increased linearly to a peak 11.6 ± 0.4 GPa at time 2h, and then declined linearly thereafter with time (recalling Figure 4.21). In accordance with the results from optical microscope and Young's Modulus testing, a 'preformed stage' was identified, in which the [C2mim][OAc] can infiltrate in between each silk filament, and transform the dissolved fibres into matrix to provide a tightly packed thread core microstructure.

From a WAXD azimuthal scan, a substantial change was observed in the intensity distribution curves of raw silk thread and the randomly oriented coagulated silk matrix, as shown in Figure 4.9b. For the single ASCs, it was found that the average value of P_2 is directly related to the fraction of the original silk fibres and the fraction of the coagulated matrix (randomly oriented structure). The average crystalline orientation of the obtained single ASC was therefore measured by analyzing the azimuthal scan diffraction curves and calculating the 2nd legendre polynomial function (P_2 value). Importantly, the construction of the master curve of the measured P_2 values vs time required only the application of a horizontal shift upon reference data set, which results in a single smooth curve across all temperature sets. The shift factors (ln a_T) were found to follow Arrhenius behaviour with a calculated activation energy of 138 ± 13 kJ/mol. Using a simple rule of mixtures (Equations 4.5 and 4.6), the dissolved silk matrix volume fraction (V_m) was determined from the calculated average P_2 values. It was found that these results can also be shifted to a single master curve with a very similar activation energy of 139 ± 15 kJ/mol.

The mechanical properties of single ASCs obtained from various times and temperatures were also determined, including the ultimate tensile strength, elongation at break and Young's modulus. It was found that the same shifting method can be applied to construct the master curves of Young's modulus (Figure 4.24a),

ultimate strength (Figure 4.27b), and elongation at break (Figure 4.28b). Interestingly, all three master curves imply time-temperature equivalence, and the corresponding shift factors against the respect inverse temperatures all reveal linear relationships, thus indicate Arrhenius-type behaviour. The corresponding activation energies were calculated, have values of 116 ± 12 kJ/mol, 139 ± 19 kJ/mol, and 118 ± 10 kJ/mol, from shifting Young's modulus values, ultimate strength values, and elongation at break values, respectively. The dissolution activation energies measured from the four different methods were found to agree with each other within the errors, giving an average value of 128 ± 6 kJ/mol (recalling Figure 4.29). In addition, the plot of Young's Modulus master curve results of each silk composite filament vs the silk matrix volume fraction master curve results was observed to lie between Voigt and Reuss boundary curves, although much closer to the upper Voigt bound (Figure 4.30). Moreover, the master curve of elongation at break was plotted with respect to the corresponding V_m master curve (Figure 4.31), and found that the fabricated single ASCs not strictly follow the iso-strain conditions, where $\epsilon_c \neq \epsilon_f \neq \epsilon_m$. Lastly, it was found that in our fabricated single ASCs system, the fibre has higher failure strain than the matrix, recalling Table 4.1. The dependence of V_f on the corresponding ultimate strength value was subsequently evaluated (Figure 4.33), and it revealed that the measured tensile strength behaviour obeys the well-established axial tensile failure theory for the system where fibre has higher failure strain (Figures 4.32a and c) [9]. It was further evident that the fibre strength is dominant in determining the ultimate strength of the resulting composites, and suggested that the proper selection of a sufficient amount of fibre volume fraction is crucial for strengthening the composites.

Chapter 5

Addition of Reducing Agent Sodium Sulfite(Na_2SO_3) to the IL to Prepare Single ASCs

5.1 Introduction

In Chapter 4, the dissolution dynamics of single silk threads in pure IL was investigated, the structural, crystalline orientational and mechanical properties of the resultant single ASCs along with the corresponding dissolution activation energies were explored and determined. Recalling section 2.4, it has been acknowledged that ILs as a type of solvent to dissolve silk fibroin owes to their ability to disrupt and break the large amounts of intra- and inter-molecular hydrogen bonds [144, 150]. However, as covered in section 2.3.1, *B. mori* silk fibroin contains H- and L- chains which are covalently linked through a disulfide bond. Interestingly, Yamaguchi, et al. and Tanaka et al. [8, 223] further investigated that there are also intramolecular disulfide linkage in the cysteine residues, recalling section 2.7, Figure 2.10.

As mentioned in section 2.7, the cleavage of disulfide bonds can occur through reduction, with the addition of reducing agents (RA) [272–274], and the extent of reaction can be controlled by temperature, pH and the addition of urea [272, 275]. Various types of reducing agents that are capable of extracting keratin from wool

fibres have been introduced previously in section 2.7, one reducing agent has drawn attention. In 1957, Swan, J.M [213] reported that using Na_2SO_3 with cupric ammonium hydroxide and urea can dissolve 75 % of wool overnight at room temperature. More recently, Ji et al. [214] has reported that Na_2SO_3 can act as an accelerant mixing with ionic liquids to extract keratin from feather, and suggested that it was necessary to add Na_2SO_3 to yield a higher content of keratin from feather. Shavandi et al. [276] also reported that using Na_2SO_3 to conduct the extraction yields a relatively high content of protein, and the reaction is cheaper, less toxic and easier to control compared to other RA, i.e. β-ME. The reported important role of Na_2SO_3 as an accelerant when using ionic liquids to extract keratin from feather inspired the question that this Chapter is aimed to address: will the addition of a reducing agent, Na_2SO_3, as part of the solvent affect the dissolution activation energy and speed of single silk threads?

The chemical structure of the chosen reducing agent, sodium sulfite (Na_2SO_3), is shown in Figure 5.1. Na_2SO_3 is an odorless white, granular or powdered solid and soluble in water. In the past, it was commonly used as bleaching agent in the pulp and paper industry. Nowadays, it is primarily used as an antioxidant (e.g., in the photographic industry to keep developer solutions from oxidizing) and food preservative to prevent dried fruit from discolouring. It is generally recognised as safe when using as a chemical preservative, and no environmental standards or regulations are found for sodium sulfite [277–279].

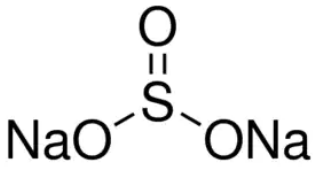

Figure 5.1: The chemical structure of Na_2SO_3 used as reducing agent in this Chapter.

In this Chapter, Na_2SO_3 will be mixed with the ionic liquid [C2mim][OAc],

termed as 'IL/RA system', and will be used as the solvent to conduct the dissolution of single silk threads under various times and temperatures and thus fabricate single ASCs. The IL/RA solvent will also be utilised to prepare silk fibroin solution and cast a silk film. The resultant single ASCs and silk film fabricated from the IL/RA system will be characterised through WAXD and mechanical tests, as described in the previous chapter. In combination with previous results when using pure IL as the solvent (Chapter 4), the effects of RA on the dissolution will be explored, including the dissolution activation energies, the dissolution rates and the influences on the mechanical performance of the resultant single ASCs and silk film.

5.2 Materials and Methods

5.2.1 Materials

Individual degummed single *B. mori* silk threads were initially introduced in section 3.2, and are used as the fibre source again in this Chapter. Sodium sulfite (Na_2SO_3) was purchased from Sigma-Aldrich with a molecular weight of 126.04 g/mol and chosen as the reducing agent in this project. The orientation of nanocrystallites within the partially dissolved single ASCs were then characterised using the WAXD, the detailed operational conditions are identical to those as outlined in section 3.4.3. The mechanical properties were determined using the method as discussed in section 3.5.

5.2.2 Fabrication of Single ASCs using the IL/RA solvent system

Na_2SO_3 was mixed into [C2mim][OAc] at a temperature of 50 °C using a hotplate with a magnetic stirrer for 5 hours, yielding a 5 wt% Na_2SO_3 in [C2mim][OAc]. The obtained IL with 5 wt% Na_2SO_3 was then applied to partially dissolve the single silk threads at various times and temperatures in the vacuum oven, following the same dissolution procedure as introduced in section 4.2.2.

5.2.3 Fabrication of SF Solution and CSF using the IL/RA solvent system

In order to study how the addition of RA influences the coagulated silk film properties, the degummed *B. mori* silk thread was chopped and dissolved in the prepared solvent ([C2mim][OAc] mixed with 5 wt% Na_2SO_3), on a hotplate for 24 hours at 85 °C, while being stirred by a magnetic bead at a speed of 80 rpm. The prepared silk fibroin solution composed of 10 wt% silk fibroin, 5 wt% Na_2SO_3 and 85 wt% [C2mim][OAc]. Next, the prepared SF solution was transferred to the petri dish and followed with the same film casting procedure as described previously in section 4.2.3.

The fabricated film displays a light amber colour with the thickness measured to be ∼38 µm, and was considered as representative of the matrix phase for the single ASCs prepared from IL/RA solvent. Following the protocols introduced in section 3.4, the crystalline structure, orientation of the film was then characterised using the WAXD 2θ and azimuthal scans, respectively. The mechanical performance was investigated using the three-point bending test (see section 3.5.2).

5.3 Results and Discussion

5.3.1 The Measurement of the Average Crystalline Orientation and the Volume of Fraction

In Chapter 4 section 4.3.2, it has already been demonstrated that WAXD azimuthal scan can be used to track the average crystalline orientation within the obtained single ASCs, and the changes can be quantified through measuring the second legendre polynomial (P_2) values. Here, the single ASCs fabricated from the IL/RA system at various times and temperatures were characterised using WAXD azimuthal scans. The numerical integration of the corresponding distribution curves were once again conducted using the Equations 3.1, and 3.2, listed

in Chapter 3.4.3, in order to determine the respective P_2 values. The resulting P_2 values were plotted as a function of both time and temperature, as shown in Figure 5.2a. Similar to what was observed previously for the changes of P_2 values from the pure IL system (Figure 4.11), as the dissolution time and temperature were increased, a corresponding broadly linear decrease was observed in the P_2 values. Therefore, it may imply again that the dissolution of single silk threads in the IL/RA system also obeys the time-temperature superposition principle. Consequently, the same shifting method was again utilised, each temperature set was expressed in natural logarithmic time (Figure 5.2b), and shifted simultaneously to a chosen reference temperature set (40 °C), in order to construct a master curve. The change of P_2 was then plotted in linear dissolution time (Figure 5.2c), and the required shift factors were plotted against their respective dissolution temperatures (Figure 5.2d), as with the previous results, a linear relation was found indicating Arrhenius behaviour and leads to the calculation of the activation energy, giving a value of 121 ± 5 kJ/mol. The detailed instruction of the shifting procedure can be found in Chapter 4, section 4.3.2.

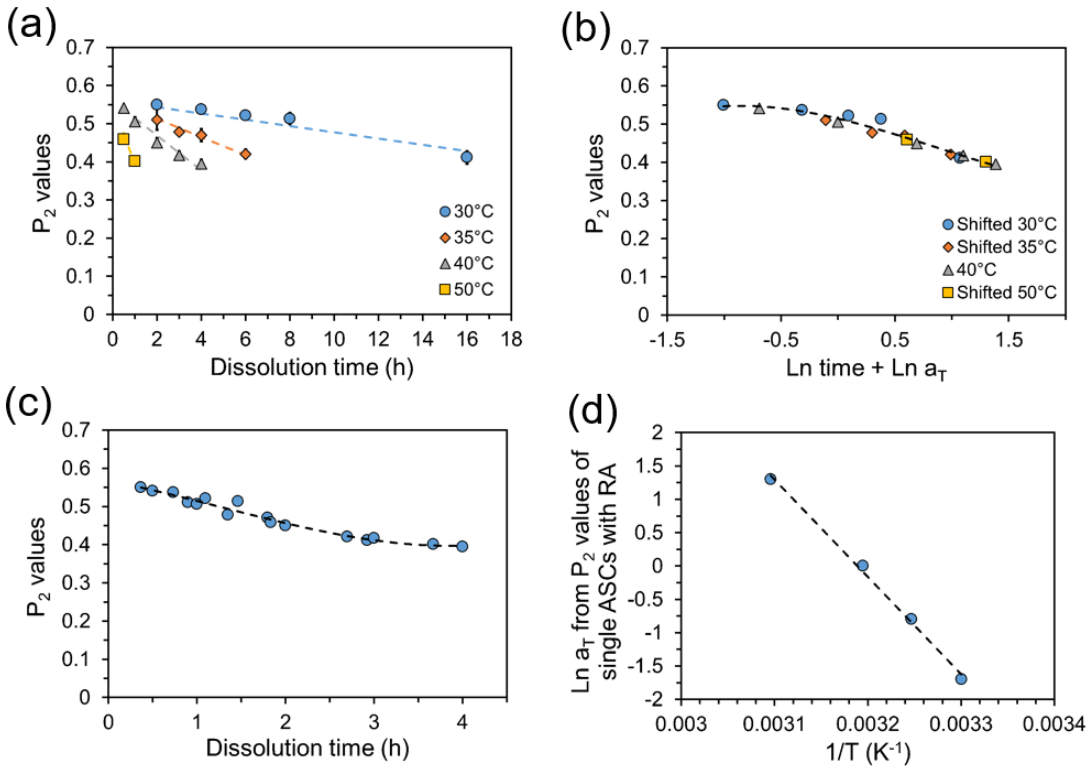

Figure 5.2: (a) P_2 values of single ASCs fabricated in IL/RA at various times and temperatures, n = 3. (b) After applying same shifting method to P_2 values, a best overlap master curve is obtained. (c) P_2 values over linear dissolution time. (d) Shift factors obtained from shifting P_2 values versus $1/T$, a linear relationship was found.

As extensively analysed and discussed prior in section 4.3.3, the amount of the dissolved and coagulated matrix fraction, V_m, displays a linear relationship with the measured corresponding P_2 values, as given in Figure 4.16 and expressed in Equations 4.5, 4.6. Therefore, the discovered relationship is now again utilised in order to calculate the V_m within the obtained single silk composites fabricated from the IL/RA system, and the results are given in Figure 5.3a. The increased time or temperature promotes an increase in the volume fraction of matrix. Next, following the same master curve construction procedure as described earlier for the P_2 results, the obtained V_m values from various temperature sets are displayed

in one master curve (Figure 5.3b), which once again implies that the dissolution obeys time-temperature superimposed. Subsequently, the change of V_m over linear dissolution time is plotted in Figure 5.3c and it is interesting to observe that the V_m values increase relatively fast at early dissolution time (0-1.5 hours) and the rate slows down thereafter. This may again be the indicative of the 'preformed stage', which was observed when single silk threads dissolved in pure IL system, recalling section 4.3.4, Figures 4.21, 4.22, 4.26. Moreover, the shift factors versus the corresponding inverse temperatures is plotted in Figure 5.3d, once again demonstrating a linear relationship and thus, an Arrhenius-like behaviour.

The dissolution activation energy was calculated from the gradient of the V_m Arrhenius plot (Figure 5.3d) and found to have a value of 121 ± 5 kJ/mol, which is identical to the E_a calculated by following the P_2 changes (Figure 5.2d).

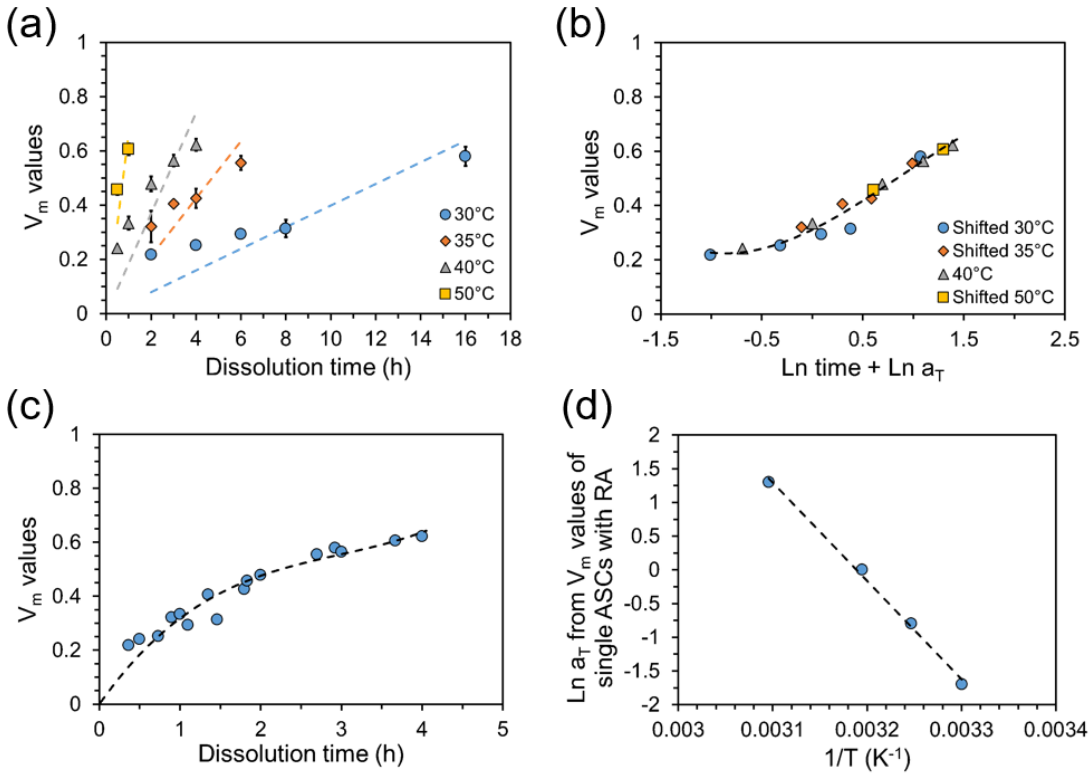

Figure 5.3: (a) Volume fraction of matrix values of single ASCs fabricated in IL/RA, n = 3. (b) Shifting different temperature sets of V_m values towards the reference temperature set (40 °C here), generated as a master curve in ln space. (c) V_m changes over a linear dissolution time. (d) Shift factors obtained from constructing V_m master curve, plotted versus $1/T$.

5.3.2 Mechanical Properties

The mechanical properties of the single ASCs dissolved in IL/RA are determined by tensile tests. The stress-strain curve for one representative single ASC (obtained from 40 °C - 1 hour) prepared from IL/RA system is shown in Figure 5.4. Figures 5.5a and 5.6a show how the modulus and strength vary as a function of time for different temperatures, respectively. It is interesting to see that both parameters display an initially increase to a maximum value at the early dissolution temperature (35 °C), and decrease with time thereafter. This trend is a clear indication of the 'preformed stage', as observed when single silk threads dissolved in pure IL system (recalling Figures 4.21, 4.22, 4.26), that the specific structure of the raw silk multifilament thread results in large gaps between each silk filament and there is a certain dissolution time needed to allow each filament dissolved and coagulated to form a close-packed thread core and conduct a sufficient stress transfer, detailed explanation can been found from the previous discussion, in Chapter 4, section 4.3.4.

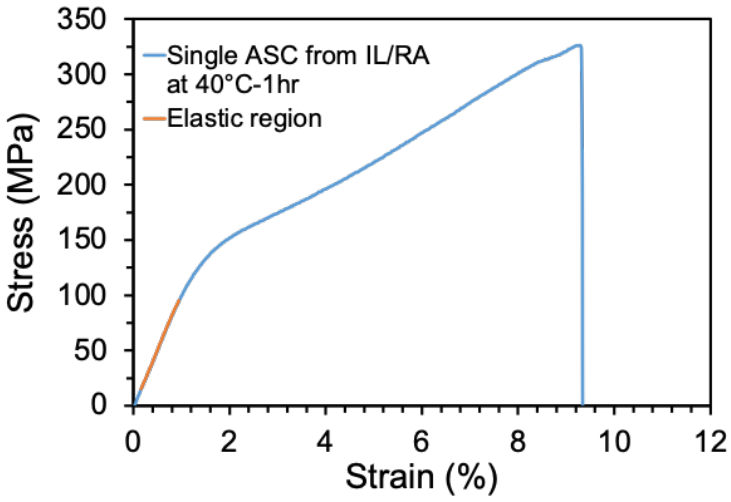

Figure 5.4: Stress-strain curve for single ASC obtained from IL/RA system at 40 °C for 1 hour.

Subsequently, applying the time-temperature superposition shifting method

to the determined modulus and strength can provide an additional quantitative measure of the dissolution activation energies, and thus to compare with the E_a values measured from P_2 and V_m measurements, as described above. Therefore, the same shifting method is once again applied, to both the modulus and strength values. The data corresponding to the 'preformed stage' was removed from the data set in order to generate a master curve only for the continuous dissolution after the matrix gel layer has formed. The complete master curves for modulus and strength are given in Figures 5.5b and 5.6b, respectively, whilst Figures 5.5c and 5.6c indicate the changes of modulus and strength with respect to a linear dissolution time. The Young's modulus, similar to the strength values, decreases with the increased dissolution time. The shift factors required to generate the master curves of Young's modulus and strength, are plotted as a function of their respective dissolution temperatures, as shown in Figures 5.5d and 5.6d, respectively. The clear linear relation can be found from the graphs, which suggests that the dissolution follows the Arrhenius behaviour, and thus leads to the measurement of dissolution activation energies.

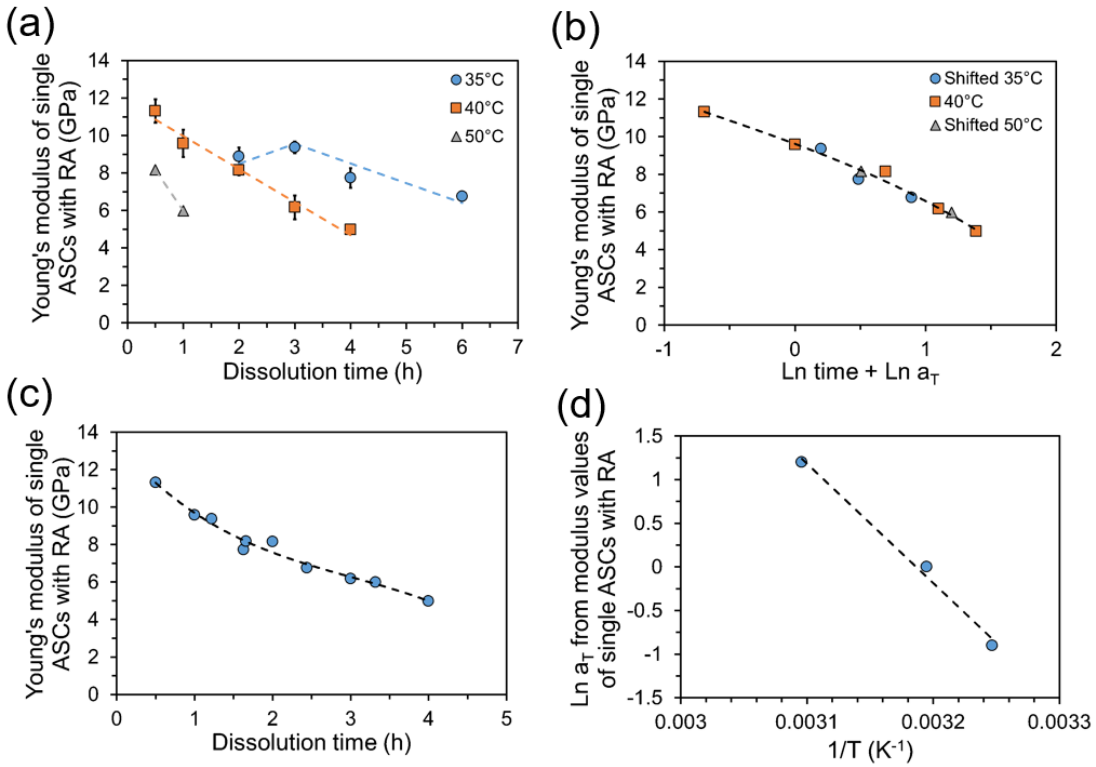

Figure 5.5: (a) Young's modulus values for each obtained single ASC fabricated in IL/RA, n = 2. (b) Shifted master curve of Young's modulus values. (c) The master curve of Young's modulus for single ASCs fabricated in IL/RA under a reference temperature at 40 °C. (d) The shift factors obtained from shifting Young's modulus master curve versus $1/T$.

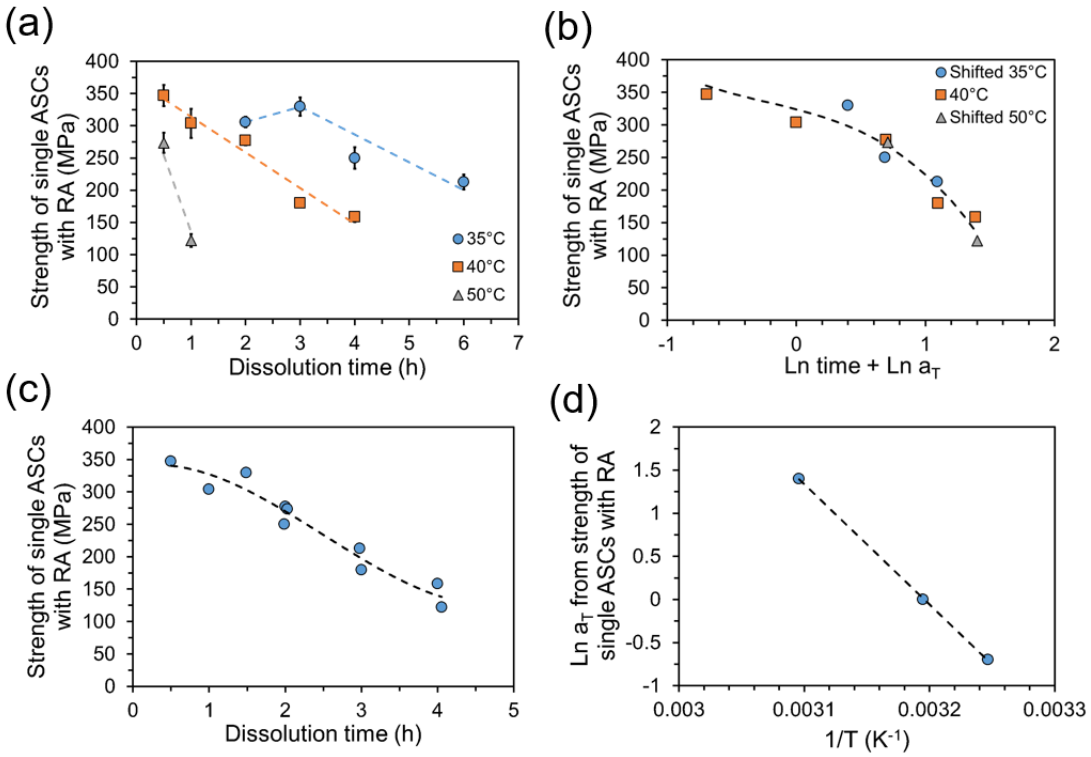

Figure 5.6: (a) Ultimate strength values for each obtained single ASC fabricated in IL/RA, n = 2. (b) Shifted master curve of ultimate strength values. (c) The master curve of ultimate strength for single ASCs fabricated in IL/RA under a reference temperature at 40 °C. (d) The shift factors obtained from shifting ultimate strength master curve versus $1/T$.

Additionally, the strain at failure values of single ASCs fabricated from IL/RA were also calculated from the respective stress-strain curves, and presented in Figure 5.7a, with respect to a range of dissolution times and temperatures. As the dissolution appeared to follow time-temperature superposition principle, the simultaneous effect of time and temperature on the breaking strain when using reducing agent is expressed as a master curve and seen in Figure 5.7b, alongside with the changes of breaking strain over linear dissolution time (Figure 5.7c) and the resulting Arrhenius plot (Figure 5.7d). Similar to the previously observed changes of breaking strain for single ASCs fabricated from pure IL system (Figure 4.28c), the failure strain of fibre is much higher than that of matrix (as expressed

in Table 4.1), which leads to the immediate reduction of the composite breaking strain values from the start of the dissolution. The previous plot of breaking strain value versus the respective V_m demonstrated in Figure 4.31 further evidence this observation.

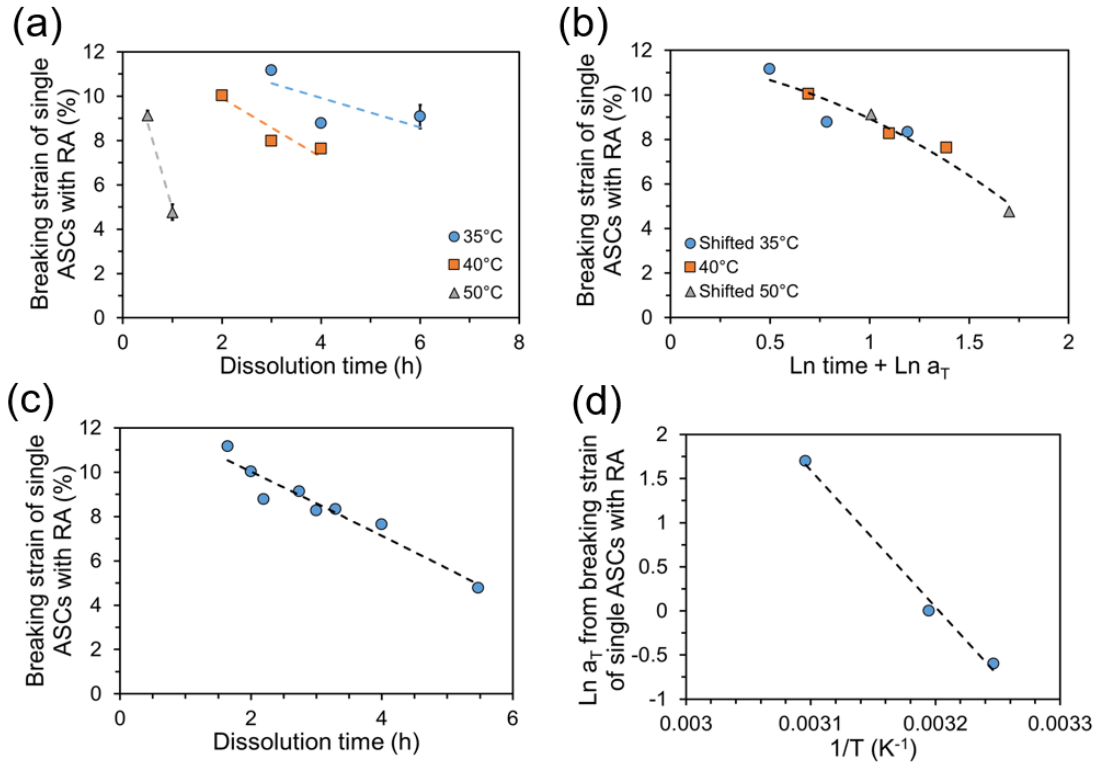

Figure 5.7: (a) Strain values for each obtained single ASC fabricated from IL/RA, n = 2. (b) Shifted master curve of strain values. (c) The master curve of strain for single ASC fabricated in IL/RA under a reference temperature at 40 °C. (d) The shift factors obtained from shifting strain master curve versus $1/T$.

The dissolution activation energies measured from the modulus, strength and strain were found to be 114 ± 11 kJ/mol, 116 ± 1 kJ/mol and 129 ± 12 kJ/mol, respectively. All of the calculated energies are within the errors of the E_a values determined previously from the P_2 and V_m methods, and lead to an average value of 120 ± 3 kJ/mol. Figure 5.8 further highlights the consistency of the measured activation energies from 4 different methods.

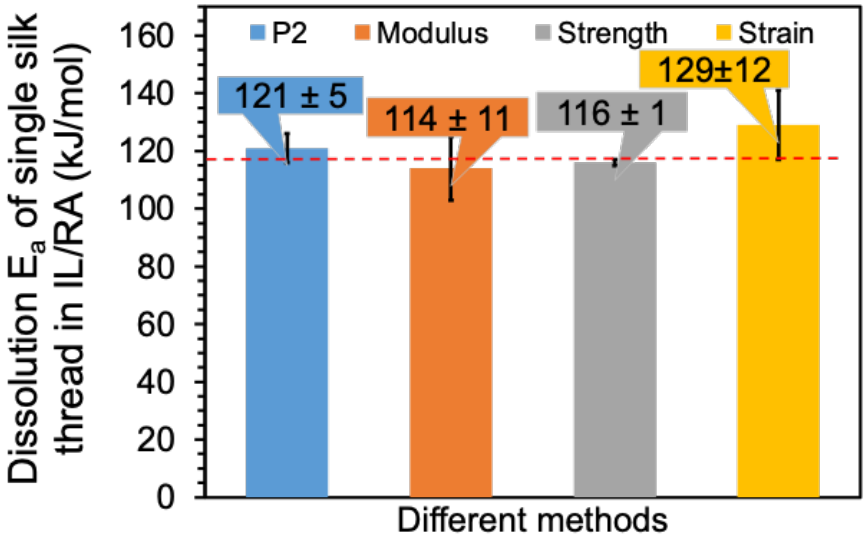

Figure 5.8: A graph to summarise the dissolution activation energies of single silk threads dissolved in IL/RA system, measured through four different methods, horizontal dashed line indicates the average value, which goes through all measurements within their error bars.

5.3.3 Effects of Reducing Agent on the Dissolution

Firstly, Table 5.1 shows the comparison of the calculated dissolution activation energies between two solvent systems, determined from four different methods. It is clear that adding RA to IL appears to require a slightly lower average E_a for the dissolution to occur. Nevertheless, the measured average E_a for two solvent systems are close to each other, though a marginally lower E_a was found for IL/RA system (120 ± 3 kJ/mol) comparing to pure IL system (128 ± 6 kJ/mol).

Method	E_a for pure IL (kJ/mol)	E_a for IL/RA (kJ/mol)
P_2	138 ± 13	121 ± 5
Young's modulus	116 ± 12	114 ± 11
Ultimate strength	139 ± 19	116 ± 1
Breaking strain	118 ± 10	129 ± 12
Average	128 ± 6	120 ± 3

Table 5.1: The dissolution activation energies for single silk threads dissolved in the pure IL and IL/RA systems, measured through four different methods.

As covered in section 5.1, the reducing agent is able to alter the secondary and tertiary structures of proteins through introducing the intramolecular interactions and intermolecular interactions between the polypeptides [280]. More specifically, Na_2SO_3 as a reducing agent can inhibit free thiol groups and break down disulfide bonds, as expressed in Equation 5.1 [281, 282]. It is well documented that in this redox reaction, sulfite transforms the disulfide bridges into two sulfonate groups, and the reaction is reversible in the presence of an oxidising agent [213, 283].

$$R - S - S - R + SO_3^{2-} \rightleftharpoons RS^- + RS - SO_3^{2-} \tag{5.1}$$

It is expected that with the addition of Na_2SO_3, there is a chance to promote the cleavage of the inter- and intramolecular disulfide bonds present in the silk fibroin, as shown in Figure 2.10. Importantly, the literature has reported that the covalent disulfide bridges have a highest bond strength of the various interactions, with a bond strength of 230 kJ/mol, compared to the strength of electrostatic interactions (21 kJ/mol) and hydrogen bonds (15 kJ/mol) [284, 285]. Consequently, the observed slightly lower E_a from the IL/RA system with respect to the pure IL system (Table 5.1), may be due to the presence of Na_2SO_3 takes part in the breakage of inter- and intramolecular disulfide bonds, hence lowers the total energy barrier to be overcome for the occurrence of dissolution reaction.

Next, the effects of the reducing agent on the dissolution rates of single silk threads processed from pure IL and the IL/RA systems are compared. The idea here is to plot the constructed master curves expressed in logarithmic time, for pure IL and IL/RA systems together in one graph. The amounts of the master curves from the IL/RA system required to be horizontally shifted, to make the best overlap with the pure IL system master curve, yields a direct measure of the relative dissolution rates. Subsequently, this analysis method was first utilised to evaluate the effects on the P_2 and V_m values, the respective master curves from pure IL and IL/RA systems (P_2-Figures 4.13 and 5.2b, V_m-Figures 4.18b and

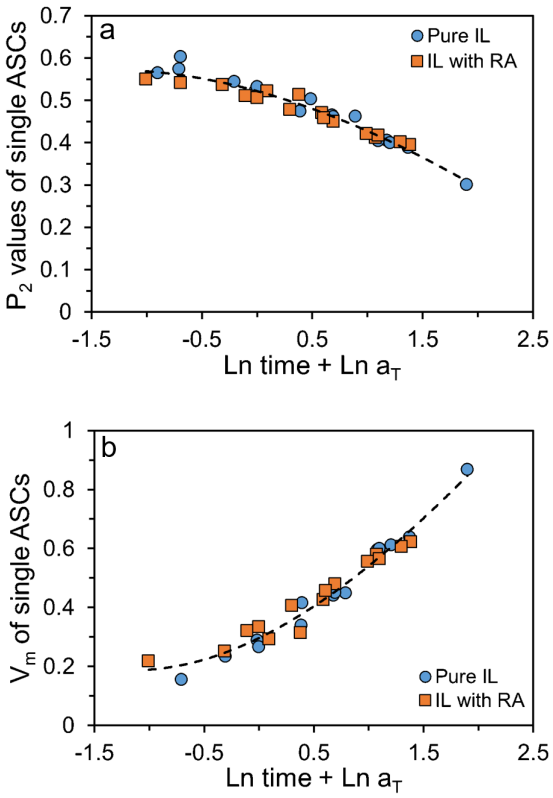

Figure 5.9: Master curves of pure IL and IL/RA systems, obtained from (a) the measurement of P_2, (b) the measurement of V_m. Data sets from both systems are shifted to a reference temperature of 40 °C. Polynomial fitting curves are guide to eye.

5.3b) were individually presented in the same graph, as given in Figures 5.9 a and b.

Interestingly, with no shifting needed, the master curves of P_2 and V_m from two systems display the same trend and being naturally overlapped, which implies that there is no change on the dissolution rates when adding the reducing agent.

It has been suggested from the P_2 and V_m values that the dissolution rates remain unchanged after adding RA, however it is still worth to investigate the influences of RA on the mechanical performance. Accordingly, the master curves of Young's modulus, strength and strain at linear dissolution time derived from pure IL system (Figures 4.24c, 4.27c, 4.28c) were individually plotted in the same graph along with that from IL/RA system (Figures 5.5c, 5.6c, 5.7c). The resulting curves are shown in Figures 5.10 a,b,c. It is observed that all three parameters from IL/RA system consistently display greater values than that from pure IL system because of vertically shifting is needed to make pure IL master curve to overlap with IL/RA master curve. Therefore, it is suggested that when adding RA as part of the solvent, the resultant single ASCs demonstrate a improved mechanical performance with respect to that from pure IL system.

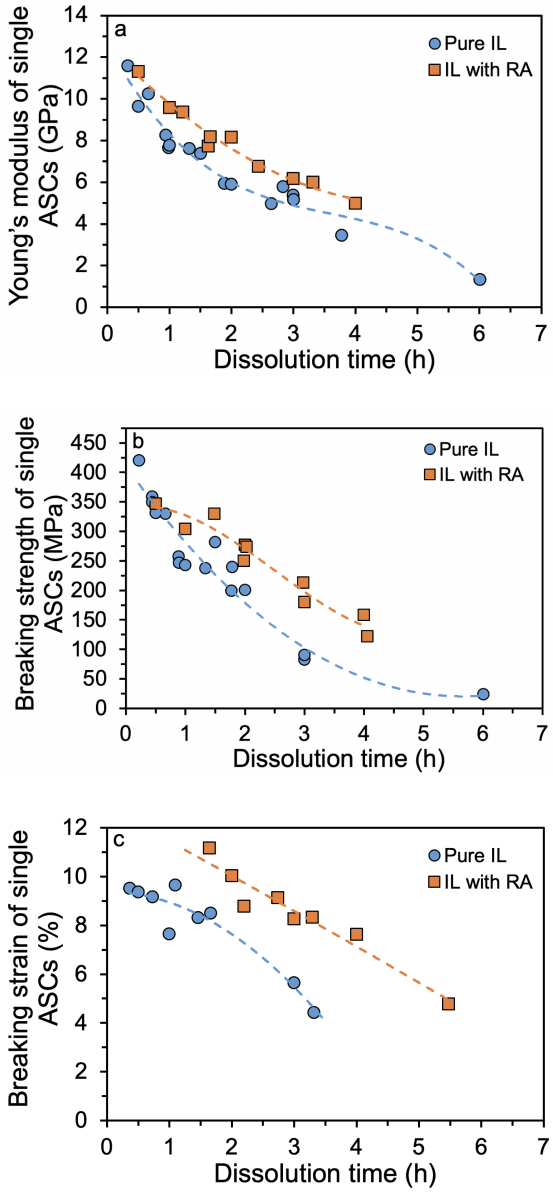

Figure 5.10: Master curves of pure IL and IL/RA systems, obtained from the measurements of (a) Young's modulus, (b) breaking strength, (c) strain. Data sets are the constructed master curves in linear dissolution time after shifting to the reference temperature at 40 °C. Polynomial fitting curves are guide to eye.

It is therefore worth to discover the possible reasons that might contribute to the observed enhanced mechanical performance. As suggested by the well documented rule of mixture theory [9], the overall composite stress is contributed by the stress of two phases, σ_{fibre} and σ_{matrix}, as expressed in Equation 4.7. Moreover, it is expected that for single ASCs fabricated from two solvent systems, σ_{fibre} values are identical because it represents the stress of raw silk thread (0 hour of dissolution). However, due to the silk films were cast from two solvent systems (recalling sections 4.2.3 and 5.2.3), it is possible that two films, and hence the two composite matrix phases have different properties, including different σ_{matrix} values, thus leading to the difference in the $\sigma_{composite}$ values, as seen in Figure 5.10a.

Consequently, the properties of the two silk films (matrix phases) cast from pure IL and IL/RA systems are compared, of which the WAXD 2θ scan diffraction curves are shown in Figure 5.11 and the mechanical properties are listed in Table 5.2. It is noted that the two diffraction curves in Figure 5.11 were normalised to give the same total area under the curves. Almost identical spectra are observed, which suggests that the crystalline structure of the films remain unchanged.

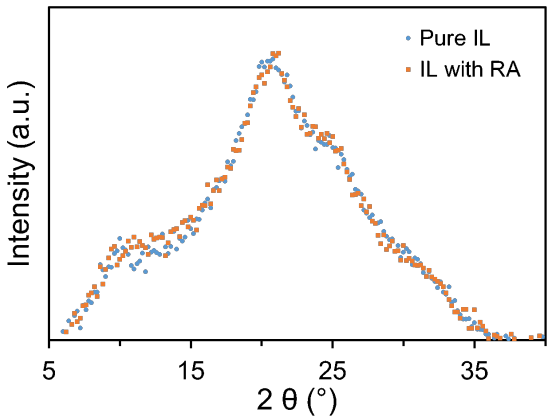

Figure 5.11: WAXD 2θ scan diffraction curves of silk fibroin films cast from pure IL and IL/RA systems.

Furthermore, the tensile stress-strain curves of silk fibroin films cast using two different solvent systems are given in Figure 5.12, along with the corresponding tensile properties presented in Table 5.2. It can be observed that the average Young's modulus values for two films remains unchanged, whilst greater strength and elongation values are observed for the film cast from the IL/RA system. Hence, as mentioned earlier (ROM theory [9]), it is expected that the increased in both the breaking strength and breaking strain values of the films (matrix phase) directly contribute to the rise in the overall composite mechanical performance, as seen in Figures 5.10b and c. However, the underlying reasons for the observed increased Young's modulus for the composites (Figure 5.10a) are currently not known. However, it is acknowledged in the literature that the ultimate strength of composite largely depends on the bonding strength [286, 287]. The observed increased strength of the single ASCs from IL/RA, is indicative of the possibility for the enhanced bonding strength within the composite, which warrants further studies.

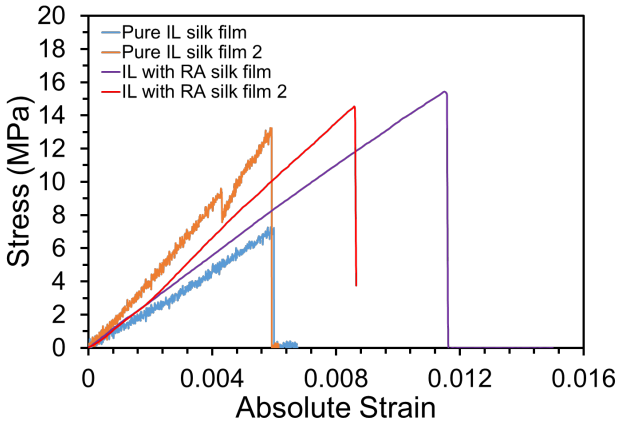

Figure 5.12: Stress-strain curves of silk fibroin films cast from pure IL and IL/RA systems.

	Strength(MPa)	Elongation(%)	Young's modulus(GPa)
Film from pure IL	10 ±2	0.60 ±0.01	1.6 ±0.3
Film from IL with RA	15.0 ±0.3	1.0 ±0.1	1.6 ±0.2

Table 5.2: The mechanical properties of films cast from pure IL and IL/RA systems, n = 2.

Lastly, it has been discovered in the last Chapter that the plot of Young's modulus as a function of the corresponding V_m along with two ROM boundary lines can be employed to study the difference between experimental and theoretical mechanical performance, in particular the effectiveness of the fibre-matrix interfacial bonding. Therefore, ROM curve for single ASCs obtained using pure IL and IL/RA systems is plotted to investigate the influence of reducing agent on the interfacial bonding, as presented in Figure 5.13. It is observed that the master curve of IL/RA system exhibits a closer fit to the theoretical Voigt series, implying a better stress transfer within the single ASCs fabricated from the IL/RA system. Schmid et al. [288] reported that the cleavage of disulfide bonds with reducing agent introduces a more flexible peptide chain structure, of which the peptide chains are easier to glide along each other, thus the cast film became more elastic. Moreover, Asloun et al. [289] has suggested that elastomeric matrix provides a far better stress transfer than a thermosetting or a thermoplastic matrix, and the increase in the mobility of the polymer matrix chains attributes to a better stress transfer. Therefore, the observed enhanced stress transfer from IL/RA system (Figure 5.13) is considerably contributed by the observed increase in the strength and elongation of the corresponding silk film. In combination with the observed overall mechanical properties of the composites (Figure 5.10) and SF film properties (Table 5.2), it can be concluded that the addition of RA improves the overall mechanical performance of the composites and matrix phase (silk film), whilst providing an enhanced stress transfer between fibre and matrix, thus a better bonding. However, this may raise further questions, such as can the effects of RA on the bond strength be quantified through conducting fibre pull-out tests or peel tests on two layers woven all silk composites. Such questions warrant the future in-depth investigation.

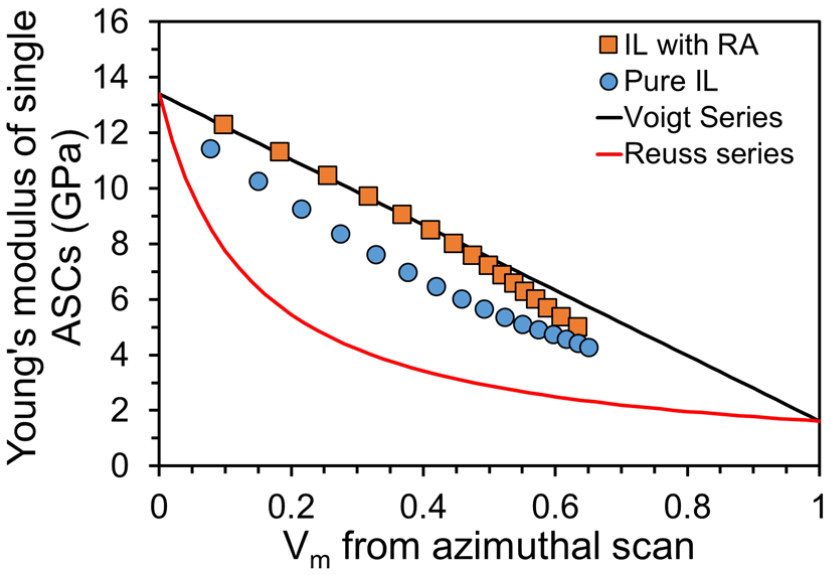

Figure 5.13: Rule of mixture plot for the single ASCs fabricated from pure IL and IL/RA systems.

5.4 Summary

In this Chapter, the dissolution behaviour of single silk threads by using the mixture of the ionic liquid [C2mim][OAc] and reducing agent Na_2SO_3 as solvent, methanol as coagulant was explored. The properties of the resultant single ASCs were studied through a combination of the average crystalline orientation, volume fraction of matrix and mechanical performance measurements.

Comparing with the results from single silk threads dissolved in pure IL solvent system (section 4.3), here similar observations have been found, the average orientation of nanocrystallites within the obtained single ASCs, expressed as P_2 values, decrease as a function of both dissolution time and temperature. The proposed linear mixing rule was once again employed to correlate the P_2 values with the respective V_m values, of which V_m values were seen to increase linearly with time and temperature, and higher temperatures cause a more rapid rise. In addition, the measured strength, modulus and strain values display similar

trends. Interestingly, both modulus and strength values undergo the same trend where they initially increase to the maximum value and drop thereafter. As observed and explained previously for single silk threads dissolved in pure IL system, likewise, this phenomenon would expect to associate with the 'preformed stage' happened during the early dissolution times.

The time and temperature equivalence on the determined parameters, P_2, V_m, Young's modulus, strength and elongation were verified by shifting the individual set of data in natural logarithmic time and generating the master curves. From which, it was evident that the dissolution also follows time-temperature superposition principle even when using the IL/RA as the solvent. Subsequently, the shift factors used to construct each master curve were separately plotted with respect to their inverse temperatures, linear relationships were clearly found, which leads to the indication of Arrhenius behaviour. Thus, the activation energies were calculated from 4 different methods, of which it was found that the four activation energies agreed with each other within the error of the measurements, giving to an average value of 120 ± 3 kJ/mol (Figure 5.8).

Next, the effects of the addition of Na_2SO_3 as part of the solvent on the dissolution of single silk threads were investigated. Firstly, adding RA as part of the solvent appeared to require a marginally lower E_a than pure IL system (Table 5.1). This may be due to Na_2SO_3 being able to break down the inter- and intramolecular disulfide bonds in silk fibroin, of which has a high bond strength (230 kJ/mol). Thus it may lower the energy barrier to be overcome in order to trigger the dissolution. Then, to compare the dissolution rates from two solvent systems, master curves in logarithmic time of four different measured parameters in this Chapter were individually plotted together with those master curves from the pure IL system. The relative dissolution rates were thus regarded as the amount needed to be horizontally shifted to make the two master curves have the best overlap. Interestingly, master curves of the measured P_2 and V_m from two solvent systems were naturally overlapped without any shifting needed (Figure 5.9). Therefore, it suggests that there is no change in the dissolution rates after adding RA as part of solvent. Meanwhile, the master curves of the tensile

properties imply that single ASCs fabricated from the IL/RA system have better mechanical performance than that from pure IL system (Figure 5.10). Additionally, the silk fibroin film cast from IL/RA system was measured to have higher strength and elongation at failure values than that from pure IL system (Table 5.2), which further validates the observed increased mechanical performance for the single ASCs (in alliance with the rule of mixture theory). Lastly, ROM curve (Figure 5.13) was employed to explore the effect of RA on the interfacial bonding for the resultant single ASCs. From which, it was found that data from IL/RA system displays a closer fit to the Voigt series which suggests there is improved stress transfer between fibre and matrix. This finding is considerably contributed by the observed increase in strength and elongation of the silk film (matrix phase), thus it introduces a better interfacial adhesion. Based on these observations, it is concluded that the single ASCs fabricated from the IL/RA system exhibit a increased overall mechanical performance, higher strength and more ductile silk film as well as a better stress transfer between fibre and matrix. This study hopefully provides a basis for the research focused on silk based composites materials, especially the need for the improvement on the ductility of coagulated silk film and the overall mechanical properties.

Chapter 6

The Properties of Array All-Silk Composites Fabricated in the Ionic Liquid 1-Ethyl-3-Methylimidazolium Acetate

6.1 Introduction

The dissolution dynamics of single silk threads using pure IL has been intensively investigated in Chapter 4. The dissolution behaviour has been quantified by the calculation of the activation energy using the time-temperature superposition principle, and the mechanical performance of all silk composites reinforced by single silk threads has been investigated.

Here in this Chapter, the study has been extended to understand the dissolution behaviour of silk fibres in a different arrangement, termed as 'array silk threads', where multiple single silk threads will be closely aligned in parallel in order to provide an increased effective fibre diameter. There has been considerable research into the influences of fibre length and diameter [290–292], fibre packing arrangement [293–296] and also the fibre shape and distribution [297–299] on the

overall composites' mechanical responses. Similar to the studies carried out on the single silk threads, the dissolution of array silk threads will be carried out with excess amount of pure [C2mim][OAc] under a series of time and temperature followed by coagulating in methanol. All silk composites reinforced by array silk threads (array ASCs) will therefore be fabricated.

As covered above, it is likely that the change of fibre geometry would result in a different constitutive structure for the growth orientation of matrix phase during coagulation. Hence, the effects of fibre arrangement on the dissolution behaviour, and the properties of the resulting array ASCs will be established. The two main questions to be investigated in this Chapter are: (i) Does the fibre arrangement change the speed of the dissolution of silk fibres? (ii) Does the fibre arrangement affect the dissolution activation energy? The studies carried on the arrays of silk threads aims to build a bridge of understanding the dissolution dynamics between two silk fibre architectures - single silk threads as reported previously in Chapter 4 and the woven silk fabrics, which will be explored in Chapter 7.

6.2 Experiments and Methodology

6.2.1 Materials

Materials including fibre source, solvent and the coagulant were previously introduced in section 3.2. The fabrication procedure for preparing array all silk composites will be introduced in section 6.2.2 below.

6.2.2 Fabrication of Array All Silk Composites (ASCs)

Figure 6.1 schematically presents the detailed fabrication procedure for preparing array ASCs. Similar to the procedure as described in section 4.2.2, here 20 single

silk threads were aligned together in parallel and closely wound around the same Teflon frame. Upon fixing the array silk threads to the frame, the frame was then submerged in the Teflon dish filled with preheated [C2mim][OAc], yielding a 0.3 % w/v (silk thread to IL). Then the array silk threads were partially dissolved at different lengths of time at 30, 35, 40, 50 °C, following the same dissolution, coagulation and drying procedures as introduced in section 4.2.2.

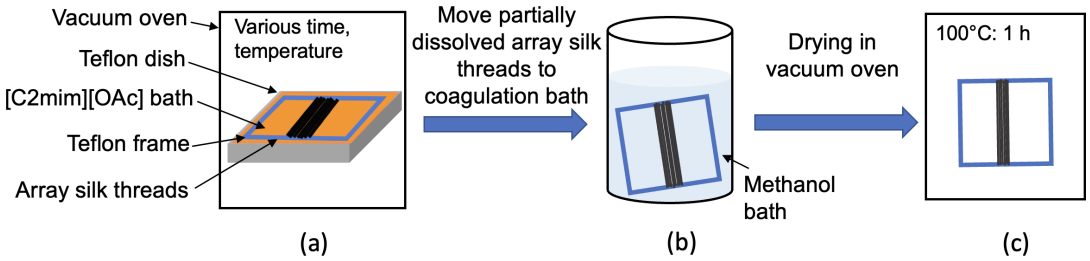

Figure 6.1: A schematic diagram to show the array all silk composite fabrication process, starting from (a) dissolution, then (b) coagulation, (c) then finally drying in vacuum oven.

6.3 Results and Discussion

Following the procedure outlined in section 6.2.2, the orientation of nanocrystallites within the prepared array ASCs were characterised using WAXD azimuthal scans, following the operational conditions as described in section 3.4.3. The partially dissolved and coagulated array silk threads were thus quantified by following the changes in the orientation factor, P_2 values. In addition, the tensile properties of each array ASC were tested using the method as introduced in section 3.5, and the findings are discussed below.

6.3.1 Characterisation of the Average Crystal Orientation within Array ASCs

In order to determine the orientation changes of nanocrystallites within the array ASCs fabricated under various times and temperatures. The second legendre polynomial function (Equations 3.1 and 3.2) was again applied to quantify the experimentally measured intensity distribution of the diffraction on the Debye ring. Figure 6.2a shows the corresponding calculated average P_2 values for each obtained array ASC. It is worth mentioning here, that the average P_2 value should be equal to 0.25 for a random 2D isotropic distribution, and equal to 1 for a perfect alignment. Figure 6.2a indicates P_2 values undergo a similar trend as previously observed when dissolving single silk threads, where the P_2 values reduce linearly with dissolution time and temperature, and the same P_2 value can be achieved at longer dissolution time or higher dissolution temperature. This trend is similar to the observed changes of P_2 for single ASCs. Thus, it would be of interest to apply the time-temperature superposition principle to combine the relationship between dissolution time and temperature into one master curve. Here, the same shifting method (as introduced in section 4.3.2) is utilised to superimpose various temperature sets toward the reference set (chosen at a temperature of 40 °C). A master curve for P_2 values with ln time shifted to 40 °C is illustrated in Figure 6.2b. Different values of shift factors ($\ln a_T$) were obtained from shifting different temperature data sets. Next, the change of P_2 values over linear dissolution time for the array silk threads dissolved in [C2mim][OAc] can be seen in Figure 6.2c. It can be observed that under 40 °C, the reduction of the orientation of nanocrystallites happens fast initially (0-3 hours of dissolution), and slows down afterwards.

As shown in Figure 6.2d, the shift factors ($\ln a_T$) are plotted with respect to the inverse of the processing temperature. Despite small differences between the shift factors obtained from the 30 °C and 35 °C data sets, a linear relationship can be seen and the dissolution energy of array silk threads in [C2mim][OAc] was thus calculated, to have a value of 121 ± 20 kJ/mol.

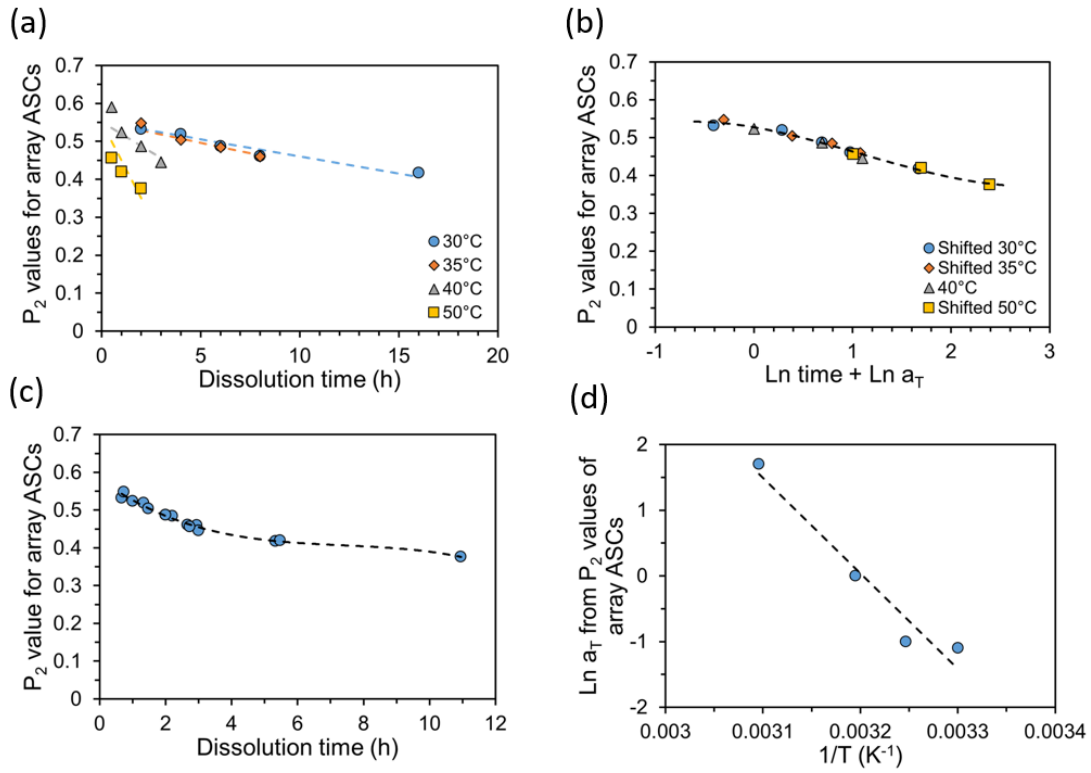

Figure 6.2: (a) P_2 values of array ASCs obtained from various times and temperatures, n = 3. (b) After applying same shifting method to P_2 values, master curve in ln space is obtained. (c) P_2 values versus linear dissolution time, at a reference temperature of 40 °C. (d) its shift factors plotted versus $1/T$.

6.3.2 Measurement of the Volume fraction of matrix (V_m) within array ASCs

As explored in previous Chapters, the coagulated matrix fraction is mathematically related to the P_2 value, recalling Figure 4.16. It was evident that the dissolution continuously changes the preferred aligned crystal orientation (raw silk fibre) and turns into a randomly distributed orientation (coagulated film). Therefore, by following a simple rule of mixtures (Equations 4.5 and 4.6), and the

experimentally measured P_2 values for the raw silk thread (0.62, previously calculated in section 4.3.3) and coagulated film (0.25, determined from WAXD scan on film); the V_m of array ASCs fabricated from various times and temperatures can thus be calculated. As seen in Figure 6.3a, the V_m values increase linearly with time and do so more rapidly at higher temperatures. Next, by following the same shifting method as described in section 4.3.2, the master curve for the variation of the V_m of the array ASCs with ln time shifted to 40 °C was constructed, as shown in Figure 6.3b. As seen in Figure 6.3c, which shows the increase of V_m with linear time, V_m values initially increased rapidly and started to slow down from 3 hours dissolution at 40 °C. This behaviour is once again indicative of the proposed 'preformed stage', which was also observed when dissolving single silk threads using either pure IL or IL/RA as the solvent. It is interesting to note that master curves of P_2 (Figure 6.2) and V_m (Figure 6.3c) are almost mirror-like images, as expected.

Finally, the determined shift factors ($\ln a_T$) were plotted against the respective inverse temperatures, as seen from Figure 6.3d. A linear relationship was clearly found, again confirming that the dissolution follows Arrhenius behaviour and the activation energy was thus calculated from the gradient of the line, with a value of 121 ± 20 kJ/mol. This E_a value determined by following the changes of V_m is identical to the one calculated using P_2 method, which arises because these two parameters are mathematically related to one another.

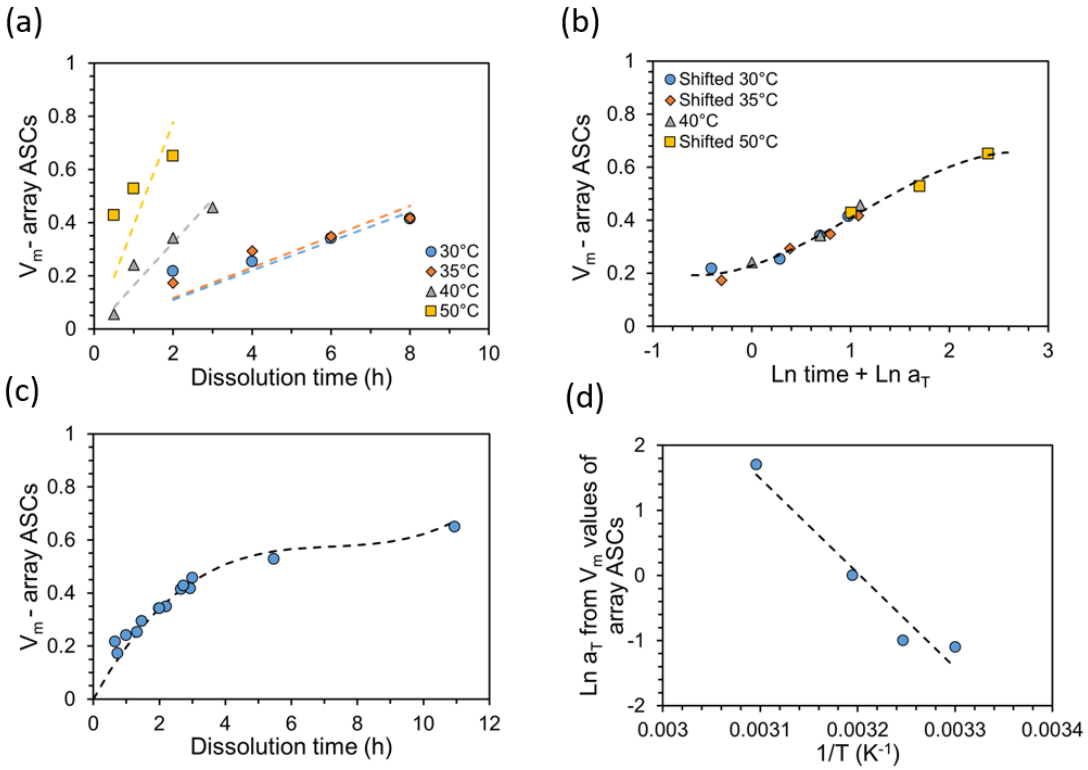

Figure 6.3: (a) V_m values for array ASCs obtained from various times and temperatures, n = 3; (b) its master curve in ln space; (c) its master curve at linear dissolution time, at a reference temperature of 40 °C; (d) its Arrhenius plot.

6.3.3 Mechanical Properties of Array ASCs

Tensile tests were performed to measure the tensile properties of the array ASCs obtained from various dissolution times and temperatures. Figure 6.4 shows the stress-strain curve for one array ASC obtained at 35 °C for 2 hours. The experimentally measured Young's modulus, breaking strength and elongation at break values are shown in Figures 6.5a, 6.6a and 6.7a, respectively. It would be expected that under same processed temperature, longer dissolution time would result in a decrease in the mechanical performance because of the reduction in

the total amount of the reinforcing fibres. In fact, this can be seen from the 50 °C data sets, where the Young's modulus, strength and elongation at break values continuously decreased with increasing dissolution time. Conversely, all three determined tensile properties from 35 °C and 40 °C data sets consistently demonstrate an initial increase to a maximum value at early dissolution times and decrease thereafter. This once again implies the 'preformed stage', as previously seen from P_2 and V_m measurements. Due to the specific structure of raw single silk thread, there are large gaps between each filament that would allow [C2mim][OAc] to penetrate through during early dissolution times. When sufficient amount of silk fibres are dissolved by [C2mim][OAc] and transformed into matrix, the spaces will then be filled up and form a close-packed thread core, thus restricting the solvent to dissolve only from the outer layer of silk filaments. The results here suggest that this phenomenon also happens when arrays of silk threads are dissolved by [C2mim][OAc].

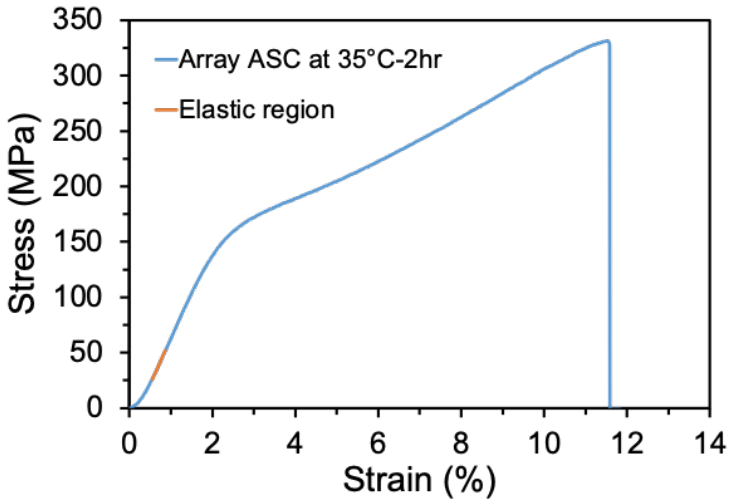

Figure 6.4: Stress-strain curve for array ASC obtained from IL system at 35 °C for 2 hours.

It is of interest to see if the variation of the Young's modulus, breaking strength and elongation at break values for the array ASCs also obey time-temperature

superposition principle. In order to construct the best master curve, the data points before the preformed stage were removed. Figure 6.5b demonstrates the shifted master curve of Young's modulus values for array ASCs after applying the same shifting method, again using 40 °C as reference temperature. The construction of master curve indicates the modulus values obtained from different temperatures are related to one another by certain shift factors. Next, by converting the x-axis into linear dissolution time, it can be seen, from Figure 6.5c, the Young's modulus values decrease rapidly, at first 3 hours of dissolution, and slows down at longer dissolution time. This is similar to the changes of P_2 values for array ASCs, as mentioned above (Figure 6.2c). This is not surprising since the orientation of nanocrystallites is one of the factors controlling the Young's modulus values of the obtained array ASCs. Figure 6.5d shows the plot of the determined shift factors against $1/T$, is again found to be linear, following Arrhenius behaviour. Thus, the dissolution activation energy was calculated from the gradient of the curve, has a value of 135 ± 15 kJ/mol.

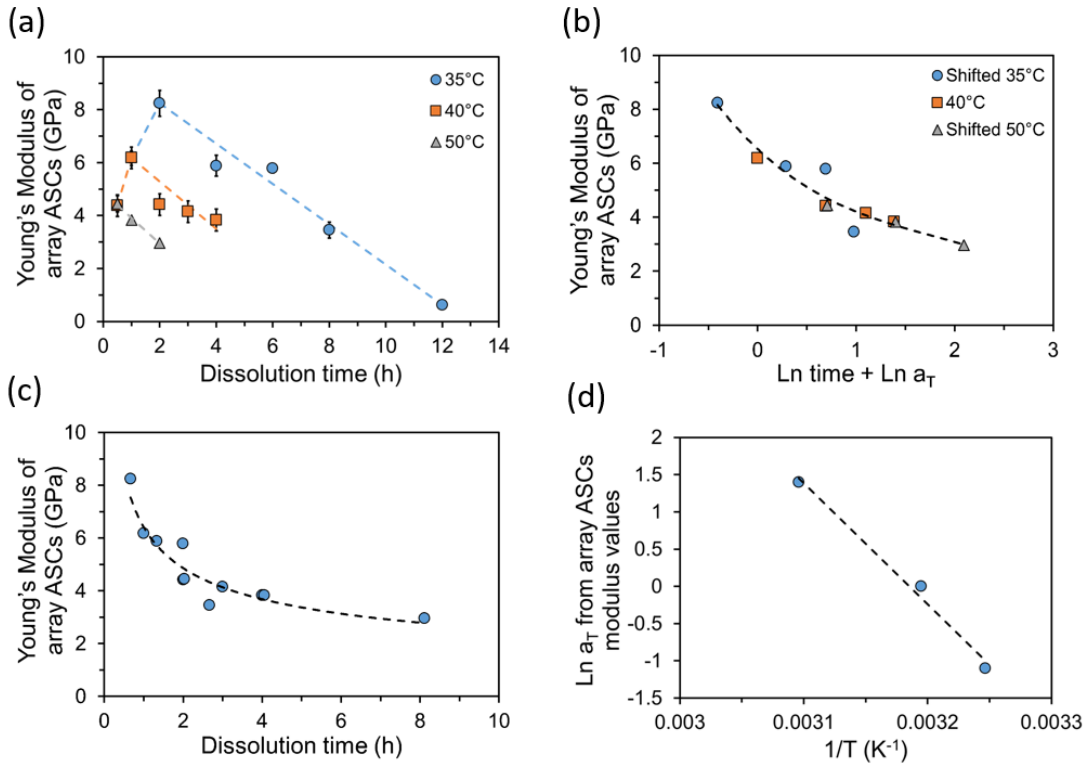

Figure 6.5: (a) Young's modulus values for array ASCs obtained from various times and temperatures, n = 3; (b) its master curve in ln space; (c) its master curve at linear dissolution time, at a reference temperature of 40 °C; (d) its Arrhenius plot.

It has been discovered in Chapter 4 that the changes of ultimate strength and elongation at break values of the single ASCs fabricated using pure IL also demonstrated time-temperature equivalence, and thus yield another two methods to determine E_a in order to compare with the E_a values previously calculated using other methods. Accordingly, the same approaches are employed, upon removing the data from 'preformed stage', each temperature set was simultaneously shifted towards the reference temperature set (40 °C) by certain shift factors (ln a_T) and master curves of breaking strength and elongation at break values were constructed, as seen in Figures 6.6b and 6.7b, respectively. The changes of breaking strength and elongation at break values versus dissolution time are expressed

in Figures 6.6c and 6.7c. Interestingly, the relatively fast decrease of strength values at first 3 hours of dissolution is similar to what observed from the changes of modulus values (Figure 6.5c). Additionally, linear relationships were found from the resultant Arrhenius plots (Figures 6.6d and 6.7d), and lead to the calculation of the activation energies of array silk threads dissolved in [C2mim][OAc] from the respective gradients of the curves, have values of 140 ± 19 kJ/mol (strength measurements) and 97 ± 22 kJ/mol (elongation at break measurements).

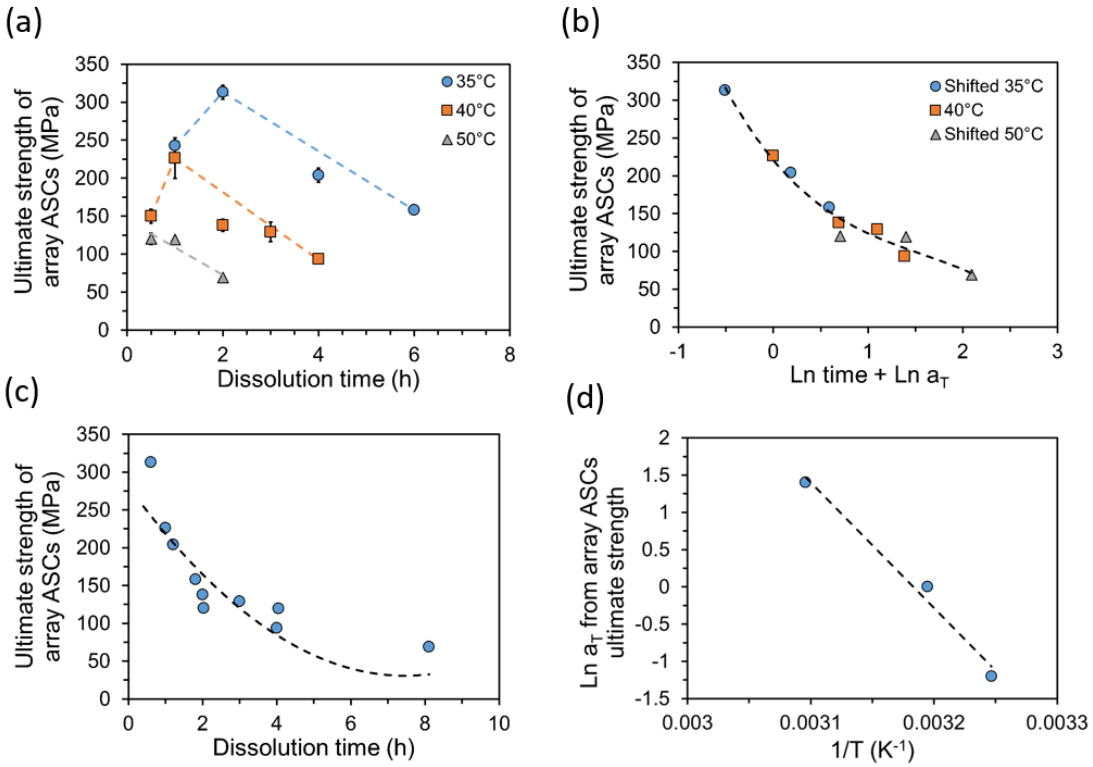

Figure 6.6: (a) Breaking strength values for array ASCs obtained from various times and temperatures, n = 3; (b) its master curve in ln space; (c) its master curve at linear dissolution time, at a reference temperature of 40 °C; (d) its Arrhenius plot.

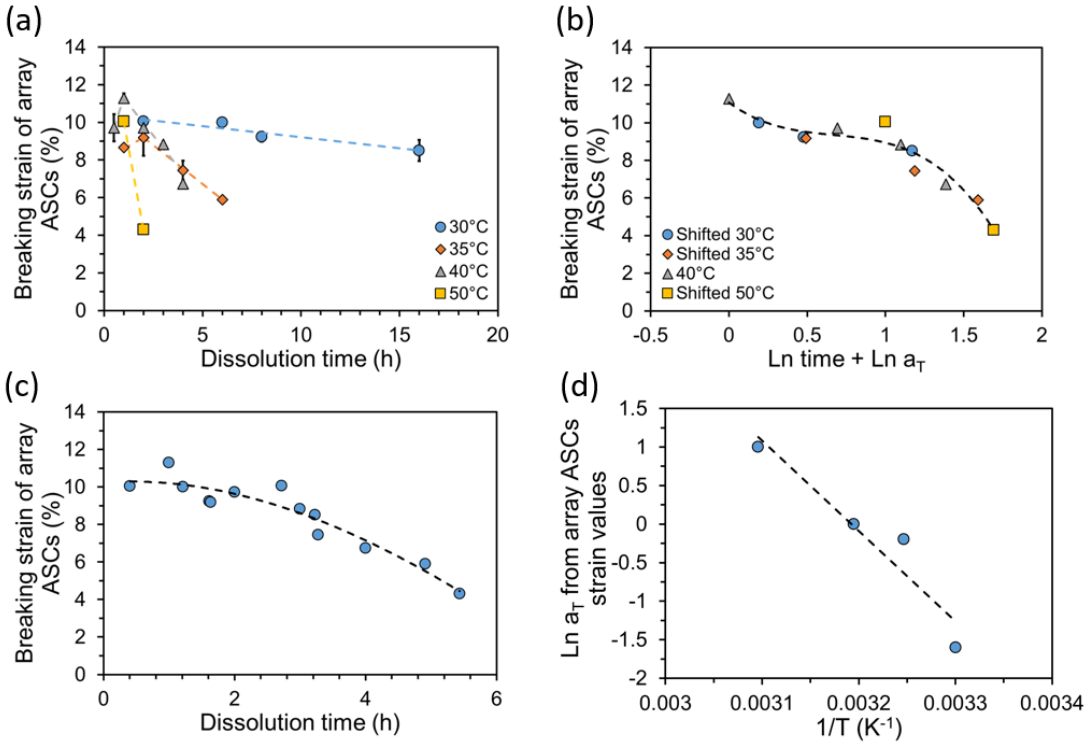

Figure 6.7: (a) Elongation at break values for array ASCs obtained from various times and temperatures, n = 3; (b) its master curve in ln space; (c) its master curve in linear dissolution time, at a reference temperature of 40 °C; (d) its Arrhenius plot.

6.3.4 Comparison between Single and Array ASCs

After exploring the single (Chapter 4) and array (earlier in this Chapter) silk threads dissolution behaviour in the ionic liquid [C2mim][OAc], it is of interest to compare the dissolution rates and activation energies between these two silk threads in different geometry. To compare the dissolution rates between single and array silk threads, the changes of V_m over linear dissolution time for single and array ASCs (Figures 4.18b and 6.3c) are plotted in one graph, with both shifted to the same chosen reference temperature (40 °C), as illustrated in Figure 6.8. It is clearly evident that the dissolution of single silk threads in [C2mim][OAc] happens faster compared to array silk threads, under the same dissolution time, greater value of V_m is achieved for single silk threads. The increase in the weight percentage of fibres can cause a increased viscosity of the IL solution, and further result in a slower dissolution rate. Similar observation has been reported by Liang et al. [228], they studied the different arrangement of cotton thread dissolved in [C2mim][OAc], and found that the dissolution rate was affected by the fibre arrangement, the rate from fast to low was ranked as single fibres $\approx$ arrays $>$ bundles. Suntharavathanan et al. [300] suggested that the viscosity of polymer solution can be increased due to the increased weight percentage of the solute. Another possible reason may be the array threads are closely packed together, thus the relative contact area where the undissolved fibres exposing to IL is smaller compared to a single silk thread. This assumption has been documented by Jiao et al. [301], they discovered that the surface area of the solute exposed to the dissolution medium can affect the kinetic solubility, and a reduced surface area exposed to the dissolution medium can cause a longer time needed to reach equilibrium.

Interestingly, a plateau stage is revealed for array threads at longer dissolution time, between 6 to 9 hours. This phenomenon where the V_m increase rate starts to flatten, may be associated with the specific microstructure of silk thread, recalling Figure 4.22. The schematic plot of the single silk threads dissolution procedure indicates that at longer dissolution hours, the surface of silk thread core was found to be surrounded by silk/IL gel, which acts like a protective layer and thus

hinders the dissolution rate. It is therefore expected that, within array silk thread system, at 6 hours dissolution time under 40 °C, the outer surface of array silk threads is entirely surrounded by this gel layer, which makes the IL more difficult to contact the remaining silk fibres and further decreases the dissolution rate. Nevertheless, since the dissolution follows the time-temperature superposition, when the silk threads immersed in IL for sufficient amount of time, eventually all the arrays of silk threads will be completely dissolved.

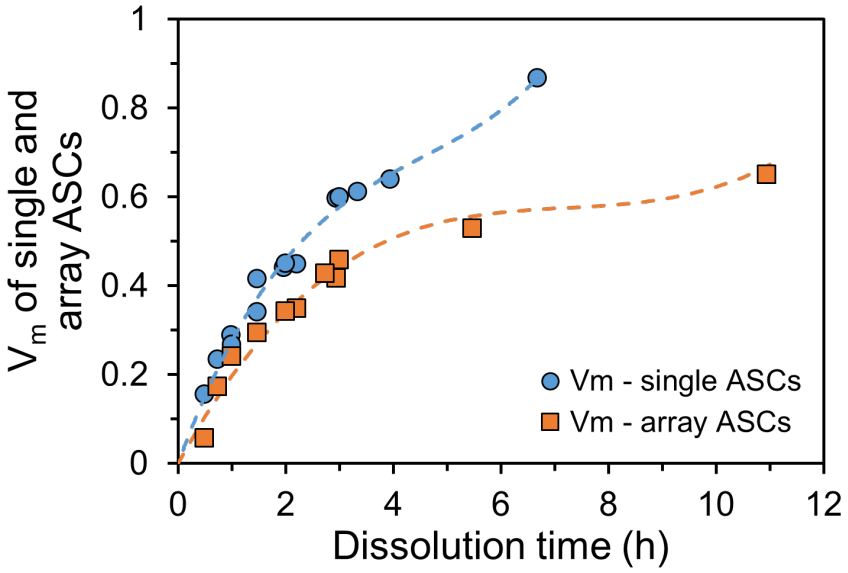

Figure 6.8: Comparison of the volume fraction of matrix as a function of dissolution time, between single and array silk threads in the ionic liquid of [C2mim][OAc], under the same reference temperature at 40 °C.

Furthermore, the activation energies of single silk threads and array silk threads dissolved in [C2mim][OAc] calculated using different experimental methods are summarised in Table 6.1. Noticeably, the activation energies measured using different methods are mostly consistent with each other for the same geometry silk fibre. The average value of E_a was determined, gives a value of 128 ± 6 kJ/mol for single ASCs, and 123 ± 10 kJ/mol for array ASCs, respectively. This suggests that the different geometry of silk fibres exhibit a similar activation energy when dissolved in [C2mim][OAc], within the errors of these measurements. The two questions proposed for this Chapter, see section 6.1, can therefore be answered - (i) The fibre arrangement does affect the speed of dissolution (Figure 6.8), (ii) however does not affect the dissolution activation energy (Table 6.1). Overall, the measurements of E_a conducted through four different methods for single and array ASCs as listed in Table 6.1, were combined and calculated to have an average value of 126 ± 4 kJ/mol.

Method	E_a for single ASCs (kJ/mol)	E_a for array ASCs (kJ/mol)
P_2	138 ± 13	121 ± 20
Young's modulus	116 ± 12	135 ± 15
Ultimate strength	139 ± 19	140 ± 19
Elongation at break	118 ± 10	97 ± 22
Average	128 ± 6	123 ± 10

Table 6.1: Comparison of activation energies of single and array silk threads dissolved in pure IL, measured through four different methods.

6.4 Summary

This Chapter has studied the dissolution dynamics of array silk threads (20 threads aligned closely in parallel), in the ionic liquid 1-ethyl-3-methylimidazolium

acetate ([C2mim][OAc]), as well as the structure and properties of the resulting composites. Partial dissolution method has been utilised to prepare array all silk composites. [C2mim][OAc] was chosen as the solvent and methanol as the coagulant. The dissolution process was carried out under various times and temperatures allowing a range of the array ASCs to be created. Different experimental techniques were performed to conduct the analysis, including wide-angle X-ray diffraction and mechanical testing.

Through performing WAXD azimuthal scans on array ASCs fabricated from a series of times and temperatures, it was found that the measurement of second legendre polynomial (P_2) can also be used to follow the dissolution of array silk threads, and hence to quantify the changes in the orientation of nanocrystallites within the obtained array ASCs. The P_2 value of each array ASC was noticed to decrease linearly with time and more rapidly at higher temperatures, as given in Figure 6.2a. By following the simple rule of mixtures, the dissolved and coagulated fraction of matrix (V_m) was thus calculated (Figure 6.3a). The time and temperature equivalence on the resulting P_2 and V_m values were individually verified by shifting various temperature data sets in natural logarithmic time and construct master curves of P_2 and V_m values (Figures 6.2b and 6.3b). In addition, the master curves of P_2 (Figure 6.2c) and V_m (Figure 6.3c) expressed in linear dissolution time are almost mirror-like images, with one decreasing and one increasing rapidly at the early dissolution stage and both slow down afterwards, indicating the 'preformed stage'. The shift factors needed to construct the master curves were next plotted against the respective inverse temperatures, and found to have linear relations thus revealing Arrhenius-like behaviour. The resulting activation energies were calculated from the gradients of the curves (Figures 6.2d and 6.3d), and both point to the same values, 121 ± 20 kJ/mol.

The tensile properties of the obtained array ASCs were also determined, including Young's modulus, breaking strength and elongation at break. It was interesting to see all three parameters (Figures 6.5a, 6.6a and 6.7a) from early dissolution hours at 35 °C and 40 °C temperature sets undergo increase to a maximum value and drop thereafter, revealing the 'preformed stage'. This indicates

that the specific loose raw silk thread microstructure also affects the dissolution of array silk threads similarly. After removing the data from the 'preformed stage', the Young's modulus, breaking strength and elongation at break data were individually explored to be time-temperature superimposed, which further induces three methods to determine the E_a. The activation energies were individually calculated from the gradients of the corresponding Arrhenius plots, and found to have similar values, 135 ± 15 kJ/mol (Young's modulus measurements), 140 ± 19 kJ/mol (breaking strength measurements), and 97 ± 22 kJ/mol (elongation at break measurements) respectively. It was evident that the E_a determined from four different methods agree with each other within the errors of the measurements, and led to an average activation energy value of 123 ± 10 kJ/mol.

In comparison with the measured E_a for single silk threads (as explored in Chapter 4), it is therefore suggested that the average required energies to allow the dissolution of single (128 ± 6 kJ/mol) and array (123 ± 10 kJ/mol) silk threads to occur are approximately the same (recalling Table 6.1). Although Figure 6.8 implies a slower dissolution speed when preparing array ASCs comparing to that for single ASCs, the increased fibres weight and the reduced surface area exposed to the IL may contribute to the reasons. Thus, the two proposed questions correlating to the dissolution of silk fibres in [C2mim][OAc] have been addressed, the fibre arrangement is (i) independent to the dissolution activation energy; (ii) however affect the dissolution speed. These findings may be helpful in the future design and fabricate silk fibres reinforced composites, or all silk composites with different fibre geometry requirements.

Chapter 7

Dissolution Dynamics of Woven All-Silk Composites Fabricated in the Ionic Liquid 1-Ethyl-3-Methylimidazolium Acetate

7.1 Introduction

Woven silk fabrics used as reinforcement in combination with a polymer matrix have been widely discussed in many studies. Shubhra, Q.T.H et al. have fabricated silk fibre reinforced polypropylene matrix composites; limited strength values were obtained likely due to lack of fibre-matrix adhesion [302]. Silk fibres reinforced with different polymer matrices Co-PP (copolypropylene), PP-g-MA (polypropylene grafted with maleic anhydride), PBS (polybutylene succinate), PBSa (polybutyl succinate/adipate) were compared; high toughness composites can be obtained by reinforcing ductile silk fibres with thermoplastic matrices which have high failure strain [303]. However, only a very few studies have so far been conducted on the all-polymer composites area, where silk fibre is both the reinforcement and the matrix phase. As covered in sections 2.2.1 and 2.3.2, Yuan et al. [2] have prepared all silk composites using the two-step method, silk fibres

were embedded in the silk fibroin matrix through solution casting; good strength properties were obtained.

In this Chapter, a one-step dissolution method will be applied to fabricate woven all silk composites, using [C2mim][OAc] as the solvent, and methanol as the coagulant. The partial dissolution of woven silk fabric will be carried out at a range of times and temperatures, with the remaining fibres serving as the reinforcement phase, while the dissolved and coagulated silk served as the matrix phase. The resultant woven ASCs will be characterised using different techniques.

By analysing azimuthal WAXD scan results of woven ASCs dissolved at various times and temperatures, it was discovered that the dissolution can be tracked through following the orientation changes of nanocrystallites within each obtained woven ASC. A time-temperature shifting method was applied to the determined P_2 values. Hence, it was discovered the dissolution has an Arrhenius-type behaviour, allowing the corresponding dissolution activation energy (E_a) to be calculated. By using a linear mixing rule, the volume fraction of dissolved and coagulated matrix (V_m) can be thus calculated. In addition, the Young's modulus values of the resultant woven ASCs were measured. It was found that the V_m and modulus values also followed the same shifting method. Master curves can be formed using the time-temperature superposition (TTS) principle, and subsequently an activation energy was calculated. The applicability of the rule of mixtures was examined. In combination with our previous study on single and array silk threads dissolution, the V_m master curves of single silk threads, array silk threads and woven silk fabrics were compared in one graph, and the dissolution activation energies and the dissolution rates were compared.

7.2 Experiments and Methodology

7.2.1 Materials and Methods

Degummed *B. mori* silk thread was hand woven into a silk fabric by following a plain weave process. The solvent and coagulant used to fabricate woven ASCs

are identical to those outlined in section 3.2. The detailed fabrication process will be introduced below, and the characterisation technique including optical microscope, WAXD and tensile testings are identical to those introduced in sections 3.3.1, 3.4.1, 3.4.3, 3.5.

7.2.2 Fabrication of Single Layer Woven All Silk Composites (ASCs)

Woven silk fabrics were cut into multiple 5 cm x 2 cm strips, ready for preparing single layer woven ASCs. Next, a poly(tetrafluoroethylene) (Teflon) dish was filled with excess [C2mim][OAc], followed by being put into vacuum oven for 1 hour to allow the IL to be preheated to a chosen temperature. Then the cut woven strips were fully immersed in the preheated IL bath inside the vacuum oven, for the designed length of time, at temperatures of 40, 50 or 60 °C.

After the dissolution finished, the partially dissolved silk strips were immediately transferred from the IL bath into the methanol bath, to start the coagulation. The used [C2mim][OAc] was collected to be recycled. Next, the woven ASCs were soaked in the methanol bath for 1 day followed by washing in water for 1 day with changing the medium twice, to remove any contained IL. Finally, the woven ASCs were dried in hot press for 1 hour at 100 °C with contact pressure approximately at 0.15 MPa.

The procedure for cast silk fibroin film is identical to the one outlined in section 4.2.3.

7.2.3 Fabrication of Two Layers Woven All Silk Composites (ASCs)

Woven silk fabrics were cut into 5 cm x 5 cm sheets and subsequently weighed. The required weight of the solvent was calculated by following the solvent to silk mass ratio of 2:1. Next, the solvent was applied to the first layer of woven silk fabric using a brush, after which a thin layer of foil at the size of 2 cm x 5 cm

was placed at the edge in order to create an unbonded region to conduct the peel test. Then the second layer of woven silk fabric was added with the remaining solvent applied. The two-layered stack was transferred into hot press, under 2 MPa at 60 °C for 1 hour. Upon dissolution, the partially dissolved woven silk fabrics were transferred into the methanol bath to start the coagulation. Same coagulation and drying processes were followed, as described in section 7.2.2. The two layers of woven ASCs were then obtained, ready to conduct the peel tests by following the procedure as outlined in section 3.5.3. It is noted that two different solvent systems were individually used, pure IL and IL/RA, in order to examine the effects of reducing agent on the peel strength.

7.3 Results and Discussion

7.3.1 Microstructure of Woven ASCs

The plain woven silk fabric is composed of individual threads in two directions, which are named 'warp' and 'weft' in weaving. The surface of the unprocessed raw woven silk fabric is presented in Figures 7.1a and b. It can be seen that weft multifilament bundles are closely packed, the distance between each weft bundle is smaller than that of the warp bundle. Optical microscopy analysis for the unprocessed raw and partially dissolved (40 °C - 5 h) woven silk ASCs in cross-sectional direction were performed and the results are shown in Figures 7.1c and d, and Figure 7.2, respectively. Figures 7.1c and d indicate that the warp threads are straight in the longitudinal direction (Figure 7.1b), whereas the weft threads pass over and under the warp threads, which is the common plain-weave structure [304]. It is also observable that under the same magnification, there are more silk threads in weft direction than warp, and the ratio of the thread count is measured to be $\sim 1.5 : 1$ (weft : warp).

Figures 7.2 a and d reveal that the overall cross-sectional size of the remaining lenticular shape of the thread core from the partially dissolved woven ASC processed at 40 °C - 5 h was decreased compared to the raw woven fabric (Figure 7.1c and d), as well as the width of the bundle that is parallel to the plane. It is

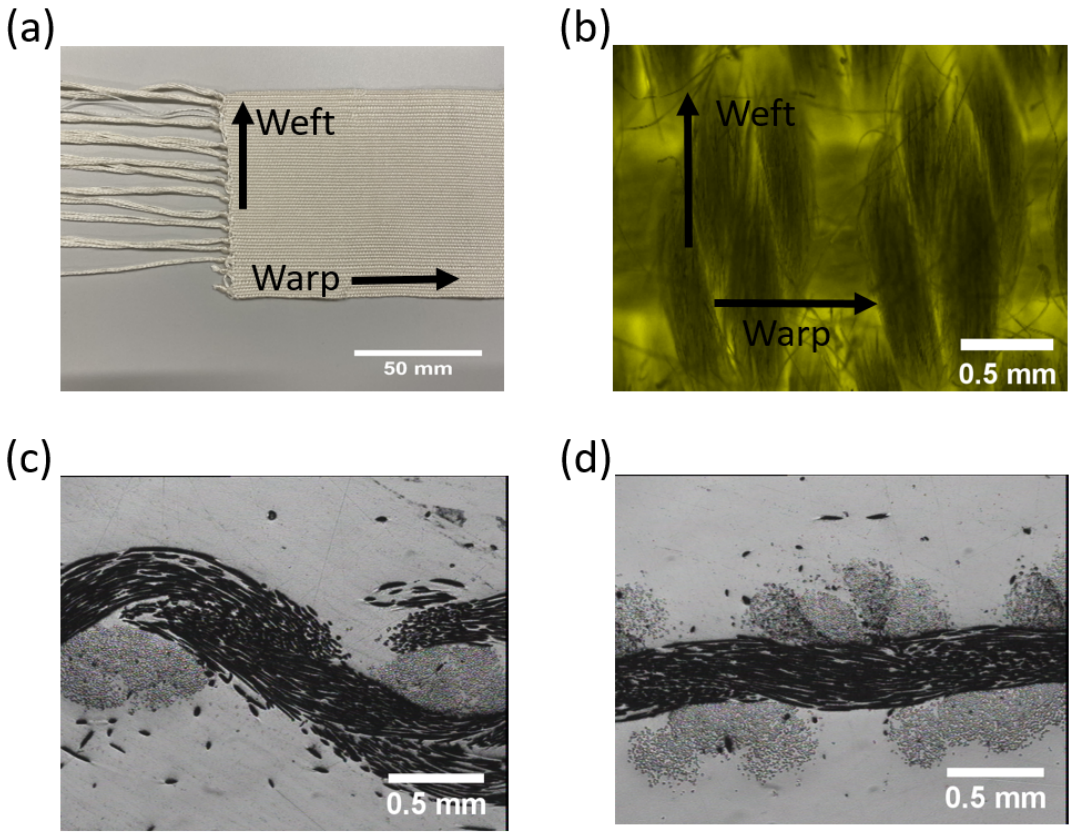

Figure 7.1: The surface of unprocessed woven silk fabric. (a) Visual aspect. (b) A optical microscope image at transmission mode, observed at 50 x magnification. Optical microscopy cross-sectional images of unprocessed raw woven silk fabrics, at (c) warp threads perpendicular to plane, (d) weft threads perpendicular to plane, both observed at 50 x magnification.

expected that as the dissolution progresses, the dissolved fibres are turning into matrix, so the proportion of matrix phase is increased, which can be seen more clearly in higher magnification images (Figures 7.2 b,c,e and f). Especially in Figures 7.2 c and f, a layer of the matrix phase is formed, which appears as a lighter colour and surrounds the outer surface of the weft and warp direction thread core. Interestingly, thicker layer of matrix can be seen along warp direction thread core. Through using the software Image J, the thickness of the matrix layer was measured. It was found that under the same dissolution condition, the ratio of the matrix thickness along the thread core between weft and warp threads is close to

$\sim 1 : 2$ (weft : warp). One of the reasons could be the distance between each warp bundles are significant larger than that of weft bundles, thus more space is left for matrix to be generated.

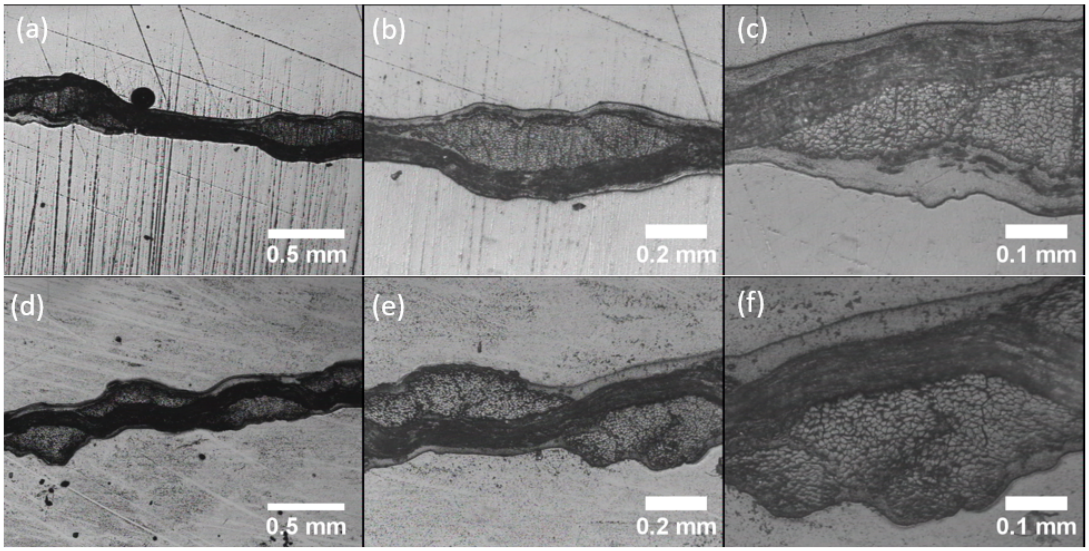

Figure 7.2: Microscope cross-sectional images of partially dissolved silk woven ASCs at 40 °C - 5 h, in two different directions, warp bundles perpendicular to the plane (a)(b)(c); weft bundles perpendicular to the plane (d)(e)(f). Magnification: (a)(d) 50 x; (b)(e) 100x ; (c)(f) 200 x.

7.3.2 Relationship of WAXD azimuthal diffraction curves on woven fabrics from weft and warp directions

Figure 7.1 shows that the hand woven silk fabric contains threads along weft and warp directions which are perpendicular to each other. It was observed from the cross-sectional images of one woven ASC that the different thickness of matrix layer is generated along weft and warp directions. Therefore, prior to the determination of the average nanocrystalline orientation within the woven ASCs, it is important to understand the relationship between WAXD azimuthal diffraction curves obtained from weft and warp thread directions, and to determine whether the average orientation of the crystalline fraction depends on the direction of the woven sample that is being held.

To start the investigation, a 2D diffraction pattern of the raw woven silk fabric was first obtained using X-ray, by following the procedure outlined in Chapter 3, section 3.4.1. It is noted that the diffraction intensities on 2D diffraction pattern were collected when weft threads were held vertically.

Figure 7.3 presents the resulting 2D diffraction pattern, it is observed that there are two sets of symmetric diffraction arcs, along equator and meridian directions, correlating to weft and warp threads, respectively. Stronger intensity arcs can be seen along the equator direction, which implies that weft threads contain more highly aligned crystallines and result in a greater diffraction intensity.

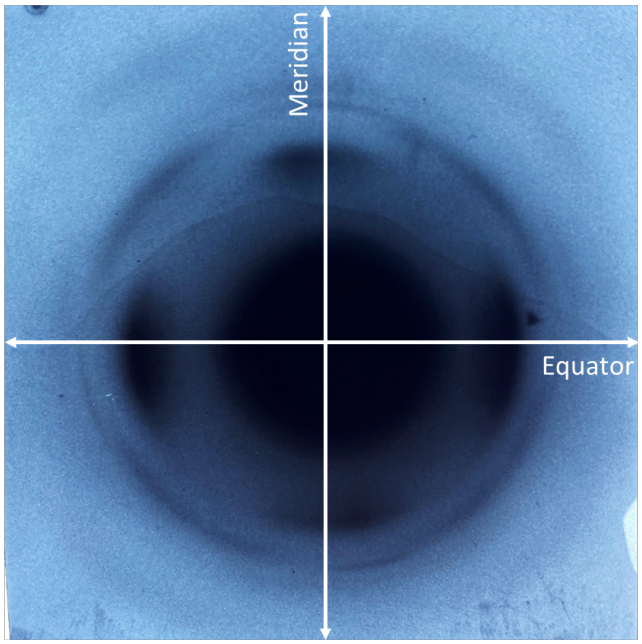

Figure 7.3: X-ray 2D diffraction pattern of raw woven silk fabric, when weft threads are held vertically.

In theory, the reflections along equatorial direction are symmetric, likewise along meridian direction. Thus, a schematic illustrating how the 2D diffraction pattern changes depending on how the orientation of the fabric is held, is given in Figure 7.4. The obtained 2D diffraction pattern shown in Figure 7.3 is illustrated schematically in Figure 7.4a, obtained by following the experimental setup as shown in Figure 7.4b. Rotating woven fabrics by 90° can allow warp threads to be located vertically, and the consequently 2D pattern would look like Figure 7.4c.

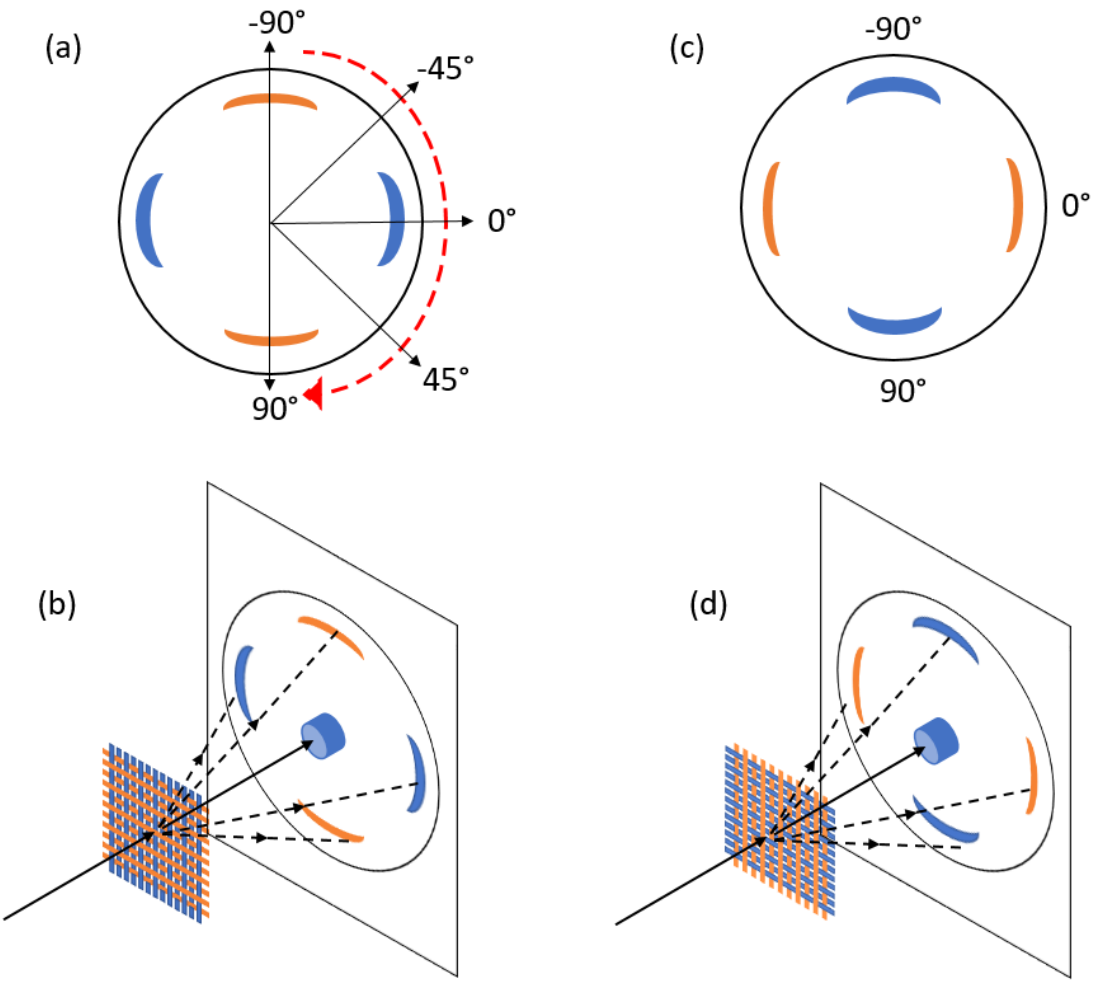

Figure 7.4: Schematic representations for the XRD 2D patterns of unprocessed raw woven silk fabric in accordance with the orientation of the fabric is held, (a)(b) when weft threads are vertical, (c)(d) when warp threads are vertical.

Upon following the detailed X-ray procedure as outlined in section 3.4.3, WAXD azimuthal scans were first conducted on the raw woven silk fabric, from alpha angle at -90° to 90°, in order to examine the unprocessed woven silk structure. Figures 7.5a and b show the resultant azimuthal diffraction curves when weft and warp threads were aligned vertically, respectively. It can be seen that the diffraction intensity peak height from weft direction scan at $\alpha = 0°$ (Figure

7.5a) is almost two times higher than warp direction (Figure 7.5b), which is in good agreement with the obtained 2D diffraction pattern (Figure 7.3), stronger intensity arcs are observed along the equator.

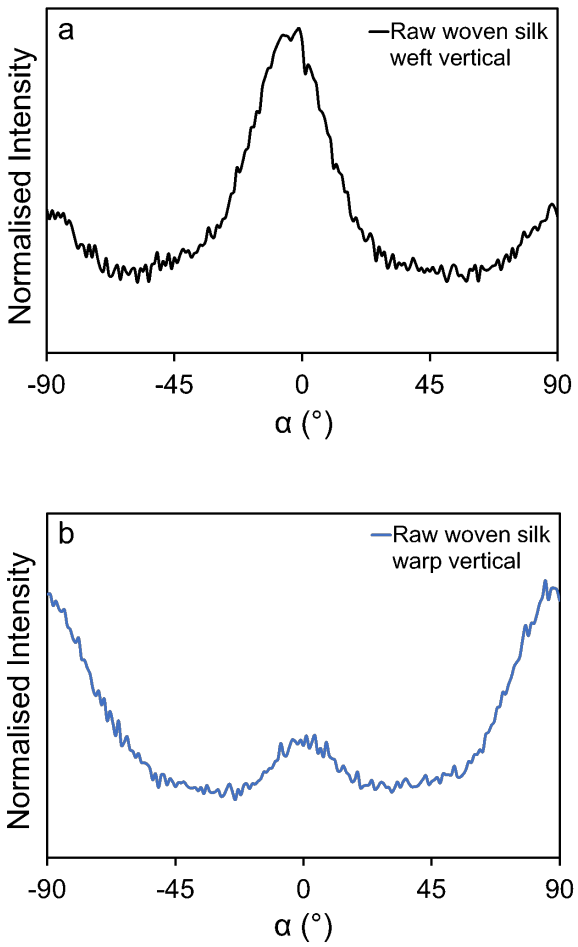

Figure 7.5: WAXD azimuthal scan on raw woven silk fabric, when (a) weft threads were aligned vertically, (b) warp threads were aligned vertically.

In addition, the diffraction curves on the raw woven silk fabric at two directions imply that 0° to 90° intensity when weft threads were aligned vertically (Figure 7.5a) shows similar values and trends as -90° to 0° intensity when warp threads were aligned vertically (Figure 7.5b) and vice versa, for the other half region. Therefore, here our hypothesis is that diffraction curves from the two directions can be overlapped after shifting alpha intensities of one direction horizontally. Here, Figure 7.6 demonstrates the details of the shifting procedure carried on raw woven silk fabric sample, alpha intensities from -180° to -90° were shifted across x-axis by 180°, which exhibits overlap, for both weft and warp direction curves. Figure 7.7 further evidences that the two direction curves can be shifted and overlapped for woven ASCs fabricated from different times and temperatures.

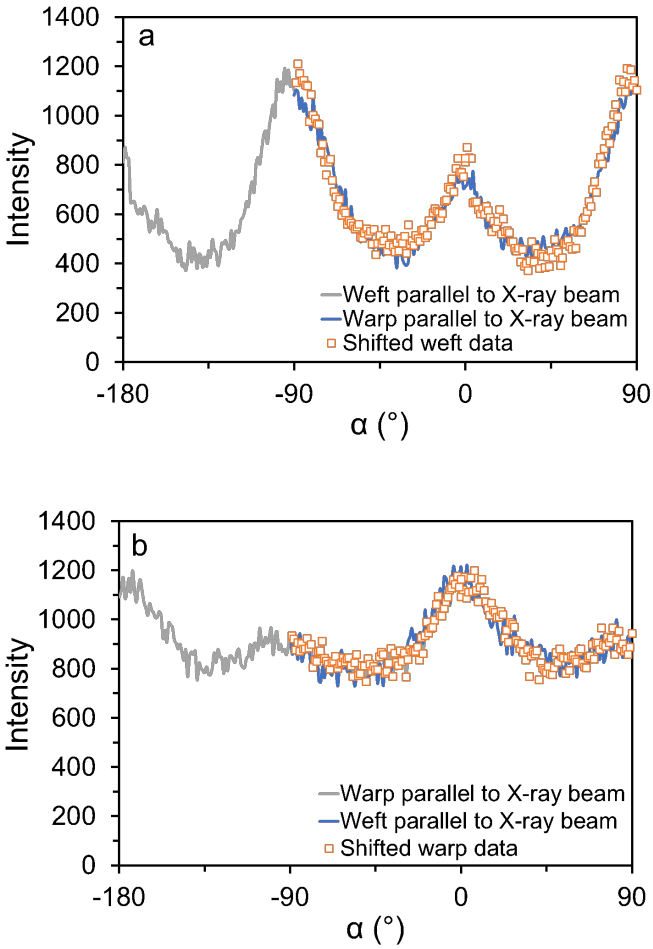

Figure 7.6: Demonstration of the results after shifting one direction alpha intensities across x-axis to overlap with the other direction alpha intensities.

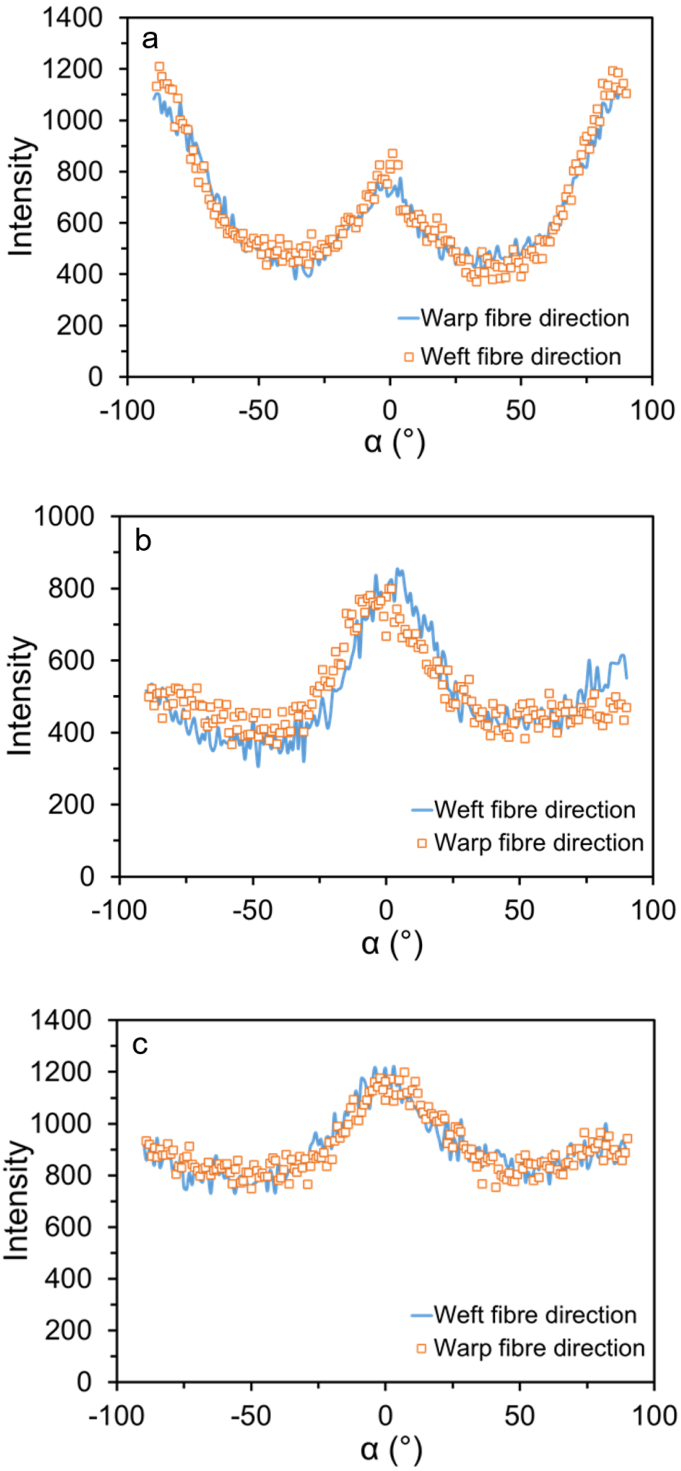

Figure 7.7: Diffraction curves from two directions scans overlapped with each other after shifting alpha intensities across x-axis, (a) 40 °C - 1 hr, (b) 50 °C - 2 hr, (c) 60 °C - 1.5 hr.

This phenomenon that diffraction curves obtained from two directions can be overlapped is indicative of the mathematical relationship between the curves and suggests that weft and warp direction curves can be mathematically transformed to one another. Equations 7.1 and 7.2 further evidence this finding.

$$\langle \cos^2(\alpha+\theta)\rangle = \frac{\int_{-\pi/2}^{\pi/2} I(\alpha)\cos^2(\alpha+\theta)\mathrm{d}\alpha}{\int_{-\pi/2}^{\pi/2} I(\alpha)\mathrm{d}\alpha} \tag{7.1}$$

$$= \sin^2\theta(1-2\langle\cos^2\alpha\rangle)+\langle\cos^2\alpha\rangle \tag{7.2}$$

if $\langle\ \cos^2\alpha\ \rangle$ represents the average cosine squared value of the azimuthal angle when weft threads were held vertically, then $\langle\cos^2(\alpha+\theta)\rangle$ implies its value when warp threads were held vertically (θ=90°). And θ indicates the angle of how much the sample is rotated. The weft and warp threads are perpendicular to each other, therefore θ=90° in this case. Subsequently,

$$\langle\cos^2(\alpha+\theta)\rangle = 1-\langle\cos^2\alpha\rangle \tag{7.3}$$

thus,

$$\langle\cos^2(\alpha+\theta)\rangle + \langle\cos^2\alpha\rangle = 1 \tag{7.4}$$

Equation 7.4 implies that when rotating the sample by 90°, the sum of the obtained $\langle\ \cos^2\ \alpha\ \rangle$ from two directions is equal to 1. Next, this relationship can then be applied to the second legendre polynomial function (Equations 3.1 and 3.2), to examine any relationships between the corresponding P_2 values. Interestingly, it is further discovered that the sum of two directions P_2 values is equal to 0.5, as expressed in Equation 7.5;

$$P_2^{weft} + P_2^{warp} = \frac{1}{2} \tag{7.5}$$

After discovering the two thread direction azimuthal diffraction curves can be overlapped and the two corresponding P_2 values are linearly related, it can

be therefore assumed that the dissolution behaviour of woven silk fabrics investigated through following the changes of crystalline average orientation (P_2 values) within the woven ASCs can be conducted along either weft or warp directions. Regardless of the direction that woven ASC is being held, the same information with respect to the dissolution behaviour should be revealed. Hence, the studies on the dissolution behaviour of woven silk fabrics in [C2mim][OAc] described in the following sections, will be carried out from one of the thread direction, here the warp thread direction is chosen.

7.3.3 Characterisation of the Crystalline Average Orientation within Woven ASCs by Calculating P_2 Values

The woven ASCs were characterised by WAXD azimuthal scans prior and subsequent to dissolution. It is expected that upon dissolution, the crystalline structure/orientation of the resultant woven ASCs, particularly for the coagulated SF film, will be different to the unprocessed raw woven silk fabric. Figure 7.8 represents WAXD azimuthal diffraction curves collected when warp threads were located vertically, for partially dissolved woven ASCs including processed at lowest temperature and shortest time - 40 °C for 1 h, and 40 °C for 5 h, 60 °C for 1.5 h; as well as the coagulated SF film from [C2mim][OAc] solution with 5 wt% silk fibre. Significant change in the intensity distribution can be observed. The change in the intensity distribution correlates to the difference between the preferred aligned crystalline orientation of the woven ASC prepared at lowest temperature and shortest time and the randomly oriented crystals in the SF film (matrix phase). The diffraction curves were normalised to give the same total area.

As mentioned in Section 3.4.3, WAXD azimuthal profiles were collected by scanning through azimuthal angles from -90 to 90° from the reflection plane (020) (2θ = 20.6°). There were three peaks in the diffraction curve, located at α = -90°, 0° and 90°, corresponding to the weft, warp and weft direction respectively; with the warp direction vertical at α = 0°. It can be seen that the partially dissolved woven ASC at 40 °C for 1 h shows the highest peak intensity at α =

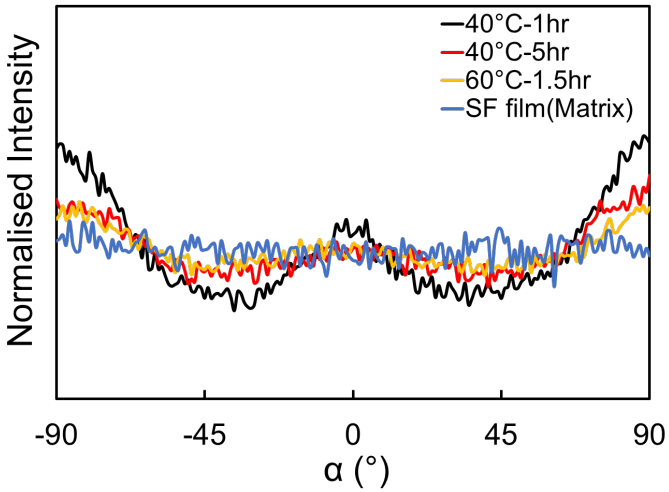

Figure 7.8: Azimuthal scans for woven silk fabrics partially dissolved at 40 °C - 1 h, 40 °C - 5 h, 60 °C - 1.5 h, completely dissolved and coagulated into SF film; diffraction curves were collected when warp threads were located vertically.

-90°, 0° and 90°, whereas the coagulated SF film shows a flat distribution curve throughout the whole scanning angle, confirming random crystalline orientation. Compared to the woven ASC at 40 °C for 1 h, the normalised peak intensity at the α angle = -90° and 90°, of the other partially dissolved woven ASCs processed at longer time or higher temperature is lower, and tending to flatten between -45° and 45°, while its baseline (from the coagulated SF component) is higher. The changes directly corresponded to the percentage of crystalline component being dissolved by the IL and transformed into a randomly oriented structure through the coagulation process. The background diffraction intensity of azimuthal scan for the reflection plane (020) was measured and subtracted.

It has been demonstrated in previous chapters that the orientation factor (P_2) is an important parameter directly related to the physical properties of the resulting ASCs, since it quantifies the axial orientation distributions of nanocrystallites. Accordingly, radial integration of the experimentally measured intensity distributions on the Debye ring around the (020) equatorial reflection was applied to determine the average orientation of the nanocrystallites within the woven ASCs

using the 2^{nd} legendre polynomial function, as given in Equations 3.1 and 3.2 [305].

The orientation factors of the nanocrystallites for each partially dissolved woven ASC obtained from processing at various times and temperatures were determined from the distribution curve by using Equations 3.1 and 3.2, the results are given in Figure 7.9. It is expected that, the dissolution continuously disrupts the preferentially oriented nanocrystallites, thus will influence the crystal orientation and subsequently differ the corresponding P_2 values. It can be seen from Figure 7.9, the P_2 was calculated to be 0.14 for the woven ASC obtained from early dissolution stage (40 °C for 1 h). Besides, theoretically, the P_2 value should be equal to 0.25 for a random 2D isotropic structure in woven fabrics. As the dissolution progress, the amount of randomly oriented component would increase, and eventually become fully isotropic. Consequently, a increased value of P_2 is expected, from 0.14 (woven ASC processed at lowest time and temperature) to 0.25 (random 2D isotropic). As expected, Figure 7.9 shows a higher P_2 value is measured for woven ASCs that fabricated under longer dissolution times or higher dissolution temperatures. For woven ASCs processed in [C2mim][OAc] at various times and temperatures, a broadly linear increase of the P_2 value was observed.

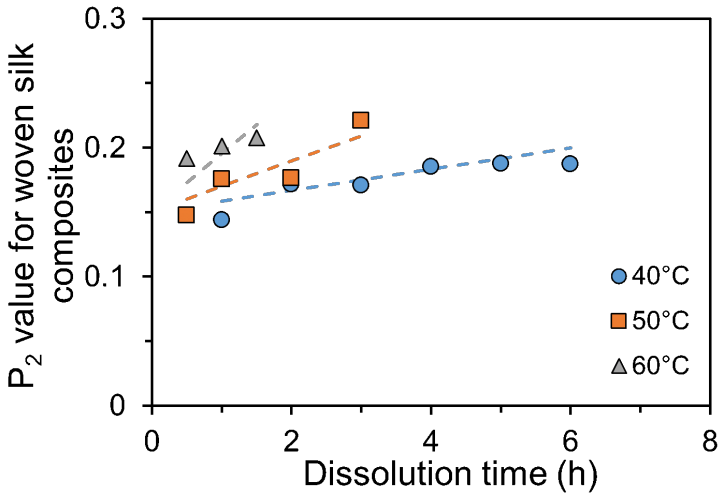

Figure 7.9: Average P_2 values calculated from WAXD azimuthal scans for woven ASCs being dissolved in [C2mim][OAc] at various times and temperatures; the dashed lines are guide for the eye. Error bars are too small to see, n = 3.

It can be seen in Figure 7.9, different temperature sets have different rates of dissolution. It has been explored in early chapters that the equivalence between dissolution time and temperature can be revealed using the time-temperature superposition (TTS) principle, by creating a single master curve, which has been widely verified in many polymer systems [50, 306–308]. The implementation of the well-established TTS approach allows to examine the data in natural logarithmic space (ln time), followed by shifting and overlapping the various temperature curves in ln time. As introduced in section 4.3.2, a simple multiplicative factor (a_T) could thus relate time and temperature results, see Equations Equations 4.1 and 4.2. Figure 7.10a illustrates the detailed shifting procedure, following the method as outlined in section 4.3.2. Upon shifting, the final master curve for the variation of the P_2 values for the obtained woven silk composites with ln time shifted to 50 °C is showed in Figure 7.10b. Subsequently, P_2 values versus linear dissolution time is plotted and shown in Figure 7.10c. It can be seen that the master curve starts to flatten after 4 hours of dissolution at 50 °C.

By plotting the shift factors (ln a_T) versus the inverse absolute temperature, it is worth to see if the rate of the dissolution obeys an Arrhenius like behaviour, as expressed in Equations 4.3 and 4.4 [246]. Figure 7.10d shows ln a_T vs $1/T$ and clearly indicates a linear relationship. The activation energy of woven silk fabric dissolved in [C2mim][OAc] can therefore be calculated from the gradient of the linear regression in the Arrhenius plot, giving a E_a value of 95 ± 17 kJ/mol.

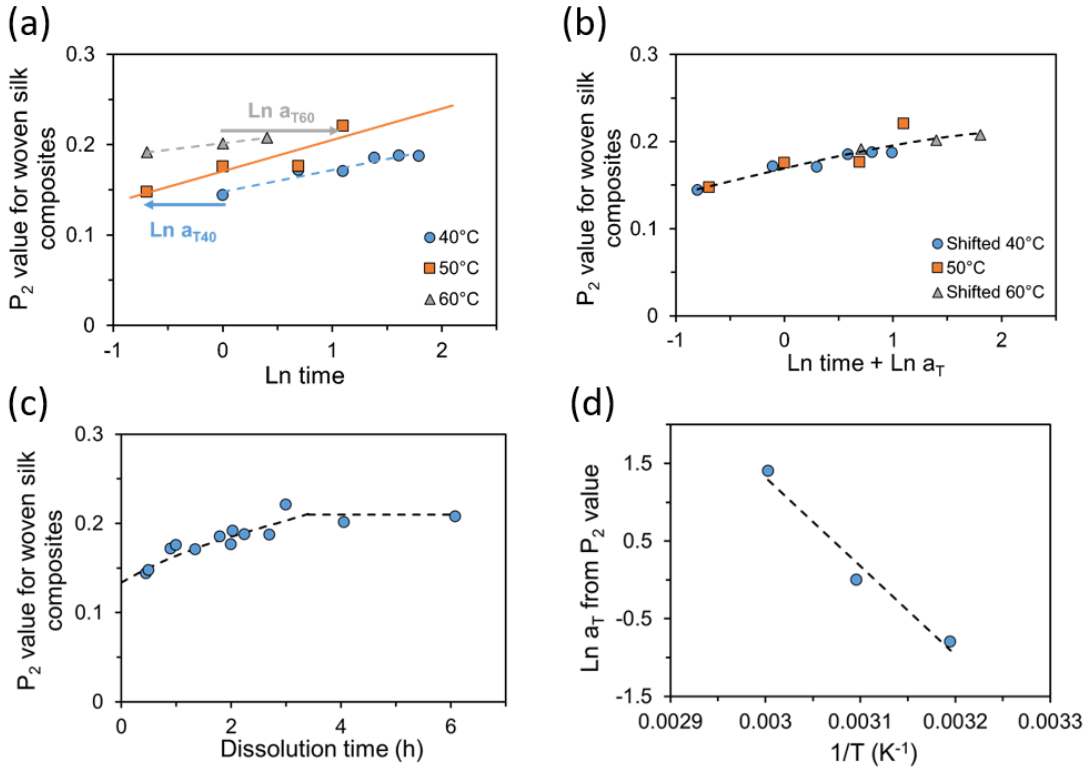

Figure 7.10: Shift method applied in P_2 values. (a) Details of shifting procedure for P_2 values, by using 50 °C as a reference temperature. (b) Shifted P_2 values of woven ASCs, generated as a master curve in ln space. (c) Master curve for measured P_2 values of woven ASCs, with respect to dissolution time at a reference temperature of 50 °C. (d) Shift factors (ln a_T) from fitting measured P_2 values, as a function of inverse temperature, indicating Arrhenius behaviour; the dashed lines in (a) and (c) are guide for the eye, and those in (b) and (d) are second-degree polynomial and linear fitting lines, respectively.

7.3.4 Measurement of the Volume Fraction of the Coagulated Silk Matrix (V_m) in the Woven ASCs

The solvent [C2mim][OAc] applied to woven silk fabrics can penetrate into silk fibroin and break the intermolecular hydrogen bonds in the crystalline regions, and transform the preferentially aligned crystalline structure into a randomly oriented coagulated fraction, which then forms the matrix of the resulting all silk composite. This was shown from the WAXD azimuthal scans, recalling Figure 7.9, as the dissolution progressed, the P_2 value was seen to increase from 0.14 to 0.25 which suggests that the content of randomly oriented matrix component was increasing with temperature and time. The partially dissolved woven ASCs are therefore composed of two components, the fibre and the matrix. Extrapolating the master curve of P_2 values (Figure 7.10c) backwards to time=0 gives a value of 0.13, which correlates to the unprocessed raw woven fabric (P_2 fibre). From the diffraction curve of the coagulated silk film, the P_2 was measured to be 0.25 (P_2 matrix). Next, the introduced linear mixing rule (Figure 4.16, Equations 4.5 and 4.6) is once again utilised in order to quantitatively measure the coagulated matrix fraction (V_m) of each partially dissolved woven ASC. Figure 7.11a indicates the coagulated matrix fraction, V_m, for woven ASCs obtained under various dissolution temperatures as a function of dissolution time. Longer dissolution times lead to a larger V_m value.

As reported above, the woven silk fabric dissolution process exhibits time-temperature superposition. Similarly, the TTS principle should be applicable for the corresponded V_m values. Therefore, as showed in Figure 7.11b, the demonstrated shifting method is now implemented to generate a master curve of the V_m values for the obtained woven ASCs, again using 50 °C as the reference temperature.

Figure 7.11c expresses the master curve of the V_m values from each woven silk composites dissolved in [C2mim][OAc] at various temperatures is now plotted as a function of dissolution time, at a reference temperature of 50 °C. It can be observed that up to 50 % of woven silk fabrics are dissolved in the first 2 hours,

and only a further 20 % dissolved between 2 to 6 hours of dissolution. A significant reduction of dissolution rate can be found. This observation also seen from the previous studies on array silk threads, where the rate of V_m growth starts to flatten at longer dissolution time and displayed a plateau stage (Figure 6.3c). This phenomenon once again implies that a silk/IL gel layer is formed at longer dissolution hours and acts like a protective layer and thus hinders the dissolution rate. Nevertheless, the dissolution process still obeys the time-temperature superposition principle and eventually all the woven silk fabrics can be entirely dissolved.

Upon V_m TTS shifting, the obtained shift factors can now be plotted as a function of inverse temperature as operated before for the P_2 results. In Figure 7.11d, a straight line is again found to fit the data points, which indicates the Arrhenius behaviour, thus the dissolution of woven silk fabric in [C2mim][OAc] was calculated to have an activation energy of 95 ± 17 kJ/mol. This value is identical to the previous E_a calculated from P_2 TTS analysis, which is to be expected as they are mathematically related to each other.

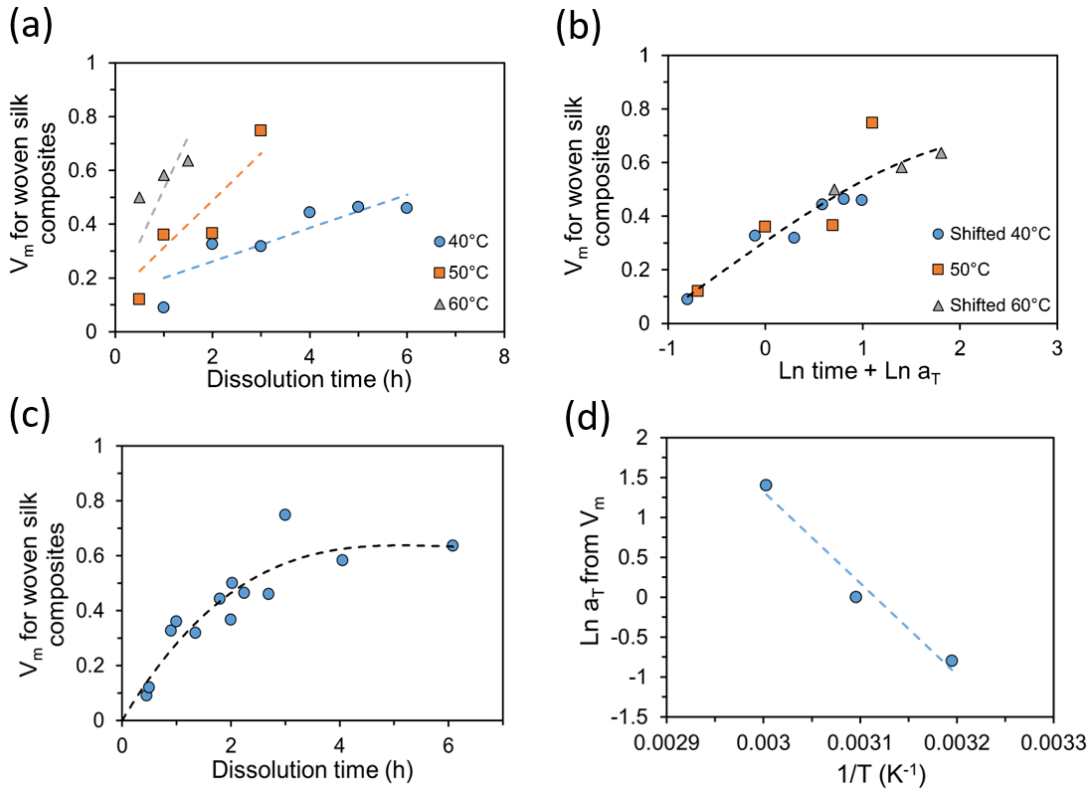

Figure 7.11: (a) V_m values for woven ASCs obtained under various dissolution times and temperatures, calculated by using P_2 full integration method, n = 3. (b) Shifted V_m values of woven ASCs, generated as a master curve in ln space. (c) Master curve for measured V_m values of woven ASCs, with respect to dissolution time at a reference temperature of 50 °C. (d) Shift factors (ln a_T) from fitting measured V_m values, as a function of inverse temperature, indicating Arrhenius behaviour; the dashed lines in (a) and (c) are guide for the eye, and those in (b) and (d) are second-degree polynomial and linear fitting lines, respectively.

7.3.5 Mechanical Properties of Woven ASCs

Through tensile tests, the mechanical performance of woven ASCs when weft direction is vertical were investigated. Figure 7.12 shows the stress-strain curve for a woven ASC obtained at 40 °C for 2 hours.

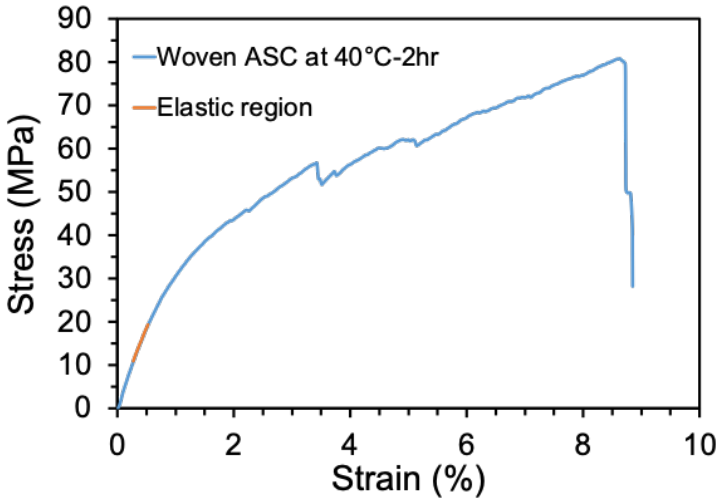

Figure 7.12: Stress-strain curve for woven ASC obtained from IL system at 40 °C for 2 hours.

The mean values of Young's modulus along the weft direction at a temperature of 40 °C for the dissolution time up to 6 hours are shown in Figure 7.13. It can be seen that the measured modulus value increases at the early dissolution stage, reaching a maximum and thereafter drops. This trend is also found in previous studies on single and array silk threads dissolved in [C2mim][OAc], where the Young's modulus and strength values initially increased to a maximum value then decreased afterwards, indicating the 'preformed stage' (Figure 4.22). Figure 7.13 provides the evidence of the 'preformed stage' can also be found during the dissolution of woven silk fabrics. When woven silk fabrics experience an immersion time of 2 h in [C2mim][OAc], sufficient amount of silk fibres dissolved and transformed into matrix to form a closely packed thread core microstructure. As a consequence, the maximum Young's modulus of the woven ASC reaches 3.6 GPa. Thereafter, a linear reduction of Young's modulus values can be seen due to thread cores continuously dissolved and more matrix created.

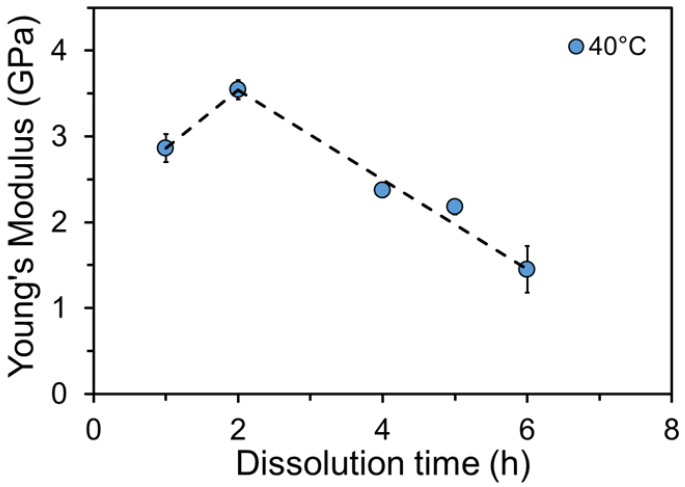

Figure 7.13: Young's modulus values of woven ASCs dissolved for different length of time, at 40 °C; the dashed line is a guide for the eye; n = 3.

The Young's modulus values of woven ASCs obtained from various times and temperatures are shown in Figure 7.14a, it is noted that the 'preformed stage' result shown in 1 hour at 40 °C is removed, since it represents the early stage of dissolution and would have a different activation energy. From Figure 7.14a, it shows a trend that the measured woven ASCs Young's modulus continuously decreases and the rate of decrease becomes more rapid at higher temperatures.

Hence, it is worthwhile to see if the variation of the modulus obeys the TTS principle. After applying the same shifting procedure as introduced above, again using 50 °C as reference temperature, a master curve of Young's modulus values can be seen in Figure 7.14b. Modulus values gained from other temperatures were superimposed towards the polynomial curve of the reference temperature set, and constructed a master curve with largest R^2 value. This also suggested that Young's modulus values determined from different temperature sets can be superimposed together through applying certain shift factors (ln a_T) scales. A complete TTS curve of woven silk ASCs Young's modulus values, in linear dissolution time using 50 °C as reference temperature, is shown in Figure 7.14c. A linear relationship between the shifting factors and temperature is shown in Figure 7.14d, when the shift factors are plotted against 1/T, which once again demonstrates Arrhenius like behaviour. The dissolution activation energy from Figure 7.14d was calculated from the gradient of the line, gave a value of 95 ± 2 kJ/mol. This is very close to the previous two values obtained from the P_2 and V_m time-temperature shifting (95 ± 17 kJ/mol).

It has already demonstrated in previous chapters that following the changes of strength and strain values of the resultant composites also enables to track the dissolution. Consequently, the strength and elongation values of each woven ASCs were calculated from the corresponding stress-strain curves, and plotted with respect to the dissolution times and temperatures, as presented in Figures 7.15a and 7.16a. The dissolution of woven silk fabrics in [C2mim][OAc] has demonstrated an equivalence between time and temperature through the construction of master curves for previous determined parameters. Therefore, here the same

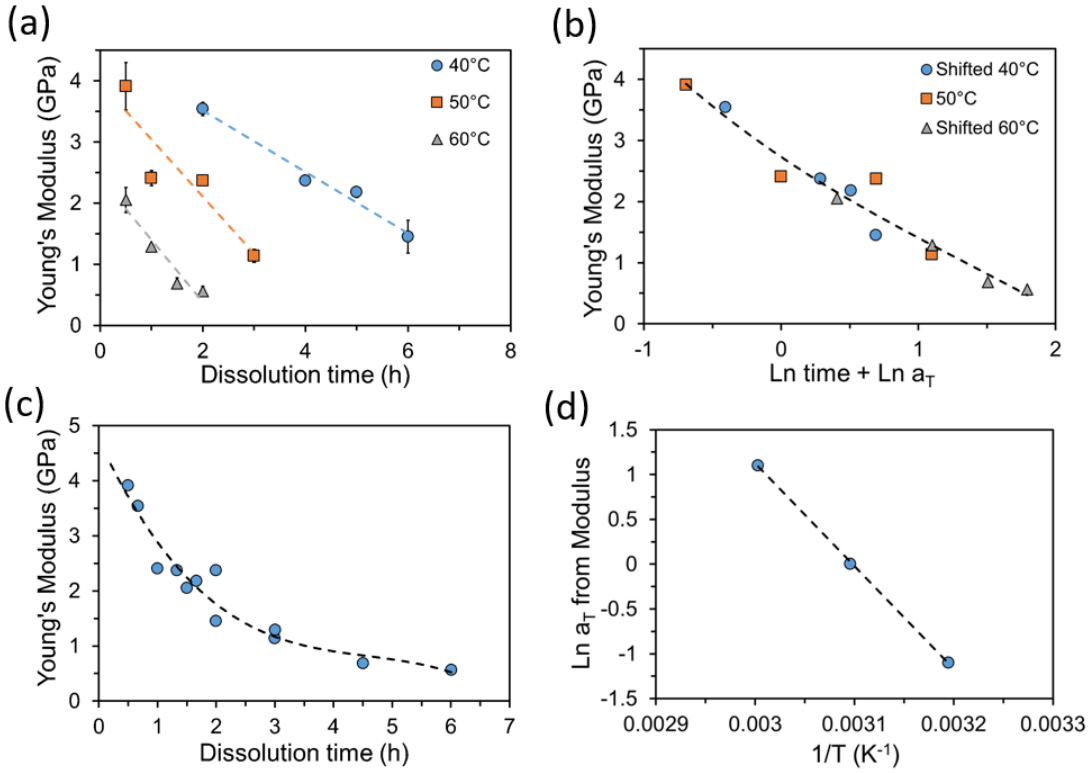

Figure 7.14: (a) Young's modulus change of each woven ASC at various dissolution times and temperatures, n = 3; (b) Master curve of shifted Young's modulus value of woven ASCs in ln space; (c) Each processed woven ASC as a function of dissolution time, at a reference temperature of 50 °C; the intercept of this curve gives unprocessed woven silk fabric Young's modulus to be 4.7 GPa; (d) Shifted factors ($\ln a_T$) from fitting Young's modulus, as a function of inverse temperature, indicating Arrhenius behaviour; the dashed lines in (a) and (c) are guide for the eye, and those in (b) and (d) are second-degree polynomial and linear fitting lines, respectively.

shifting method was employed for strength and strain values, with data from each temperature were individually shifted in the natural logarithmic time and the master curves were formed (Figures 7.15b and 7.16b). Next, the change of strength and strain were next expressed in linear dissolution time and shown in Figures 7.15c and 7.16c. As expected, the strength value of woven ASCs decrease with the increased dissolution time as a result of the amount of weak matrix phase is continuously during dissolution, recalling Equation 4.7. Similarly, elongation

at break values start to decrease from the beginning of the dissolution due to the brittle matrix phase is formed during the fabrication of woven ASCs, see Table 4.1 for the determined matrix phase tensile properties. The shift factors needed to generate the master curves were plotted against the inverse temperatures and presented in Figures 7.15d and 7.16d, which yield another two measurements of E_a, have values of 87 ± 7 kJ/mol (strength data) and 92 ± 26 kJ/mol (strain data). Consequently, the dissolution activation energies for woven silk fabrics dissolved in [C2mim][OAc] measured from four different methods give an average value of 92 ± 2 kJ/mol.

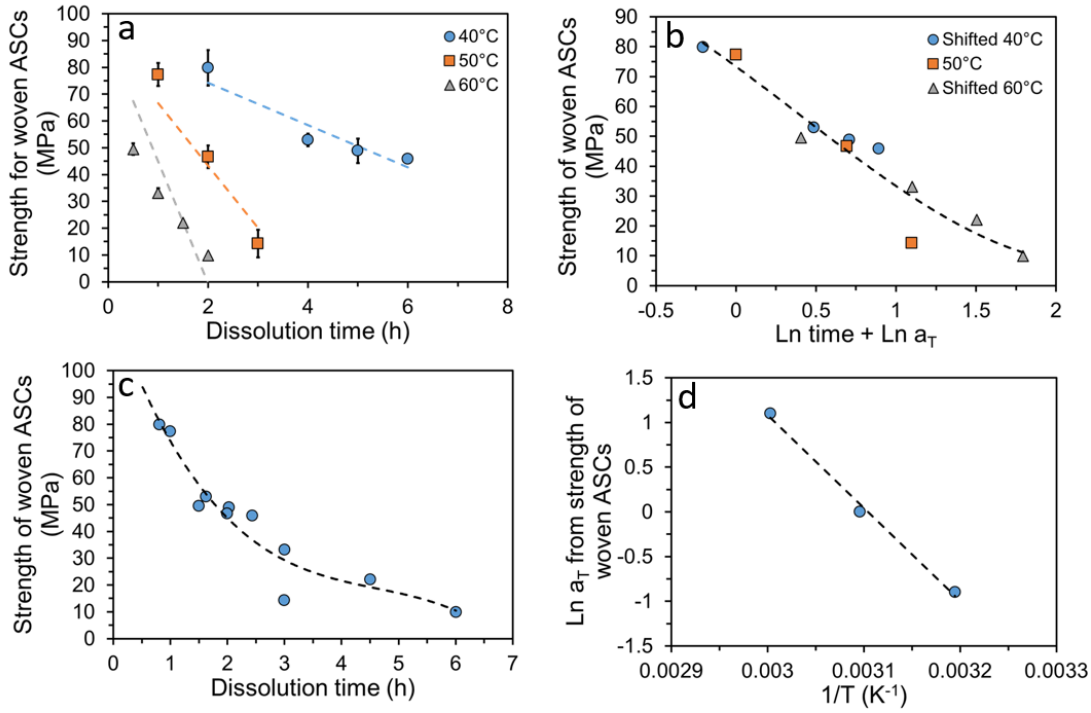

Figure 7.15: (a) The changes of strength values of each woven ASC at various dissolution times and temperatures, n = 3; (b) Master curve of shifted strength value of woven ASCs in ln space; (c) Each processed woven ASC as a function of dissolution time, at a reference temperature of 50 °C; (d) Shift factors ($\ln a_T$) from fitting strength, as a function of inverse temperature, indicating Arrhenius behaviour; the dashed lines in (a) and (c) are guide for the eye, and those in (b) and (d) are second-degree polynomial and linear fitting lines, respectively.

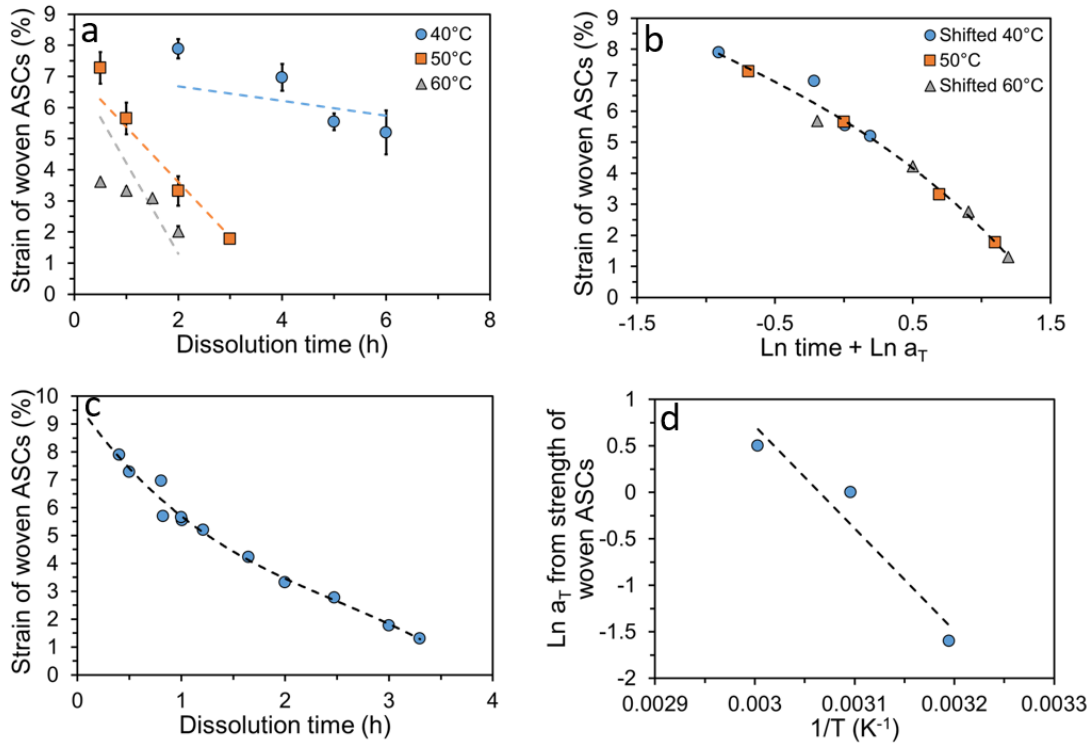

Figure 7.16: (a) The changes of strain values of each woven ASC at various dissolution times and temperatures, n = 3; (b) Master curve of shifted strain value of woven ASCs in ln space; (c) Each processed woven ASC as a function of dissolution time, at a reference temperature of 50 °C; (d) Shift factors ($\ln a_T$) from fitting strain, as a function of inverse temperature, indicating Arrhenius behaviour; the dashed lines in (a) and (c) are guide for the eye, and those in (b) and (d) are second-degree polynomial and linear fitting lines, respectively.

7.3.6 Comparison of Dissolution Activation Energies and Dissolution Speed between Three Arrangements of Silk Fibres

In combination with the studies on woven silk fabrics displayed in this chapter, and the findings on the other different arrangement of silk fibres - single silk threads (Chapter 4), and array silk threads (Chapter 6), here it is interesting to summarise and compare the measured corresponding E_a and dissolution speeds for three different arrangement of silk fibres.

A comparison of the measured dissolution activation energies of three arrangements of silk fibres in [C2mim][OAc] is presented in Table 7.1. Considering the errors of the measurements, it is suggested that the energies required for the dissolution of single or array silk threads to occur are approximately equal, however, a slightly lower E_a is calculated for dissolving woven silk fabrics. One of the possible reasons could be the weaving process introduces excessive abrasion which would result in the fabric damage [309], therefore a lower activation energy is observed for the woven silk fabrics.

Method	Dissolution activation energy (kJ/mol)		
	Single ASCs	Array ASCs	Woven ASCs
P_2	138 ± 13	121 ± 20	95 ± 17
Young's Modulus	116 ± 12	135 ± 15	95 ± 2
Strength	139 ± 19	140 ± 19	87 ± 7
Strain	118 ± 10	97 ± 22	92 ± 26
Average	128 ± 6	123 ± 10	92 ± 2

Table 7.1: A comparison of the activation energies of three arrangements of silk fibres dissolved in [C2mim][OAc], measured through four different methods, alongside with the individual average E_a values.

Studies on the kinetics and mechanisms of the dissolution of silk are still

very limited. Laity and Holland [310] have reported that the rheology of the liquid feedstock of *B. mori* changes with temperature, and was found to have an activation energy (E_a) of flow range from 30.9 to 55.4 kJ/mol. Some researchers have done thermal analyses on silk, Liu et al. [311] has reported the decomposition E_a for the native silkworm silk, ranging 194 - 217 kJ/mol; Liu et al. [312] has studied the decomposition E_a for silk fibroin films and found values between 158 to 190 kJ/mol. However, to the best of author's knowledge, there are no studies that investigate the dissolution dynamics of woven silk fabrics when using the partial dissolution method to prepare woven all silk composites.

Additionally, the dissolved and coagulated matrix within three ASCs with different fibre arrangements have been individually quantified through the measurement of V_m, and the change of V_m with respect to linear dissolution time have been presented as master curves with all three curves displaying time-temperature equivalence, recalling Figures 4.18b, 6.3c and 7.11c. Hence, it would be of interest to compare the dissolution speeds for these three arrangement silk fibres when dissolved in the same chosen solvent - [C2mim][OAc]. Consequently, master curves of V_m from single, array and woven were implemented and combined in one graph, with various temperature sets individually superimposed towards the same chosen reference temperature (50 °C), the resulting curve is presented in Figure 7.17. Different dissolution speeds between three fibre systems are revealed through the observed different gradients of the curves. Interestingly, the dissolution speeds decrease with the increased silk:solvent ratio, when impregnating woven silk fabrics in [C2mim][OAc], longest dissolution time is needed to achieve the same amount of V_m under same dissolution temperature comparing to single and array silk threads systems.

It is likely that the viscosity of [C2mim][OAc] is increased with the increased silk:solvent ratio, thus the solvent diffusion rate is dramatically decreased in the woven silk fabric system. In addition, due to the geometry difference, single thread is expected to expose larger relative contact area to [C2mim][OAc] than the woven fabric, which would lead to a easier access for [C2mim][OAc] to break

inter- and intra-hydrogen bonds between silk molecules to conduct the dissolution process, thus resulting in the observed fastest dissolution speed.

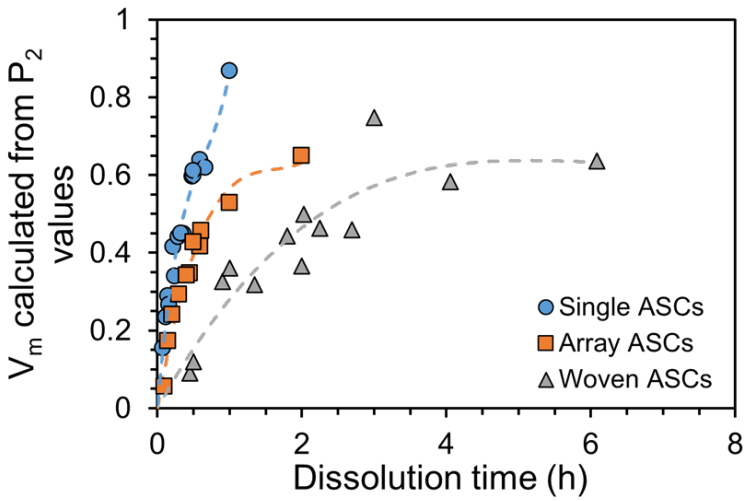

Figure 7.17: Comparison of V_m master curves from single, array and woven ASCs over a linear dissolution time, at a reference temperature of 50 °C; the lines are guide for the eye.

7.3.7 Rule of Mixture Theory Applied on Young's Modulus and Volume Fraction of Matrix (V_m)

It would be of interest to see how measured Young's modulus values of each fabricated woven ASC correlate with the V_m (measured from P_2), and to assess the applicability of the rule of mixtures (ROM) in our woven composite, as well as evaluate the effect of reinforced fibre volume on the resulting mechanical performance.

Consequently, as showed in Figure 7.18, the previously measured master curve of woven ASCs Young's modulus value (Figure 7.14c) is plotted against the corresponding V_m master curve values (Figure 7.11c). According to the well-established ROM principle [9, 313], the behaviour of certain properties in a composite material lies within two boundary lines, the Voigt (parallel and upper bound) [260, 261] and Reuss (series and lower bound) [262]. Plotting the two boundary curves requires input of two limiting moduli values, from the ordered raw woven silk fabric and the coagulated SF film (matrix), respectively. The modulus value of raw woven silk fabric is obtained from extrapolating the modulus TTS curve (Figure 7.14c), and shows a value of 4.7 GPa. While the matrix modulus is acquired from previous three-point bending tests on coagulated SF film, and gave a value of 0.5 GPa.

The Voigt series assumes a perfect bonding between fibre and matrix, as well as that both the fibre and matrix are arranged in parallel, so that the strain in each phase will be the same when the stress is loaded axially. Whereas the Reuss series assumes both phases are arranged in series so that the stress in each phase will be equal [9, 263]. It can be noticed that, as expected, all the master curve data points lie between the two boundary lines, and the modulus reduces with the decrease in volume fraction of fibre. A similar observation can be found from a paper by Yan et al. [314], where they fabricated woven natural fibre/polymer composites using three different fibres including flax, linen and bamboo, comprising the epoxy as matrix, and use ROM Voigt series to predict their theoretical tensile strength and tensile modulus values. In their work [314],

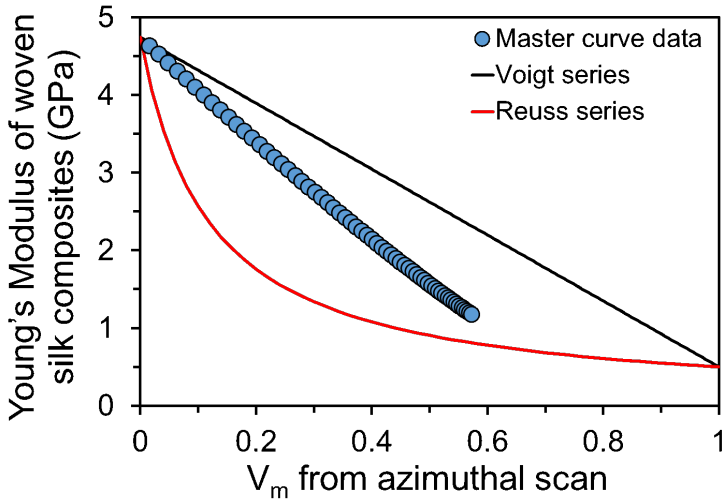

Figure 7.18: Rule of mixture curve for woven ASCs Young's modulus in the weft direction as a function of the corresponding V_m, with Voigt and Reuss boundary lines to demonstrate the rule of mixture theory.

they found the tensile modulus values of woven flax/epoxy, woven linen/epoxy and bamboo/epoxy are deviated by -12.3 %, -15.6 % and -8.2 %, respectively, from the predicted Voigt model when the fibre volume fraction is ∼55 %.

7.3.8 Effects of Reducing Agent on the Mechanical Behaviour of the Woven ASCs

It has been discovered in Chapter 5, section 5.3.3, that the addition of reducing agent, Na_2SO_3, as part of the solvent to prepare single ASCs does not change the dissolution rate when compared to single ASCs fabricated from pure IL system (see Figure 5.9). However, recalling Figure 5.10, it is demonstrated that the mechanical performance of the resultant single ASCs were improved, including the corresponding Young's modulus, strength and elongation values. From the plotted ROM curve, the single ASCs prepared from IL/RA system displayed a better stress transfer compared to that from pure IL system, recalling Figure 5.13. There was one question arose from Chapter 5 regards the quantification of the effects of RA on the interfacial bonding between fibre and matrix.

Therefore, it is of interest here to investigate the effects of Na_2SO_3 on the mechanical properties of the resultant woven ASCs, including the strength, elongation, Young's modulus and most importantly, the peel strength. Table 7.2 compares the mechanical properties of woven ASCs fabricated from the same time and temperature (60 °C for 1 hour), when using pure IL and IL/RA solvent systems.

	Strength(MPa)	Elongation(%)	Young's modulus(GPa)
Woven ASC from pure IL	33 ±2	3.3 ±0.11	1.3 ±0.030
Woven ASC from IL/RA	32 ±1	4.1 ±0.10	2.0 ±0.10

Table 7.2: The mechanical properties of woven ASCs fabricated from 60 °C for 1 hour, when using pure IL and IL/RA solvent systems, n = 2.

Additionally, the peel tests were conducted on the two layers woven ASCs fabricated from 60 °C for 1 hour with and without the presence of RA, following the protocols introduced in section 3.5.3, in order to evaluate the effects of RA on the adhesion between fibre and matrix, which was quantified as peel strength value. Figure 7.19 illustrates the corresponding force-extension graphs obtained from the peel tests. By neglecting the initial and final state, the individual average peel force was only calculated from the steady region and plotted as a solid line across the respective region. Figure 7.19a clearly demonstrates an increased average peel force for the woven ASCs fabricated using the IL/RA solvent system, 27.5 N, when comparing to that from the pure IL system, 25.5 N. Similarly, a higher average peak peel force is measured for woven ASCs fabricated from IL/RA system, 33.5 N, comparing to 30.0 N from pure IL system, as presented in Figure 7.19b. While the width of the two tested woven ASCs were equal (20 mm), utilising Equation 3.8 leads to the calculation of the peel strength on the corresponding woven ASCs fabricated from pure IL and IL/RA systems, give values of 1.28 N/mm and 1.37 N/mm, respectively.

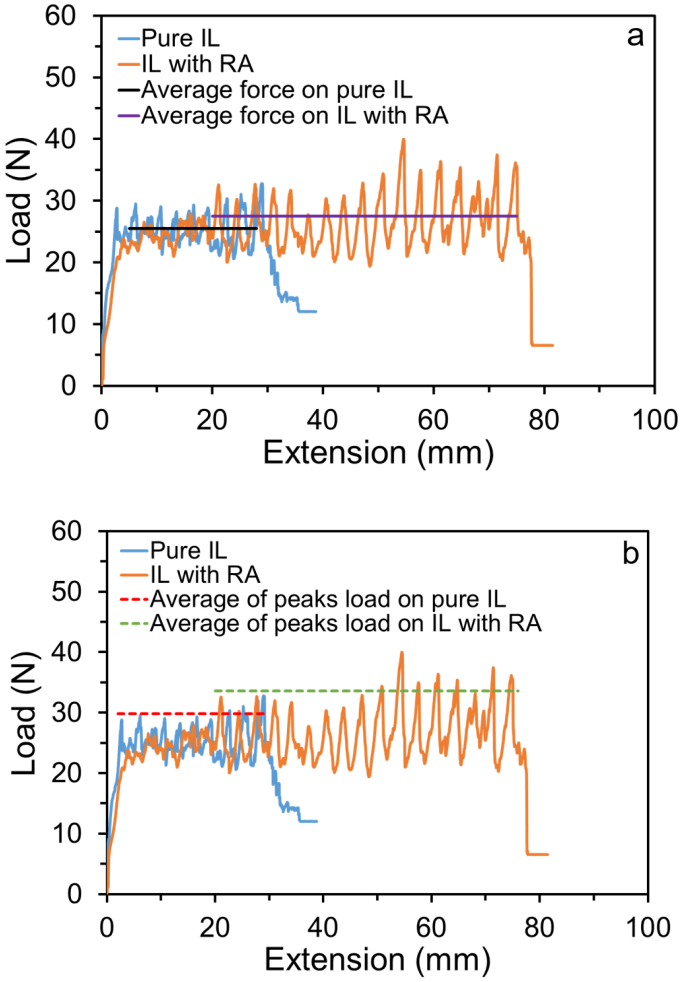

Figure 7.19: Peel test conducted on woven ASCs fabricated at 60 °C for 1 hour, using IL and IL/RA solvent systems. (a) The respective average peel force is indicated using different colour solid lines. (b) The average load from all peaks is expressed in different colour dashed lines.

The interfacial adhesion is a significant factor in controlling the performance of laminated composites. The woven ASC fabricated using IL/RA displays a higher average peel force and increased peel strength value, which suggests the interfacial adhesion between fibre and matrix is coherently improved when using reducing agent as part of the solvent. This observation indeed agree with the initial study on single ASCs fabricated using IL/RA (Chapter 5) that rule of

mixture plot (Figure 5.13) indicated a enhanced stress transfer between fibre and matrix when comparing with single ASCs fabricated only with IL.

7.4 Summary

In this Chapter, single layer woven all silk composites were fabricated from various times and temperatures using the partial dissolution method with the ionic liquid 1-ethyl-3-methylimidazolium acetate ([C2mim][OAc]) as the solvent and methanol as the coagulant. The resulting woven ASCs properties were studied using optical microscopy, WAXD azimuthal scans and tensile tests measurements. The WAXD azimuthal scans obtained from two thread directions were found to be overlapped to one another after shifting one direction alpha intensities across x-axis. Correspondingly, the average orientation (P_2) from two directions were revealed to be linearly related, the sum of individual P_2 was found to be 0.5. Hence the characterisation on the woven ASCs was carried out on one thread direction.

Through following the changes in the orientation of crystallites in woven ASCs, and the employment of the second legendre polynomial function, different P_2 values were obtained from woven ASCs processed at various times and temperatures. In accordance with the TTS principle, the master curve of P_2 obtained from various times and temperatures was constructed. Tracking the amount of matrix generated was achieved by calculating the V_m from the corresponding P_2 values using a linear mixing rule. They were both found to have Arrhenius-type behaviour, and the dissolution rate was increased rapidly at early dissolution hours and slowed down afterwards (Figure 7.11c). The dissolution activation energy was calculated to be 95 ± 17 kJ/mol. To our best knowledge, it is the first time using time-temperature superposition principle to quantify the dissolution activation energy of woven silk fabrics with [C2mim][OAc].

The tensile properties of each woven ASC were also measured, including the

measurements of Young's modulus, breaking strength and elongation at break values. It was evident from the construction of master curve that the dissolution of woven silk fabrics in [C2mim][OAc] follows time-temperature superposition principle. Thus, the same TTS shifting method was applied to three determined tensile parameters. Activation energies were individually calculated from the gradients of the Arrhenius plots, give values of 95 ± 2 kJ/mol (Young's modulus measurements), 87 ± 7 kJ/mol (breaking strength measurements) and 92 ± 26 kJ/mol (elongation at break measurements). Three different methods all point to a very close dissolution activation energy of woven silk fabric in [C2mim][OAc], within the errors of each measurement. Hence, the average activation energies obtained from four different methods in this chapter for the dissolution of woven silk fabrics in [C2mim][OAc] to occur is measured to be 92 ± 2 kJ/mol.

In combination with the studies present in early Chapters on single and array silk threads, the dissolution activation energies and dissolution speeds of silk fibres in three different arrangements were compared. The required energies for the dissolution of single and array silk threads were found to be approximately the same, 128 ± 6 kJ/mol (single silk threads) and 123 ± 10 kJ/mol (array silk threads); while a slight lower E_a was measured for dissolving woven silk fabrics (92 ± 2 kJ/mol). This may due to the excessive abrasion during the weaving process and causes fabric damage, thus a lower required energy was observed. Though the E_a for dissolving woven silk fabrics was found to be lowest within three silk fibres, the slowest dissolution speed was observed when dissolving woven silk fabrics (Figure 7.17). The dissolution speeds were found to follow the order (from fast to slow): single silk threads > array silk threads > woven silk fabrics. It is likely due to the increased silk : solvent ratio leads to an increase in the viscosity of [C2mim][OAc] thus decreased the solvent diffusion rate. Another possible reason may be single silk thread is likely to expose larger relative contact area for [C2mim][OAc] to act upon, and provide an easier access to break inter- and intra-hydrogen bonds between silk molecules. These observations imply that the dissolution activation energy is an independent factor to the dissolution speed.

The measured Young's modulus values of woven ASCs were also correlated

with V_m to generate a rule of mixture curve (Figure 7.18), and found our prepared woven ASCs lies between two boundary lines. However, discrepancies were observed between experimental results and theoretical predicted values (Voigt boundary line), which is likely due to the imperfections in the fibre-matrix interface [265–269]. Last but not least, the effects of reducing agent on the mechanical performance of woven ASCs were explored. Woven ASCs fabricated from 60 °C for 1 hour using IL/RA as the solvent system found to have enhanced ductility and stiffness comparing to the one fabricated from pure IL system (Table 7.2). The observed higher peel strength value for woven ASCs processed from IL/RA system further reveal that the addition of reducing agent as part of solvent improves the interfacial adhesion between fibre and matrix, which is in good agreement with the studies on single silk threads dissolved in IL/RA system. These findings can hopefully be helpful for future research into silk-based woven composites with many broad applications.

Chapter 8

Conclusions and Outlook

8.1 Summary of Findings

In the present studies, the dissolution dynamics of *B. mori* silk fibres in the ionic liquid [C2mim][OAc] were explored. The effects of time, temperature, fibre geometry, addition of reducing agent on the dissolution behaviour and the properties of the resulting all-silk composites were investigated. A new approach was introduced where following the orientation change of silk nanocrystallites allowed to track the dissolved and coagulated silk matrix fraction (V_m). It was evident the dissolution depends on both time and temperature, and construction of master curves further suggests the dissolution procedure follows time-temperature superposition principle. The findings described in this thesis provide a fundamental understanding of the dissolution kinetics of silk fibres in [C2mim][OAc]. The main findings and achievements are summarised below.

Dissolution of single silk threads in [C2mim][OAc]

In Chapter 4, single silk threads were first employed as the fibre source, to study the dissolution behaviour. All-silk composites derived from single silk threads were fabricated using partial dissolution method, with [C2mim][OAc] as the solvent and methanol as the coagulant. Through varying the dissolution time and temperature, a series of single ASCs were fabricated. The dissolution dynamics and properties of the prepared single ASCs were analysed using various tech-

niques, including optical microscope, scanning electron microscope, WAXD azimuthal scans and mechanical testing.

The cross-sectional images of the single ASC fabricated from relatively low temperature and short time (30 °C-0.5 h) revealed that one raw silk thread contains several hundred filaments, and large gaps between each filament were seen. The cross-sectional images of single ASCs prepared from 30, 40 and 50 °C for different length of time revealed that under the same dissolution temperature, the diameter of the remaining silk thread core reduces with time. In combination with the SEM images, it is evident that the dissolved fibres were coagulated and turned into the matrix phase, appearing in the outer layer of the thread core and surrounding at the surface of individual filaments, to fill the gaps and form a close-packed silk composite. Meanwhile, the changes of tensile strength and Young's modulus values of single ASCs prepared from various time under 30 °C individually displayed an initial increase to a peak value at time 2h, 420 ± 3 MPa (tensile strength), 11.6 ± 0.4 GPa (Young's modulus), then declined thereafter. This phenomenon was then proposed as the 'preformed stage', correlates to the process when the ionic liquid infiltrated into the large gaps between each silk filament, dissolved the surface layer of filaments which will then further coagulate into matrix to fill the gaps and form a tightly packed thread core. As a result, strong bond between fibre and matrix was subsequently formed, and provided a good stress transfer, leading to the observed peak values of tensile strength and Young's modulus. In combination with the microscope images and measured tensile properties, the dissolution procedure for a single silk thread was proposed.

Through conducting WAXD azimuthal scans on the fabricated single ASCs, distinct differences were observed for the diffraction curves collected from unprocessed silk thread, single ASC (partially dissolved) and silk fibroin film (completely dissolved and coagulated matrix phase). The differences were found corresponding to the changes of their average crystalline orientation. Radial integrations were carried out on the corresponding curves, enabling the calculation of P_2 values. Average P_2 values were found directly related to the fraction of original silk fibres and the fraction of matrix. Consequently, the dissolved silk

volume fraction of matrix (V_m) was measured using the corresponding P_2 values, through a simple linear mixing rule. Both P_2 and V_m values were found to have time and temperature dependencies, and the success construction of their master curves further revealed both parameters obey time-temperature superposition principle. Upon plotting the required shift factors against the inverse temperatures, linear relationships were shown. Arrhenius-type behaviour was therefore established, leading to the calculation of the activation energies, gave values of 138 ± 13 kJ/mol (P_2 measurements) and 139 ± 15 kJ/mol (V_m measurements).

Upon applying the same shifting method to the measured tensile parameters, including ultimate tensile strength, Young's modulus and elongation at break, it was interesting to notice from their master curves that all three parameters demonstrated time-temperature equivalence. These observations led to the construction of their Arrhenius plots, yielding another three methods to determine activation energies. The dissolution activation energies were suggested to have values of 116 ± 12 kJ/mol, 139 ± 19 kJ/mol, and 118 ± 10 kJ/mol, from Young's modulus, ultimate strength, and elongation at break measurements, respectively. The average dissolution activation energy for single silk threads in [C2mim][OAc] derived from four measurements were found to give a value of 128 ± 6 kJ/mol. Additionally, the effectiveness of stress transfer between fibre and matrix was able to be estimated through the application of rule of mixtures models. From the plot of Young's modulus versus the corresponding V_m, it was suggested that the fabricated single ASCs lie between Voigt and Reuss model with a closer fit to the Voigt model. It was also evident from the plot of elongation at break against V_m that single ASCs not strictly follow the iso-strain conditions. Moreover, tensile strength values versus V_f followed the well-documented axial tensile failure theory for the system when fibre has higher breaking strain than matrix, and revealed that the strength of the resulting composites heavily depends on the fibre strength, leading to the suggestion that a proper selection of V_f plays a key role for strengthening the composites.

Dissolution of single silk threads in [C2mim][OAc] with the addition of reducing agent, sodium sulfite

In Chapter 5, single ASCs were prepared from a number of times and temperatures using the same dissolution method, however, this time reducing agent Na_2SO_3 was added as part of solvent. The effects of the addition of reducing agent on the dissolution activation energy and dissolution rate were investigated. Comparing to the results obtained from pure IL system, similar observations on the changes of P_2 and V_m as a function of time and temperature were separately observed. Moreover, both measured Young's modulus and breaking strength exhibited initial rise to the maximum value and fall afterwards, it is perceptible that the changes associate with the 'preformed stage', as elucidated when using pure IL as the solvent.

Data derived from P_2, V_m, Young's modulus, strength and elongation at break were individually shifted towards their chosen reference temperature sets in natural logarithmic time, enabled the construction of master curves. Upon doing so, the equivalence of time and temperature on the four measured parameters were separately displayed, and indicated that dissolution of silk threads in IL/RA system equally followed time-temperature superposition. From their Arrhenius plots, it was intriguing to see four different methods yielded similar activation energies and gave an average value of 120 ± 3 kJ/mol, which led to the suggestion that a marginally lower E_a was required in IL/RA system than pure IL system (128 ± 6 kJ/mol) for the occurrence of dissolution.

Moreover, master curves of four measured parameters in logarithmic time obtained from IL/RA system were separately plotted together with those obtained from pure IL system, and the dissolution rates were compared through analysing the amount needed to be horizontally shifted to make them overlapped. Interestingly, the dissolution rates between two solvent systems were found to remain unchanged, however, enhanced tensile properties were observed for single ASCs fabricated from IL/RA system with respect to those from pure IL system. SF film cast from IL/RA solvent appeared to have higher strength and elongation

at break values (15.0 ± 0.3 MPa, 1.0 ± 0.1 %) than that from pure IL system (10 ± 2 MPa, 0.60 ± 0.01 %), which was expected to result in a better interfacial adhesion between fibre and matrix. In fact, single ASCs fabricated from IL/RA system demonstrated a closer fit to Voigt model, which further verified that there is improved stress transfer between fibre and matrix. These results demonstrated that adding reducing agent as part of solvent is clearly useful if one is interested in improving the ductility of the silk fibroin film and the overall mechanical performance of the silk-based composites.

Dissolution of array silk threads in [C2mim][OAc]

In Chapter 6, silk threads in a different alignment-array silk threads, were employed to explore the potential influences of fibre arrangement on the dissolution activation energy and dissolution speed. WAXD azimuthal scans and mechanical testing were performed as a means to determine the average crystalline orientation (quantified as P_2 values), V_m, Young's modulus, breaking strength and elongation at break values for the obtained array ASCs.

P_2 values undergo a linear decline with time and more rapidly at higher temperatures, time-temperature equivalence was once again verified through the construction of its master curve. Same shifting method was applied to V_m values as a means to form its master curve. Mirror-like images were noticed for P_2 and V_m master curves, with one decreasing and one increasing rapidly during early dissolution hours, and both slow down afterwards. Similarly, all three measured tensile parameters were separately found to increase to a maximum value and fall thereafter. It was interesting to see all four measurements consistently suggested the existence of 'preformed stage' when array silk threads were dissolved in pure IL system. After removing the data associated with 'preformed stage', three measured tensile properties were individually time-temperature superimposed, their master curves were subsequently generated. Upon separately plotting obtained shift factors versus the inverse temperatures, linear relations were once again found, indicating Arrhenius behaviour. Accordingly, the average E_a when array threads dissolved in [C2mim][OAc] was therefore measured from four different

methods, gave a value of 123 ± 10 kJ/mol, which was approximately the same as the dissolution of single silk threads in [C2mim][OAc] system (128 ± 6 kJ/mol), when errors of measurements were taken into account. Furthermore, the plot of master curves of V_m with respect to dissolution time, derived from two different fibre alignments, revealed that array silk threads have a slower dissolution rate. Overall, the work presented in this Chapter showed that the fibre arrangement has very little effect on the dissolution activation energy, however, significantly impact the dissolution speed. This work may have some utility on the design and fabrication of silk fibres reinforced composites with different fibre geometry requirements.

Dissolution of woven silk fabrics in [C2mim][OAc]

In Chapter 7, the study on the dissolution dynamics was carried out on the single layer of woven silk fabrics in the ionic liquid [C2mim][OAc]. The optical microscope cross-sectional images revealed that raw woven silk fabric possesses a thread count of $\sim 1.5 : 1$ (weft : warp); whilst the thickness of matrix layer was measured to be $\sim 1 : 2$ (weft : warp) within one woven ASC, the significantly larger space between each warp bundle allowed more matrix to be generated might be the cause of this. 2D diffraction pattern on raw woven silk fabric revealed that weft threads contain more highly aligned crystallites, which agreed with the corresponding WAXD azimuthal diffraction curves, that peak height at $\alpha = 0°$ from weft direction scan was almost two times higher than warp direction. Moreover, diffraction curves of woven ASCs collected when either weft or warp threads held perpendicular to the x-ray incident beam were found able to be overlapped after shifting alpha intensities of one direction horizontally across. It was further evident that their corresponding P_2 values were linearly related to one another, with a relationship of $P_2^{weft} + P_2^{warp} = \frac{1}{2}$. This finding confirms that the same information with regards to the changes of average crystalline orientation (P_2) values should be revealed regardless the direction that the woven ASC is being held.

The average crystalline orientation within woven ASCs was then analysed

through collecting WAXD azimuthal diffraction curves from one of the thread directions. Time-temperature equivalence on the measured P_2 and V_m values were again revealed through the successful construction of their master curves. Through calculating the gradients of their Arrhenius plots, activation energies were separately measured. It was interesting to note that both parameters being mathematically related, same E_a values were determined, gave value of (95 ± 17 kJ/mol). Once again, three measured tensile properties were demonstrated to follow TTS principle, yielding another three methods to calculate the E_a. Activation energies determined from four different methods were found to have similar values, giving an average E_a value of 92 ± 2 kJ/mol.

Overall, E_a derived from three different alignments of silk fibres studied in this work were compared, it was found that dissolving single (128 ± 6 kJ/mol) and array (123 ± 10 kJ/mol) silk threads required approximately the same E_a, while a noticeable lower E_a was measured for the dissolution of woven silk fabrics in [C2mim][OAc] (92 ± 2 kJ/mol). The potential of the fabric damage during the weaving process was thought to result in the observed lower required E_a for dissolving woven silk fabrics in [C2mim][OAc]. Furthermore, the speeds for dissolving these three alignments of silk fibres were found to follow the order (from fast to slow): single silk threads > array silk threads > woven silk fabrics. This was thought heavily related to the changes in the solvent diffusion rate and the exposed contact area of silk fibres. Nevertheless, it was evident from this study that the dissolution activation energy is an independent factor to the dissolution speed. Moreover, it was intriguing to see ductility, stiffness and peel strength of woven ASC fabricated using IL/RA were improved compared to that prepared from pure IL. Furthermore, it is demonstrated that in order to better design and control the properties of the fabricated composites, sufficient amount of fibre volume fraction must be considered. The work discussed in this thesis opens up new possibilities to fabricate all silk composites or silk fibres reinforced composites using ionic liquid. This is an important step in understanding and, in future, exploiting the time-temperature superposition principle on investigation of the dissolution behaviour and opening the door to experimentally fabricate all silk composites with many broad applications.

8.2 Suggestions for Future Work

The summary of the findings has been presented, the following suggestions aim to serve as a guide for any potential future work. These suggestions can be divided into two categories.

The first series of suggestions regarding the improvements for the studies on the dissolution kinetics, are listed below:

- It was suggested in Chapter 7, that the solvent diffusion rate may have an impact on the dissolution rate, thus future investigation can be performed on studying the viscosity of the solution, in order to explore the apparent energy of viscous flow within different fibre arrangement systems.
- It would also be interesting to study the heat transfer/enthalpy during dissolution, in particular comparing the enthalpies between the dissolution of silk fibres and silk fibroin films, in order to gain insight into the associated heat/energy to break the highly ordered crystalline structure.
- The effects of water on the solubility for dissolving silk fibres in ionic liquid or other solvents are worth exploring. It is anticipated that the presence of water can change the solvent properties, thus the solubility.
- The work present in this study was limited to one type of ionic liquid, due to the restrictions in terms of laboratory access times. However, it is known that a number of different ionic liquids are capable of dissolving silk fibres. Hence, it might also be interesting to expand the experimental matrix and investigate the dependence of activation energy on the type of ionic liquid, since it should provide a bigger picture for the dissolution kinetics study.

The next group of suggestions focuses on the enhancements of the properties of silk-based composites, which are considered below:

- It was evident from the study in Chapter 4 that the reinforcing silk fibre has much higher ductility than the coagulated silk matrix, and results from

Chapters 5 and 7 revealed that adding reducing agent as part of solvent improved the SF film mechanical properties, and the overall adhesion between fibre and matrix in 2 layers woven composites. Therefore, an in-depth study, focusing on the improvement of matrix ductility would be helpful to enhance the properties of woven composites. It is expected that coagulation conditions have significant impact on the structure and properties of the resulting silk fibroin film due to the conformational transitions. It would be interesting to further measure the molecular weight, secondary structure of the silk fibroin film as an aid for exploring the optimum coagulation condition. Another possible way to improve the ductility of the matrix is to employ binary systems, such as blending with other natural fibres (cellulose, wool, chicken feathers, etc.)

- The master curves constructed in this study as well as the proposed 'preformed stage' indicates that a proper selection of volume fraction of matrix is crucial for strengthening the composite, thus it is important to further investigate other methods to analyse the V_m.

- To prepare the composite with desirable properties, the information gained from the constructed master curves must be utilised. Furthermore, model-based design of experiments may be employed to explore the optimum fabrication condition and required V_m, as a result of preparing the composite with preferred properties.

References

[1] T.W. Clyne and D. Hull. *An Introduction to Composite Materials*. Cambridge solid state science series. Cambridge University Press, 2019. xiii, 6, 7

[2] Qingqing Yuan, Jinrong Yao, Xin Chen, Lei Huang, and Zhengzhong Shao. The preparation of high performance silk fiber/fibroin composite. *Polymer*, 51(21):4843–4849, 2010. xiii, 11, 16, 17, 18, 135

[3] N. Soykeabkaew, T. Nishino, and T. Peijs. All-cellulose composites of regenerated cellulose fibres by surface selective dissolution. *Composites Part A: Applied Science and Manufacturing*, 40(4):321–328, 2009. xiii, 3, 10, 11, 12

[4] I. Belhaj Khalifa, N. Ladhari, and M. Touay. Application of sericin to modify textile supports. *Journal of the Textile Institute*, 103(4):370–377, 2012. xiii, 13

[5] M.K. DeBari and R.D. Abbott. Microscopic considerations for optimizing silk biomaterials. *Wiley Interdisciplinary Reviews: Nanomedicine and Nanobiotechnology*, 11(2), 2019. xiii, 14, 15

[6] J. Stanton, Y. Xue, P. Pandher, L. Malek, T. Brown, X. Hu, and D. Salas-de la Cruz. Impact of ionic liquid type on the structure, morphology and properties of silk-cellulose biocomposite materials. *International Journal of Biological Macromolecules*, 108:333–341, 2018. xiii, 20, 21, 22, 23

[7] Kurt Ueberreiter and Frithjof Asmussen. Velocity of dissolution of polymers. part i. *Journal of Polymer Science*, 57(165):187–198, 1962. xiii, 29, 30

[8] Kazunori Tanaka, Naoki Kajiyama, Kiyohide Ishikura, Shou Waga, Aiko Kikuchi, Kohei Ohtomo, Takashi Takagi, and Shigeki Mizuno. Determination of the site of disulfide linkage between heavy and light chains of silk fibroin produced by bombyx mori. *Biochimica et Biophysica Acta (BBA)-Protein Structure and Molecular Enzymology*, 1432(1):92–103, 1999. xiv, 31, 32, 92

[9] D. Hull and T. W. Clyne. *Strength of composites*, page 158–207. Cambridge Solid State Science Series. Cambridge University Press, 2 edition, 1996. xvii, 85, 87, 88, 91, 111, 112, 167

[10] Gokul V Mahajan and Vishnu S Aher. Composite material: A review over current development and automotive application. *International journal of scientific and research publications*, 2(11):1–5, 2012. 1

[11] José Antonio Butenegro, Mohsen Bahrami, Juana Abenojar, and Miguel Ángel Martínez. Recent progress in carbon fiber reinforced polymers recycling: A review of recycling methods and reuse of carbon fibers. *Materials*, 14(21):6401, 2021. 1

[12] TP Sathishkumar, S Satheeshkumar, and Jesuarockiam Naveen. Glass fiber-reinforced polymer composites–a review. *Journal of reinforced plastics and composites*, 33(13):1258–1275, 2014. 1

[13] S Job. The uk carbon fibre composites industry. *NetComposites,. Connectra*, 2009. 1

[14] G Lin. Global carbon fibre composites market report; ata carbon fiber tech. *Guangzhou Co., Ltd.: Germany*, 2016.

[15] Sonia Melendi-Espina, CN Morris, TA Turner, and SJ Pickering. Recycling of carbon fibre composites. *Carbon 2016*, 2016. 1

[16] SJ Pickering and TA Turner. Research and development in support of carbon fibre recycling. *CAMX 2014–composite and advanced materials expo: Combined Strength. Unsurpassed Innovation*, 2014. 1

[17] Jin Zhang, Venkata S Chevali, Hao Wang, and Chun-Hui Wang. Current status of carbon fibre and carbon fibre composites recycling. *Composites Part B: Engineering*, 193:108053, 2020. 1

[18] Muhammad Furqan Khurshid, Martin Hengstermann, Mir Mohammad Badrul Hasan, Anwar Abdkader, and Chokri Cherif. Recent developments in the processing of waste carbon fibre for thermoplastic composites–a review. *Journal of Composite Materials*, 54(14):1925–1944, 2020. 1

[19] National Composites Centre. Uk to lead the development of the next generation of sustainable composite materials. 2020. 1

[20] Géraldine Oliveux, Luke O Dandy, and Gary A Leeke. Current status of recycling of fibre reinforced polymers: Review of technologies, reuse and resulting properties. *Progress in materials science*, 72:61–99, 2015. 2

[21] Géraldine Oliveux, Jean-Luc Bailleul, Arnaud Gillet, Olivier Mantaux, and Gary A Leeke. Recovery and reuse of discontinuous carbon fibres by solvolysis: Realignment and properties of remanufactured materials. *Composites Science and Technology*, 139:99–108, 2017. 2

[22] Steven Mulligan, Paul V Hatton, and Nicolas Martin. Resin-based composite materials: elution and pollution. *British Dental Journal*, 232(9):644–652, 2022. 2

[23] Tamara S Ledley, Eric T Sundquist, Stephen E Schwartz, Dorothy K Hall, Jack D Fellows, and Timothy L Killeen. Climate change and greenhouse gases. *Eos, Transactions American Geophysical Union*, 80(39):453–458, 1999. 2

[24] Donald J Wuebbles and Atul K Jain. Concerns about climate change and the role of fossil fuel use. *Fuel processing technology*, 71(1-3):99–119, 2001.

[25] TF Stocker, D Qin, GK Plattner, MMMB Tignor, SK Allen, J Boschung, A Nauels, Y Xia, V Bex, PM Midgley, et al. Contribution of working group i to the fifth assessment report of the intergovernmental panel on climate change. *Climate change*, 5:1–1552, 2013.

[26] YUE Xi-Liu and GAO Qing-Xian. Contributions of natural systems and human activity to greenhouse gas emissions. *Advances in Climate Change Research*, 9(4):243–252, 2018. 2

[27] Mikael Höök and Xu Tang. Depletion of fossil fuels and anthropogenic climate change—a review. *Energy policy*, 52:797–809, 2013. 2

[28] UN Desa et al. Transforming our world: The 2030 agenda for sustainable development. 2016. 2, 8

[29] A.-C. Corbin, D. Soulat, M. Ferreira, A.-R. Labanieh, X. Gabrion, P. Malécot, and V. Placet. Towards hemp fabrics for high-performance composites: Influence of weave pattern and features. *Composites Part B: Engineering*, 181, 2020. 2, 8

[30] Furqan Ahmad, Heung Soap Choi, and Myung Kyun Park. A review: natural fiber composites selection in view of mechanical, light weight, and economic properties. *Macromolecular materials and engineering*, 300(1):10–24, 2015. 2, 8, 9

[31] Lawrence T Drzal, AK Mohanty, and M Misra. Bio-composite materials as alternatives to petroleum-based composites for automotive applications. *Magnesium*, 40(60):1–3, 2001. 2, 8

[32] Michael Karus and Markus Kaup. Natural fibres in the european automotive industry. *Journal of Industrial Hemp*, 7(1):119–131, 2002. 2

[33] R Kozlowski, M Muzyczek, and B Mieleniak. Upholstery fire barriers based on natural fibers. *Journal of Natural Fibers*, 1(1):85–95, 2004. 2

[34] Yanjun Xie, Callum AS Hill, Zefang Xiao, Holger Militz, and Carsten Mai. Silane coupling agents used for natural fiber/polymer composites: A review. *Composites Part A: Applied Science and Manufacturing*, 41(7):806–819, 2010. 2

[35] Zili Yan, Jianchun Zhang, Hua Zhang, and Hao Wang. Improvement of mechanical properties of noil hemp fiber reinforced polypropylene composites by resin modification and fiber treatment. *Advances in materials science and engineering*, 2013, 2013. 2

[36] Owonubi J Shesan, Agwuncha C Stephen, Anusionwu G Chioma, Revaprasadu Neerish, and Sadiku E Rotimi. Fiber-matrix relationship for composites preparation. *Renewable and sustainable composites*, pages 1–30, 2019. 3

[37] Chengcheng Gao, Long Yu, Hongsheng Liu, and Ling Chen. Development of self-reinforced polymer composites. *Progress in Polymer Science*, 37(6):767–780, 2012. 3, 9, 10

[38] Numa J Capiati and Roger S Porter. The concept of one polymer composites modelled with high density polyethylene. *Journal of materials science*, 10(10):1671–1677, 1975. 3

[39] IM Ward and PJ Hine. Novel composites by hot compaction of fibers. *Polymer Engineering & Science*, 37(11):1809–1814, 1997. 3, 10

[40] P.J. Hine, I.M. Ward, N.D. Jordan, R. Olley, and D.C. Bassett. The hot compaction behaviour of woven oriented polypropylene fibres and tapes. I. Mechanical properties. *Polymer*, 44(4):1117–1131, 2003. 10

[41] IM Ward and PJ Hine. The science and technology of hot compaction. *Polymer*, 45(5):1413–1427, 2004. 10

[42] N Cabrera, B Alcock, J Loos, and T Peijs. Processing of all-polypropylene composites for ultimate recyclability. *Proceedings of the Institution of Mechanical Engineers, Part L: Journal of Materials: Design and Applications*, 218(2):145–155, 2004. 3

[43] T. Nishino, I. Matsuda, and K. Hirao. All-cellulose composite. *Macromolecules*, 37(20):7683–7687, 2004. 3, 10

[44] Chen Qin, Nattakan Soykeabkaew, Ni Xiuyuan, and Ton Peijs. The effect of fibre volume fraction and mercerization on the properties of all-cellulose composites. *Carbohydrate polymers*, 71(3):458–467, 2008. 3

[45] Haisong Qi, Jie Cai, Lina Zhang, and Shigenori Kuga. Properties of films composed of cellulose nanowhiskers and a cellulose matrix regenerated from alkali/urea solution. *Biomacromolecules*, 10(6):1597–1602, 2009. 3

[46] Raquel Arévalo, Olivier T Picot, Rory M Wilson, Nattakan Soykeabkaew, and Ton Peijs. All-cellulose composites by partial dissolution of cotton fibres. *Journal of Biobased Materials and Bioenergy*, 4(2):129–138, 2010.

[47] Mitsuhiro Shibata, Naozumi Teramoto, Taro Nakamura, and Yoshinobu Saitoh. All-cellulose and all-wood composites by partial dissolution of cotton fabric and wood in ionic liquid. *Carbohydrate polymers*, 98(2):1532–1539, 2013. 3

[48] Sirisart Ouajai and Robert A Shanks. Preparation, structure and mechanical properties of all-hemp cellulose biocomposites. *Composites Science and Technology*, 69(13):2119–2126, 2009. 3

[49] Ke Chen, Weixin Xu, Yun Ding, Ping Xue, Pinghou Sheng, Hui Qiao, and Jimin He. Hemp-based all-cellulose composites through ionic liquid promoted controllable dissolution and structural control. *Carbohydrate polymers*, 235:116027, 2020. 3

[50] J.E. Hawkins, Y. Liang, M.E. Ries, and P.J. Hine. Time temperature superposition of the dissolution of cellulose fibres by the ionic liquid 1-ethyl-3-methylimidazolium acetate with cosolvent dimethyl sulfoxide. *Carbohydrate Polymer Technologies and Applications*, 2, 2021. 3, 152

[51] W Gindl and Jozef Keckes. All-cellulose nanocomposite. *Polymer*, 46(23):10221–10225, 2005. 3, 10

[52] Wolfgang Gindl, Klaus J Martinschitz, Peter Boesecke, and Jozef Keckes. Changes in the molecular orientation and tensile properties of uniaxially drawn cellulose films. *Biomacromolecules*, 7(11):3146–3150, 2006.

[53] Benoît JC Duchemin, Roger H Newman, and Mark P Staiger. Structure-property relationship of all-cellulose composites. *Composites Science and Technology*, 69(7-8):1225–1230, 2009.

[54] Anthony Abbott and Alexander Bismarck. Self-reinforced cellulose nanocomposites. *Cellulose*, 17(4):779–791, 2010. 3

[55] Nattakan Soykeabkaew, Noriko Arimoto, Takashi Nishino, and Ton Peijs. All-cellulose composites by surface selective dissolution of aligned lignocellulosic fibres. *Composites Science and Technology*, 68(10-11):2201–2207, 8 2008. 3, 10, 71

[56] Bapan Adak and Samrat Mukhopadhyay. A comparative study on lyocell-fabric based all-cellulose composite laminates produced by different processes. *Cellulose*, 24(2):835–849, 2017.

[57] Wolfgang Gindl-Altmutter, Jozef Keckes, Johannes Plackner, Falk Liebner, Karl Englund, and Marie-Pierre Laborie. All-cellulose composites prepared from flax and lyocell fibres compared to epoxy–matrix composites. *Composites Science and Technology*, 72(11):1304–1309, 2012. 3

[58] Jinyang Li, Haq Nawaz, Jin Wu, Jinming Zhang, Jiqiang Wan, Qinyong Mi, Jian Yu, and Jun Zhang. All-cellulose composites based on the self-reinforced effect. *Composites Communications*, 9:42–53, 2018. 3

[59] Hoi-yan Cheung, Mei-po Ho, Kin-tak Lau, Francisco Cardona, and David Hui. Natural fibre-reinforced composites for bioengineering and environmental engineering applications. *Composites Part B: Engineering*, 40(7):655–663, 2009. 4

[60] Nathaniel Huebsch and David J Mooney. Inspiration and application in the evolution of biomaterials. *Nature*, 462(7272):426–432, 2009. 4

[61] Sinan Keten, Zhiping Xu, Britni Ihle, and Markus J Buehler. Nanoconfinement controls stiffness, strength and mechanical toughness of β-sheet crystals in silk. *Nature materials*, 9(4):359–367, 2010. 4

[62] Zhengzhong Shao and Fritz Vollrath. Surprising strength of silkworm silk. *Nature*, 418(6899):741–741, 2002. 12, 80

[63] Lin Römer and Thomas Scheibel. The elaborate structure of spider silk: structure and function of a natural high performance fiber. *Prion*, 2(4):154–161, 2008. 4

[64] Banani Kundu, Nicholas E Kurland, Subia Bano, Chinmoy Patra, Felix B Engel, Vamsi K Yadavalli, and Subhas C Kundu. Silk proteins for biomedical applications: Bioengineering perspectives. *Progress in polymer science*, 39(2):251–267, 2014. 4, 16

[65] Banani Kundu, Rangam Rajkhowa, Subhas C Kundu, and Xungai Wang. Silk fibroin biomaterials for tissue regenerations. *Advanced drug delivery reviews*, 65(4):457–470, 2013.

[66] Lorenz Meinel, Sandra Hofmann, Vassilis Karageorgiou, Ludwig Zichner, Robert Langer, David Kaplan, and Gordana Vunjak-Novakovic. Engineering cartilage-like tissue using human mesenchymal stem cells and silk protein scaffolds. *Biotechnology and bioengineering*, 88(3):379–391, 2004.

[67] Chengchen Guo, Chunmei Li, Xuan Mu, and David L Kaplan. Engineering silk materials: From natural spinning to artificial processing. *Applied Physics Reviews*, 7(1):011313, 2020.

[68] Gregory H Altman, Frank Diaz, Caroline Jakuba, Tara Calabro, Rebecca L Horan, Jingsong Chen, Helen Lu, John Richmond, and David L Kaplan. Silk-based biomaterials. *Biomaterials*, 24(3):401–416, 2003.

[69] Leng-Duei Koh, Yuan Cheng, Choon-Peng Teng, Yin-Win Khin, Xian-Jun Loh, Si-Yin Tee, Michelle Low, Enyi Ye, Hai-Dong Yu, Yong-Wei Zhang, et al. Structures, mechanical properties and applications of silk fibroin materials. *Progress in Polymer Science*, 46:86–110, 2015. 4, 14, 16

[70] Ever J Barbero. *Introduction to composite materials design*. CRC press, 2010. 6

[71] Carl Zweben. *Composite Materials*, chapter 10, pages 1–37. John Wiley Sons, Ltd, 2015. 6, 7, 8

[72] Yue Liu, Bernd Zwingmann, and Mike Schlaich. Carbon fiber reinforced polymer for cable structures—a review. *Polymers*, 7(10):2078–2099, 2015. 6

[73] Pankar K Mallick. *Fiber-reinforced composites: materials, manufacturing, and design*. CRC press, 2007. 7, 9

[74] Sujit Das. *The cost of automotive polymer composites: a review and assessment of DOE's lightweight materials composites research*. Oak Ridge National Laboratory Oak Ridge, TN, USA, 2001. 7

[75] K.L. Pickering, M.G. Aruan Efendy, and T.M. Le. A review of recent developments in natural fibre composites and their mechanical performance. *Composites Part A: Applied Science and Manufacturing*, 83:98–112, 2016. Special Issue on Biocomposites. 8

[76] Seçkin Erden and Kingsley Ho. 3 - fiber reinforced composites. In M. Özgür Seydibeyoğlu, Amar K. Mohanty, and Manjusri Misra, editors, *Fiber Technology for Fiber-Reinforced Composites*, Woodhead Publishing Series in Composites Science and Engineering, pages 51–79. Woodhead Publishing, 2017. 8

[77] Faris M Al-Oqla and SM Sapuan. Natural fiber reinforced polymer composites in industrial applications: feasibility of date palm fibers for sustainable automotive industry. *Journal of Cleaner Production*, 66:347–354, 2014. 8

[78] Rosalind Dalefield. Chapter 18 - industrial and occupational toxicants. In Rosalind Dalefield, editor, *Veterinary Toxicology for Australia and New Zealand*, pages 333–341. Elsevier, Oxford, 2017. 8

[79] James Holbery and Dan Houston. Natural-fiber-reinforced polymer composites in automotive applications. *Jom*, 58(11):80–86, 2006. 8

[80] P Balakrishnan, Maya J John, L Pothen, MS Sreekala, and S Thomas. Natural fibre and polymer matrix composites and their applications in aerospace engineering. In *Advanced composite materials for aerospace engineering*, pages 365–383. Elsevier, 2016. 9

[81] Mohammad Asim, Naheed Saba, Mohammad Jawaid, and Mohammad Nasir. Potential of natural fiber/biomass filler-reinforced polymer composites in aerospace applications. In *Sustainable composites for aerospace applications*, pages 253–268. Elsevier, 2018. 8

[82] Kim Hill, Bernard Swiecki, and Joshua Cregger. The bio-based materials automotive value chain. *Center for Automotive Research*, 112, 2012. 9

[83] Brett C Suddell and William J Evans. Natural fiber composites in automotive applications. In *Natural fibers, biopolymers, and biocomposites*, pages 253–282. CRC Press, 2005. 9

[84] Amar K Mohanty, Manjusri Misra, and Lawrence T Drzal. *Natural fibers, biopolymers, and biocomposites*. CRC press, 2005.

[85] Georgios Koronis, Arlindo Silva, and Mihail Fontul. Green composites: A review of adequate materials for automotive applications. *Composites Part B: Engineering*, 44(1):120–127, 2013. 9, 18

[86] Mohammad Jawaid and Mohamed Thariq. *Sustainable composites for aerospace applications*. Woodhead publishing, 2018. 9

[87] A O'donnell, MA Dweib, and RP Wool. Natural fiber composites with plant oil-based resin. *Composites science and technology*, 64(9):1135–1145, 2004. 9

[88] Navin Chand and Mohammed Fahim. *Tribology of natural fiber polymer composites*. Woodhead publishing, 2020. 9

[89] KP Matabola, AR De Vries, FS Moolman, and AS Luyt. Single polymer composites: a review. *Journal of Materials Science*, 44(23):6213–6222, 2009. 9

[90] Ákos Kmetty, Tamás Bárány, and József Karger-Kocsis. Self-reinforced polymeric materials: A review. *Progress in Polymer Science*, 35(10):1288–1310, 2010. 9, 10

[91] Nektaria-Marianthi Barkoula, Ton Peijs, Tilo Schimanski, and Joachim Loos. Processing of single polymer composites using the concept of constrained fibers. *Polymer composites*, 26(1):114–120, 2005. 10

[92] IM Ward. Developments in oriented polymers, 1970–2004. *Plastics, Rubber and Composites*, 33(5):189–194, 2004. 10

[93] J Rasburn, PJ Hine, IM Ward, RH Olley, DC Bassett, and MA Kabeel. The hot compaction of polyethylene terephthalate. *Journal of Materials Science*, 30(3):615–622, 1995. 10

[94] Long Yu, Hongsheng Liu, Katherine Dean, and Ling Chen. Cold crystallization and postmelting crystallization of pla plasticized by compressed carbon dioxide. *Journal of Polymer Science Part B: Polymer Physics*, 46(23):2630–2636, 2008. 10

[95] Ian Macmillan Ward, Phil D Coates, and Michel M Dumoulin. *Solid phase processing of polymers*. Hanser Publishers Munich, Germany:, 2000. 10

[96] DM Bigg, EG Smith, MM Epstein, and RJ Fiorentino. High modulus semicrystalline polymers by solid state rolling. *Polymer Engineering & Science*, 22(1):27–33, 1982.

[97] Galina K Elyashevich, EA Karpov, Olga V Kudasheva, and E Yu Rosova. Structure and time-dependent mechanical behavior of highly oriented polyethylene. *Mechanics of Time-Dependent Materials*, 3(4):319–334, 1999. 10

[98] NB Karthik Babu, Rhoda Afriyie Mensah, Vigneshwaran Shanmugam, Ahmad Rashedi, Pugazhenthi Athimoolam, J Ronald Aseer, and Oisik Das. Self-reinforced polymer composites: An opportunity to recycle plastic wastes and their future trends. *Journal of Applied Polymer Science*, page e53143, 2022. 10

[99] F.V. Lacroix, M. Werwer, and K. Schulte. Solution impregnation of polyethylene fibre/polyethylene matrix composites. *Composites Part A: Applied Science and Manufacturing*, 29(4):371–376, 1998. 10

[100] W. Gindl and J. Keckes. All-cellulose nanocomposite. *Polymer*, 46(23):10221–10225, 2005. 10, 11

[101] R. Chennakeshava, A.M. Sabith, M.A. Amruth, Jevil C.M., and B.C. Shashank. A review on mechanical characterization of natural composites. *International Journal of Engineering Research Technology (IJERT)*, 10(3):246–250, 2021. 12

[102] Gabriele Greco, Hamideh Mirbaha, Benjamin Schmuck, Anna Rising, and Nicola M Pugno. Artificial and natural silk materials have high mechanical property variability regardless of sample size. *Scientific reports*, 12(1):1–9, 2022. 12

[103] Cristina Belda Marín, Vincent Fitzpatrick, David L Kaplan, Jessem Landoulsi, Erwann Guénin, and Christophe Egles. Silk polymers and nanoparticles: a powerful combination for the design of versatile biomaterials. *Frontiers in Chemistry*, 8:604398, 2020. 14, 16

[104] Miguel F Astudillo, Gunnar Thalwitz, and Fritz Vollrath. Life cycle assessment of indian silk. *Journal of Cleaner Production*, 81:158–167, 2014. 12

[105] Chris Holland, Keiji Numata, Jelena Rnjak-Kovacina, and F Philipp Seib. The biomedical use of silk: past, present, future. *Advanced healthcare materials*, 8(1):1800465, 2019. 12

[106] Irene L Good, Jonathan Mark Kenoyer, and Richard Henry Meadow. New evidence for early silk in the indus civilization. *Archaeometry*, 51(3):457–466, 2009.

[107] Thang Phan Nguyen, Quang Vinh Nguyen, Van-Huy Nguyen, Thu-Ha Le, Vu Quynh Nga Huynh, Dai-Viet N Vo, Quang Thang Trinh, Soo Young Kim, and Quyet Van Le. Silk fibroin-based biomaterials for biomedical applications: a review. *Polymers*, 11(12):1933, 2019.

[108] Wenwen Huang, Shengjie Ling, Chunmei Li, Fiorenzo G Omenetto, and David L Kaplan. Silkworm silk-based materials and devices generated using bio-nanotechnology. *Chemical Society Reviews*, 47(17):6486–6504, 2018.

[109] Shanyi Guang, Yang An, Fuyou Ke, Dongmei Zhao, Yuhua Shen, and Hongyao Xu. Chitosan/silk fibroin composite scaffolds for wound dressing. *Journal of Applied Polymer Science*, 132(35), 2015. 12

[110] S.K. Ramamoorthy, M. Skrifvars, and A. Persson. A review of natural fibers used in biocomposites: Plant, animal and regenerated cellulose fibers. *Polymer Reviews*, 55(1):107–162, 2015. 13

[111] F. Vollrath and D. Porter. Silks as ancient models for modern polymers. *Polymer*, 50(24):5623–5632, 2009. 13

[112] Y. Qi, H. Wang, K. Wei, Y. Yang, R.-Y. Zheng, I.S. Kim, and K.-Q. Zhang. A review of structure construction of silk fibroin biomaterials from single structures to multi-level structures. *International Journal of Molecular Sciences*, 18(3), 2017. 13, 16

[113] M.A. Tomeh, R. Hadianamrei, and X. Zhao. Silk fibroin as a functional biomaterial for drug and gene delivery. *Pharmaceutics*, 11(10), 2019.

[114] K. Mori, K. Tanaka, Y. Kikuchi, M. Waga, S. Waga, and S. Mizuno. Production of a chimeric fibroin light-chain polypeptide in a fibroin secretion-deficient naked pupa mutant of the silkworm Bombyx mori. *Journal of Molecular Biology*, 251(2):217–228, 1995.

[115] T. Wongpinyochit, B.F. Johnston, and F.P. Seib. Degradation Behavior of Silk Nanoparticles - Enzyme Responsiveness. *ACS Biomaterials Science and Engineering*, 4(3):942–951, 2018. 13

[116] Cong-Zhao Zhou, Fabrice Confalonieri, Nadine Medina, Yvan Zivanovic, Catherine Esnault, Tie Yang, Michel Jacquet, Joel Janin, Michel Duguet, Roland Perasso, and Zhen-Gang Li. Fine organization of Bombyx mori fibroin heavy chain gene. *Nucleic Acids Research*, 28(12):2413–2419, 06 2000. 14, 15

[117] M.S. Zafar, D.J. Belton, B. Hanby, D.L. Kaplan, and C.C. Perry. Functional material features of Bombyx mori silk light versus heavy chain proteins. *Biomacromolecules*, 16(2):606–614, 2015. 14

[118] S. Inoue, K. Tanaka, F. Arisaka, S. Kimura, K. Ohtomo, and S. Mizuno. Silk fibroin of Bombyx mori is secreted, assembling a high molecular mass elementary unit consisting of H-chain, L-chain, and P25, with a 6:6:1 molar ratio. *Journal of Biological Chemistry*, 275(51):40517–40528, 2000. 14

[119] K. Tanaka, S. Inoue, and S. Mizuno. Hydrophobic interaction of P25, containing Asn-linked oligosaccharide chains, with the H-L complex of silk fibroin produced by Bombyx mori. *Insect Biochemistry and Molecular Biology*, 29(3):269–276, 1999. 14

[120] C.-Z. Zhou, F. Confalonieri, M. Jacquet, R. Perasso, Z.-G. Li, and J. Janin. Silk fibroin: Structural implications of a remarkable amino acid sequence. *Proteins: Structure, Function and Genetics*, 44(2):119–122, 2001. 14

[121] T. Asakura and T. Ito. Structure of alanine and glycine residues of samia cynthia ricini silk fibers studied with solid-state ¡sup¿15¡/sup¿N and¡sup¿13¡/sup¿C NMR. *Macromolecules*, 32(15):4940–4946, 1999. 14

[122] L.P. Gage and R.F. Manning. Internal structure of the silk fibroin gene of Bombyx mori. I The fibroin gene consists of a homogeneous alternating array of repetitious crystalline and amorphous coding sequences. *Journal of Biological Chemistry*, 255(19):9444–9450, 1980.

[123] R. Fedič, M. Žurovec, and F. Sehnal. Correlation between fibroin amino acid sequence and physical silk properties. *Journal of Biological Chemistry*, 278(37):35255–35264, 2003. 14

[124] M. Ishida, T. Asakura, M. Yokoi, and H. Saito. Solvent- and Mechanical-Treatment-Induced Conformational Transjtion of Silk Fibroins Studied by High-Resolution Solid-State 13C NMR Spectroscopy. *Macromolecules*, 23(1):88–94, 1990. 15

[125] Regina Valluzzi, Samuel P Gido, Wayne Muller, and David L Kaplan. Orientation of silk iii at the air-water interface. *International Journal of Biological Macromolecules*, 24(2-3):237–242, 1999. 15

[126] R. Valluzzi and S.P. Gido. The crystal structure of bombyx mori silk fibroin at the air-water interface. *Biopolymers - Nucleic Acid Sciences Section*, 42(6):705–717, 1997. 15

[127] C. Vepari and D.L. Kaplan. Silk as a biomaterial. *Progress in Polymer Science (Oxford)*, 32(8-9):991–1007, 2007. 15, 23, 80

[128] S.Y. Cho, Y.S. Yun, S. Lee, D. Jang, K.-Y. Park, J.K. Kim, B.H. Kim, K. Kang, D.L. Kaplan, and H.-J. Jin. Carbonization of a stable β-sheet-rich silk protein into a pseudographitic pyroprotein. *Nature Communications*, 6, 2015. 16

[129] P. Cebe, B.P. Partlow, D.L. Kaplan, A. Wurm, E. Zhuravlev, and C. Schick. Silk I and Silk II studied by fast scanning calorimetry. *Acta Biomaterialia*, 55:323–332, 2017. 16

[130] W. Sun, D.A. Gregory, M.A. Tomeh, and X. Zhao. Silk fibroin as a functional biomaterial for tissue engineering. *International Journal of Molecular Sciences*, 22(3):1–28, 2021. 16

[131] Simin Ataollahi Oshkovr, Siavash Talebi Taher, Azim Ataollahi Oshkour, Ahmad Kamal Ariffin, and Che Husna Azhari. Finite element modelling of axially crushed silk/epoxy composite square tubes. *Composite Structures*, 95:411–418, 2013. 16

[132] SA Oshkovr, RA Eshkoor, ST Taher, AK Ariffin, and CH Azhari. Crashworthiness characteristics investigation of silk/epoxy composite square tubes. *Composite Structures*, 94(8):2337–2342, 2012.

[133] S Ataollahi, Siavash Talebi Taher, Rahim A Eshkoor, Ahmad Kamal Ariffin, and Che Husna Azhari. Energy absorption and failure response of silk/epoxy composite square tubes: Experimental. *Composites Part B: Engineering*, 43(2):542–548, 2012. 16

[134] Rahim A Eshkoor, Simin Ataollahi Oshkovr, AB Sulong, R Zulkifli, Ahmad Kamal Ariffin, and Che Husna Azhari. Comparative research on the crashworthiness characteristics of woven natural silk/epoxy composite tubes. *Materials & Design*, 47:248–257, 2013. 16

[135] RA Eshkoor, SA Oshkovr, AB Sulong, R Zulkifli, AK Ariffin, and CH Azhari. Effect of trigger configuration on the crashworthiness characteristics of natural silk epoxy composite tubes. *Composites Part B: Engineering*, 55:5–10, 2013. 16

[136] AU Ude, AK Ariffin, and CH Azhari. An experimental investigation on the response of woven natural silk fiber/epoxy sandwich composite panels under low velocity impact. *Fibers and Polymers*, 14(1):127–132, 2013. 16

[137] AU Ude, AK Ariffin, and CH Azhari. Impact damage characteristics in reinforced woven natural silk/epoxy composite face-sheet and sandwich foam, coremat and honeycomb materials. *International Journal of Impact Engineering*, 58:31–38, 2013. 16

[138] Hoi Yan Cheung and Alan Kin Tak Lau. Mechanical performance of silk-based structural composites. In *Experimental Mechanics in Nano and Biotechnology*, volume 326 of *Key Engineering Materials*, pages 457–460. Trans Tech Publications Ltd, 12 2006. 16, 48

[139] Darshil U. Shah, David Porter, and Fritz Vollrath. Opportunities for silk textiles in reinforced biocomposites: Studying through-thickness compaction behaviour. *Composites Part A: Applied Science and Manufacturing*, 62:1–10, 7 2014.

[140] D.U. Shah, D. Porter, and F. Vollrath. Can silk become an effective reinforcing fibre? A property comparison with flax and glass reinforced composites. *Composites Science and Technology*, 101:173–183, 2014.

[141] C. Sealy. Silk shows new strengths in composites. *Reinforced Plastics*, 59(6):294–301, 2015. 16

[142] M. Wojcieszak, A. Percot, and P. Colomban. Regenerated silk matrix composite materials reinforced by silk fibres: Relationship between processing and mechanical properties. *Journal of Composite Materials*, 52(17):2301–2311, 2018. 16, 17, 18

[143] Edilane Laranjeira, LH De Carvalho, SM De L. Silva, and JRM d'Almeida. Influence of fiber orientation on the mechanical properties of polyester/jute composites. *Journal of Reinforced plastics and composites*, 25(12):1269–1278, 2006. 18

[144] Jingyu Chen, Kylie Vongsanga, Xungai Wang, and Nolene Byrne. What happens during natural protein fibre dissolution in ionic liquids. *Materials*, 7(9):6158–6168, 2014. 18, 92

[145] Qichun Liu, Fang Wang, Zhenggui Gu, Qingyu Ma, and Xiao Hu. Exploring the structural transformation mechanism of chinese and thailand silk fibroin fibers and formic-acid fabricated silk films. *International journal of molecular sciences*, 19(11):3309, 2018. 18

[146] F Ren, Z Zhu, and J Li. Nutritious foodstuff-silk extract made from natural silk and making method. *China Patent. CN1152410A*, 1997. 18

[147] Robert A. Mantz, Douglas M. Fox, J. Marshall Green, Paul A. Fylstra, Hugh C. De Long, and Paul C. Trulove. Dissolution of biopolymers using ionic liquids. *Zeitschrift für Naturforschung A*, 62(5-6):275–280, 2007. 18, 19, 20, 23

[148] D.A. Fort, R.C. Remsing, R.P. Swatloski, P. Moyna, G. Moyna, and R.D. Rogers. Can ionic liquids dissolve wood? Processing and analysis of lignocellulosic materials with 1-n-butyl-3-methylimidazolium chloride. *Green Chemistry*, 9(1):63–69, 2007. 18

[149] Richard P. Swatloski, Scott K. Spear, John D. Holbrey, and Robin D. Rogers. Dissolution of cellose with ionic liquids. *Journal of the American Chemical Society*, 124(18):4974–4975, 2002. PMID: 11982358. 19

[150] D.M. Phillips, L.F. Drummy, D.G. Conrady, D.M. Fox, R.R. Naik, M.O. Stone, P.C. Trulove, H.C. De Long, and R.A. Mantz. Dissolution and regeneration of Bombyx mori silk fibroin using ionic liquids. *Journal of the American Chemical Society*, 126(44):14350–14351, 2004. 19, 20, 23, 25, 92

[151] Qin Wang, Yuhong Yang, Xin Chen, and Zhengzhong Shao. Investigation of rheological properties and conformation of silk fibroin in the solution of amimcl. *Biomacromolecules*, 13(6):1875–1881, 2012. 19, 25

[152] G. Carissimi, C.M. Baronio, M.G. Montalbán, G. Víllora, and A. Barth. On the secondary structure of silk fibroin nanoparticles obtained using ionic liquids: An infrared spectroscopy study. *Polymers*, 12(6), 2020.

[153] Omar A El Seoud, Marc Kostag, Shirley Possidonio, Marcella T Dignani, Paulo AR Pires, and Matheus C Lourenço. Dissolution of silk fibroin in mixtures of ionic liquids and dimethyl sulfoxide: On the relative importance of temperature and binary solvent composition. *Polymers*, 14(1):13, 2021.

[154] Hai-Yan Wang, Zheng-Guo Wei, and Yu-Qing Zhang. Dissolution and regeneration of silk from silkworm bombyx mori in ionic liquids and its application to medical biomaterials. *International journal of biological macromolecules*, 143:594–601, 2020. 19

[155] Mercedes G Montalbán, Jeannine M Coburn, A Abel Lozano-Pérez, José L Cenis, Gloria Víllora, and David L Kaplan. Production of curcumin-loaded silk fibroin nanoparticles for cancer therapy. *Nanomaterials*, 8(2):126, 2018.

[156] Nicolas Goujon, Xungai Wang, Rangam Rajkowa, and Nolene Byrne. Regenerated silk fibroin using protic ionic liquids solvents: towards an all-ionic-liquid process for producing silk with tunable properties. *Chemical communications*, 48(9):1278–1280, 2012. 19, 24

[157] H.-Y. Wang, Y.-Q. Zhang, and Z.-G. Wei. Dissolution and processing of silk fibroin for materials science. *Critical Reviews in Biotechnology*, 41(3):406–424, 2021. 19

[158] Hang Heng, Qianqian Deng, Yipeng Yang, and Fang Wang. Recent research progress of ionic liquid dissolving silks for biomedicine and tissue engineering applications. *International Journal of Molecular Sciences*, 23(15):8706, 2022. 19

[159] Cheng-kung Liu, John A Cuculo, and Brent Smith. Coagulation studies for cellulose in the ammonia/ammonium thiocyanate (nh3/nh4scn) direct solvent system. *Journal of Polymer Science Part B: Polymer Physics*, 27(12):2493–2511, 1989. 22

[160] John G. Hardy and Thomas R. Scheibel. Composite materials based on silk proteins. *Progress in Polymer Science*, 35(9):1093–1115, 9 2010. 23

[161] Simone S Silva, Elena G Popa, Manuela E Gomes, Mariana B Oliveira, Sunita Nayak, Bano Subia, João F Mano, Subhas C Kundu, and Rui L Reis. Silk hydrogels from non-mulberry and mulberry silkworm cocoons processed with ionic liquids. *Acta biomaterialia*, 9(11):8972–8982, 2013. 23

[162] G. Cheng, P. Varanasi, C. Li, H. Liu, Y.B. Melnichenko, B.A. Simmons, M.S. Kent, and S. Singh. Transition of cellulose crystalline structure and surface morphology of biomass as a function of ionic liquid pretreatment and its relation to enzymatic hydrolysis. *Biomacromolecules*, 12(4):933–941, 2011. 23

[163] L. Liu, X. Yang, H. Yu, C. Ma, and J. Yao. Biomimicking the structure of silk fibers via cellulose nanocrystal as β-sheet crystallite. *RSC Advances*, 4(27):14304–14313, 2014. 23

[164] Christopher R Gough, Ashley Rivera-Galletti, Darrel A Cowan, David Salas-De La Cruz, and Xiao Hu. Protein and polysaccharide-based fiber materials generated from ionic liquids: A review. *Molecules*, 25(15):3362, 2020. 23

[165] Stacy A Love, Xiao Hu, and David Salas-de la Cruz. Controlling the structure and properties of semi-crystalline cellulose/silk-fibroin biocomposites by ionic liquid type and hydrogen peroxide concentration. *Carbohydrate Polymer Technologies and Applications*, 3:100193, 2022. 23

[166] Narges Johari, Lorenzo Moroni, and Ali Samadikuchaksaraei. Tuning the conformation and mechanical properties of silk fibroin hydrogels. *European Polymer Journal*, 134:109842, 2020. 23

[167] Xin Chen, David P. Knight, and Zhengzhong Shao. β-turn formation during the conformation transition in silk fibroin. *Soft Matter*, 5:2777–2781, 2009. 23

[168] G. Zhou, Z. Shao, D.P. Knight, J. Yan, and X. Chen. Silk fibers extruded artificially from aqueous solutions of regenerated bombyx mori silk fibroin are tougher than their natural counterparts. *Advanced Materials*, 21(3):366–370, 2009. 24

[169] Shengjie Ling, Li Zhou, Wen Zhou, Zhengzhong Shao, and Xin Chen. Conformation transition kinetics and spinnability of regenerated silk fibroin with glycol, glycerol and polyethylene glycol. *Materials Letters*, 81:13–15, 2012. 24

[170] Christopher Hardacre, John D Holbrey, Mark Nieuwenhuyzen, and Tristan GA Youngs. Structure and solvation in ionic liquids. *Accounts of Chemical Research*, 40(11):1146–1155, 2007. 25

[171] Congxia Xie, Wenjing Li, Qingqing Liang, Shitao Yu, and Lu Li. Fabrication of robust silk fibroin film by controlling the content of β-sheet via the synergism of uv-light and ionic liquids. *Applied Surface Science*, 492:55–65, 2019.

[172] Inês P Moreira, Carina Esteves, Susana ICJ Palma, Efthymia Ramou, Ana LM Carvalho, and Ana CA Roque. Synergy between silk fibroin and ionic liquids for active gas-sensing materials. *Materials Today Bio*, page 100290, 2022. 25

[173] Shweta K Vyas and Sanjeev R Shukla. Degumming of tasar silk using imidazolium-based ionic liquids. *The Journal of The Textile Institute*, 111(9):1364–1370, 2020. 25

[174] HP Ren, SQ Sun, and L Li. Dissolution performance of ionic liquid for silk fibroin. *Appl. Chem. Ind.*, 43(7):1255–1257, 2014. 25

[175] AI Susanin, ES Sashina, NP Novoselov, and VV Zakharov. Change of silk fibroin molecular mass during dissolution in ionic liquids. *Fibre Chemistry*, 52(3):208–213, 2020. 25, 30

[176] Antonio Abel Lozano-Pérez, Mercedes García Montalbán, Salvador David Aznar-Cervantes, Francesca Cragnolini, José Luis Cenis, and Gloria Víllora. Production of silk fibroin nanoparticles using ionic liquids and high-power ultrasounds. *Journal of Applied Polymer Science*, 132(12), 2015. 25

[177] Guzmán Carissimi, Cesare M Baronio, Mercedes G Montalbán, Gloria Víllora, and Andreas Barth. On the secondary structure of silk fibroin nanoparticles obtained using ionic liquids: an infrared spectroscopy study. *Polymers*, 12(6):1294, 2020.

[178] CJ Dymek Jr, David A Grossie, Albert V Fratini, and W Wade Adams. Evidence for the presence of hydrogen-bonded ion-ion interactions in the molten salt precursor, 1-methyl-3-ethylimidazolium chloride. *Journal of Molecular Structure*, 213:25–34, 1989.

[179] AI Susanin, ES Sashina, VV Zakharov, M Zaborski, and DA Kashirskii. Conformational transitions of silk fibroin in solutions under the action of ultrasound. *Russian Journal of Applied Chemistry*, 91(7):1193–1197, 2018. 25

[180] Feng Zhang, Xinran You, Hao Dou, Zhi Liu, Baoqi Zuo, and Xueguang Zhang. Facile fabrication of robust silk nanofibril films via direct dissolution of silk in cacl2–formic acid solution. *ACS applied materials & interfaces*, 7(5):3352–3361, 2015. 25

[181] G Freddi, G Pessina, and M Tsukada. Swelling and dissolution of silk fibroin (bombyx mori) in n-methyl morpholine n-oxide. *International Journal of Biological Macromolecules*, 24(2-3):251–263, 1999. 25

[182] Christophe Chipot and Andrew Pohorille. *Free energy calculations*, volume 86. Springer, 2007. 26

[183] A Kayode Coker. *Modeling of chemical kinetics and reactor design*. Gulf Professional Publishing, 2001. 26

[184] Margaret Robson Wright. *Introduction to chemical kinetics*. John Wiley & Sons, 2005. 29

[185] Beth A Miller-Chou and Jack L Koenig. A review of polymer dissolution. *Progress in Polymer Science*, 28(8):1223–1270, 2003. 29

[186] Frithjof Asmussen and Kurt Ueberreiter. Velocity of dissolution of polymers. part ii. *Journal of Polymer Science*, 57(165):199–208, 1962. 29, 30

[187] Harry L. Frisch. "diffusion in polymers" edited by j. crank and g. s. park, academic press, london and new york, 1968; 452 pg. *Journal of Applied Polymer Science*, 14:1657–1657, 1970. 30

[188] Edward Gipstein, Augustus C Ouano, Duane E Johnson, and Omar U Need III. Parameters, affecting the sensitivity of poly (methyl methacrylate) as a positive lithographic resist. *Polymer Engineering & Science*, 17(6):396–401, 1977. 30

[189] AC Ouano and JA Carothers. Dissolution dynamics of some polymers: solvent-polymer boundaries. *Polymer Engineering & Science*, 20(2):160–166, 1980.

[190] RJ Groele and F Rodriguez. Dissolution rates of polymers and copolymers based on methyl, ethyl, and butyl methacrylate. *J Coat Technol*, 61(774):55–8, 1989.

[191] Michael E Ries, Asanah Radhi, Alice S Keating, Owen Parker, and Tatiana Budtova. Diffusion of 1-ethyl-3-methyl-imidazolium acetate in glucose, cellobiose, and cellulose solutions. *Biomacromolecules*, 15(2):609–617, 2014. 30, 34

[192] Wendy J Cooper, Philip D Krasicky, and Ferdinand Rodriguez. Dissolution rates of poly (methyl methacrylate) films in mixed solvents. *Journal of applied polymer science*, 31(1):65–73, 1986. 30

[193] AC Ouano. Dissolution kinetics of polymers: effect of residual solvent content. In *Macromolecular Solutions*, pages 208–217. Elsevier, 1982.

[194] Christopher S Lovell, Adam Walker, Robin A Damion, Asanah Radhi, Steven F Tanner, Tatiana Budtova, and Michael E Ries. Influence of cellulose on ion diffusivity in 1-ethyl-3-methyl-imidazolium acetate cellulose solutions. *Biomacromolecules*, 11(11):2927–2935, 2010.

[195] Qin Wang, Quan Chen, Yuhong Yang, and Zhengzhong Shao. Effect of various dissolution systems on the molecular weight of regenerated silk fibroin. *Biomacromolecules*, 14(1):285–289, 2013. 30

[196] Michael Wöltje, Arthur Kölbel, Dilbar Aibibu, and Chokri Cherif. A fast and reliable process to fabricate regenerated silk fibroin solution from degummed silk in 4 hours. *International Journal of Molecular Sciences*, 22(19):10565, 2021. 30

[197] Nan Zhang, Qiang Wang, Jiugang Yuan, Li Cui, Ping Wang, Yuanyuan Yu, and Xuerong Fan. Highly efficient and eco-friendly wool degradation by l-cysteine-assisted esperase. *Journal of Cleaner Production*, 192:433–442, 2018. 30

[198] Peter Alexander, Robert Francis Hudson, et al. Wool, its chemistry and physics. 1954. 30

[199] Jeanette M Cardamone, JIMING Yao, and Alberto Nuñez. Dcca shrinkproofing of wool: Part i: Importance of antichlorination. *Textile research journal*, 74(6):555–560, 2004. 30

[200] AJ Farnworth. Shrinkproofing of wool with reducing agents. *Journal of the Society of Dyers and Colourists*, 77(10):483–488, 1961.

[201] Sara Campinoti, Asllan Gjinovci, Roberta Ragazzini, Luca Zanieri, Linda Ariza-McNaughton, Marco Catucci, Stefan Boeing, Jong-Eun Park, John C Hutchinson, Miguel Muñoz-Ruiz, et al. Reconstitution of a functional human thymus by postnatal stromal progenitor cells and natural whole-organ scaffolds. *Nature communications*, 11(1):1–16, 2020. 30

[202] Raju Bej, Pradip Dey, and Suhrit Ghosh. Disulfide chemistry in responsive aggregation of amphiphilic systems. *Soft Matter*, 16(1):11–26, 2020. 30

[203] Danielle M Beaupre and Richard G Weiss. Thiol-and disulfide-based stimulus-responsive soft materials and self-assembling systems. *Molecules*, 26(11):3332, 2021. 30

[204] Péter Nagy. Kinetics and mechanisms of thiol–disulfide exchange covering direct substitution and thiol oxidation-mediated pathways. *Antioxidants & redox signaling*, 18(13):1623–1641, 2013. 30

[205] Wilbur I Patterson, WB Geiger, LR Mizell, and M Harris. The rôle of cystine in the structure of the fibrous protein, wool. *Textile Research*, 11(9):379–393, 1941. 31

[206] IJ O'donnell and EOP Thompson. Studies on reduced wool. *Australian Journal of Biological Sciences*, 17(4):973–978, 1964. 31

[207] Kiyoshi Yamauchi, Asao Yamauchi, Tomoo Kusunoki, Akio Kohda, and Yotaro Konishi. Preparation of stable aqueous solution of keratins, and physiochemical and biodegradational properties of films. *Journal of Biomedical Materials Research: An Official Journal of The Society for Biomaterials and The Japanese Society for Biomaterials*, 31(4):439–444, 1996. 31

[208] Takayuki Amiya, Akiyoshi Kawaguchi, Takeaki Miyamoto, and Hiroshi Inagaki. Ordered structure of high-glycine proteins from reduced merino wool. *Sen'i Gakkaishi*, 36(11):T479–T483, 1980. 31

[209] Andrew J Poole and Jeffrey S Church. The effects of physical and chemical treatments on na2s produced feather keratin films. *International journal of biological macromolecules*, 73:99–108, 2015. 31

[210] Andrew J Poole, Russell E Lyons, and Jeffrey S Church. Dissolving feather keratin using sodium sulfide for bio-polymer applications. *Journal of Polymers and the Environment*, 19(4):995–1004, 2011. 31

[211] Long-Tao Zhou, Guang Yang, Xue-Xia Yang, Zhang-Jun Cao, and Mei-Hua Zhou. Preparation of regenerated keratin sponge from waste feathers by a simple method and its potential use for oil adsorption. *Environmental Science and Pollution Research*, 21(8):5730–5736, 2014. 31

[212] Izabela Sinkiewicz, Agata Śliwińska, Hanna Staroszczyk, and Ilona Kołodziejska. Alternative methods of preparation of soluble keratin from chicken feathers. *Waste and biomass valorization*, 8(4):1043–1048, 2017. 31

[213] JM Swan. Thiols, disulphides and thiosulphates: some new reactions and possibilities in peptide and protein chemistry. *Nature*, 180(4587):643–645, 1957. 31, 93, 107

[214] Yimei Ji, Jinyang Chen, Jingxiao Lv, Zhilian Li, Luyao Xing, and Siyuan Ding. Extraction of keratin with ionic liquids from poultry feather. *Separation and Purification Technology*, 132:577–583, 2014. 93

[215] Manpreet Kaur, Muhammad Arshad, and Aman Ullah. In-situ nanoreinforced green bionanomaterials from natural keratin and montmorillonite (mmt)/cellulose nanocrystals (cnc). *ACS Sustainable Chemistry & Engineering*, 6(2):1977–1987, 2018.

[216] Laura Navone and Robert Speight. Understanding the dynamics of keratin weakening and hydrolysis by proteases. *PLoS One*, 13(8):e0202608, 2018. 31

[217] Niloofar Eslahi, Fatemeh Dadashian, and Nahid Hemmati Nejad. An investigation on keratin extraction from wool and feather waste by enzymatic hydrolysis. *Preparative Biochemistry and Biotechnology*, 43(7):624–648, 2013. 31

[218] Xiaoqing Wang, Zhiming Shi, Qinglong Zhao, and Yu Yun. Study on the structure and properties of biofunctional keratin from rabbit hair. *Materials*, 14(2):379, 2021. 31

[219] F Lucas, JTB Shaw, and SG Smith. The silk fibroins. In *Advances in protein chemistry*, volume 13, pages 107–242. Elsevier, 1958. 31

[220] A Robson, JM Woodhouse, and ZH Zaidi. Cystine in silk fibroin, bombyx mori. *International journal of protein research*, 2(1-4):181–189, 1970. 31

[221] Christopher Earland and Simon P Robins. A study of the cystine residues in bombyx mori and other silks. *International Journal of Peptide and Protein Research*, 5(5):327–335, 1973. 31

[222] Kensuke SHIMURA, Aiko KIKUCHI, Yotaro KATAGATA, and Kohei OHOTOMO. The occurrence of small component proteins in the cocoon fibroin of bombyx mori. *The Journal of Sericultural Science of Japan*, 51(1):20–26, 1982. 31

[223] Kazunori Yamaguchi, Yoshimi Kikuchi, Takashi Takagi, Aiko Kikuchi, Fumitaka Oyama, Kensuke Shimura, and Shigeki Mizuno. Primary structure of the silk fibroin light chain determined by cdna sequencing and peptide analysis. *Journal of molecular biology*, 210(1):127–139, 1989. 31, 92

[224] S Grip, J Johansson, and My Hedhammar. Engineered disulfides improve mechanical properties of recombinant spider silk. *Protein Science*, 18(5):1012–1022, 2009. 32

[225] Fujian Jiang, Kai Liu, Meihui Zhao, Xiaocheng Tao, Xiao Hu, and Shenzhou Lu. Tunable high-molecular-weight silk fibroin polypeptide materials: fabrication and self-assembly mechanism. *ACS Applied Bio Materials*, 3(5):3248–3259, 2020. 32

[226] Youssef Hamidi, M. Yalcinkaya, Gorkem Guloglu, Maya Pishvar, Mehrad Amirkhosravi, and M. Altan. Silk as a natural reinforcement: Processing and properties of silk/epoxy composite laminates. *Materials*, 11:2135, 10 2018. 34

[227] James Hawkins, Yunhao Liang, Michael Ries, and Peter Hine. Time temperature superposition of the dissolution of cellulose fibres by the ionic liquid 1-ethyl-3-methylimidazolium acetate with cosolvent dimethyl sulfoxide. *Carbohydrate Polymer Technologies and Applications*, 2:100021, 12 2021. 34, 61

[228] Yunhao Liang, James E. Hawkins, Michael E. Ries, and Peter J. Hine. Dissolution of cotton by 1-ethyl-3-methylimidazolium acetate studied with time–temperature superposition for three different fibre arrangements. *Cellulose*, 28:715 – 727, 2020. 57, 130

[229] Michael E Ries, Asanah Radhi, Stephen M Green, Jamie Moffat, and Tatiana Budtova. Microscopic and macroscopic properties of carbohydrate solutions in the ionic liquid 1-ethyl-3-methyl-imidazolium acetate. *The Journal of Physical Chemistry B*, 122(37):8763–8771, 2018.

[230] Asanah Radhi, Kim Anh Le, Michael E Ries, and Tatiana Budtova. Macroscopic and microscopic study of 1-ethyl-3-methyl-imidazolium acetate–dmso mixtures. *The Journal of Physical Chemistry B*, 119(4):1633–1640, 2015. 34

[231] David M Phillips, Lawrence F Drummy, Deborah G Conrady, Douglas M Fox, Rajesh R Naik, Morley O Stone, Paul C Trulove, Hugh C De Long, and Robert A Mantz. Dissolution and regeneration of bombyx mori silk fibroin using ionic liquids. *Journal of the American Chemical Society*, 126(44):14350—14351, November 2004. 35

[232] M.A. Graewert and D.I. Svergun. Impact and progress in small and wide angle X-ray scattering (SAXS and WAXS). *Current Opinion in Structural Biology*, 23(5):748–754, 2013. 36

[233] N.E. Widjonarko. Introduction to advanced X-ray diffraction techniques for polymeric thin films. *Coatings*, 6(4), 2016. 37

[234] N.G. McCrum, C.P. Buckley, and C.B. Bucknall. *Principles of Polymer Engineering*. Oxford science publications. Oxford University Press, 1988. 40

[235] J. J. Hermans, P. H. Hermans, D. Vermaas, and A. Weidinger. Quantitative evaluation of orientation in cellulose fibres from the x-ray fibre diagram. *Recueil des Travaux Chimiques des Pays-Bas*, 65(6):427–447, 1946. 41

[236] James L. White and Joseph E. Spruiell. The specification of orientation and its development in polymer processing. *Polymer Engineering & Science*, 23(5):247–256, 1983. 41

[237] Luiz F Kawashita, D Roy Moore, and J Gt Williams. Protocols for the measurement of adhesive fracture toughness by peel tests. *The Journal of Adhesion*, 82(10):973–995, 2006. 47

[238] Fritz Vollrath and David Porter. Silks as ancient models for modern polymers. *Polymer*, 50(24):5623–5632, 2009. 48

[239] Johanna Melke, Swati Midha, Sourabh Ghosh, Keita Ito, and Sandra Hofmann. Silk fibroin as biomaterial for bone tissue engineering. *Acta Biomaterialia*, 31:1–16, 2016. 48

[240] Fujia Chen, David Porter, and Fritz Vollrath. Silk cocoon (bombyx mori): multi-layer structure and mechanical properties. *Acta biomaterialia*, 8 7:2620–7, 2012. 48

[241] JO Warwicker. The crystal structure of silk fibroin. *Acta Crystallographica*, 7(8-9):565–573, 1954. 59

[242] Y. Shen, M.A. Johnson, and D.C. Martin. Microstructural characterization of Bombyx mori silk fibers. *Macromolecules*, 31(25):8857–8864, 1998. 59

[243] Ralph H Colby. Breakdown of time-temperature superposition in miscible polymer blends. *Polymer*, 30(7):1275–1278, 1989. 61

[244] Marnix Van Gurp and Jo Palmen. Time-temperature superposition for polymeric blends. *Rheol. Bull*, 67(1):5–8, 1998.

[245] Khushboo Rinawa, SN Maiti, Rodolphe Sonnier, and J-M Lopez Cuesta. Dynamic rheological studies and applicability of time–temperature superposition principle for pa12/sebs-g-ma blends. *Polymer Bulletin*, 72(12):3305–3324, 2015. 61

[246] Keith J. Laidler. The development of the arrhenius equation. *Journal of Chemical Education*, 61(6):494, 1984. 64, 153

[247] Kang Yang, Sujun Wu, Juan Guan, Zhengzhong Shao, and Robert O Ritchie. Enhancing the mechanical toughness of epoxy-resin composites using natural silk reinforcements. *Scientific reports*, 7(1):1–9, 2017. 70

[248] Jutarat Sirichaisit, Victoria L Brookes, Robert J Young, and Fritz Vollrath. Analysis of structure/property relationships in silkworm (bombyx mori) and spider dragline (nephila edulis) silks using raman spectroscopy. *Biomacromolecules*, 4(2):387–394, 2003. 80

[249] Philip M Cunniff, Stephen A Fossey, Margaret A Auerbach, John W Song, David L Kaplan, W Wade Adams, Ronald K Eby, David Mahoney, and Deborah L Vezie. Mechanical and thermal properties of dragline silk from the spider nephila clavipes. *Polymers for advanced technologies*, 5(8):401–410, 1994.

[250] John M Gosline, PA Guerette, CS Ortlepp, and KN Savage. The mechanical design of spider silks: from fibroin sequence to mechanical function. *Journal of Experimental Biology*, 202(23):3295–3303, 1999. 80

[251] Chaoyang Jiang, Xianyan Wang, Ray Gunawidjaja, Y-H Lin, Maneesh K Gupta, David L Kaplan, Rajesh R Naik, and Vladimir V Tsukruk. Mechanical properties of robust ultrathin silk fibroin films. *Advanced functional materials*, 17(13):2229–2237, 2007. 80

[252] Giuliano Freddi, Masuhiro Tsukada, and Silvia Beretta. Structure and physical properties of silk fibroin/polyacrylamide blend films. *Journal of applied polymer science*, 71(10):1563–1571, 1999.

[253] Ratana Rujiravanit, Sopon Kruaykitanon, Alexander M Jamieson, and Seiichi Tokura. Preparation of crosslinked chitosan/silk fibroin blend films for drug delivery system. *Macromolecular Bioscience*, 3(10):604–611, 2003.

[254] Giuliano Freddi, Maria Romanò, Maria Rosaria Massafra, and Masuhiro Tsukada. Silk fibroin/cellulose blend films: preparation, structure, and physical properties. *Journal of Applied Polymer Science*, 56(12):1537–1545, 1995. 80

[255] M.W. Tham, M.R.N. Fazita, H.P.S. Abdul Khalil, N.Z. Mahmud Zuhudi, M. Jaafar, S. Rizal, and M.K.M. Haafiz. Tensile properties prediction of natural fibre composites using rule of mixtures: A review. *Journal of Reinforced Plastics and Composites*, 38(5):211–248, 2019. 82, 84

[256] S.S. Shinde, A.V. Salve, and S. Kulkarni. Theoretical modeling of mechanical properties of woven jute fiber reinforced polyurethane composites. In *Materials Today: Proceedings*, volume 4, pages 1683–1690, 2017. 82

[257] M.A. Escalante-Solís, A. Valadez-González, and P.J. Herrera-Franco. A note on the effect of the fiber curvature on the micromechanical behavior of natural fiber reinforced thermoplastic composites. *Express Polymer Letters*, 9(12):1119–1132, 2015. 82

[258] J. Andersons, E. Sparniņš, and R. Joffe. Stiffness and strength of flax fiber/polymer matrix composites. *Polymer Composites*, 27(2):221–229, 2006. 82

[259] David I. Bower. *An Introduction to Polymer Physics*. Cambridge University Press, 2002. 83

[260] W. Voigt. Ueber die Beziehung zwischen den beiden Elasticitätsconstanten isotroper Körper. *Annalen der Physik*, 274(12):573–587, 1889. 83, 167

[261] Woldemar Voigt. *Lehrbuch der kristallphysik:(mit ausschluss der kristalloptik)*, volume 34. BG Teubner, 1910. 83, 167

[262] A. Reuss. Berechnung der Fließgrenze von Mischkristallen auf Grund der Plastizitätsbedingung für Einkristalle . *ZAMM - Journal of Applied Mathematics and Mechanics / Zeitschrift für Angewandte Mathematik und Mechanik*, 9(1):49–58, 1929. 83, 167

[263] Hyoung-Seop Kim. On the rule of mixtures for the hardness of particle reinforced composites. *Materials Science and Engineering A-structural Materials Properties Microstructure and Processing*, 289:30–33, 2000. 84, 167

[264] N.F.M. Rawi, K. Jayaraman, and D. Bhattacharyya. A performance study on composites made from bamboo fabric and poly(lactic acid). *Journal of Reinforced Plastics and Composites*, 32(20):1513–1525, 2013. 84

[265] Benjamin Raju, SR Hiremath, and D Roy Mahapatra. A review of micromechanics based models for effective elastic properties of reinforced polymer matrix composites. *Composite Structures*, 204:607–619, 2018. 84, 173

[266] MA Sawpan. Hemp fibre reinforced poly (lactic acid) composites ma sawpan, kl pickering and a. fernyhough 2, c. 2007.

[267] KB Shingare and S Naskar. Probing the prediction of effective properties for composite materials. *European Journal of Mechanics-A/Solids*, 87:104228, 2021.

[268] Fatima-Zahra Semlali Aouragh Hassani, Wafa Ouarhim, Mohammed Ouadi Bensalah, Hamid Essabir, Denis Rodrigue, Rachid Bouhfid, and Abou el Kacem Qaiss. Mechanical properties prediction of polypropylene/short coir fibers composites using a self-consistent approach. *Polymer Composites*, 40(5):1919–1929, 2019.

[269] Joseph F Rakow and Anthony M Waas. The effective isotropic moduli of random fibrous composites, platelet composites, and foamed solids. *Mechanics of Advanced Materials and Structures*, 11(2):151–173, 2004. 84, 173

[270] Harry Ku, Hao Wang, N Pattarachaiyakoop, and Mohan Trada. A review on the tensile properties of natural fiber reinforced polymer composites. *Composites Part B: Engineering*, 42(4):856–873, 2011. 88

[271] S.B. Brahim and R.B. Cheikh. Influence of fibre orientation and volume fraction on the tensile properties of unidirectional Alfa-polyester composite. *Composites Science and Technology*, 67(1):140–147, 2007. 88

[272] Oliver Smithies. Disulfide-bond cleavage and formation in proteins. *Science*, 150(3703):1595–1598, 1965. 92

[273] Philip J Hogg. Disulfide bonds as switches for protein function. *Trends in biochemical sciences*, 28(4):210–214, 2003.

[274] Katra Kolšek, Camilo Aponte-Santamaría, and Frauke Gräter. Accessibility explains preferred thiol-disulfide isomerization in a protein domain. *Scientific reports*, 7(1):1–10, 2017. 92

[275] Xueliang Xiao and Jinlian Hu. Influence of sodium bisulfite and lithium bromide solutions on the shape fixation of camel guard hairs in slenderization process. *International Journal of Chemical Engineering*, 2016, 2016. 92

[276] Amin Shavandi, Alaa El-Din A Bekhit, Alan Carne, and Adnan Bekhit. Evaluation of keratin extraction from wool by chemical methods for bio-polymer application. *Journal of bioactive and compatible polymers*, 32(2):163–177, 2017. 93

[277] S.R. Clough. Sodium sulfite. In Philip Wexler, editor, *Encyclopedia of Toxicology (Third Edition)*, pages 341–343. Academic Press, Oxford, third edition edition, 2014. 93

[278] M.D. Danyluk, M.E. Parish, R.M. Goodrich-Schneider, and R.W. Worobo. 6 - microbial decontamination of juices11the opinions and conclusions expressed in this manuscript are solely the views of the authors and do not necessarily reflect those of the food and drug administration. In Ali Demirci

and Michael O. Ngadi, editors, *Microbial Decontamination in the Food Industry*, Woodhead Publishing Series in Food Science, Technology and Nutrition, pages 163–189. Woodhead Publishing, 2012.

[279] S.C. Gad. Sulfites. In Philip Wexler, editor, *Encyclopedia of Toxicology (Third Edition)*, pages 416–419. Academic Press, Oxford, third edition edition, 2014. 93

[280] John Andrew Brydson. *Plastics materials*. Elsevier, 1999. 107

[281] Theodore W Thannhauser, Yasuo Konishi, and Harold A Scheraga. Sensitive quantitative analysis of disulfide bonds in polypeptides and proteins. *Analytical biochemistry*, 138(1):181–188, 1984. 107

[282] M-H Morel, Joëlle Bonicel, V Micard, and S Guilbert. Protein insolubilization and thiol oxidation in sulfite-treated wheat gluten films during aging at various temperatures and relative humidities. *Journal of Agricultural and Food Chemistry*, 48(2):186–192, 2000. 107

[283] J Leggett Bailey and R David Cole. Studies on the reaction of sulfite with proteins. *J Biol Chem*, 234(7):1733–1739, 1959. 107

[284] H-D Belitz, Werner Grosch, and Peter Schieberle. *Food chemistry*. Springer Science & Business Media, 2008. 107

[285] Felicia Hammann and Markus Schmid. Determination quantification of molecular interactions in protein films: A review. *Materials*, 7(12):7975–7996, 2014. 107

[286] Krishan K Chawla. *Composite materials: science and engineering*. Springer Science & Business Media, 2012. 112

[287] Paul E McMahon and Lincoln Ying. Effects of fiber/matrix interactions on the properties of graphite/epoxy composites. Technical report, CELANESE RESEARCH CO SUMMIT NJ, 1982. 112

[288] M. Schmid, T.K. Prinz, A. Stäbler, and S. Sängerlaub. Effect of sodium sulfite, sodium dodecyl sulfate, and urea on the molecular interactions and properties of whey protein isolate-based films. *Frontiers in Chemistry*, 5(JAN), 2017. 113

[289] Ei M Asloun, M Nardin, and J Schultz. Stress transfer in single-fibre composites: effect of adhesion, elastic modulus of fibre and matrix, and polymer chain mobility. *Journal of materials science*, 24(5):1835–1844, 1989. 113

[290] JL Thomason. The influence of fibre length, diameter and concentration on the strength and strain to failure of glass fibre-reinforced polyamide 6, 6. *Composites Part A: applied science and manufacturing*, 39(10):1618–1624, 2008. 117

[291] Christoph Unterweger, Tina Mayrhofer, Francesco Piana, Jiri Duchoslav, David Stifter, Claudia Poitzsch, and Christian Fürst. Impact of fiber length and fiber content on the mechanical properties and electrical conductivity of short carbon fiber reinforced polypropylene composites. *Composites Science and Technology*, 188:107998, 2020.

[292] Praveena Bindiganavile Anand, Avinash Lakshmikanthan, Manjunath Patel Gowdru Chandrashekarappa, Chithirai Pon Selvan, Danil Yurievich Pimenov, and Khaled Giasin. Experimental investigation of effect of fiber length on mechanical, wear, and morphological behavior of silane-treated pineapple leaf fiber reinforced polymer composites. *Fibers*, 10(7):56, 2022. 117

[293] Changming Zhu and CT Sun. Micromechanical modeling of fiber composites under off-axis loading. *Journal of Thermoplastic Composite Materials*, 16(4):333–344, 2003. 117

[294] Jia-Lin Tsai and Yang-Kai Chi. Effect of fiber array on damping behaviors of fiber composites. *Composites Part B: Engineering*, 39(7-8):1196–1204, 2008.

[295] Royan J D'Mello and Anthony M Waas. Influence of unit cell size and fiber packing on the transverse tensile response of fiber reinforced composites. *Materials*, 12(16):2565, 2019.

[296] Sabarinathan P Subramaniyan, Muhammad A Imam, and Pavana Prabhakar. Fiber packing and morphology driven moisture diffusion mechanics in reinforced composites. *Composites Part B: Engineering*, 226:109259, 2021. 117

[297] Marek-Jerzy Pindera and Brett A Bednarcyk. An efficient implementation of the generalized method of cells for unidirectional, multi-phased composites with complex microstructures. *Composites part B: engineering*, 30(1):87–105, 1999. 117

[298] Nicolas Le Moigne, Martien van Den Oever, and Tatiana Budtova. A statistical analysis of fibre size and shape distribution after compounding in composites reinforced by natural fibres. *Composites Part A: Applied Science and Manufacturing*, 42(10):1542–1550, 2011.

[299] Dong Gi Seong, Chul Kang, Seong Yeol Pak, Chai Hwan Kim, and Young Seok Song. Influence of fiber length and its distribution in three phase poly (propylene) composites. *Composites Part B: Engineering*, 168:218–225, 2019. 117

[300] Suntharavathanan Mahalingam, Bahijja Tolulope Raimi-Abraham, Duncan Q.M. Craig, and Mohan Edirisinghe. Solubility–spinnability map and model for the preparation of fibres of polyethylene (terephthalate) using gyration and pressure. *Chemical Engineering Journal*, 280:344–353, 11 2015. 130

[301] J. Sun, F. Wang, Y. Sui, Z. She, W. Zhai, C. Wang, and Y. Deng. Effect of particle size on solubility, dissolution rate, and oral bioavailability: Evaluation using coenzyme Q¡inf¿10¡/inf¿ as naked nanocrystals. *International Journal of Nanomedicine*, 7:5733–5744, 2012. 130

[302] Quazi TH Shubhra, M. Saha, AKMM Alam, MDH Beg, and Mubarak A Khan. Effect of matrix modification by natural rubber on the performance of silk-reinforced polypropylene composites. *Journal of Reinforced Plastics and Composites*, 29(22):3338–3344, 2010. 135

[303] Aart Willem Van Vuure, Jan Vanderbeke, Yasmine Mosleh, Ignaas Verpoest, and Nedda El-Asmar. Ductile woven silk fibre thermoplastic composites with quasi-isotropic strength. *Composites Part A: Applied Science and Manufacturing*, 147:106442, 2021. 135

[304] M. Grujicic, R. Yavari, J. Snipes, S. Ramaswami, Chian-Feng Yen, and B. Cheeseman. The effect of plain-weaving on the mechanical properties of warp and weft p-phenylene terephthalamide (ppta) fibers/yarns. *Journal of Materials Science*, 49, 12 2014. 138

[305] J.J. Hermans, P.H. Hermans, D. Vermaas, and A. Weidinger. Quantitative evaluation of orientation in cellulose fibres from the X-ray fibre diagram. *Recueil des Travaux Chimiques des Pays-Bas*, 65(6):427–447, 1946. 151

[306] J.D. Ferry. *Viscoelastic properties of polymers*. 1980. 152

[307] A. Amiri, C.A. Ulven, and S. Huo. Effect of chemical treatment of flax fiber and resin manipulation on service life of their Composites using time-temperature superposition. *Polymers*, 7(10):1965–1978, 2015.

[308] Y. Liang, J.E. Hawkins, M.E. Ries, and P.J. Hine. Dissolution of cotton by 1-ethyl-3-methylimidazolium acetate studied with time–temperature superposition for three different fibre arrangements. *Cellulose*, 28(2):715–727, 2021. 152

[309] Yehia E. Elmogahzy. Finished fibrous assemblies. *Engineering Textiles*, pages 275–298, 1 2020. 164

[310] P.R. Laity and C. Holland. Thermo-rheological behaviour of native silk feedstocks. *European Polymer Journal*, 87:519–534, 2017. 165

[311] Y. Liu, L. Yang, and C. Ma. Thermal analysis and kinetic study of native silks. *Journal of Thermal Analysis and Calorimetry*, 139(1):589–595, 2020. 165

[312] Q. Liu, F. Wang, Y. Li, H. Yu, Q. Ma, and Z. Gu. Comparative studies of structure, thermal decomposition mechanism and thermodynamic parameters of two kinds of silk fibroin films. *Scientia Sinica Chimica*, 49(7):1014–1029, 2019. 165

[313] R Hill. The elastic behaviour of a crystalline aggregate. *Proceedings of the Physical Society. Section A*, 65(5):349–354, may 1952. 167

[314] L. Yan, N. Chouw, and X. Yuan. Improving the mechanical properties of natural fibre fabric reinforced epoxy composites by alkali treatment. *Journal of Reinforced Plastics and Composites*, 31(6):425–437, 2012. 167